Dissertation presented

as a partial requirement for the degree of

Doctor of Science

First Measurement of Muon Neutrino Charged Current Quasi-elastic to Charged Current Inclusive Cross Section Ratio on a Hydrocarbon Target at Neutrino Energies 2-10 GeV

David Alejandro Martínez Caicedo

Advisor:
Hélio da Motta Filho

Centro Brasileiro de Pesquisas Físicas

Rio de Janeiro, August 2014

Dedicado a mi abuela, mi madre y tia.

Acknowledgements

First of all !Thank you God!.
I would like to thank my advisor Dr. Hélio da Motta. There was really nice work with him since I arrive to CBPF in 2008. From MINERνA collaboration, a huge thanks to the spokespersons Dr. Deborah Harris, Dr. Kevin McFarland, Dr. Jorge Morfin for the amazing effort for the sucess of the experiment. Thanks to Dr. David Schmitz for his enormous help and teaching during the first stages of this analysis, also to Dr. Brian Tice, Dr. Trung Lee, Dra. Laura Fields and Dr. Mousumi Datta, I have learn a lot from their experience to figure out the puzzles that appear at the time to make the analysis presented in this dissertation. To all my FERMILAB friends, specially Laza and his wife Hansu, they were always dispossed to help in good and not so good times, their wisdow and humility are unique, it is a privilege have friends like them. To FERMILAB administrative staff Amanda Thompson, Samantha Poeppelman, Kappatolia Sherman, Barbara Book, Crae Tate, Jackie Cyko and Cheryl Patrick.
This work is dedicated to my family. Specially to my mother, and my aunt Kathy, they were very important during the development of this thesis. To all my uncles, specially Villa and Hugo, for their wisdom and advices. To Ruth and Jose, that more than friends they are like my sister and brother! always giving good advices in personal and academic aspects. Thanks for all FISHYS. To the **Ilustre** Dr. Arturo Fiorentini, an amazing person and worker, I have learn a lot from him and was a really nice experience work by the side of the famous **Ninja**.
To my professors Juan Florez and Alberto Quijano at the University of Nariño. Finally, to all my friends, many of them following this academic life, to Alex, Richard and their families, they were a big support in the beginning of my career. To my friends from Pasto Edwin, William, Alex, Lorena, Andrea, Leidy, Greis, Cesar, Diego and from Peru Elvis and Cesar Sotelo. This work was made possible by a scholarship from the Brazilian Coordenação de Aperfeiçoamento de Pessoal de Nível Superior (CAPES) from 2010 to 2014.

Agradecimientos

Primero que todo !Gracias Dios!.
Aagradezco a mi asesor Dr. Helio da Motta, fue una gran experiencia trabajar con el desde que llegue al CBPF en 2008. A los directores de la colaboración del experimento MINERνA Dr. Deborah Harris, Dr. Kevin MacFarland, Dr. Jorge Morfin por su constante esfuerzo para el éxito del experimento y por consiguiente que este resultado sea presentado. Al Professor David Schmitz por su gran ayuda y enseñanzas durante las diferentes etapas de este análisis, también al Dr. Brian Tice, Dr. Trung Lee, Dra. Laura Fields y la Dra. Mousumi Datta, aprendí mucho de la experiencia de ellos para resolver diferentes los diferentes retos presentes en el desarrollo de este trabajo. Este trabajo de varios años de esfuerzo es dedicado a mi familia. En especial a mi Madre, y mi tía Kathy, dos personas que han sido muy importantes durante todo el trayecto para lograr los resultados presentes en este trabajo. A todos mis tios en especial a Villa y Hugo, siempre con sus sabios consejos en el momento que era necesario. A mis hermanas y primo daniel los cuales ya estan a punto de comenzaran la vida académica. A Jose y a Ruth que mas que amigos son mis hermanos y siempre estuvieron dado los consejos necesarios en todos los aspectos no solo el académico! Gracias por todo Fishys! Al ilustre Dr. Arturo Fiorentini! un gran trabajador, una gran persona de la cual aprendí mucho para desarrollar esta tesis, fue una gran experiencia trabaja de lado del Ninja! A mis profesores de la Universidad de Nariño Juan Florez y Alberto Quijano. A todos los amigos que conocí durante mi estancia en Fermilab y en el CBPF, Hector, Elvis, Cesar Sotelo. En especial a Laza y su esposa Hansu, siempre dispuestos a ayudarme en los buenos y malos momentos, su sabiduría y humildad son únicos, es un privilegio tener amigos como ustedes. A mis amigos de Colombia, de los cuales gran parte siguen en este camino académico, Edwin, William, Alex, Lorena, Andrea, Leidy, Greis y Cesar (y a todos los que no mencione :)). Alex, Richard y sus familias, gracias por todo su apoyo, sobretodo en el comienzo de la carrera. Este trabajo fue posible gracias a una beca de Coordenação de Aperfeiçoamento de Pessoal de Nível Superior (CAPES) de Brasil entre 2010 y 2014.

Abstract

In this thesis, we present the first measurement of muon neutrino charged current quasi-elastic to charged current inclusive cross section ratio on a polystyrene scintillator (CH) in the MINERνA detector at neutrino energies between 2 and 10 GeV. The dataset used was taken between March and July 2010 with a total of 9.60×10^{19} protons on target. The charged current inclusive interactions were selected by requiring a negative muon. The charged current quasi-elastic interactions were selected by requiring a negative muon and a low calorimetric recoil energy out of the interaction vertex. The analysis was performed on 105,245 charged current inclusive candidates and 30,000 charged current quasi-elastic candidates in MINERνA fine-grained scintillator tracker region. The measurement is reported in function of neutrino energy. Taking the ratio, reduces the systematic uncertainties, mainly coming from the flux. We compare our results to the prediction of the models implemented in the neutrino event generator (GENIE 2.6.2).

Resumo

Apresentamos a primeira medida da razão entre a seção de choque quase-elástica e a seção de choque inclusiva de interações de corrente carregada de neutrinos muônicos em cintilador de poliestireno (CH) no detector MINERνA com a energia dos neutrinos na faixa entre 2 e 10 GeV. Empregamos dados tomados entre março e julho de 2010 num total de $9{,}60\times10^{19}$ prótons em alvo. As interações inclusivas em corrente carregada foram selecionadas exigindo-se a presença de um múon negativo. As interações quase-elásticas em corrente carregada foram selecionados exigindo-se a presença de um múon negativo e uma baixa energia de recuo fora do vértice de interação. A análise foi realizada em 105.245 candidatos a eventos inclusivos em corrente carregada e em 30.000 candidatos a eventos quase-elásticos em corrente carregada na região de rastreamento do MINERνA. A medida é apresentada em função da energia do neutrino. O emprego da razão reduz as incertezas sistemáticas que são, majoritariamente, devidas ao fluxo. Comparamos nossos resultados com as previsões dos modelos implementados no gerador de eventos GENIE 2.6.2.

The MINERνA Collaboration

I.Albayrak[7],L. Aliaga[15],M. Andrews[5],S. Avvakumov[16], B. Baldin[5],J.L. Bazo[15],G. Blazey[12], A. Bodek[16], D. Boehnlein[5],S. Boyd[14], R. Bradford[16],W.K. Brooks[10], A. Bruell[10], D. Buchholtz[13], H. Budd[16],D. Casper[3],C. Castromonte[2],D. Cherdack[19],M.E. Christy[7], J. Chvojka[16],M.A.C. Cummings[12],D.S. Damiani[21],D. Drakoulakos[1],S. Dytman[14],R. Ent[10], G.A.Fiorentini[2],J. Felix[6],R. Flight[16],A. Gago[15],H. Gallagher[19],D. Gaskell[10],R. Gilman[17], C. Gingu[5],C. Glasshausser[17],R. Gran[11], N. Grossman[5],D. A. Harris[5],X. Jiang[17],T. Kafka[19], C.E Keppel[7],J. Kilmer[5],S. M.S. Kim[14],Kopp[18], M. Kostin[5],S.Kulagin[8],G. Kumbartzki[17], L. Loiacano[18],S. Manly[16], W.A. Mann[19],K. McFarland[16],D. Meekins[10],W. Melnitchouk[10], G. Moreno[6],J.G. Morfin[5],H. da Motta[2],D. Naples[14],J.K. Nelson[21], G. Niculescu[9], I. Niculescu[9],R. Ochoa[20],W. Oliver[19],J.L.Palomino[2],V. Paolone[14],J. Park[16],E. Paschos[4], O. Pereyra[20],A. Pla-Dalmau[5],M. Proga[18],R. Ransome[17],M. A. Reyes[6],P. Rubinov[5], V. Rykalin[12],W. Sakumoto[16],P. Shanahan[5],H. Schellman[13],R.M. Schneider[21],E. Schulte[17], C. Simon[3],J. Solano[20],P. Spentzouris[5],P. Stamoulis[1],J. Steinman[16],J. Tatar[3],V. Tvaskis[7], G. Tzanakos[1],M. Vaz[2],S. Wood[10],G. Zavala[6],B. Ziemer[3],M. Zois[1]

University of Athens, Athens, Greece[1]
Centro Brasileiro de Pesquisas Fisicas, Rio de Janeiro, Brazil[2]
University of California, Irvine, California[3]
University of Dortmund, Dortmund, Germany[4]
Fermi National Accelerator Laboratory, Batavia, Illinois[5]
Universidad de Guanajuato, Guanajuato, Mexico[6]
Hampton University, Hampton, Virginia[7]
Institute for Nuclear Research, Moscow, Russia[8]
James Madison University, Harrisonburg, Virginia[9]
Jefferson Lab, Newport News, Virginia[10]
University of Minnesota Duluth, Duluth, Minnesota[11]
Northern Illinois University, DeKalb, Illinois[12]
Northwestern University, Evanston, IL[13]
University of Pittsburgh, Pittsburgh, Pennsylvania[14]
Pontificia Universidad Catolica del Peru, Lima, Peru[15]
University of Rochester, Rochester, New York[16]
Rutgers University, New Brunswick, New Jersey[17]
University of Texas-Austin, Texas[18]
Tufts University, Medford, Massachusetts[19]
Universidad Nacional de Ingenieria. Lima, Peru[20]
William and Mary College, Williamsburg, Virginia[21]

Contents

Acknowledgements **ii**

Agradecimientos **iii**

Abstract **iv**

Resumo **v**

The MINERνA Collaboration **vi**

1 Introduction **1**

2 Neutrino Physics **3**

2.1 History 3

2.2 Neutrino Properties 5

2.2.1 Neutrino Flavors 5

2.2.2 Helicity 5

2.2.3 Neutrino mass 5

2.3 Neutrino Sources 6

2.4 The Weak Interaction 9

2.5 Neutrino in the Standard Model 11

2.6 Oscillation 13

2.7 The EMC Effect 14

2.8 Neutrino cross sections 15

2.8.1 Inclusive cross section 16

2.8.2 Resonant single pion, photon , η and kaon production 20

2.8.3 Coherent pion production 21

2.8.4 Deep Inelastic Scattering (DIS) 23

2.8.5 Quasielastic scattering 24

2.9 Interaction Reconstruction for Charged Current Quasi-Elastic and Charged Current Inclusive scattering . . . 28
2.10 Summary and status of charged current neutrino and antineutrino cross sections measurements and results from oscillation experiments . . . 29
2.10.1 Recent results from MINERνA experiment: . . . 30
2.10.2 Results from oscillation experiments . . . 34

3 MINERνA Detector 38
3.1 The ν_μ at Main Injector (NuMI Beam) . . . 38
3.2 Proton Production for NuMI beamline . . . 39
3.3 The MINERνA detector . . . 41
3.4 The Veto wall . . . 46
3.5 The scintillating strips . . . 46
3.6 Photodevices . . . 47
3.7 Calorimeters . . . 48
3.7.1 Electromagnetic calorimeter . . . 49
3.7.2 Hadronic calorimeter . . . 50
3.8 Nuclear targets . . . 50
3.9 The Outer Detector OD . . . 51
3.10 Electronic and data acquisition (DAQ) . . . 52
3.10.1 DAQ hardware . . . 53
3.10.2 DAQ software . . . 54
3.10.3 MINOS Near Detector . . . 54
3.10.4 Data Run Periods . . . 55

4 Reconstruction and Simulation 58
4.1 Introduction . . . 58
4.2 Hit Calibration . . . 58
4.2.1 Position . . . 59
4.2.2 Time . . . 59
4.2.3 Energy . . . 59
4.3 Ex situ calibrations . . . 60
4.3.1 Front End Boards . . . 60
4.3.2 Photomultiplier Tubes . . . 60
4.3.3 Mapper Modules . . . 61
4.4 In situ calibrations . . . 61
4.4.1 Pedestals . . . 61

4.4.2 PMT Gains 62
4.4.3 Channel to Channel Calibrations 62
4.4.4 Absolute Energy Scale 63
4.4.5 Timing 64
4.4.6 CrossTalk 64
4.5 Reconstruction 64
4.5.1 Clustering Hits by time 65
4.5.2 Clustering Hits by position 65
4.5.3 Event information based on a track 67
4.5.4 Vertex Fitting 70
4.5.5 Muon Reconstruction 71
4.5.6 Reconstruction of Recoil System 72
4.6 The Simulation 74
4.6.1 NuMI Flux 74
4.6.2 Reweighting of $p + C$ interactions 77
4.6.3 Flux Results 79
4.6.4 GENIE: The neutrino event generator 79
4.6.5 Event simulation on the MINERνA detector 85

5 Measuring the total cross section for charged current inclusive $\sigma_{ccinc}(E_\nu)$ and charged current quasi-elastic $\sigma_{ccqe}(E_\nu)$ interactions in MINERvA 88

5.1 Introduction 88
5.2 Event Selection 89
5.2.1 Muon Identification: CCINC and CCQE 90
5.2.2 Fiducial Volume: CCINC and CCQE 91
5.2.3 Reconstructing the neutrino Energy 92
5.2.4 Recoil Energy 94
5.3 Selected Samples 98
5.4 Measurement of CCINC and CCQE cross sections 99
5.4.1 Background Subtraction 100
5.4.2 Unfolding 103
5.4.3 Efficiency Correction 106
5.4.4 Flux and target normalization 108
5.5 Systematic Uncertainties 111
5.5.1 Flux 113
5.5.2 Muon Energy Reconstruction 115

5.5.3 Unfolding . . . 115
5.5.4 Recoil Reconstruction . . . 116
5.5.5 Final State Interaction Models (FSI Models) . . . 117
5.5.6 Cross section Models (XSec Models) . . . 119
5.5.7 Reconstruction efficiency corrections (Norm. Corrections) . . . 119
5.5.8 Detector Mass Scale . . . 120
5.5.9 Absolute Eneryg Scale (MEU) . . . 120

6 Measurement of ratio $\frac{\sigma_{ccqe}(E_\nu)}{\sigma_{ccinc}(E_\nu)}$ in neutrino energy range 2 - 10 GeV 121
6.1 Introduction . . . 121
6.2 Ratio Calculation . . . 121
6.2.1 Results . . . 122
6.3 Angular acceptance cut . . . 123
6.3.1 Results obtained with $\theta_\mu < 20^0$ . . . 125

7 Conclusions 129

A Work inside MINERνA collaboration 131
A.1 Commisioning of the Test Beam Project . . . 131
A.2 PMT Testing . . . 132
A.3 Charged current inclusive cross section machinery over different datasets . . . 134
A.4 Special Runs . . . 135
A.5 Rock Muon Algorithm . . . 135
A.6 Cross talk studies . . . 136
A.7 RawDigit Checker . . . 136
A.8 Multiple Vertex Studies Algorithm . . . 137
A.9 Data taking Shifts . . . 137

Bibliography 139

List of Figures

2.1 Solar cycle and the resulting solar neutrino energy spectrum. 8

2.2 Thermal history of the universe. 9

2.3 Feynman diagram of neutrino interaction vertex in the case of charged current interactions. 10

2.4 Feynman diagrams of neutrino interaction vertex in the case of neutral current interactions. 10

2.5 Feynman diagramas of neutrino interactions for charged and neutral current interactions. The leptons are noted by l. 15

2.6 Variable definition for the Charged Current Inclusive channel. 17

2.7 Total charged current ν_μ (top) and $\overline{\nu}_\mu$ nucleon (bottom) inclusive cross section as a function of neutrino energy. Low energy region is dominated by the quasi-elastic contribution (QE dotted), the intermediate region by resonance (RES) contribution (dashed) and the high energy region by the Deep Inelastic Scattering (DIS) contribution (dashed-dotted). As can be seen, measurements mainly concentrate in the DIS region and measurements in the RES region suffer from larger uncertainties, while very few measurements cover the QE region [53]. . . . 19

2.8 Feynman diagram of a single nucleon resonance. 20

2.9 Feynman diagram of coherent pion production. 21

2.10 Measurements of absolute coherent pion production cross sections from a variety of nuclear targets and samples. Both NC and CC data are displayed on the same plot after rescaling the CC data using the prediction that $\sigma_{NC} = \frac{1}{2}\sigma_{CC}$. In addition, data from various targets have been corrected to carbon cross sections assuming $A^{1/3}$ scaling. Figure taken from reference [50]. 23

2.11 Feynman diagram of Deep Inelastic Scattering. 24

2.12 Cross section, $\nu_\mu n \to \mu^- p$, as a function of neutrino energy on a variety of nuclear targets. The free nucleon scattering prediction assuming $M_A = 1.0\ GeV$ is shown for comparison. 27

2.13 Cross section, $\bar{\nu}_\mu p \to \mu^+ n$, as a function of neutrino energy on a variety of nuclear targets. 27
2.14 Total neutrino per nucleon CC cross sections (for an isoscalar target) per neutrino energy as a function of energy. Same data as in figures 2.12 and 2.13, plus additional low energy CC inclusive data from ▲ ([65]), $*$ ([66]), ■ ([67]), and ★ ([68]). Predictions provided by the NUANCE generator. Figure taken from reference [50]. 30
2.15 Total anti-neutrino per nucleon CC cross sections per neutrino energy as a function of energy. Same data as in figures (2.12, 2.13), plus additional low energy CC inclusive data from ▲ ([65]), $*$ ([66]), ■ ([67]), and ★ ([68]). Predictions provided by the NUANCE generator. Figure taken from reference [50]. 31
2.16 Ratios of the charged-current inclusive ν_μ cross section per nucleon as a function of reconstructed Bjorken x for C/CH (top), Fe/CH (middle), and Pb/CH (bottom). Error bars on the data (simulation) show the statistical (systematic) uncertainties [69]. 32
2.17 Ratio between the measured neutrino $d\sigma/dQ^2_{QE}$ shape in Q^2_{QE} and several different models where the denominator is the GENIE default quasi-elastic cross section [70]. 33
2.18 Reconstructed vertex energy of events passing the selection criteria in the data (points with statistical errors) compared to the GENIE RFG model (shown with systematic errors) for $Q^2_{QE} < 0.2GeV^2/c^2$ (top) and for $Q^2_{QE} > 0.2GeV^2/c^2$ (bottom) [70]. 33
2.19 Ratio between the measured neutrino $d\sigma/dQ^2_{QE,p}$ shape in $Q^2_{QE,p}$ and several different models where the denominator is the GENIE default quasi-elastic cross section [72]. 34
2.20 Comparisons of the one-pion measurements to various models. The cross sections are on the top, and the shape measurements are on the bottom [73]. 35
2.21 Results from the Double-CHOOZ, Daya Bay and RENO experiment (left, middle and right respectively). Each result is shown in the same unified manner. **TOP**: Measured prompt energy spectrum of the far detector compared with the no-oscillation prediction from the measurements of the two near detectors. Spectra were background subtracted (for Daya Bay and RENO) and includes background for Double-CHOOZ. Inset (Double-CHOOZ and RENO): stacked histogram of backgrounds. Uncertainties are statistical only. **BOTTOM**: The ratio of measured and predicted no-oscillation spectra. The red curve is the best-fit solution and the dashed line is the no-oscillation prediction [75], [76], [77]. 36

2.22 Left: T2K distributions of ν_e event selection variables vs reconstructed neutrino energy. Blue arrows indicate the selection criteria. Right: MINOS reconstructed energy distribution. The NC background is shown in blue. 36

3.1 NuMI beamline components. 38
3.2 Schematic showing positions of the NuMI target, baffle and horns. [82] 39
3.3 The NuMI secondary absorbers and muon monitors. 40
3.4 NuMI configurations. Low Energy and Medium Energy, Flux estimation using a GEANT4 based simulation of the NuMI beam line. 41
3.5 Top view of the MINERνA detector. 42
3.6 Schematic view of the MINERνA detector. 43
3.7 Detector active module, X, U and V planes. Note the $\pm$ 60^0 rotation of the planes U and V relative to the X planes. 44
3.8 Detector active module. Structure of a module is depicted on the right. 44
3.9 Module of the electromagnetic calorimeter. Structure of modules is depicted on the right. 45
3.10 Module of the hadronic calorimeter. Structure of the modules with alternating Fe and scintillating planes is depicted on the right. 45
3.11 Transversal cut of the triangular scintillating prism used in the Inner Detector. . 46
3.12 Scintillating prisms arranged to form a plane. Each prism holds an optical fiber along its full length. 47
3.13 Fiber mapping of MINERνA PMT. 49
3.14 MINERνA Nuclear targets. 52
3.15 Schematic diagram of MINERνA data acquisition system. 55
3.16 The MINOS near detector (left) as viewed from above and (right) as seen by the beam.[87]. 56
3.17 NuMI beam data recorded by MINERνA. The first months were taken with half of the detector installed. Vertical bars indicate changes in the beam. Special runs are related to different NuMI horn currents and target configurations. . . . 56

4.1 Effects to be taking into account in hit calibration [88]. 59
4.2 Rutgers PMT test stand. 61
4.3 Example of a high gain pedestal distribution for a single channel. The outlier can be originated from a cosmic ray event. 62
4.4 Peak muon energy per length for all planes. Consistency in energy response is related to the channel-to-channel calibration. 63

4.5 (Left) The energy distribution of clusters along a muon track in data and the simulation. (Right) Fit to the peak of the energy distribution gives the value for MEU. 63
4.6 Time distribution of hits in a NuMI beam spill. 65
4.7 Example of cluster formation in the inner detector when particles pass trough the scintillator planes. Colors are associated with the energy deposition. 66
4.8 Ilustration of procedure for creating a track-based event for a high multiplicity neutrino interaction in the MINERA detector. 68
4.9 Difference between the fitted positions relative to the measured cluster positions for rock muon events. 69
4.10 Neutrino energy distributions using the same montecarlo geometry with different input hadronic physics models. The green arrow shows the discrepancy between the peaks of the distributions [95]. 75
4.11 Neutrino energy distributions for a set of special runs taken with different target positions and horn currents for charged current inclusive events in the tracker region. 76
4.12 Pion yields as a function of p_z in bins of p_T. Different colors and markers represent bins of p_T , and the yields are scaled such that the points in different p_T bins do not overlap. All efficiency corrections have been applied. Statistical and systematic error bars are plotted. 77
4.13 The plots show a comparison of the FTFP BERT predicted cross section to the NA49 data for the $p + C \to \pi^+ + X$ (left) and $p + C \to \pi^- + X$ (right). 78
4.14 Right: Ratio of the hadron reweighting distributions where the dip region corresponds to the fallind edge of the focusing peak. Left: ν_μ and $\overline{\nu}_\mu$ simulated fluxes with and without the hadron production weights. 80
4.15 A comparison of GENIEs charged current inclusive NuMI cross section for an isoscalar target to world data. The shaded band is the uncertainty on free nucleon cross sections. 82
4.16 Cross sections used in the hA model [109]. Right: $p + Fe$ Left: $\pi^+ + Fe$. 84
4.17 Differences between the h_A and h_N intranuke cascade models. 85
4.18 Spill batch structure. Left: Data Right: Montecarlo.[110] 86

5.1 Event display for a charged current inclusive interaction in the fiducial tracker region. 89
5.2 Event display for a simulated charged current quasi-elastic interaction in the fiducial tracker region. 90
5.3 Classification of different types of muons present in MINERνA. 90

5.4 Muon Angle distribution for charged current inclusive interactions in the tracker region. 91
5.5 Neutrino Energy resolution using the CCQE Hypothesis definition. 93
5.6 Neutrino Energy resolution using the implemented definition. 94
5.7 Non CCQE interaction and different recoil energy classifications. 96
5.8 Non-vertex recoil energy in function of Q^2. CCQE events in red and non-CCQE events are in blue. 97
5.9 Neutrino Energy distribution for charged current inclusive (CCINC) candidates. 98
5.10 Neutrino Energy distribution for charged current quasi-elastic (CCQE) candidates. 99
5.11 Left: Neutrino Energy background subtracted distribution for charged current inclusive interactions. Right: Ratio $\frac{DATA}{MC}$. 101
5.12 Q^2 distribution for events in the sideband. 102
5.13 Background scale in bins of Q^2. 102
5.14 Q^2 distribution after applying the background scale to the background events in the sideband. 103
5.15 Left: Neutrino Energy background subtracted distribution for charged current quasi-elastic interactions. Right: Ratio $\frac{DATA}{MC}$. 104
5.16 Migration Matrix for CCINC analysis. The different values in the matrix represent the probability of an event to migrate from a generated to a reconstructed E_ν bin. 105
5.17 Migration Matrix for CCQE analysis. 105
5.18 Left: Neutrino Energy background subtracted and unfolded distribution for charged current inclusive interactions. Right: Ratio $\frac{DATA}{MC}$. 106
5.19 Left: Neutrino Energy background subtracted and unfolded distribution for charged current quasi-elastic interactions. Right: Ratio $\frac{DATA}{MC}$. 106
5.20 Efficiency in function of generated E_ν for CCINC analysis. 108
5.21 Efficiency in function of generated E_ν for CCQE analysis. 109
5.22 Left: Neutrino Energy background subtracted, unfolded and efficiency corrected distribution for charged current inclusive interactions. Right: Ratio $\frac{DATA}{MC}$. . . . 109
5.23 Left: Neutrino Energy background subtracted, unfolded and efficiency corrected distribution for charged current quasi-elastic interactions. Right: Ratio $\frac{DATA}{MC}$. . 110
5.24 Neutrino Flux used in CCQE and CCINC analysis and obtained as was described in section 4.6.1. 110
5.25 Left: Total cross section in function of E_ν for charged current inclusive interactions as defined in equation 5.13. The inner (outer) error bars correspond to the statistical (total) uncertainties. Right: Ratio $\frac{DATA}{MC}$. 111

5.26 Left: Total cross section in function of E_ν for charged current quasi-elastic interactions as defined in equation 5.13 The inner (outer) error bars correspond to the statistical (total) uncertainties. Right: Ratio $\frac{DATA}{MC}$. 111
5.27 Fractional uncertainties for the total charged current inclusive cross section in function of reconstructed E_ν. 112
5.28 Fractional uncertainties for the total charged current quasi-elastic cross section in function of reconstructed E_ν. 113
5.29 Flux uncertainties for charged current inclusive events in the tracker region in function of reconstructed E_ν. 114

6.1 Left: Total cross section ratio $\frac{\sigma_{ccqe}}{\sigma_{ccinc}}$ in function of neutrino energy Right: $\frac{Data}{MC}$ comparison. 122
6.2 Fractional Uncertainties in the total cross section ratio $\frac{\sigma_{ccqe}}{\sigma_{ccinc}}$ in function of neutrino energy. 123
6.3 Muon Angle vs Muon Energy for MC CCINC generated events in the tracker region. 124
6.4 Selection efficiency for CCINC interactions in function of true E_ν for $\theta_\mu < 20^0$. . 124
6.5 Selection efficiency for CCQE interactions in function of true E_ν for $\theta_\mu < 20^0$. . 125
6.6 Left: Total cross section in function of E_ν for charged current inclusive interactions as defined in equation 6.5 with $\theta_\mu < 20^0$. Right: Ratio $\frac{DATA}{MC}$. 126
6.7 Left: Total cross section in function of E_ν for charged current quasi-elastic interactions as defined in equation 6.5 with $\theta_\mu < 20^0$. Right: Ratio $\frac{DATA}{MC}$. 126
6.8 Fractional uncertainties for total CCINC cross section in function of reconstructed E_ν with $\theta_\mu < 20^0$. 127
6.9 Fractional uncertainties for the total CCQE cross section in function of reconstructed E_ν with $\theta_\mu < 20^0$. 127
6.10 Left: Total cross section ratio $\frac{\sigma_{ccqe}}{\sigma_{ccinc}}$ in function of neutrino energy for $\theta_\mu < 20^0$ .Right: $\frac{Data}{MC}$ comparison. 127
6.11 Fractional Uncertainties in the total cross section ratio $\frac{\sigma_{ccqe}}{\sigma_{ccinc}}$ in function of neutrino energy for $\theta_\mu < 20^0$. 128

7.1 Flux-unfolded MiniBooNE muon neutrino CCQE cross section in function of neutrino energy compared with results from LSND and NOMAD experiments. . 130

A.1 Picture of the beamline installed in MT6 at Fermilab. 131
A.2 Left: Wire Chamber source testing configuration Right: WC occupancy plots on a test beam run. 132

A.3 Magnetic field measurement for one of the magnets in the beamline. 133
A.4 Left: Time of flight system (TOF) testing Right: Resolution for different TOF configurations. 133
A.5 Event display for a 600 MeV pion interacting on the MINERνA testbeam detector. 134
A.6 Crosstalk distribution for the 4 neirest neighborhoods. 134
A.7 Muon energy ratio for charged current interactions on tracker between two datasets with different NuMI beam intensities. 135
A.8 Neutrino energy spectrum for different NuMI beam configurations. 136
A.9 Event display where is presented the rock muon superposed with a physics event. 136
A.10 Neutrino enery distribution for a subsample with (RED) and without (BLACK) cross talk rejection. 137
A.11 Event display for multiple vertices that should be only one physics event. 138
A.12 Data run periods for MINERνA. 138

List of Tables

2.1 Particles in the SM [44] [45] [46]. 12
2.2 Three matter fermion generations. Each generation consists of five different representations of the gauge group. 13

3.1 Decay modes of π^+, K^+ resulting in ν_μ in the NuMI beam. 40
3.2 Inner detector modular composition. 46
3.3 Charged current events expected at each nuclear target. 51
3.4 Some parameters and requirements for the electronics at MINERνA 53
3.5 Data run periods from the ν_μ focusing NuMI beam mode. 57

4.1 Summary for the kinematic regimes of hadron production interaction constrained by the NA49 and Barton measurements. 79
4.2 Relativistic Fermi Gas parameters in GENIE. 81

5.1 Muon tracking reconstruction efficiency corrections. 107
5.2 Unfolding uncertainties for the CCINC and CCQE channels for each neutrino energy bin. 116
5.3 Uncertainties on detector response. 117
5.4 Uncertainties in FSI models in GENIE. 118
5.5 Uncertainties on cross section models [109]. 119

Chapter 1

Introduction

In the last decades neutrino physics has become a very active and exciting research field. Many experiments around the world are trying to figure out the diverse properties of these particles describing their oscillation and how they interact with the matter. The neutrino interaction with matter is still waiting for experimental results with high statitics measurements in the energy range between 1 GeV and 20 GeV where three different processes overlap: charged current quasi-elastic, resonance pion production and deep inelastic scattering. Measuring neutrino interaction cross sections facilitates high precision neutrino oscillation measurements. Furthermore, neutrinos play a very important role in various branches of subatomic physics as well as in astrophysics and cosmology. Currently there is evidence that neutrinos have mass [1] and can change flavor [2]. This thesis describes the Main Injector Neutrino Experiment for $\nu - A$, known as MINERνA, a neutrino scattering experiment that uses Fermilab NuMI beamline. This thesis presents the first measurement of the muon neutrino charged current quasi-elastic to charged current inclusive cross section ratio on a hydrocarbon target at neutrino energies in the 2-10 GeV range. Chapter 2 introduces aspects of neutrino physics including a brief summary of cross sections for the processes that are taking into account in the analysis. It also presents the current results from MINERνA collaboration in the different neutrino interaction proceses and discusses the neutrino oscillation phenomena and recent results from oscillation experiments. It gives a short summary of the history of neutrino from its theoretical conception to the present day. Chapter 3 describes how the neutrinos are produced and studied in Fermilab using the NuMI beamline and the MINERνA detector. Chapter 4 describes the detector calibration, simulation and how events are reconstructed from the raw data. The first part of chapter 5 presents a detailed explanation of the event selection for both charged current inclusive (CCINC) and charged current quasi-elastic (CCQE) neutrino scattering channels. The second part describes the measurements of total cross sections for CCINC and CCQE. In the chapter 6 presents the first reported measurement of muon neutrino charged current quasi-elastic to charged current inclusive cross section ratio on a hydrocarbon target at neutrino energies 2-10 GeV and, finally, chapter 7 presents the conclusions and future perspectives. Developing an understanding of neutrinos is rightfully one of the top priorities of the particle physics community because it has the potential to reveal new physics.

Chapter 2

Neutrino Physics

2.1 History

In 1911, an experiment realized by von Bayer, Otto Hahn and Lise Meitner [3] suggested that the energy emitted in the β decay has a continuos rather than discrete spectrum. In 1927, Ellis e Wooster [4] established, without doubts, that the energy spectrum of the β decay is, in fact, continuous. These observations were in contradiction with the energy conservation law since, apparently, there was energy loss in the process.

In an open letter to *Liebe Radioaktive Damen und Herren*[1] in a physics conference in Tubingen, Germany, in 1930 Wolfgang Pauli proposed [5] that the existence of a neutral weakly interacting fermion emitted in the β decay could solve the problem. This neutral fermion, with mass close to the electron mass and no electric charge, was called neutron. When in 1932 Chadwick discovered the neutron that we know today [6] Fermi called Pauli's particle neutrino (little neutron) to diferentiate it from the heavy Chadwick's neutron. In 1933 after comparisons between Fermi [7] and Perrin [8] spectrums it was postulated that the neutrino should have no mass.

In 1934, Fermi [9] used Dirac, Heisenberg and Pauli's quantum electrodinamics to formally develop the β decay theory. That also predicted that inverse beta decay was also possible,

$$\overline{\nu}_e + p \to n + e^+ \tag{2.1}$$

In 1956 Reines and Cowan [10] made the first direct observation of the neutrino through inverse β decay. They employed a nuclear reactor as a source of few MeV antineutrinos and

[1]Dear Radioactive Ladies and Gentlemen

a target of 200 liters of water and cadmium chloride to observe both, the neutron and the positron from the reaction[2]

In 1958, Goldhaber observed that neutrinos have left hand helicity [11] and in 1959 Davis showed that a ν can be distinguished from its antiparticle $\overline{\nu}$ [12]. In 1960 an experiment led by Lederman [13] at the Brookhaven Alternating Gradient Synchrotron (AGS) detected a new type of neutrino, the ν_μ.

In 1973 the Gargamelle giant bubble chamber at CERN announced the experimental observation of weak neutral currents[14]. Experiments with solar neutrinos began on 1968 when Davis [15] revealed a discrepancy between theoretical predictions and the measured solar neutrino flux. This discrepancy came to be known as the solar neutrino problem.

The first detection of actual ν_τ interactions was made by the DONUT collaboration at Fermilab in 2000 [16].

A discrepancy between the expected and the measured flux was also observed in experiments with atmospheric neutrinos that registered the apparent disappearance of muon neutrinos in a few hundred kilometers of propagation. Experiments that measured the flux of solar neutrinos found results suggesting that electron neutrinos disappeared in the traveling distance between Sun and Earth.

In order to explain the observed deficit of solar neutrino flux, Gribov and Pontecorvo [17], in 1968, discussed the neutrino flavor oscillation which can occur if the neutrinos have masses. The disappearance of atmospheric neutrinos (ν_μ) and solar neutrinos (ν_e) is not easy to explain in oscillation terms if mass terms are not included. It is important to notice that neutrino oscillation is not predicted by Standard Model.

It has been a long journey since the pioneers hitherto during which we have witnessed an intense experimental and theoretical activity aimed at a better understanding of neutrino interactions with nucleons and nuclei. The discovery of the neutrinos and neutrino oscillations started a new era of physics. We have found evidences that neutrinos have mass, a fact that goes beyond the Standard Model. Many important neutrino beam facilities have been built at JPARC, CERN and Fermilab in the past years aimed at the detailed study of neutrinos.

[2]The very small interaction probability required the very intense flux of antineutrinos provided by the reactor or a very large volume of the target.

2.2 Neutrino Properties

Everything we see around us is made of only three particles: protons, neutrons and electrons. So, a natural question rises: is the entire universe made only of these three particles. We know that for every proton, neutron or electron, the universe contains 1 billion neutrinos. Neutrinos are not rare in the universe; therefore, it is important to have a comprehensive knowledge about them. Several properties of neutrinos have already been observed and measured like the ones briefly described below.

2.2.1 Neutrino Flavors

The standard model of particle physics contains three neutrino flavors: ν_e, ν_μ and ν_τ. Each neutrino forms a doublet with a corresponding charged lepton. The ν_τ was discovered not even 13 years ago[16]. The number of neutrinos participating in the electroweak interaction can be determined by the Z^0 decay width. It was beautifully confirmed at LEP (CERN)[18, 19, 20, 21], long before the observation of the ν_τ, that there are only three light neutrinos.

In 1995 Liquid Scintillator Neutrino Detector (LSND) claimed that three neutrinos were not enough to explain their results and introduced a sterile neutrino [22]. This sterile neutrino does not undergo weak interactions nor interacts in any other way (except gravity).
MiniBooNE results from March 2007 shows no evidence of muon neutrino to electron neutrino oscillations in the LSND region, refuting a simple 2-neutrino oscillation interpretation of the LSND results. More advanced analyses of their data are currently being undertaken by the MiniBooNE collaboration.

2.2.2 Helicity

Wu showed in the late 1950s that parity is violated in weak interactions [23] and Goldhaber [11] observed that neutrinos have spin antiparallel to their momentum (left-handed) and antineutrinos have it parallel (right-handed). Therefore, only left-handed neutrinos and right-handed antineutrinos are included in the Standard Model.

2.2.3 Neutrino mass

Currently, the absolute values of the neutrino masses are unknown and the Standard Model assumes that neutrinos are massless. However, no fundamental aspect of the Standard Model forbids massive neutrinos and it is quite straightforward to insert neutrino mass terms into the

Standard Model Lagrangian. There are two basic methods to generate neutrino mass terms that are both gauge and Lorentz invariant [24].

Dirac mass. This can be obtained by assuming the same mecanism (Higgs Mecanism) which explains the generation of masses of charged fermions and quarks, also for neutrinos, though in this case, the much smaller Yukawa couplings for neutrinos would be a mistery [3]. The mass term in the Lagrangian is:

$$\mathcal{L}_{Dirac} = -(\overline{\nu}_L M \nu_R + \overline{\nu}_R M \nu_L), \tag{2.2}$$

where ν_{L_R} are the neutrino flavour eigenstates and M is the 3x3 neutrino mass matrix.

Majorana mass. A massive Majorana neutrino can be created by modifying the Higgs sector in the Standard Model. An additional singlet, doublet or triplet is added to the original Higgs doublet, although this introduces a new mass scale in the form of the Higgs vacuum expectation value. The mass term in the Lagrangian is:

$$\mathcal{L}_{Majorana} = \frac{1}{2}\overline{\nu}^c_R M \nu_R + h.c. \tag{2.3}$$

In this case neutrinos are their own anti-particles since ν^c_L is a right-handed neutrino. These mass terms violate lepton number conservation by two units and their presence could be indicated by the observation of neutrino double beta decay, nuclear transitions of the type,

$$(Z, A) \rightarrow (Z-2, A) + 2e-, \tag{2.4}$$

which are only possible in the presence of massive Majorana neutrinos. The non-observation of this transition in current experiments sets a limit to the mass of the electron neutrino of m_{ν_e} < 0.5 eV if the ν_e is assumed to be a Majorana particle. If both types of masses, Dirac and Majorana masses exist simultaneously, and if the right handed Majorana mass is very large such as one close to the GUT scale, it is possible to explain very small mass of neutrinos by the so called Seesaw Mechanism [25], [26], [27].

2.3 Neutrino Sources

The neutrino sources can be divided into natural and man-made neutrinos.

The natural sources:

[3]These neutrinos appear in many Grand Unified Theories

- Primordial neutrinos: neutrinos that have been created in the early stage of the universe and decoupled from the matter just before the primordial nucleosynthesis (see figure 2.2) and remain, as universe expands, as cosmic background neutrinos similar to that of photons (CMB). Cosmological data is able to give an upper limit on neutrino masses in the sub-electronvolt range and is consistent with the three families of neutrinos [28], [29].

- Cosmogenic neutrinos: neutrinos that are produced when very high energy cosmic rays, mainly protons, interact with the cosmic microwave background (CMB) via photo-pion production at energies $E > 10^{20} eV$. The neutrinos are then produced during the decay of the pions following the reaction: $p + \gamma \rightarrow n + \pi^+$ or $p + \gamma \rightarrow p + \pi^+ + \pi^-$. This leads to an important decrease of the proton energy that is generally called the GZK (after Greisen [30], Zatseptin and Kuzmin [31]) cutoff. The flux of such high energetic neutrinos is expected to be in the range of 0.001-0.1 $km^{-2} year^{-1}$ [[32], [33]].

- Neutrinos from fusion processes in the stars: figure 2.1, shows the way that they are produced mainly in 3 reactions that are part of the proton-proton chain in the core of the stars.

$$p + p \rightarrow d + e^+ + \nu_e \tag{2.5}$$

$$e^- +^7 Be \rightarrow^7 Li + \nu_e \tag{2.6}$$

$$^8Be \rightarrow^8 Be^* + e^+ + \nu_e \tag{2.7}$$

  The Sun, for example, produces electron neutrinos with a flux of 6.4 x $10^{10} cm^{-2} s^{-1}$ on Earth [34]. Neutrinos are also produced in explosive stellar processes [35]. When the core of a large star ($M \geq 8M_{\odot}$) runs out of nuclear fuel, it collapses to a proton-neutron star. About 99 percent of the gravitational binding energy change, about 3×10^{53} ergs, is carried away, from the inner part of the collapse, by neutrinos of all flavors and energies of order 20 MeV [36].

- Neutrinos coming from Earth: the neutrinos coming from the different nuclear reactions inside the Earth (geo-neutrinos) or in several physical processes that make life on Earth possible. They come from the decays of radiogenic elements as uranium, thorium or potassium that keep our planet heated and produce a flux of $\bar{\nu}_e$ and constitute a background to the solar neutrino searches.

- Atmospheric neutrinos: neutrinos that come from the interactions of cosmic rays in the atmosphere producing charged pions and kaons that decay into muons and ν_μ. The muons

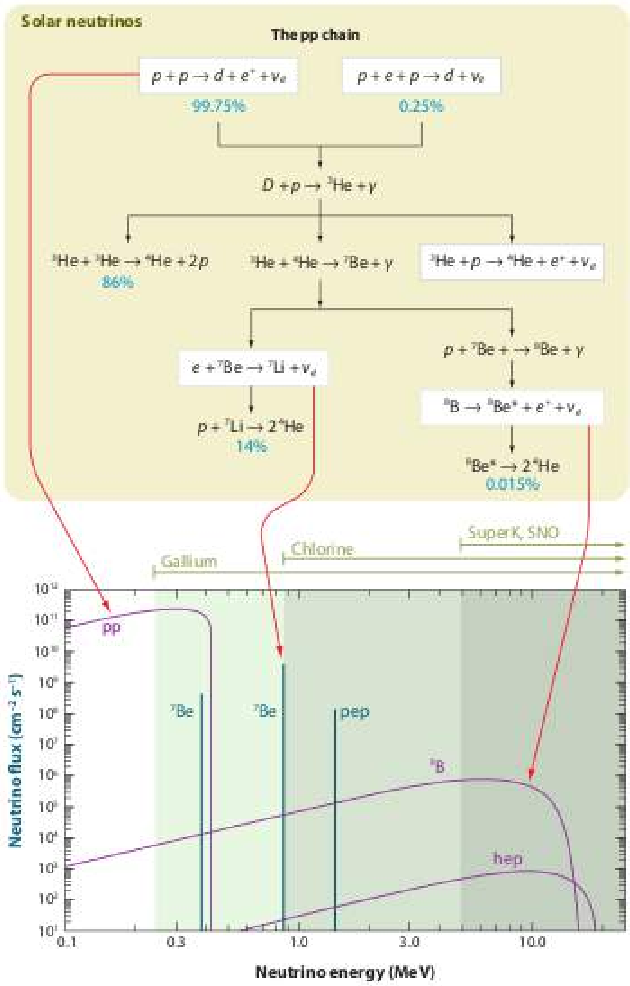

Figure 2.1: Solar cycle and the resulting solar neutrino energy spectrum.

decay afterwards into e, ν_e and ν_μ [37]

$$K, \pi \rightarrow \mu + \nu_\mu \tag{2.8}$$

$$\mu \rightarrow \nu_\mu + \nu_e + e \tag{2.9}$$

The man made neutrinos:

- Nuclear reactors: fission of the ^{235}U, for example, produces two new elements with atomic massed centered near 95 and 135 and free neutrons. These new elements are extremely unstable, since they are too rich of neutrons, and decay toward stable nuclei with an average of 6 beta decays: $n \rightarrow p + e^- + \bar{\nu}_e$. This corresponds to a very intense and isotropic flux of $\bar{\nu}_e$: $9.3 \times 10^{20} \bar{\nu}_e s^{-1}$ for a 5 GW (thermal) reactor [[34], [38]].
- Accelerators: the Main Injector at Fermilab produces a beam of protons that interact in a target producing mesons, mainly pions and kaons that are focused by a set of magnetic

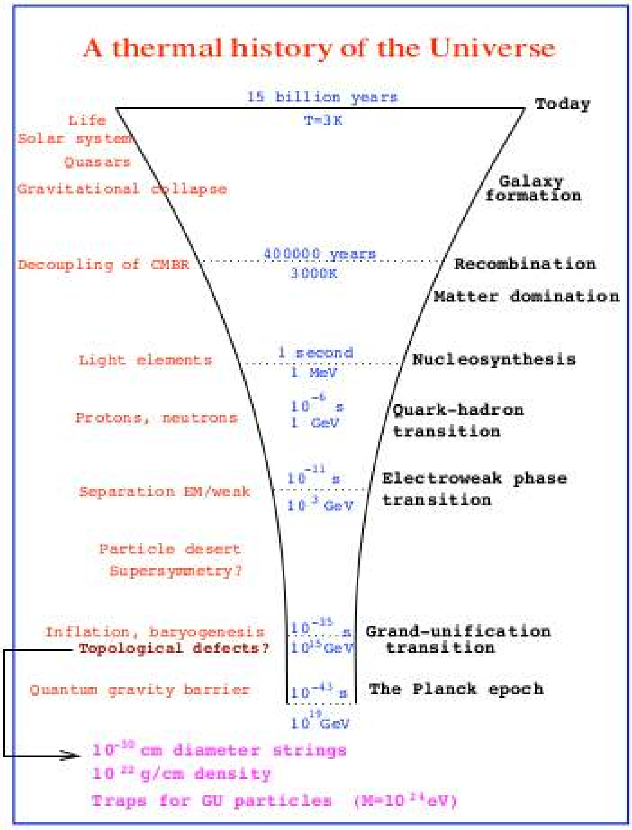

Figure 2.2: Thermal history of the universe.

horns and directed to a long decay tunnel in which they decay and produce mainly muon neutrinos. Depending on the horn current, one can focus positively or negatively charged particles that will give a flux of neutrinos or anti-neutrinos. This is explained in more details in chapter 3.

Depending on the sources, different kinds of neutrinos are produced. While the sun and the reactors produce electron neutrinos and anti-neutrinos respectively, atmospheric processes and accelerators produce mainly muon neutrinos or anti-neutrinos.

2.4 The Weak Interaction

The weak interaction is one of the four fundamental forces of nature alongside gravity, electromagnetism and the strong force. Above the unification energy, of the order of 100 GeV, electromagnetism and the weak interaction merge in a single interaction called the electroweak interaction. In the Standard Model Z^0, $W^{\pm}$ and the photon are produced by the spontaneous symmetry breaking of the electroweak symmetry $SU(2)XU(1)$ The left-handed fermion fields of the i^{th} fermion family transforms as doublets: $\Phi = \begin{pmatrix} \nu_i \\ l_i^- \end{pmatrix}$ and $\begin{pmatrix} u_i \\ d_i^{'} \end{pmatrix}$ under $SU(2)$, where $d_i^{'} \equiv \sum_j V_{ij} d_j$ and V is the Cabibbo-Kobayashi-Maskawa (CKM) mixing matrix. In spontaneous symmetry breaking, the bosons acquire a non-vanishing mass through the absorption of Nambu-Goldstone bosons [39], [40], [41]. This process is known as the Higgs mechanism. At low energy, the weak interaction is mediated by the three bosons with significant masses: $W^{\pm}, Z^0$. The neutral vector bosons Z^0 mediate the neutral current interaction (NC) and the two charged bosons $W^{\pm}$ mediate the charged current interaction (CC). While charged leptons are converted into neutrinos (or vice versa) via the CC interaction, leptons do not change charge in the NC channel. Figures 2.3 and 2.4 show the possible interaction vertices. Weak interaction is the

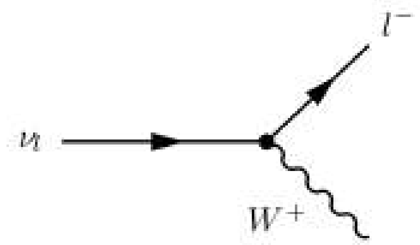

Figure 2.3: Feynman diagram of neutrino interaction vertex in the case of charged current interactions.

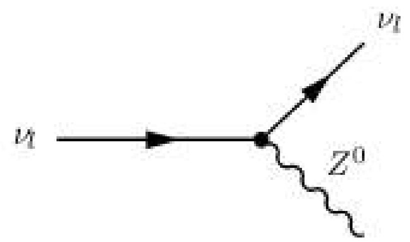

Figure 2.4: Feynman diagrams of neutrino interaction vertex in the case of neutral current interactions.

only force that violates parity, as Chen Ning Yang and Tsung-Dao Lee suggested in mid-1950. This parity violation is represented, in the following by $\gamma_\mu(1-\gamma_5)$ or $\gamma_\mu(g_V^i) - g_A^i\gamma_5$ where γ_μ and γ_5 are the Dirac matrices, g_V^i and g_A^i are the vector and axial vector coupling constant for the i^{th} fermion family

$$g_V^i \equiv t_{3L}(i) - 2q_i \sin^2\theta_W \tag{2.10}$$

$$g_A^i \equiv t_{3L}(i) \tag{2.11}$$

where t_{3L} is the weak isospin of the fermion i (+ 1/2 for u_i and ν_i; -1/2 for d_i and l_i) and q_i is the charge.

$$J^{CC}_{f_i \to f'_{i,\mu}}(x) = \bar{f}'_i(x)\gamma_\mu \frac{1-\gamma_5}{2} f_i(x) \tag{2.12}$$

where we have used the notation $f_i(x)$ for the fermion field.

2.5 Neutrino in the Standard Model

The standard model is a theoretical base that describes fundamental particles and how they interact. The standard model is conceptually simple and comprehensive and it is the most succesful theory with various measurements confirming its predictions. However, it is incomplete since it does not describe everything (gravity, for instance, is not included). The Standard model is only able to describe three of the four forces[4]. Moreover, there are many free parameters in the Standard Model such as the fermion masses as they can not be predicted theoretically but must be determined experimentally.

Everything around us is made of matter particles and complex interactions, that could be explained with only 6 quarks, 6 leptons and force carrier particles (see table 2.1). Quarks and Leptons consist of six particles, which are related in pairs, or generations. The lightest and most stable particles make up the first generation, whereas the heavier and less stable particles belong to the second and third generations. Force carrier particles (bosons) mediate the interactions: gluons for the strong interaction; $W^{\pm}$ and Z^0 for the weak interaction and the photon for the electromagnetic interaction.

The Standard Model (SM) is based on the gauge group, with three fermion generations, where a single generation consists of five different representations of the gauge group equation:

$$GSM = SU(3)_C \times SU(2)_L \times U(1)_Y \tag{2.13}$$

The Standard Model of weak and electromagnetic interactions was first proposed in 1967 by A.Salam [42] and S.Weinberg [43]. The neutrino interactions within the SM are given by equations 2.14 and 2.15 where SM has three active neutrinos. They reside in six left-handed weak isospin doublets[5] and nine right-handed singlets (see table 2.2)

$$-\mathcal{L}_{CC} = \frac{g}{2\sqrt{2}}\left(j^{\mu}_{W} W_\mu + j^{\mu,\dagger}_{W} W^{\dagger}_{\mu}\right) \tag{2.14}$$

[4]the strong force, the weak force and the electromagnetic force

[5]the right-handed neutrino are not included in the SM because the neutrinos interact only weakly and are presumed massless in the model

QUARKS		
Quarks	Mass	Electric charge
up (u)	$2.3^{+0.7}_{-0.5}$ MeV/c^2	$+\frac{2}{3}$
down (d)	$4.8^{+0.7}_{-0.3}$ MeV/c^2	$-\frac{1}{3}$
strange (s)	95$\pm$5 MeV/c^2	$-\frac{1}{3}$
charm (c)	1.275$\pm$0.025 GeV/c^2	$+\frac{2}{3}$
bottom (b)	4.65$\pm$0.03 GeV/c^2	$-\frac{1}{3}$
top (t)	173.5$\pm$0.6 $\pm$ 0.8 GeV/c^2	$+\frac{2}{3}$
LEPTONS		
Leptons	Mass	Electric charge
electron (e)	0.510998928 $\pm$ 0.000000011 MeV/c^2	-1
electron neutrino (ν_e)	$<$ 2 eV/c^2	0
muon (μ)	105.6583715 $\pm$ 0.0000035 MeV/c^2	-1
muon neutrino (ν_μ)	$<$ 0.19 MeV/c^2	0
tau (τ)	1776.82 $\pm$ 0.16 MeV/c^2	-1
tau neutrino (ν_τ)	$<$ 18.2 MeV/c^2	0
BOSONS		
Bosons	Mass	Electric charge
photon(γ)	$< 1 \times 10^{-18}$ eV/c^2	0
W$^{\pm}$	80.385$\pm$ 0.015 GeV/c^2	$\pm$1
Z^0	91.1876 $\pm$ 0.0021 GeV/c^2	0
gluon (g)	0	0
Higgs	125 GeV/c^2	0

Table 2.1: Particles in the SM [44] [45] [46].

$$- \mathcal{L}_{NC} = \frac{g}{2cos\theta_W} j_Z^\mu Z_\mu \tag{2.15}$$

where N_ν is the number of neutrino flavors.

L_L(1,2,-1/2)	Q_L(3,2, 1)	E_R(1,1,-1)	U_R(3,1, 2/3)	D_R(3,1,-1/3)
$\binom{\nu_e}{e}_L$	$\binom{u}{d}_L$	e_R	u_R	d_R
$\binom{\nu_\mu}{\mu}_L$	$\binom{c}{s}_L$	μ_R	c_R	s_R
$\binom{\nu_\tau}{\tau}_L$	$\binom{t}{b}_L$	τ_R	t_R	b_R

Table 2.2: Three matter fermion generations. Each generation consists of five different representations of the gauge group.

The measurement of the decay width of the Z^0 boson into neutrinos makes the existence of three, and only three, light (that is, $m_\nu < m_Z/2$) active neutrinos an experimental fact. When expressed in units of the SM prediction for a single neutrino generation, one gets:

$$\begin{aligned} N_\nu &= 2.994 \pm 0.012 \qquad \text{(Standard Model fits to LEP data)} \\ N_\nu &= 3.00 \pm 0.06 \qquad \text{(Direct measurement of invisible Z width)} \end{aligned} \tag{2.16}$$

2.6 Oscillation

The discovery of non-zero neutrino masses is closely related to the discovery of neutrino oscillations. That are only possible with massive neutrinos due to a distinction between flavor and mass eigenstates[6]. The principle is analogous to the time evolution of a classical coupled oscillator starting with an excitation that is not a normal mode. For simplicity we consider a system with only two neutrinos. Neutrinos produced in charged current interactions are flavor eigenstates denoted as ν_e and ν_μ. Those eigenstates have no well defined mass and are linear superpositions of the mass eigenstates ν_1 and ν_2 with masses m_1 and m_2, respectively:

$$|\nu_e\rangle = |\nu_1\rangle cos\theta + |\nu_2\rangle sin\theta, \tag{2.17}$$

$$|\nu_\mu\rangle = -|\nu_1\rangle sin\theta + |\nu_2\rangle cos\theta, \tag{2.18}$$

where θ is the neutrino mixing angle. At time t = 0 we have a pure weak eigenstate, say $|\nu(0)\rangle$ = $|\nu_\mu\rangle$. But ν_μ is a superposition of the mass eigenstates each of which is propagating with the time dependence dictated by the free Hamiltonian. Therefore, at a time t the state will be given by

$$|\nu(t)\rangle = -|\nu_1\rangle sin\theta e^{-iE_1 t} + |\nu_2\rangle cos\theta e^{-iE_2 t}, \tag{2.19}$$

[6]The idea was first introduced by Gribov and Pontecorvo [47], [48]

where $E_{1,2} = \sqrt{(p^2 + m_{1,2}^2)} \sim p + \frac{m_{1,2}^2}{2p}$. The probability of finding a neutrino with electron flavor is then

$$\begin{aligned} P(\nu_\mu \to \nu_e; t) &= |\langle \nu_e | \nu(t) \rangle|^2 \\ &= sin^2 2\theta cos^2\theta | - e^{-iE_1 t} + e^{-iE_2 t}|^2 \\ &= sin^2 2\theta cos^2 \left(\frac{\Delta m^2 t}{4E} \right) \\ &= sin^2 2\theta cos^2 \left(\frac{\Delta m^2 L}{4E} \right) \end{aligned} \tag{2.20}$$

where $\Delta m^2 = m_2^2 - m_1^2$ is the squared mass difference and $E = p$. The last line is valid for highly relativistic particles ($L = t$) with L being the travelled distance. Note that only the mass difference squared appears, hence measuring oscillation probabilities will not give absolute values of the neutrino masses, it can only say definitely that at least one of the two neutrinos has a non-zero mass. The two-flavor-oscillation scheme can be easily extended to three flavor mixing. The neutrino mixing Pontecorvo-Maki-Nakagawa-Sakata matrix then contains three angles θ_{12}, θ_{13}, θ_{23}, one Dirac CP violating phase and possibly two Majorana phases. Further we have three squared mass differences: Δm_{12}^2, Δm_{13}^2, Δm_{23}^2. Since the off-diagonal matrix elements seem to be large, also CP violation might be larger than in the quark sector. Most of these parameters but the CP violating phase have been measured. The existence of oscillation requires the neutrino masses to be different and, thus, that they have non-zero mass. Yet, neutrinos in Standard Model do not have mass.

2.7 The EMC Effect

In 1983 , the European Muon Collaboration (EMC) reported measurements of the structure of the proton that exhibited new and, even today, not fully understood behavior [49]. The measurements of the structure function F_2, which describes the momenta of constituents of the proton and neutron, were made by scattering muons inelastically off iron and deuterium. The interesting and unexpected result was that F_2 was different in the two targets. This means that the quark structure of a nucleon is effectively modified inside a nucleus. The modifications observed were a suppression of quarks with very low momenta ($x_{bj} < 0.14$), an enhancement at slightly higher momenta ($0.1 < x_{bj} < 0.3$), and a significant suppression again at moderate momenta ($0.3 < x_{bj} < 0.7$). Because no physical mechanism could be used to explain the observation, it became known as the **EMC effect**, after the collaboration that first reported it. Since the first observation of the EMC effect, there have been numerous precision measurements of the nuclear dependence of quark distributions, mostly through the use of deep inelastic electron or muon scattering. These have led to a deeper understanding of quantum chromodynamics (QCD) which describes the interactions among quarks and gluons in the nucleus. The behavior in regions of lower x_{bj} are now understood to be due to interference between the scattering from different quarks/nucleons in the nucleus. The term **EMC effect** is now commonly used to refer only to the behavior at $0.3 < x_{bj} < 0.7$, which still is not understood.

2.8 Neutrino cross sections

Neutrino interactions can be classified in two types. The first one related to neutrinos interacting with electrons inside the atom and the second type related to neutrinos interacting with nucleons inside the nucleus, in charged or neutral current interactions. Figure 2.5 shows the different kind of neutrino interactions. In the last decades, scientists have detected neutrinos from a variety of sources, both natural and man-made. Knowledge of the neutrino interaction cross sections is an important and necessary key in any precise measurement of neutrino properties. With the advent of new precision experiments, like MINERνA , the demands on our understanding of neutrino interactions is increasing.

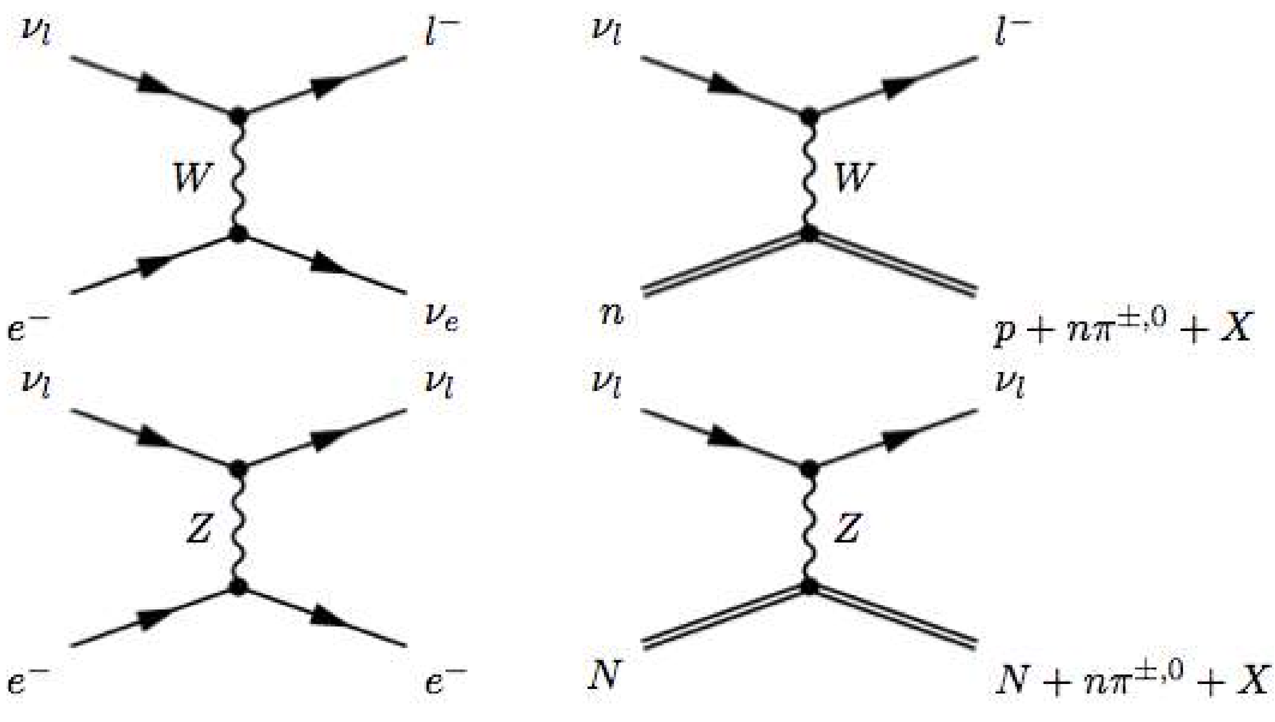

Figure 2.5: Feynman diagramas of neutrino interactions for charged and neutral current interactions. The leptons are noted by l.

There is a summary of all neutrino interactions [50] where the authors first establish the formalism of neutrino interactions by considering the simplest case of neutrino-electron scattering, then they shift to neutrino interaction cross sections in nucleons and nucleus at,

Thresholdless processes: $E_\nu = 0 - 1MeV$

Low-energy nuclear processes: $E_\nu = 1 - 100MeV$

Intermediate energy cross sections: $E_\nu = 1 - 20GeV$

High-energy cross sections: $E_\nu = 20 - 500GeV$

Ultra-high-energy neutrinos: $E_\nu = 0.5TeV - 1EeV$

We concentrate our study in the intermediate energy[7] where several distinct neutrino scattering mechanisms start to play a role.

In order to better understand these neutrino cross sections, several experiments such as KEK to Kamioka (K2K), Mini Booster Neutrino Experiment (MiniBooNE), Main INjector ExpeRiment: ν-A (MINERνA), Main Injector Neutrino Oscillation Search (MINOS), Neutrino Oscillation MAgnetic Detector (NOMAD), SciBar Booster Neutrino Experiment (SciBooNE), and Tokai to Kamioka experiment (T2K) are strudying or have studied this intermediate energy region in greater detail.

2.8.1 Inclusive cross section

The neutrino interactions can be described by the following charged current and neutral current reactions:

$$\nu + N \rightarrow l^- + X \tag{2.21}$$

$$\nu + N \rightarrow \nu + X \tag{2.22}$$

where N is the target nucleon and X is the hadron final state (see figure 2.6). The differential cross section for neutrino scattering in the center of mass frame of the nucleon is given by:

$$d\sigma = \frac{|M|^2}{4(M_N)|\overrightarrow{k}|} d\phi^{n+1}(k, p; k^{'}, p_1, .., p_n) \tag{2.23}$$

$$d\sigma = \frac{|M|^2}{8(2\pi)^3 M_N |\overrightarrow{k}|} \frac{d^3k^{'}}{\epsilon^{'}} d\phi^n \tag{2.24}$$

[7]This energy range is often called as the **transition region** because it corresponds to the boundary between quasielastic scattering on the one end and deep inelastic scattering on the other

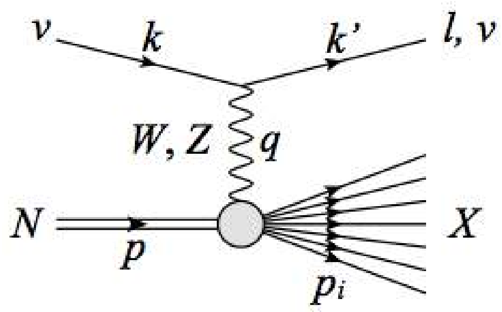

Figure 2.6: Variable definition for the Charged Current Inclusive channel.

$$\frac{d^2\sigma}{d\epsilon' d\Omega} = \frac{1}{2\pi^2}\frac{|M|^2}{32M_N\pi}\frac{|\vec{k}'|}{|\vec{k}|}d\phi^n \tag{2.25}$$

Where:

- Neutrino is massless. The neutrino and charged lepton four momentum given by $k = (E_\nu, 0, 0, E_\nu)$, $k' = (\epsilon', \vec{k}')$
- The four momentum transer $q = k - k'$ is the difference of the charged lepton with neutrino four-momentum.
- $d^3k' = |\vec{k}'|^2 d|\vec{k}'|d\omega$, where ω is the solid angle ($d\omega = d(cos\theta)d\phi$).
- $|\vec{k}'|d|\vec{k}'| = \epsilon' d\epsilon'$
- We used the definition of the n-body phase space $d\phi^n \equiv (2\pi)^4\delta^4(\sum_i p_i - p - q)\prod_{i=1}^{n}\frac{d^3p_i}{2E_i(2\pi)^3}$

Now we can calculate the invariant amplitude, M_{CC} for a charged current interaction:

$$M_{CC} = \left(\frac{g}{2\sqrt{2}}\right)^2 \bar{l}(k')\gamma_\alpha(1-\gamma_5)\nu(k)\frac{-i(g^{\alpha\beta} - q^\alpha q^\beta/M_W^2)}{q^2 - M_W^2}\langle X(p_1, .., p_n)|J_\beta^{CC}|N(p)\rangle \tag{2.26}$$

where $l(k')$ and $\nu(k)$ are the lepton and neutrino spinors. Assuming low momentum transfer ($|q^2| << M_W$) the propagator is:

$$\frac{-ig^2(g^{\alpha\beta} - q^\alpha q^\beta/M_W^2)}{8(q^2 - M_W^2)} \approx -ig^{\alpha\beta}\frac{G_F}{\sqrt(2)} \tag{2.27}$$

Replacing in equation 2.26 we obtain:

$$M_{CC} = \frac{G_F}{\sqrt{2}}\bar{l}(k')\gamma_\alpha(1-\gamma_5)\nu(k)\langle X|J_{CC}^\alpha|N\rangle \tag{2.28}$$

then the spin-average squared amplitude is:

$$|\overline{M_{CC}}|^2 = \frac{G_F^2}{2}\Big(\sum_{s\nu}\sum_{s\mu}\big([\bar{l}\gamma_\alpha(1-\gamma_5)\nu][\bar{l}\gamma_\beta(1-\gamma_5)\nu]^\dagger\big)\frac{1}{4}\sum_{s_N}\sum_{s_X}\langle X|J^\alpha|N\rangle\langle X|J^\beta|N\rangle^\dagger\Big) \tag{2.29}$$

Where the factor 1/4 corresponds to $\frac{1}{(2s_\nu+1)(2s_N+1)}$ with $s_\nu, s_N = 1/2$ are the neutrino and nucleon spin values. Simplyfing the leptonic term:

$$\sum_{s\nu}\sum_{s\mu}\big([\bar{l}\gamma_\alpha(1-\gamma_5)\nu][\bar{l}\gamma_\beta(1-\gamma_5)\nu]^\dagger\big) = Tr\big([\bar{l}\gamma_\alpha(1-\gamma_5)\nu][\bar{\nu}\gamma_\beta(1-\gamma_5)l]\big) \tag{2.30}$$

$$= 8[k_\alpha^{'}k_\beta + k_\alpha^{'}k_\beta^{'} - g_{\alpha\beta}k\cdot k^{'} + \epsilon_{\alpha\beta\rho\sigma}k^\rho k^{'\sigma}] = 8L_{\alpha\beta} \tag{2.31}$$

where the leptonic tensor $L_{\alpha\beta}$ is defined as in [51]. Definning, in addition, a hadronic tensor $W^{\alpha\beta}$, allow us to express equation 2.24 as the multiplication of the leptonic tensor and the hadronic tensor defined in [51]

$$W^{\alpha\beta} = \frac{1}{2M_N}\sum_X \frac{(2\pi)^4\delta^4(P_X - p_N - q)}{2\pi}\langle X|J^\alpha|N\rangle^\dagger\langle X|J^\beta|N\rangle \tag{2.32}$$

$$W^{\alpha\beta} = \frac{1}{2M_N}\sum_X (2\pi)^3\delta^4(P_X - p_N - q)\langle X|J^\alpha|N\rangle^\dagger\langle X|J^\beta|N\rangle \tag{2.33}$$

where the sum includes the sum over the final states as well as the average over the initial spins. The integration is over $\frac{dp_i^3}{2E_i(2\pi)^3}$, and $P_X = \sum_i p_i$ is the total four momentum of the hadronic final state. With the definitions given in equations 2.31 and 2.33 used together with equation 2.25, we obtain the general expresion of the differential cross section:

$$\frac{d^2\sigma}{d\epsilon' d\Omega} = \frac{G_F^2}{4\pi^2}\frac{|\overrightarrow{k'}|}{|\overrightarrow{k}|}L_{\alpha\beta}W^{\alpha\beta} \tag{2.34}$$

The expression for neutral current M_{NC} can be obtained by changing $g \to \bar{g} = \frac{g}{cos\theta_W}$, $M_W \to M_Z$,$\bar{l} \to \bar{\nu}$ and $J_{CC} \to J_{NC}$ in equations 2.26, 2.27 and 2.28. From equations 2.31 and 2.33 can be noted that the leptonic tensor is exactly calculable while the hadronic tensor is not and depends on the energy transferred. At lower energies, where the neutrinos interact only with bound nucleons or the entire nucleus, strong interactions prevent the hadronic current from being exactly calculable. At low neutrino energies, the most common neutrino interaction energies are those that minimally affect the interaction target. In the case of the charged current interaction this implies the change of electric charge in the baryon target: this interaction is called quasi-elastic interaction(see section 2.8.5). If the $W^\pm$ transfers enough momentum, so that the target gets a resonance state, the decay of the resonance will tipically produce a nucleon and a pion (see section 2.8.2).

At low energies, the neutrino interacts with bound nucleons. Hence, any interaction with a bound nucleon will affect the other nucleons in the nucleus. Therefore, nuclear effect has to be taken into account. In the following, we study first the simple neutrino interaction with a free nucleon (section 2.8.2 and section 2.9.5). In section 2.8.3 we study the particular case of neutrinos interacting with the entire nucleus producing coherently a pion without changing the nucleus. At higher energies many mesons and baryons can be produced. This case is called deep inelastic scattering (see section 2.8.4). Figure 2.7 shows the actual knowledge of the total neutrino cross sections for low energies.

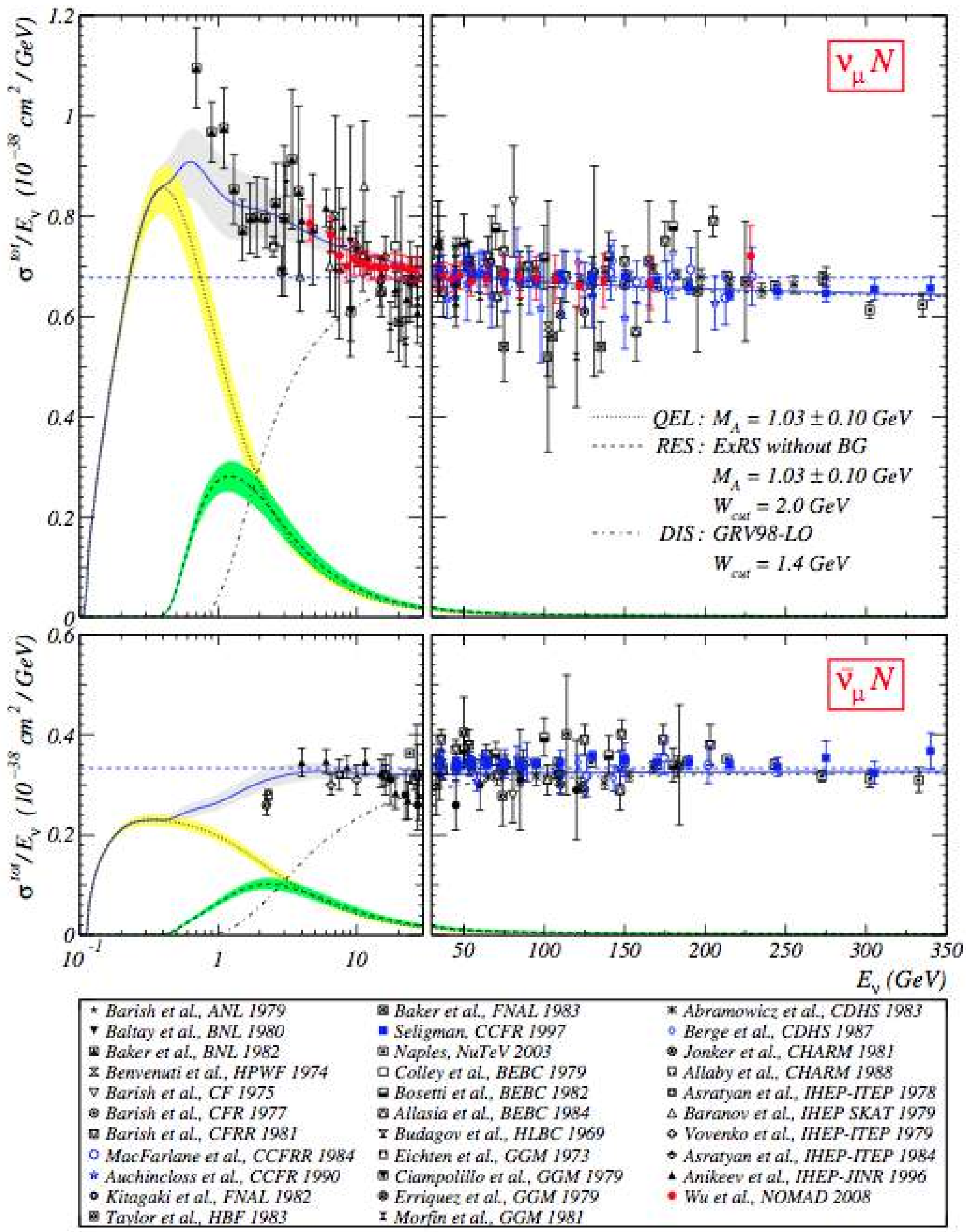

Figure 2.7: Total charged current ν_μ (top) and $\overline{\nu}_\mu$ nucleon (bottom) inclusive cross section as a function of neutrino energy. Low energy region is dominated by the quasi-elastic contribution (QE dotted), the intermediate region by resonance (RES) contribution (dashed) and the high energy region by the Deep Inelastic Scattering (DIS) contribution (dashed-dotted). As can be seen, measurements mainly concentrate in the DIS region and measurements in the RES region suffer from larger uncertainties, while very few measurements cover the QE region [53].

2.8.2 Resonant single pion, photon , η and kaon production

The Rein-Sehgal model describes single pion production in the charged and neutral current neutrino scattering. The pions are produced by excitations of 18 resonances [52]. In resonant production the neutrino scatters from a free nucleon. In this section we consider a single nuclear resonance (see figure 2.8) that can be expressed by:

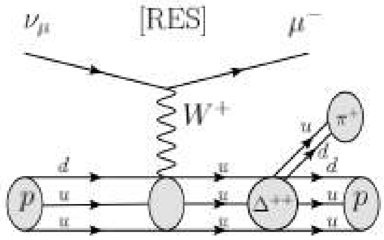

Figure 2.8: Feynman diagram of a single nucleon resonance.

$$\nu + N \rightarrow l + N^* \tag{2.35}$$

$$\nu + N \rightarrow \nu + N^* \tag{2.36}$$

$$N^* \rightarrow N^{'} + \pi \tag{2.37}$$

where N^* denotes one of the 18 nucleon resonances. Because we are looking at only single pion production, the kinematical region of this reaction is restricted to the regime of low Q^2 ($Q^2 < 2GeV$). At higher momentum transfer multi-meson resonances and deep inelastic scattering start to be important and are relatively well known (see section 2.8.4). The ampliude of transition is given by:

$$M_{CC} = \frac{G_F cos\theta_C}{\sqrt(2)}[\bar{l}\gamma^\alpha(1-\gamma^5)\nu]\langle N^*|J_\alpha|N\rangle \tag{2.38}$$

where J_α is the hadronic current operator containing a vector and an axial vector part. The expression for neutral current can be obtained using $\bar{l} \rightarrow \bar{\nu}$ and $G_F cos\theta_C \rightarrow G_F$. The cross section for a single resonance with mass M_{N^*} and negligible width is given by:

$$\frac{d^2\sigma}{dQ^2 dE_q} = \frac{1}{32 M_N E^2}\frac{1}{2}\sum_{spins}|M|^2\delta(W^2 - M_{N^*}^2) \tag{2.39}$$

where M_N is the nucleon mass and W the observed resonance mass. In the cases of non-negligible width, the delta function is replaced by a Breit-Wigner factor:

$$\delta(W - M_N) \rightarrow \frac{1}{2\pi}\frac{\Gamma}{(W - M_{N^*})^2 + \Gamma^2/4} \tag{2.40}$$

where Γ is the decay width of N^*, and E_q is the energy of the virtual $W^\pm$ or Z^0. Since the Rein-Sehgal model provides the amplitudes of neutrino resonance production, it is possible to calculate the cross section of single photon, kaon and η productions. Therefore, we only need to change the decay probabilites of the resonances.

2.8.3 Coherent pion production

In addition to resonance production, neutrinos can also coherently produce single pion final states. In this case, the neutrino coherently scatters from the entire nucleus, transferring negligible energy to the target (A). These low Q^2 interactions produce no nuclear recoil and a distinctly forward-scattered pion, compared to their resonance mediated counterparts. Both CC (see figure 2.9) and NC coherent pion production processes are possible.

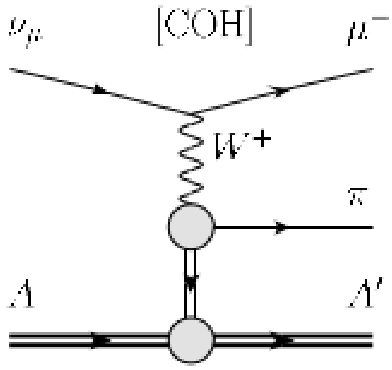

Figure 2.9: Feynman diagram of coherent pion production.

$$\nu_\mu A \rightarrow \nu_\mu A\pi^0, \qquad \bar{\nu}_\mu A \rightarrow \bar{\nu}_\mu A\pi^0 \tag{2.41}$$

$$\nu_\mu A \rightarrow \mu^- A\pi^+, \qquad \bar{\nu}_\mu A \rightarrow \mu^+ A\pi^- \tag{2.42}$$

The coherent π^0 cross section used in the Rein-Seghal model is based on the Adlers PCAC formula (Partially Conserved Axial-vector Current) [54]. In particular PCAC states that the hadronic axial current $J^a_{\mu 5}$ must satisfy the following continuity equation [55].

$$\partial^\mu J^a_{\mu 5} = -f_\pi m_\pi^2 \prod^a \tag{2.43}$$

where $\prod^a$ is the pion field operator, m_π is the pion mass and $f_\pi = 0.93 m_\pi$ is the pion decay constant [56]. In the forward scattering configuration, for any elastic neutral current reaction $\nu + N \rightarrow \nu + X$, where X denotes an inelastic channel, the cross section is:

$$\left(\frac{d\sigma}{dxdy}\right)_{PCAC} = \frac{G^2 M_N E_\nu}{2\pi^2}(1-y) f_\pi^2 \times \sigma(\pi_0 N \rightarrow X)\Big|_{E_\pi = E_y} \tag{2.44}$$

where the muon mass is neglected and the cross section is given in terms of the Bjorken kinematical variables:

$$\nu = \frac{p \cdot q}{M_N}, Q^2 = -(k - k')^2 \rightarrow x = \frac{Q^2}{2M_N\nu}, y = \frac{\nu}{E_\nu} \tag{2.45}$$

In order to calculate the charged current cross section $\nu + A \rightarrow l^- + X$ it is necessary to take into account the effect of lepton mass that is neglected in equation 2.44. The correction factor of the lepton mass (C) is defined in [57] as:

$$C = \left(1 - \frac{1}{2}\frac{Q^2_{min}}{Q^2 + m^2_\pi}\right)^2 + \frac{1}{4}y\frac{Q^2_{min}(Q^2 - Q^2_{min})}{(Q^2 + m^2_\pi)^2} \tag{2.46}$$

where

$$Q^2_{min} = m^2_l \frac{y}{1-y} \tag{2.47}$$

The range of the variable Q^2 is :

$$Q^2_{min} \leq Q^2 \leq 2M_N E y_{max} \tag{2.48}$$

where y lies between $y_{min} = m_\pi/E$ and $y_{max} = 1 - m_l/E$. Thus , the corrected PCAC formula valid for small angle scattering for $\nu + A \rightarrow l^- + X$ is [57]:

$$\left(\frac{d\sigma}{dxdy}\right)_{PCAC,m_l\neq 0} = \frac{G^2 M_N E}{\pi^2} f^2_\pi (1-y)\sigma(\pi^+ + A \rightarrow X)\Big|_{E_\pi = E_y} \times C\Theta(Q^2 - Q^2_{min})\Theta(y - y_{min})\Theta(y_{max} - y) \tag{2.49}$$

The cross section for $nu + A \rightarrow l^- + A + \pi^+$ is given by:

$$\left(\frac{d\sigma^{\pi^+}}{dxdydt}\right) = \left(\frac{d\sigma^{\pi^0}}{dxdydt}\right) C\Theta(Q^2 - Q^2_{min})\Theta(y - y_{min})\Theta(y_{max} - y) \tag{2.50}$$

The physical interpretation of the correction factor is as follows: when the muon mass is not neglected , the reaction $\nu + A \rightarrow l^- + X$ receives a contribution from the exchanged of a charged pion between the lepton vertex and the hadron vertex. The coupling at the lepton vertex is $f_\pi m_l \bar{l}\gamma_5\nu$ and the amplitude contains the characteristic pion propagator $(Q^2 + m^2_\pi)^{-1}$. This so called pseudo scalar amplitude interferes with the remaining amplitude, which is free of the pion singularity. The two amplitudes interfere destructively and the destructive nature of the interference is visible in the first term of the correction factor. While the cross sections for these processes are predicted to be comparatively small, coherent pion production has been observed across a broad energy range in both NC and CC interactions of neutrinos and antineutrinos. Figure 2.10 shows the measurements of coherent pion production cross sections for a variety of nuclei.

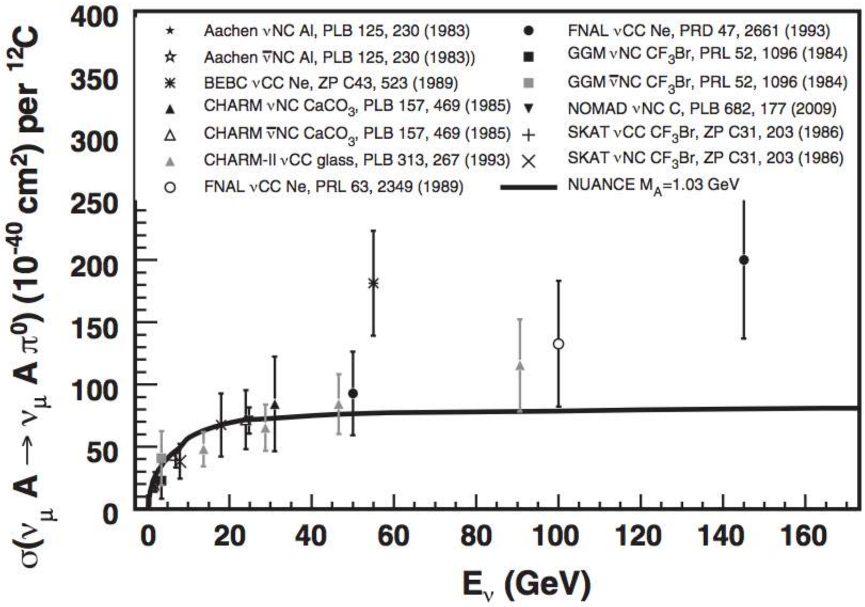

Figure 2.10: Measurements of absolute coherent pion production cross sections from a variety of nuclear targets and samples. Both NC and CC data are displayed on the same plot after rescaling the CC data using the prediction that $\sigma_{NC} = \frac{1}{2}\sigma_{CC}$. In addition, data from various targets have been corrected to carbon cross sections assuming $A^{1/3}$ scaling. Figure taken from reference [50].

2.8.4 Deep Inelastic Scattering (DIS)

Deep inelastic scattering begins to appears at high neutrino energy and is well known at $Q^2 > 2$ GeV^2. DIS can be described by:

$$\nu_l + A \rightarrow l^- + X \tag{2.51}$$

$$\nu_l + A \rightarrow \nu_l + X \tag{2.52}$$

where A is the nucleus. The feynman diagram associated to this procces is shown in figure 2.11. The differential cross section of the process $\nu + A \rightarrow l^- + X$ is given in its general form by equation:

$$\frac{d^2\sigma}{d\Omega d\epsilon} = \frac{G_F^2}{4\pi^2} \frac{|\overrightarrow{k'}|}{|\overrightarrow{k}|} L_{\mu\nu} W^{\mu\nu} \tag{2.53}$$

where ϵ' is the energy of the outgoing lepton, $W^{\mu\nu}$ can be expressed in its most general way as:

$$W^{\mu\nu} = W_1(-g^{\mu\nu} + \frac{q^\mu q^\nu}{q^2}) + \frac{W_2}{M_N^2}(p^\mu - \frac{p \cdot q}{q^2} p^\mu)(p^\nu - \frac{p \cdot q}{q^2} p^\nu) - W_3 \frac{i\epsilon^{\mu\nu\alpha\beta}}{2M_N^2} p_\alpha p_\beta \tag{2.54}$$

where M_N is the mass of the nucleon and the W_i are the hadronic structure functions. In the limit of high Q^2 ($Q^2 > 2$GeV), they represent the parton distribution functions. This can be

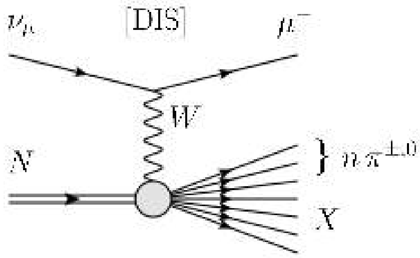

Figure 2.11: Feynman diagram of Deep Inelastic Scattering.

shown by changing the Bjorken kinematical variables in the laboratory frame:

$$\nu = \frac{p \cdot q}{M_N}, \quad Q^2 = -(k - k^{'})^2 \rightarrow x = \frac{Q^2}{2M_N(E_\nu - \epsilon^{'})}, \quad y = \frac{(E_\nu) - \epsilon^{'}}{E_\nu} \tag{2.55}$$

For high Q^2, we then have:

$$M_N W_1(Q^2, \nu) \rightarrow F_1(x) \tag{2.56}$$

$$\nu W_2(Q^2, \nu) \rightarrow F_2(x) \tag{2.57}$$

$$\nu W_3(Q^2, \nu) \rightarrow F_3(x) \tag{2.58}$$

where F_1, F_2 and xF_3, are the parton distribution functions. Using Callan-Gross relation, $2xF_1 = F_2$, we obtain:

$$\frac{d^2\sigma}{dxdy} = \frac{G_F^2 M_N E_\nu}{\pi}[(1 - y + \frac{1}{2}y^2 + C_1)F_2(x, q^2) \pm y(1 - y + \frac{1}{2}y^2 + C_2)xF_3(x, q^2)] \tag{2.59}$$

$$C_1 = \frac{1}{2E_\nu}\Big(\frac{yM_l^2}{2M_N x} - xyM_N - \frac{M_l^2}{2E_\nu} - \frac{M_l^2}{2M_N x}\Big) \tag{2.60}$$

$$C_2 = -\frac{M_l^2}{4M_N E_\nu x} \tag{2.61}$$

where M_l is the mass of the lepton and E_ν is the energy of the incoming neutrino.

2.8.5 Quasielastic scattering

For neutrino energies less than ~ 2 GeV, neutrino-nucleon interactions are predominantly quasielastic (QE). In a charged current neutrino QE interaction, the target neutron is converted to a proton. In the case of an antineutrino interaction, the target proton is converted to a neutron,

$$\nu n \rightarrow \mu^- p, \qquad \bar{\nu} p \rightarrow \mu^+ n \tag{2.62}$$

The most used theoretical description of this proccess is given in a review on neutrino interactions made by Llewellyn Smith [58] in 1972. Where the author uses the standard theory of weak interactions considering the neutrino scattering off free nucleons that are not necessarely point particles. All experiments rely heavily on this formalism and according to it, the quasielastic differential cross section can be expressed as

$$\frac{d\sigma}{dQ^2} = \frac{G_f^2 M^2 \cos^2\theta_C}{8\pi E_\nu^2}\left[A(Q^2) \pm \frac{s-u}{M^2}B(Q^2) + \frac{(s-u)^2}{M^4}C(Q^2)\right] \tag{2.63}$$

where (-)+ refers to (anti)neutrino scattering, G_F is the Fermi coupling constant, θ_C is the Cabbibo angle, Q^2 is the squared four-momentum transfer ($Q^2 = -q^2 > 0$) from the leptonic to hadronic system, M is the nucleon mass, m is the lepton mass, E_ν is the incident neutrino energy, and $(s-u) = 4ME_\nu - Q^2 - m^2$ is a simple combination of two Mandelstam invariants. The factors $A(Q^2)$, $B(Q^2)$, and $C(Q^2)$ are functions of the Q^2-dependent vector, F_1 and F_2, axial-vector F_A, and pseudoscalar F_P form factors of the nucleon (the form factors describes how different the nucleon is from a point like particle in an elastic scattering). The explicit dependence is shown in formulae 2.64, 2.65 and 2.66 where the definition $\tau = Q^2/4M^2$ is used.

$$\begin{aligned} A(Q^2) = \frac{m^2+Q^2}{M^2}\Big[&(1+\tau)F_A^2 - (1-\tau)F_1^2 + \tau(1-\tau)F_2^2 \\ &+ 4\tau F_1^2F_2^2 - \frac{m^2}{4M^2}((F_1^2+F_2^2)^2 + (F_A^2+2F_P^2)^2 - 4(1+\tau)F_P^2)\Big] \end{aligned} \tag{2.64}$$

$$B(Q^2) = \frac{Q^2}{M^2}F_A(F_1+F_2) \tag{2.65}$$

$$C(Q^2) = \frac{1}{4}(F_A^2 + F_1^2 + \tau F_2^2) \tag{2.66}$$

The vector part of the neutrino cross section, F_1 and F_2, can also be expresed in terms of the electric and magnetic vector form factors, G_E and G_M. Under the conserved vector current (CVC) hypothesis, these electric and magnetic vector form factors are related to the elastic nucleon form factors in electron scattering G_E^n, G_E^p, G_M^n and G_M^p.

$$G_E = G_E^p - G_E^n \tag{2.67}$$

$$G_M = G_M^p - G_M^n \tag{2.68}$$

These form factors have been measured in electron scattering experiments and their data used to parametrize their functional form which are close to a dipole form. One of this parametrizations is called *BBBA05* [59] and is used in neutrino interaction Monte Carlo simulations. Small contributions to the total cross section from the pseudo-scalar form factor F_P is expected for muon neutrino scattering [60]. The only remaining unknown in the model is the nucleon axial form factor which can only be measured using neutrinos. It is costumary to assume a dipole form for the axial form factor, equation 2.69, which depends on two empirical parameters: the value of the axial-vector form factor at $Q^2 = 0 \rightarrow g_A = F_A(0) = 1.2694 \pm 0.0028$ and the value of the Axial mass (M_A).

$$F_A(Q^2) = \frac{g_A}{(1 + Q^2/M_A^2)^2} \tag{2.69}$$

The main interest in experiments between 1970-1990, was testing the vector-axial vector (V-A) nature of the weak interaction and measuring the axial-vector form factor of the nucleon, topics that were considered particularly important in providing an anchor for the study of NC interactions. By the end of this period, the neutrino QE cross section could be accurately and consistently described by the model assuming a dipole axial-vector form factor with M_A $= 1.026 \pm 0.021$ GeV [61]. To complete the description of charged current QE interactions, a model for nucleons in a nucleus is needed. The most common and simplest approach in Monte Carlo simulations used by most experiments is to use the Impulse Approximation (IA), where the nucleus is considered a collection of independent nucleons, and the relativistic Fermi-gas model (RFG) [62]. In this model, nucleons form a Fermi gas with an average fermi momentum and binding energy that were adjusted to reproduce data of electron scattering experiments. For carbon, a binding energy of 34 MeV and fermi momentum of 200 MeV is used. More recent experiments, such as neutrino oscillation experiments, use heavy target such as carbon, oxygen or iron to improve data rates. Measured cross section are 20% higher than the prediction and inconsistencies as function of Q^2 were found (Miniboone, K2K, minos [63]). They have also measured values of M_A ~1.2 GeV which differs from the value obtained in the old experiments that used hidrogen or deuterium targets. Figure 2.12 summarizes the existing measurements of ν_μ QE scattering cross sections as a function of neutrino energy. Figure 2.13 shows the status of measurements of the corresponding antineutrino QE scattering cross section. Recent results from the NOMAD [53] experiment have expanded the reach out to higher neutrino energies, however, there are currently no measurements of the antineutrino QE scattering cross section below 1 GeV. The difference between old and more recent experiments has been attributed to nuclear effects that have not been taken into account in the simulations. Better models of the nucleus are needed to account for nuclear effects. Approaches beyond the Fermi-gas model have been developed in recent years to incorporate more sophisticated treatments,

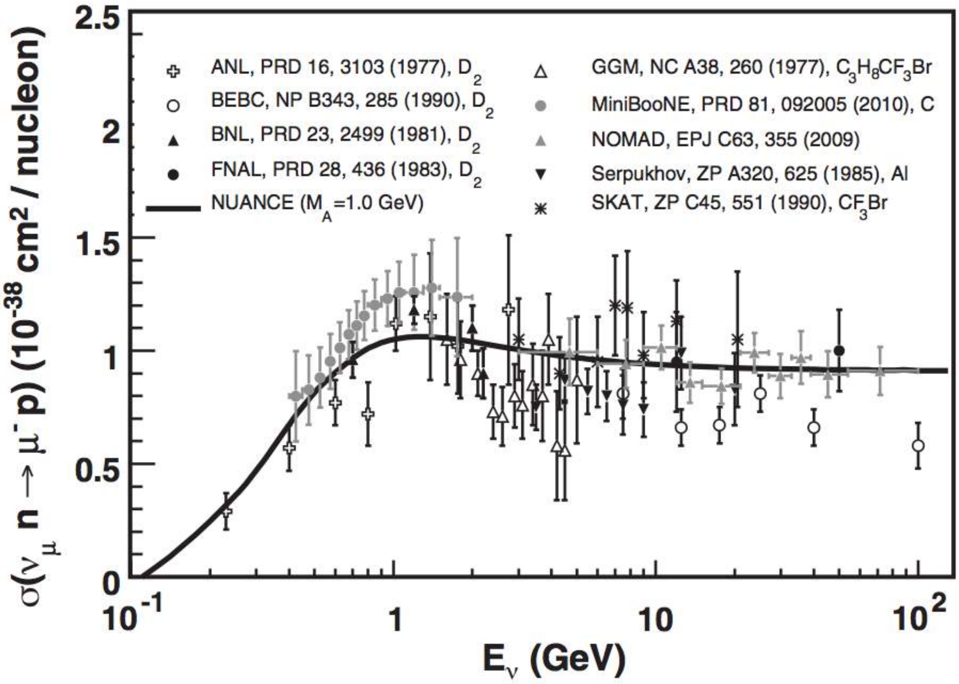

Figure 2.12: Cross section, $\nu_\mu n \rightarrow \mu^- p$, as a function of neutrino energy on a variety of nuclear targets. The free nucleon scattering prediction assuming $M_A = 1.0\ GeV$ is shown for comparison.

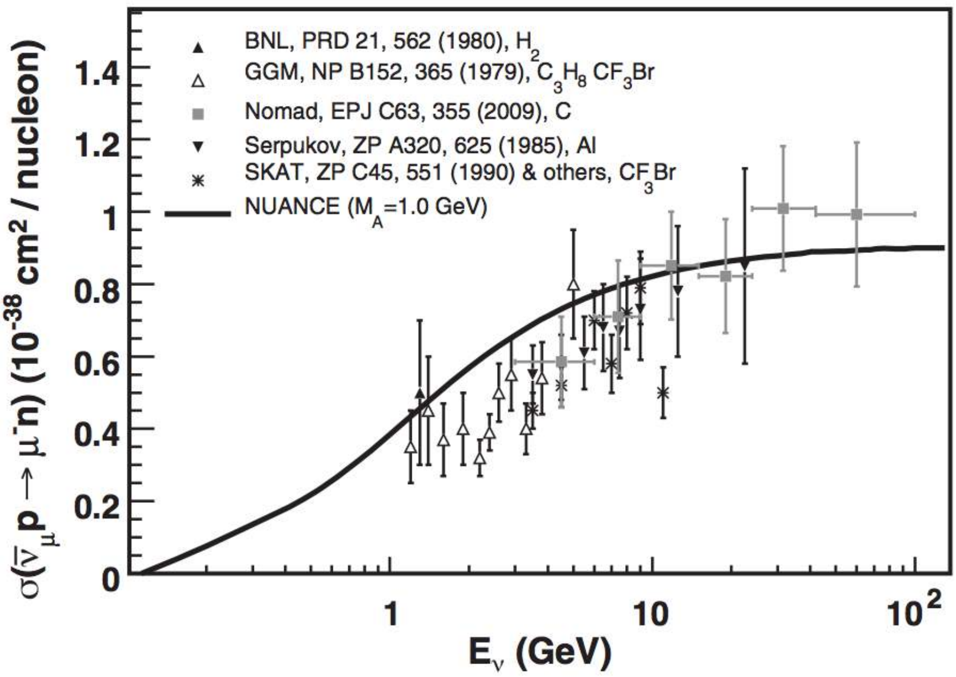

Figure 2.13: Cross section, $\bar{\nu}_\mu p \rightarrow \mu^+ n$, as a function of neutrino energy on a variety of nuclear targets.

Spectral Functions

The probability distribution of finding a nucleon with a given momentum and binding energy in the target nucleus is calculated using electron scattering data and theory predictions. The Relativistic Fermi Gas is the simplest version of the spectral function.

The Transfer Enhancement Model (TEM)

An enhacement in the transverse electron quasi-elastic (QE) response function for nucleons bound in carbon was observed. This effect was parametrized as a function of Q^2 in terms of a correction to the magnetic form factors of bound nucleons. The authors of this model [64] claim that the parametrization should also be applicable to the transverse cross section in neutrino scattering. If the observed tranverse enhacement is due to meson exchage currents (MEC) then, from theory, it is expected that enhacement in the longitudinal or axial contributions is small. The TEM is an effective model that accounts for nuclear effects that can be readily incorporated into existing neutrino Monte Carlo generators. One implementation exists in the NuWro neutrino Monte Carlo generator.

2.9 Interaction Reconstruction for Charged Current Quasi-Elastic and Charged Current Inclusive scattering

In this dissertation we need to reconstruct the neutrino energy for charged current inclusive and charged current quasi-elastic events with the purpose to calculate the first ever reported measurement of the ratio between CCQE and CCINC neutrino scattering on an hydrocarbon target in the energy range 2-10 GeV. The reconstruction using muon and recoil energy can be used to infer the properties of the interaction.

Charged current QE interactions are very useful for neutrino experiments because the neutrino flavor can be identified by the charge of the final state muon and the neutrino energy can be calculated by measuring muon kinematics or using muon energy and recoil energy of the system. This is possible thanks to the relatively simple two body kinematics involved. In order to reconstruct the neutrino energy we assume that the target nucleon in the reaction,

$$\nu_\mu + n \to p + \mu^- \tag{2.70}$$

is at rest and free, or quasi-free inside the nucleus (Relativistic Fermi Gas aproximation). Using the conservation of 4-momentum in a two body elastic colision and neglecting the neutrino mass leads us to our neutrino energy expression for Charged Current QE scattering.

$$E_\nu^{\mathrm{QE}} = \frac{2(M_n - \mathrm{E_B})E_\mu - \left[(M_n - \mathrm{E_B})^2 + m_\mu^2 - M_p^2\right]}{2\left[(M_n - \mathrm{E_B}) - E_\mu + \sqrt{E_\mu^2 - m_\mu^2} cos\theta_\mu\right]} \tag{2.71}$$

where M_n, M_p and m_μ are the neutron, proton and muon masses, $E_\mu = T_\mu + m_\mu$ is the total muon energy, θ_μ is the angle of the muon track with respect to the neutrino direction, and $\mathrm{E_B}$ is the nuclear binding energy in carbon ($\mathrm{E_B} = 34$ MeV).

The 4-momentum transfer to the target nucleon represented by the relativistic invariant, $Q^2 = -q^2$, where q is the 4-momentum of the $W^\pm$ boson, can be constructed as,

$$Q^2_{\mathrm{QE}} = -m_\mu^2 + 2E_\nu^{\mathrm{QE}}\left(E_\mu - \sqrt{E_\mu^2 - m_\mu^2} cos\theta_\mu\right) \tag{2.72}$$

Both expression are going to be used in our main reconstruction. The superscript QE in both expresions, E_ν^{QE} and Q^2_{QE}, are there to remain us that these formulas are deduced using a CCQE hypothesis (they won't work for background events or interactions where the nucleon interacts with its neighbors). In the latter cases we can think about this expresions as a parametrization of the muon kinematics. The charged current inclusive analysis is the base for understanding a series of fundamental aspects such as the detector performance, reconstruction quality, efficiency, acceptance effects and serve as a reference to compare their kinematics and physics distributions with exclusive topologies. It is also the first step towards deep-inelastic scattering measurements. For the Charged Current Inclusive and the Charged Current Quasi-Elastic without using the muon kinematics (CCQE hypothesis) we are able to reconstruct the neutrino energy that is going to be used by:

$$E_\nu = E_\mu + Recoil \tag{2.73}$$

Where the recoil energy is computed calorimetrically like all the energy that is not associated to the muon track.

2.10 Summary and status of charged current neutrino and antineutrino cross sections measurements and results from oscillation experiments

Many results from CC (anti)neutrino interactions have been accumulated over several decades using a variety of neutrino targets and detector technologies. Figures 2.14 and 2.15 summarize the existing measurements of CC neutrino and antineutrino cross sections across this intermediate energy range.

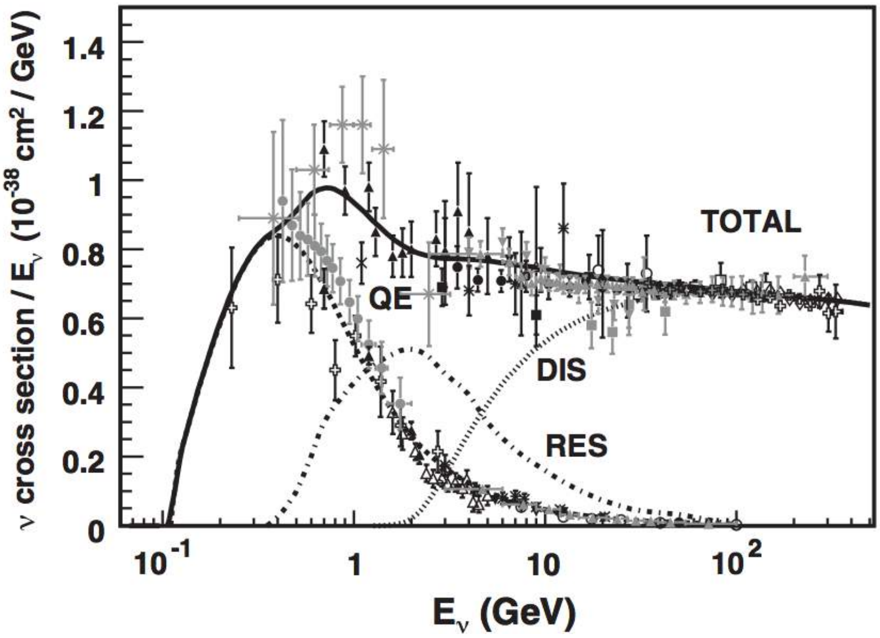

Figure 2.14: Total neutrino per nucleon CC cross sections (for an isoscalar target) per neutrino energy as a function of energy. Same data as in figures 2.12 and 2.13, plus additional low energy CC inclusive data from ▲ ([65]), $*$ ([66]), ■ ([67]), and ★ ([68]). Predictions provided by the NUANCE generator. Figure taken from reference [50].

Most of our knowledge of neutrino cross sections in this intermediate energy range comes from early experiments that collected relatively small data samples (few thousand events). Historically, adequate theoretical descriptions of quasielastic, resonance-mediated, and deep inelastic scattering have been formulated; however, there is no uniform description that globally describes the transition between these processes or how they should be combined. Moreover, the full extent to which nuclear effects impact this region is a topic that has only recently been addressed.

2.10.1 Recent results from MINERνA experiment:

Nuclear Target Cross Section Ratios at MINERνA:
Measurements of ν_μ inclusive charged-current cross section ratios on carbon, iron, and lead relative to scintillator are presented in [69]. Data was collected by the fine-grained MINERνA detector in the NuMI beamline at Fermilab. This is the first direct measurement of nuclear dependence in neutrino scattering. The ratios show a depletion at low Bjorken x and enhancement at large x, both of which increase with the nucleon number of the target. The data exhibit trends not found in GENIE, a standard neutrino-nucleus event generator, or alternative models of nuclear modification to inelastic structure functions (see figure 2.16)

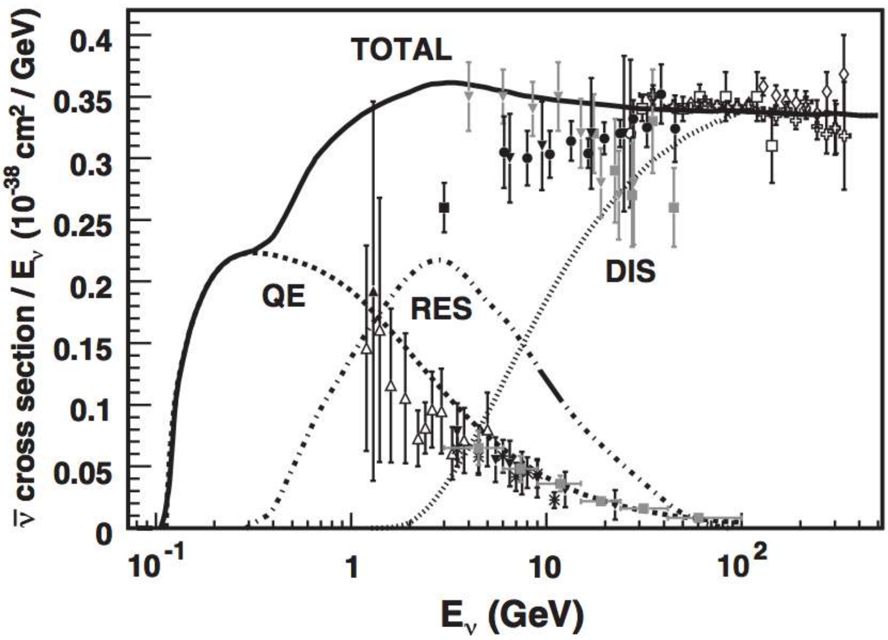

Figure 2.15: Total anti-neutrino per nucleon CC cross sections per neutrino energy as a function of energy. Same data as in figures (2.12, 2.13), plus additional low energy CC inclusive data from ▲ ([65]), $*$ ([66]), ■ ([67]), and ★ ([68]). Predictions provided by the NUANCE generator. Figure taken from reference [50].

Quasi Elastic Scattering at MINERνA:

A study of ν_μ charged-current quasi-elastic events in the segmented scintillator inner tracker of the MINERνA experiment has been reported [70]. The events were selected by requiring a μ and low calorimetric recoil energy separated from the interaction vertex. The flux-averaged differential cross-section,$\frac{d\sigma}{dQ^2}$ was measured. Deviations were found between the measured $\frac{d\sigma}{dQ^2}$ and the expectations from a model of independent nucleons in a relativistic Fermi gas (see figure 2.17). The results (see figure 2.18) also show an excess of energy near the vertex consistent with multiple protons in the final state [70], [71].

Two track Quasi Elastic Scattering at MINERνA:

Charged-current ν_μ scattering from a hydrocarbon target in which a μ^- is accompanied by a proton with momentum greater than 450 MeV and no pions is studied using the high-resolution MINERνA detector (see figure 2.19. This event topology is consistent with quasi-elastic (QE) scattering from neutrons, and the four-momentum transfer, Q^2, is estimated using the four-momentum of the leading proton. The extracted $d\sigma/dQ^2$ [72] consists of both QE and inelastic components, and is well-described by an unadorned relativistic Fermi gas (RFG) nuclear model with final-state interactions treated according to a particle cascade prescription. This agreement is in contrast with MINERνAs previous ν_μ QE measurement, where Q^2 is estimated using

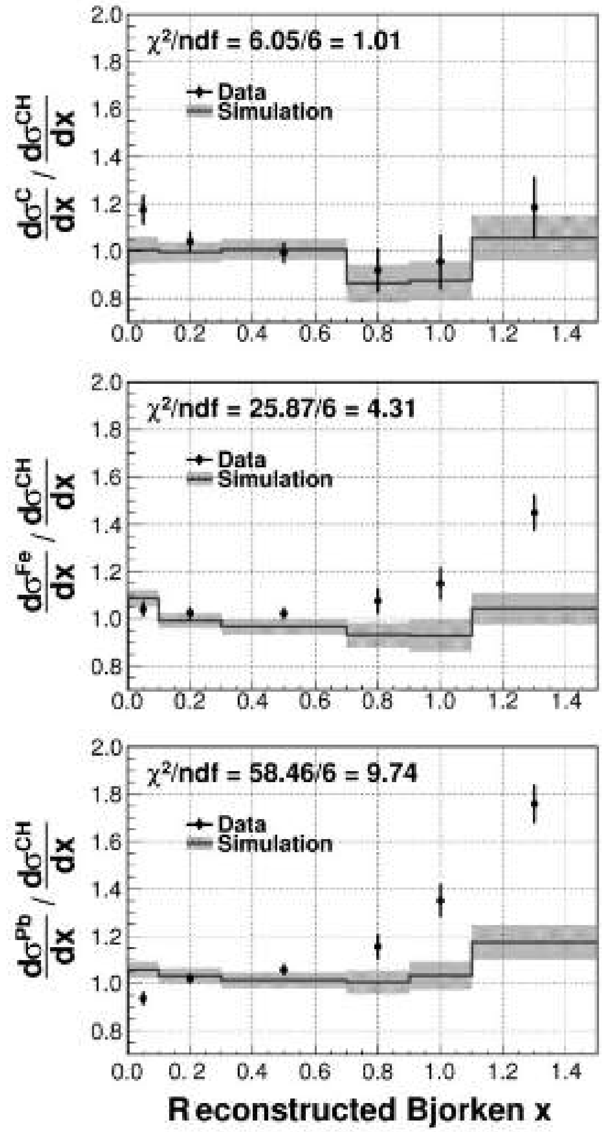

Figure 2.16: Ratios of the charged-current inclusive ν_μ cross section per nucleon as a function of reconstructed Bjorken x for C/CH (top), Fe/CH (middle), and Pb/CH (bottom). Error bars on the data (simulation) show the statistical (systematic) uncertainties [69].

muon kinematics and the extracted cross section had the inelastic component removed. That previous result is better described by accounting for nuclear medium effects that are observed in electron-nucleus scattering. The measurement presented in [72] guides the formulation of a theoretically motivated description of neutrino-nucleus interactions intended to encompass the hadronic as well as the leptonic aspects of this process.

Resonant Pion Production:

Charged pion production via charged current ν_μ interactions in plastic (CH) is studied using the MINERνA detector. Events with hadronic mass W < 1.4 GeV are selected to isolate single

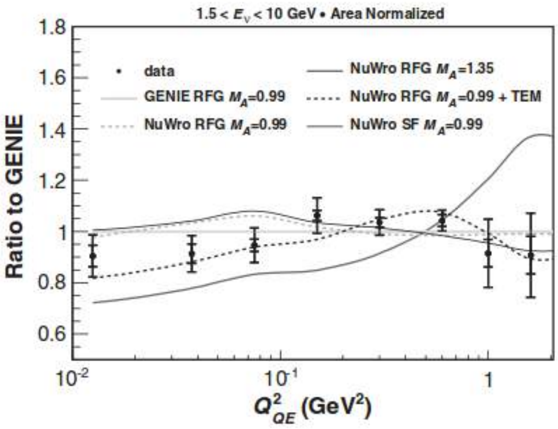

Figure 2.17: Ratio between the measured neutrino $d\sigma/dQ^2_{QE}$ shape in Q^2_{QE} and several different models where the denominator is the GENIE default quasi-elastic cross section [70].

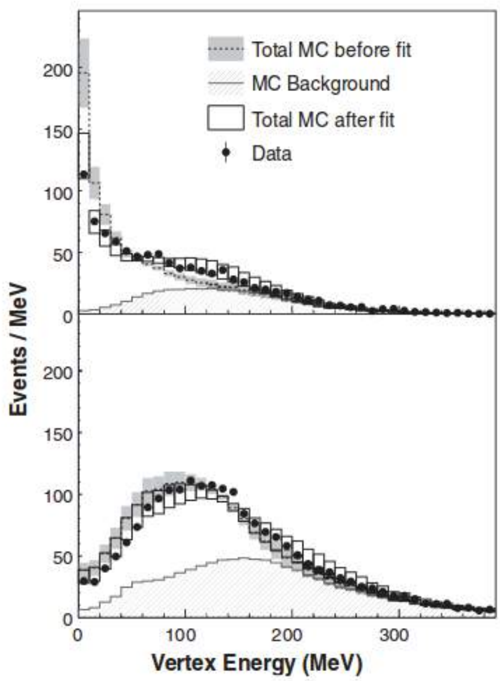

Figure 2.18: Reconstructed vertex energy of events passing the selection criteria in the data (points with statistical errors) compared to the GENIE RFG model (shown with systematic errors) for $Q^2_{QE} < 0.2GeV^2/c^2$ (top) and for $Q^2_{QE} > 0.2GeV^2/c^2$ (bottom) [70].

pion production, which is expected to occur primarily through the $\Delta(1232)$ resonance. Cross sections as functions of pion production angle and kinetic energy were measured (see figure 2.20) and compared to predictions from different theoretical calculations and generator-based models, for neutrinos ranging in energy from 1.5 GeV to 10 GeV. The data are best described by

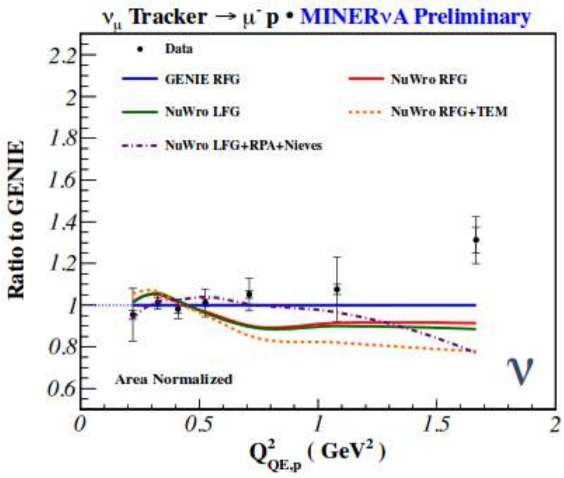

Figure 2.19: Ratio between the measured neutrino $d\sigma/dQ^2_{QE,p}$ shape in $Q^2_{QE,p}$ and several different models where the denominator is the GENIE default quasi-elastic cross section [72].

calculations which include significant contributions from pion intranuclear rescattering. These measurements constrain the primary interaction rate and the role of final state interactions in pion production, both of which need to be well understood by neutrino oscillation experiments [73]

2.10.2 Results from oscillation experiments

In 2011 T2K was the first experiment to directly measure a non-zero value of θ_{13}. The precision on this value has then been strengthened by subsequent results from MINOS [74] and Double-CHOOZ [75], culminating in the announcement of a 5.2σ and 4.9σ by Daya Bay [76] and RENO [77] respectively. Thanks to these experiment the value of θ_{13} is now known at the same level of precision as the other mixing angles. The current knowledge of angle and mass differences is found in [78]. We have in the solar sector:

$$\Delta m^2_{21} = (7.62 \pm 0.19) \times 10^{-5} eV^2 \tag{2.74}$$

$$\sin^2\theta_{12} = 0.320^{+0.015}_{-0.017} \tag{2.75}$$

In the atmospheric sector and 1-3 sector, we have in the case of normal hierarchy $\Delta m^2_{31} > 0$

$$\Delta m^2_{31} = 2.53^{+0.08}_{-0.10} \times 10^{-3} eV^2 \tag{2.76}$$

$$\sin^2\theta_{23} = 0.49^{+0.08}_{-0.05} \tag{2.77}$$

$$\sin^2\theta_{13} = 0.026^{+0.003}_{-0.004} \tag{2.78}$$

And for the inverted hierarchy case $\Delta m^2_{31} < 0$

$$\Delta m^2_{31} = -2.40^{+0.10}_{-0.08} \times 10^{-3} eV^2 \tag{2.79}$$

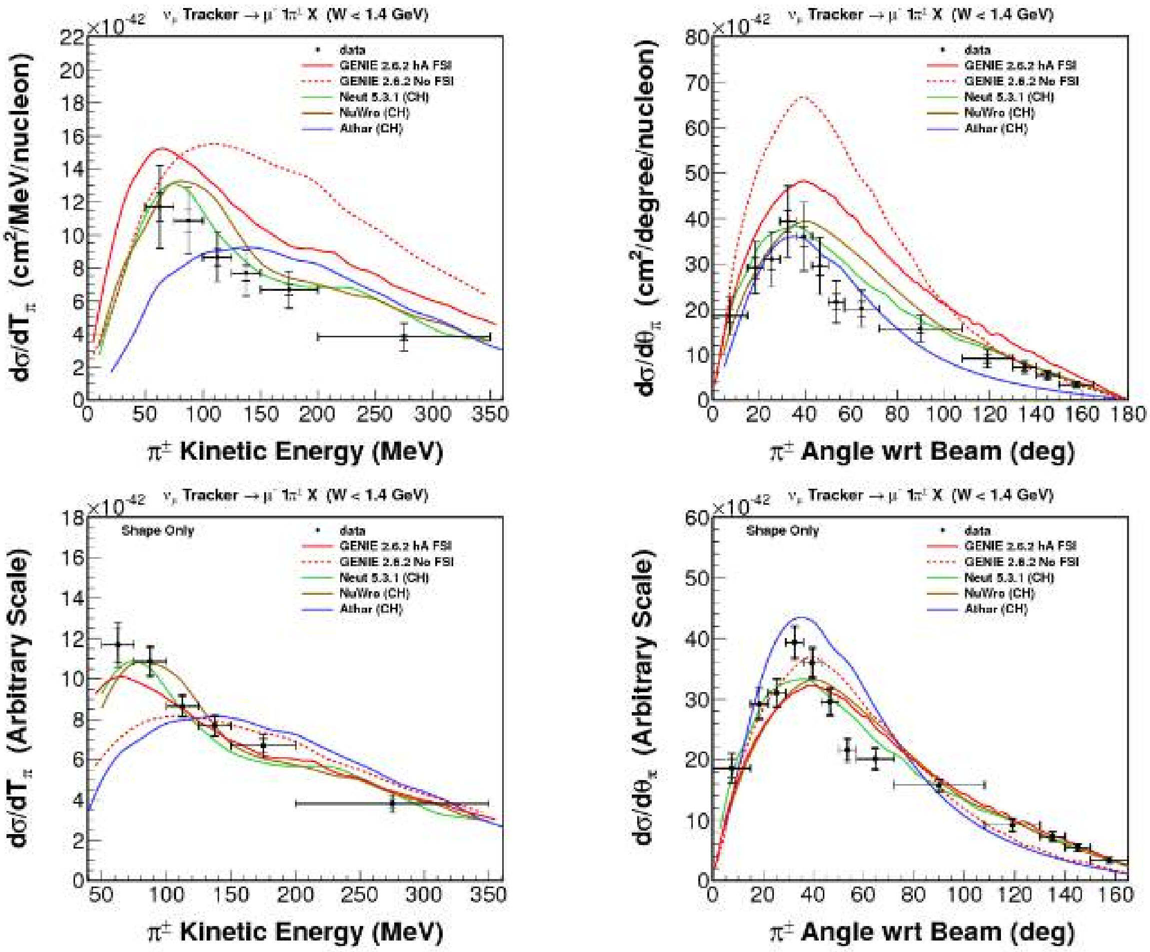

Figure 2.20: Comparisons of the one-pion measurements to various models. The cross sections are on the top, and the shape measurements are on the bottom [73].

$$\sin^2\theta_{23} = 0.53^{+0.05}_{-0.07} \tag{2.80}$$

$$\sin^2\theta_{13} = 0.027^{+0.003}_{-0.004} \tag{2.81}$$

Results obtained from the experiments previously mentioned are shown in Figs. 2.21 and 2.22 A brief summary of the results:

$$\sin^2 2\theta_{13}|_{DoubleCHOOZ} = 0.109 \pm 0.030(stat) \pm 0.025(syst) \tag{2.82}$$

$$\sin^2 2\theta_{13}|_{DayaBay} = 0.089 \pm 0.010(stat) \pm 0.005(syst) \tag{2.83}$$

$$\sin^2 2\theta_{13}|_{RENO} = 0.113 \pm 0.013(stat) \pm 0.019(syst) \tag{2.84}$$

$$\sin^2 2\theta_{13}|_{MINOS} = 0.094^{+0.04}_{-0.05} \tag{2.85}$$

$$\sin^2 2\theta_{13}|_{T2K} = 0.104^{+0.060}_{-0.045} \tag{2.86}$$

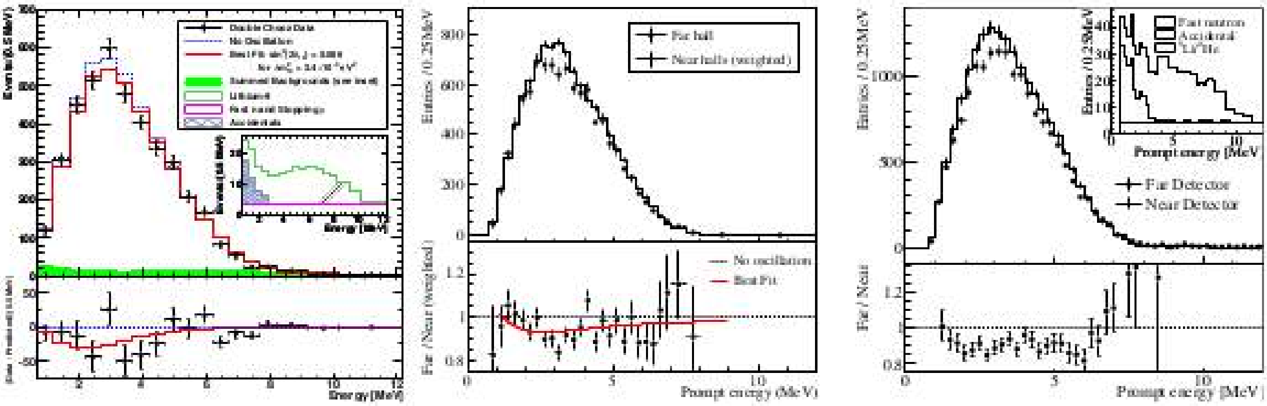

Figure 2.21: Results from the Double-CHOOZ, Daya Bay and RENO experiment (left, middle and right respectively). Each result is shown in the same unified manner. **TOP**: Measured prompt energy spectrum of the far detector compared with the no-oscillation prediction from the measurements of the two near detectors. Spectra were background subtracted (for Daya Bay and RENO) and includes background for Double-CHOOZ. Inset (Double-CHOOZ and RENO): stacked histogram of backgrounds. Uncertainties are statistical only. **BOTTOM**: The ratio of measured and predicted no-oscillation spectra. The red curve is the best-fit solution and the dashed line is the no-oscillation prediction [75], [76], [77].

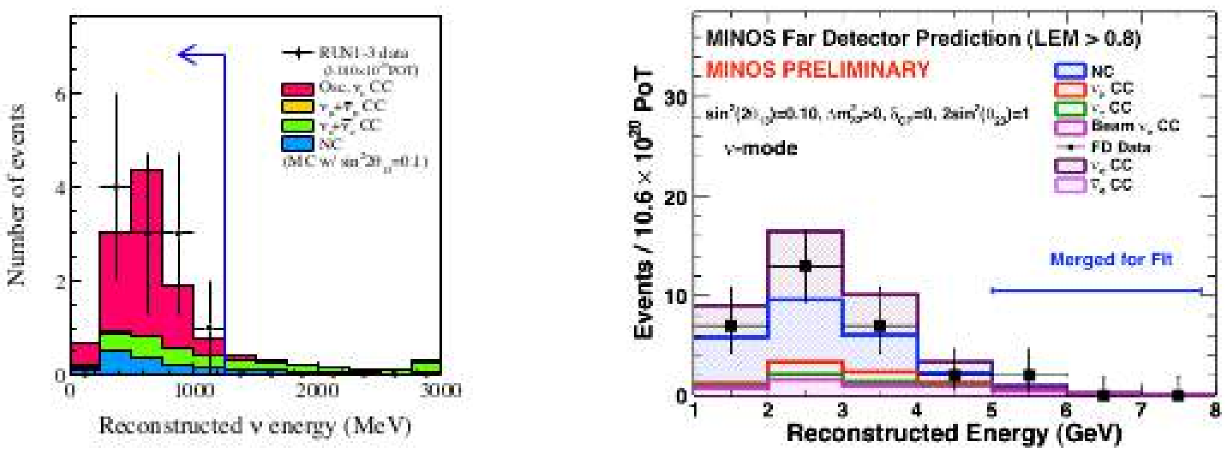

Figure 2.22: Left: T2K distributions of ν_e event selection variables vs reconstructed neutrino energy. Blue arrows indicate the selection criteria. Right: MINOS reconstructed energy distribution. The NC background is shown in blue.

These latest results open the possibility that neutrinos violate CP and therefore have played an important role in the early age of the Universe contributing to the creation of the baryon asymmetry, which is responsible for the dominance of the matter in our universe. The observation of the CP violation in the leptonic sector is therefore very important to improve the knowledge beyond the standard model. To reach this goal, several unknowns need to be solved first, like the mass hierarchy of the neutrino eigenstates or the maximality of the θ_{23} angle. While existing (NOvA [79]), or near future experiments as INO [80] (2017), might be able to have sensitivity to the mass hierarchy, there is a clear need to improve current experiments or build new experiments to reach the sensitivity needed to measure the CP phase. This second phase of experiments is meant to deliver precise measurement 20 years from now.

Chapter 3

MINERνA Detector

3.1 The ν_μ at Main Injector (NuMI Beam)

Fermilab NuMI beamline provides an intense flux of either mostly ν_μ or $\overline{\nu}_\mu$ to short and long baseline neutrino experiments like MINOS, MINERνA , NOνA [79]. NuMI neutrinos are the final decay product of charged mesons, most kaons and pions, generated by the collision of 120 GeV protons [1], with a graphite target. Two pulsed magnetic horns focus positive (negative) mesons that will decay to produce ν_μ ($\overline{\nu}_\mu$). The flux of neutrinos along the focusing axis has energies in the range of 1 to 50 GeV. Figure 3.1 shows NuMI main parts and components. A detailed description may be found in [81] and [82].

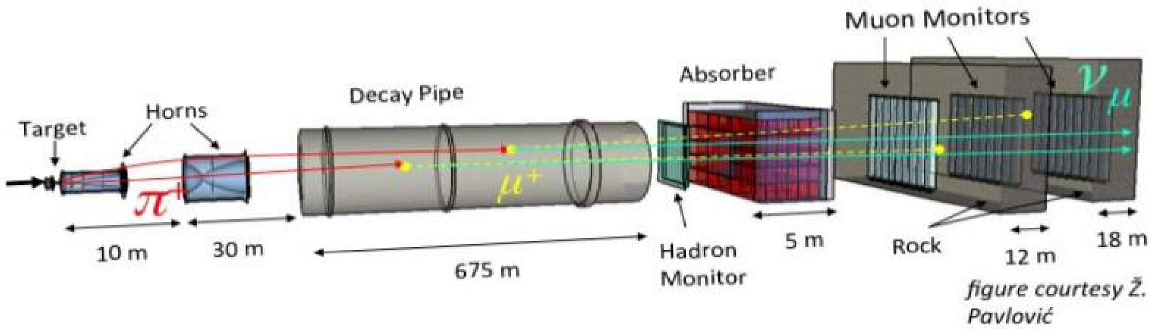

Figure 3.1: NuMI beamline components.

[1]extracted from the Fermilab Main Injector

3.2 Proton Production for NuMI beamline

Protons go through several stages before acquiring the energy of 120 GeV: the LINAC, the booster and the Main Injector. The LINAC accelerates the protons up to 400 MeV and sends them to the booster that accelerates them up to 8 GeV. At the final stage protons from the Main Injector are extracted to NuMI target with a frequency of 0.53 Hz using a single turn extraction. Every 1.9 s a 8.4 μs spill with about $3,5 \times 10^{13}$ protons is extracted and sent towards a 0.95 m long segmented water cooled graphite target. Around 15 cm prior to striking the target, the proton beam passes through a toroid that measures the number of protons, and the beam profile is monitored to guarantee an appropiate behavior.

Mesons produced in the target are focused by two 3 meter magnetic horns acting as parabolic magnetic lenses that create a toroidal field around 3 Teslas, these are located downstream of the target (see figure 3.2). The horns are water cooled and operated by a pulsed +(-) 185 kA

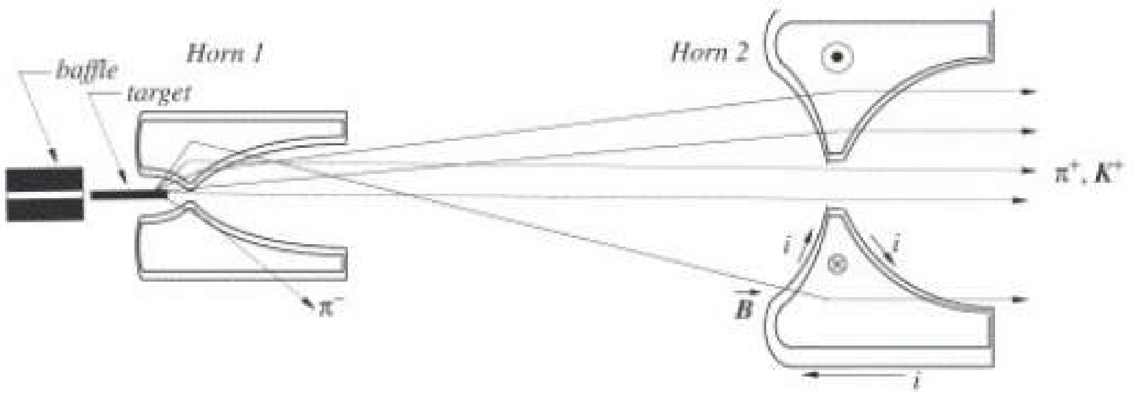

Figure 3.2: Schematic showing positions of the NuMI target, baffle and horns. [82]

current [82] to bend pions and kaons towards the proton beam path. It is possible to vary the current of the horns to make special studies and characterization of the beamline. If the target is moved 2.5 meters upstream relative to the horns there wil be a change in momentum spectra of the focused particles resulting in a different energy spectrum. Moving the target away from the horn focuses mesons with a high energy obtaining a higher energy beam. Passing the horns, mesons decay and contribute to the neutrino flux in the MINOS detector cavern. From this mesons 97% are pions and the rest are kaons [83]. Table 3.1 shows different mesons decay modes that produce neutrinos. The decay area is a 675 m long and 2 m diameter cylinder kept at a residual pressure of about 1 Torr or less. Protons and undecayed mesons still present at this stage at the end of the decay pipe are stopped at a hadron absorber consisting a water

Decay Mode	Fraction (%)
$\pi^+ \to \mu^+ + \nu_\mu$	99.99
$\pi^+ \to \mu^+ + \nu_\mu + \gamma$	$2X10^{-4}$
$\pi^+ \to e + \nu_e$	$1.23X10^{-4}$
$K^+ \to \mu^+ + \nu_\mu$	63.55
$K^+ \to \pi^0 + e + \nu_e$	5.07
$K^+ \to \pi^0 + \mu^+ + \nu_\mu$	3.35

Table 3.1: Decay modes of π^+, K^+ resulting in ν_μ in the NuMI beam.

cooled aluminum core surrounded by a steel block and an external concrete chamber. The hadron absorber removes all the hadronic content of the beam, leaving only neutrinos and muons. After the hadron absorbers three muon monitors are separated by dolomite rock. The purpose of the muon monitors is measure the muon energy spectrum that can be used to predict the neutrino flux in situ [73] . Between the hadron absorber and the detector hall there is around 240 meters of dolomite rock, enough to stop all muons present in the beam, leaving only neutrinos. The resulting neutrino beam consists of 97,8% ν_μ and few $\bar{\nu}_\mu$ (1.8%) and ν_e (0.4%) the last being the result of the decay of muons. Figure 3.3 shows the muon monitors and hadron absorbers location in the NuMI beamline.

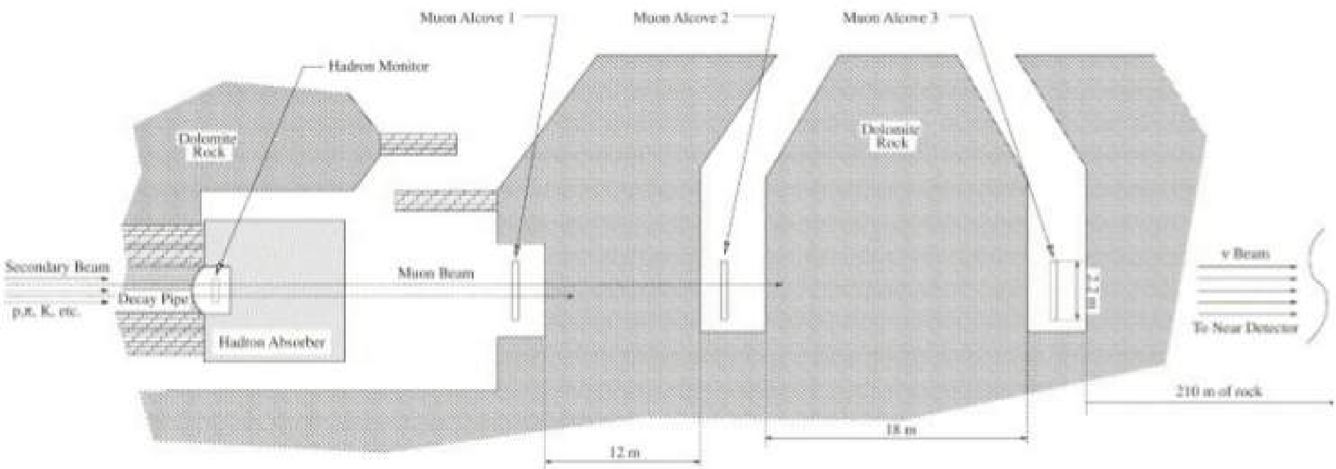

Figure 3.3: The NuMI secondary absorbers and muon monitors.

Figure 3.4 shows the possible energy configurations of the NuMI beam: low energy (LE) and medium energy (ME). Different energies are achieved by changing the distance between the target and the second horn in a movement similar to the lenses of an optical system[2].

[2] The target is assembled on a system of rails that allows moving the target for a distance of 2.5 m.

Pions and kaons of different momenta are selected and focused in the decay region resulting in different energy spectra.

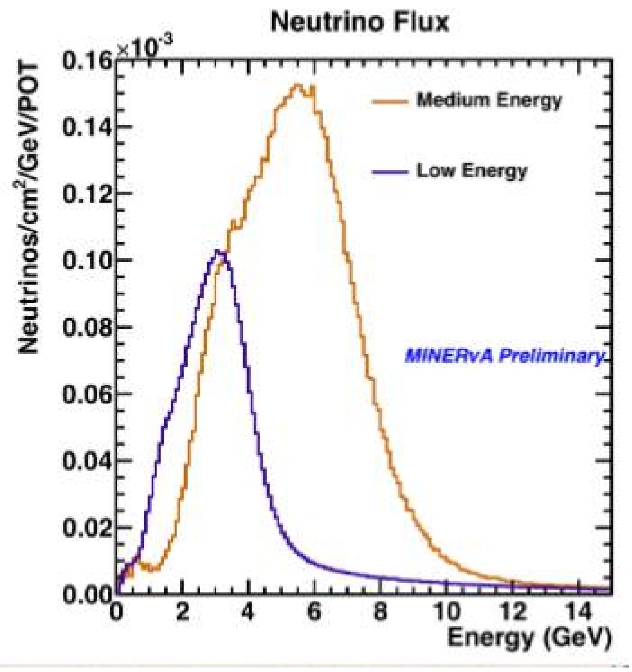

Figure 3.4: NuMI configurations. Low Energy and Medium Energy, Flux estimation using a GEANT4 based simulation of the NuMI beam line.

The capability of changing the horn makes it possible to focus mesons of the opposite signal, so the NuMI beam is able to produce neutrinos or antineutrinos. The NuMI neutrino beam is delivered to MINOS experiment whose near detector is housed in an experimental hall 100 m underground at FERMILAB grounds. MINERνA detector is placed just upstream the MINOS near detector.

3.3 The MINERνA detector

The MINERνA detector employs fine grained polystyrene scintillator for tracking and calorimetry. In addition to the scintilllator the detector contains nuclear targets of iron, lead, carbon, liquid helium and water. MINERνA main objective is to study neutrino scattering with matter with high statistics for neutrino energies from 1 - 50 GeV. Figure 3.5 shows the MINERνA detector in the experimental hall 100 m underground. The MINERνA detector, shown schematically in figure 3.6, consists basically of two subdetectors: the Inner Detector and the Outer Detector. The Inner Detector itself is subdivided in four subdetectors:

- Nuclear targets;

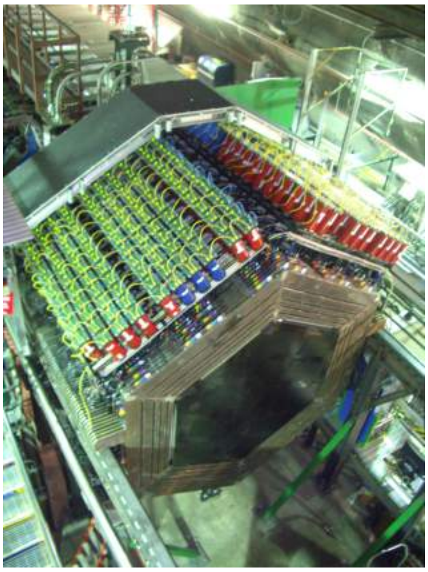

Figure 3.5: Top view of the MINERνA detector.

- Active target;
- Electromagnetic calorimeter (ECAL);
- Hadronic calorimeter (HCAL).

The active target (the core of the detector) consists of strips of solid scintillator and is the primary volume where interactions happen and where all the analysis is centered. That includes deep inelastic scattering, photon tracking, detection of protons, particle identification through $\frac{dE}{dx}$ (loss of energy by unit of length). Since scintillators, due to their low density, can not hold the whole event, its volume is surrounded by a sampling detector that constitutes the electromagnetic and hadronic calorimeters. In these detectors scintillating strips are interleaved with absorbers (lead sheets in the electromagnetic calorimeter and steel sheets in the hadronic calorimeter). Upstream the detector a veto wall is used to identify charged particles that traverse the detector.

The detector has the shape of a 5.9 m hexagonal prism of cross section varying from 3.35 m to 4.10 m. The total mass of scintillators is 6.4 ton. Nuclear targets consisting of Fe (998kg), Pb(1023kg), C(120kg), liquid He ($250kg$) and H_2O are upstream of the detector[3]. The detector high granularity (see scintillating strip description in section 3.5) assures precise vertex reconstruction. The detector is segmented in scintillating planes (section 3.5) and use the Outer Detector(OD) as a supporting structure.

[3]Considering a transversal section with radius = 90 cm

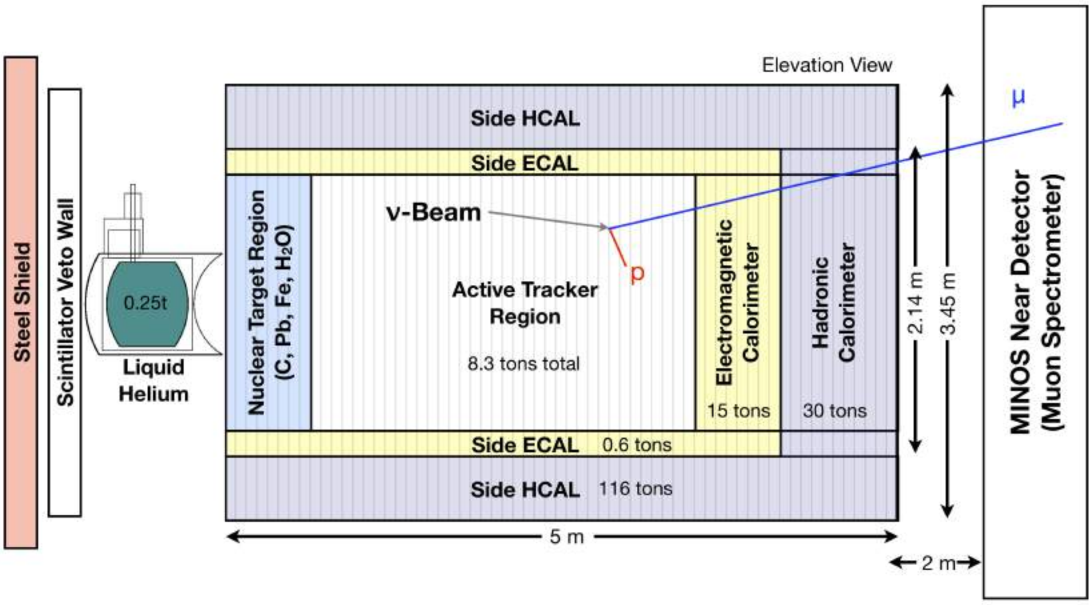

Figure 3.6: Schematic view of the MINERνA detector.

The Inner Detector(ID) has scintillating planes with strips arranged in three different orientations: X, U and V as shown in figure 3.7. U and V planes are rotated $\pm 60^{\circ}$ relative to X. Two scintillating planes XU or XV make a module. This arrangement allows tracking reconstruction. Figure 3.8 illustrates one module of the detector active region (structure of a module is depicted on the right) and figure 3.9 shows a module of the electromagnetic calorimeter.

The Inner Detector(ID) is surrounded by a system of absorbers and scintillators that constitute the Outer Detector(OD) (formed by towers arranged at the sides of the hexagon). The downstream part of the detector has a hadronic calorimeter (HCAL) with 1 inch thick absorbers per scintillating plane as shown in figure 3.10. The electromagnetic calorimeters(ECAL) have 0.2 cm thick Pb sheets as absorbers. The ECAL high granularity assures a good resolution for the energy of electrons and photons and makes it possible to determine their direction. The Inner Detector(ID) is a regular hexagon of apothem 1.07 m with a vertical major axis composed of 120 modules stacked longitudinally, numbered in the range $[-5, 114]$. Except for the passive targets modules, each module type employs scintillator as active element. The arrangment of modules into subdetectors is summarized in the table 3.2. The nuclear target region (figure 3.6) has absorbers placed between active targets making it possible the study of events in different

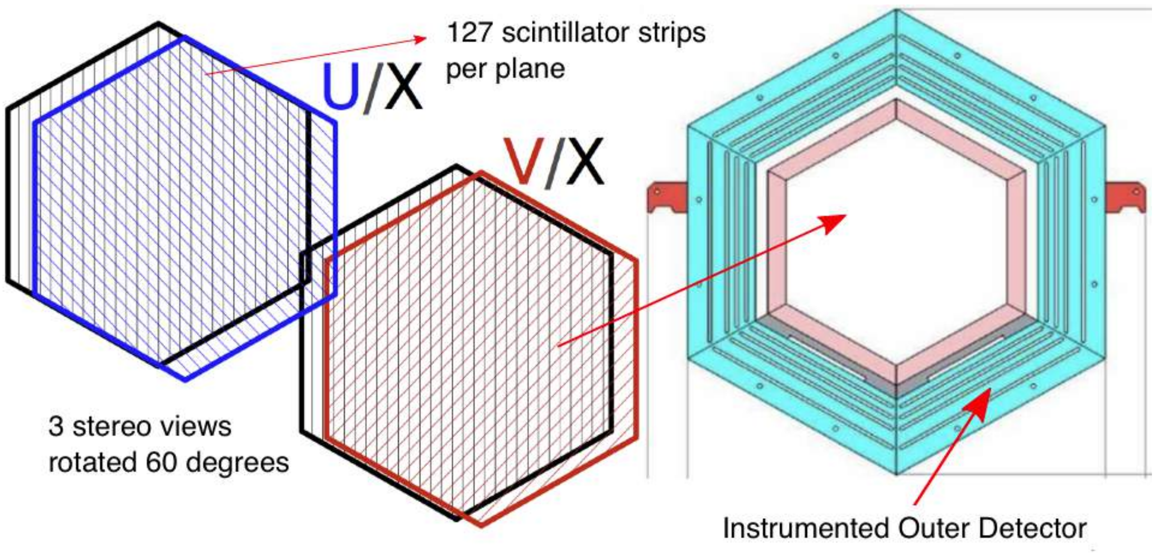

Figure 3.7: Detector active module, X, U and V planes. Note the $\pm\ 60^0$ rotation of the planes U and V relative to the X planes.

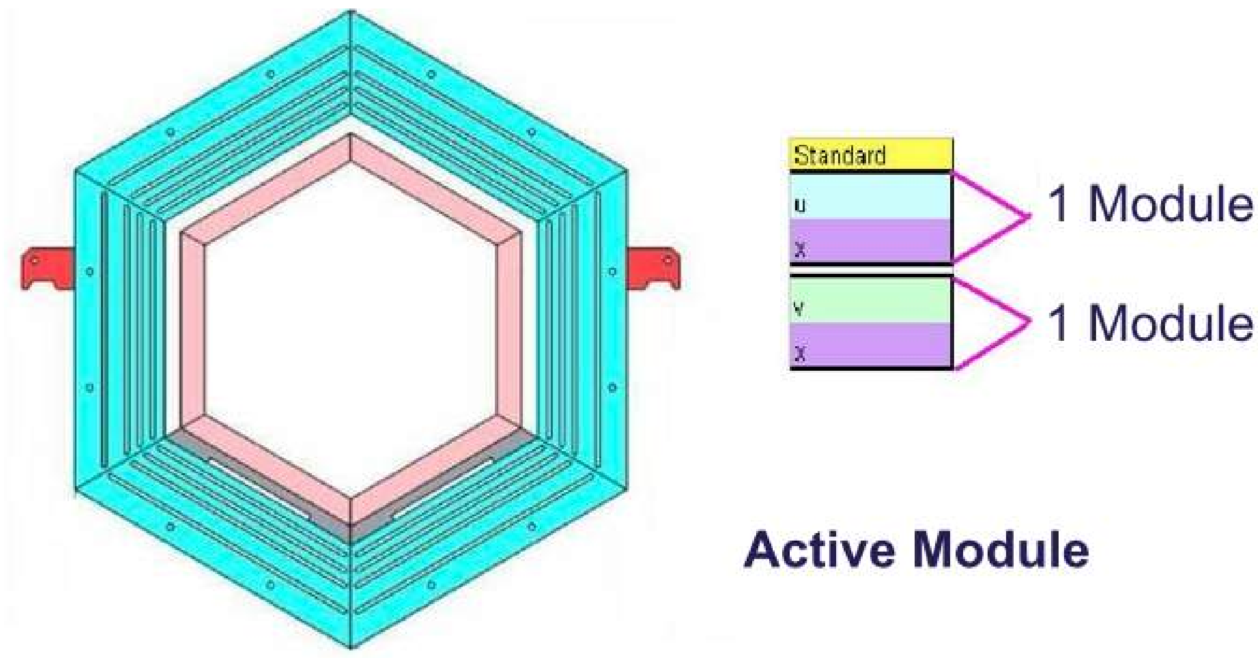

Figure 3.8: Detector active module. Structure of a module is depicted on the right.

nuclear targets.

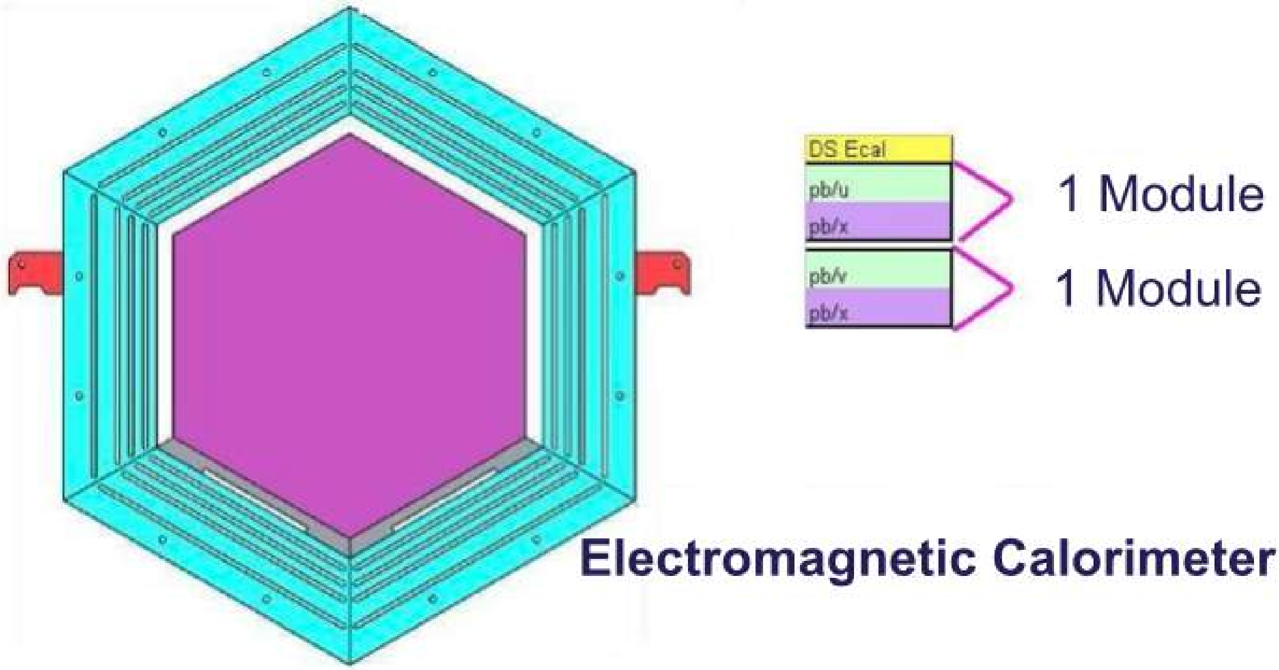

Figure 3.9: Module of the electromagnetic calorimeter. Structure of modules is depicted on the right.

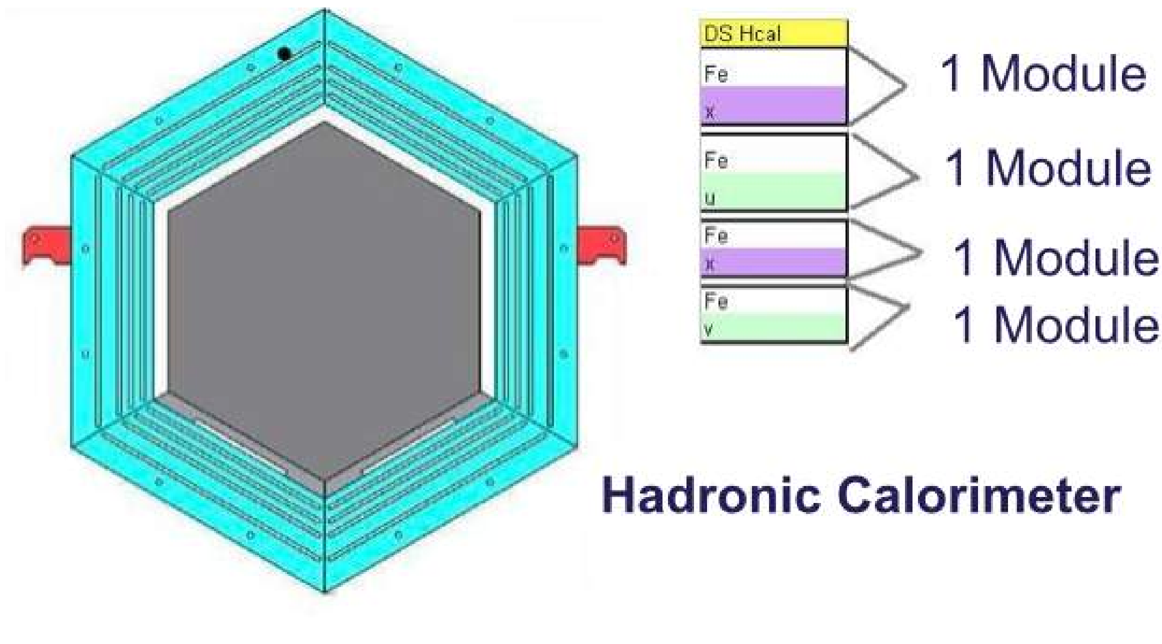

Figure 3.10: Module of the hadronic calorimeter. Structure of the modules with alternating Fe and scintillating planes is depicted on the right.

Subdetector	Module Type	Module Numbers	Num. Scint. Planes
Nuclear Targets	22 Tracking, 5 pasive	$[-5, 22]$	44
Tracking region	62 Tracking modules	$[23, 84]$	114
ECAL	10 ECAL	$[85, 94]$	20
ECAL	20 HCAL	$[95, 114]$	20

Table 3.2: Inner detector modular composition.

3.4 The Veto wall

A veto wall consisting of iron slabs and scintillator paddles is used to identify particles entering the MINERνA detector. The paddles tag muons produced upstream of the central MINERνA detector and helium target. The steel slabs can stop low energy hadrons or induce them to shower so that they might be detected by the paddles. A liquid helium target encased in a cryogenic vessel is located between the veto wall and the MINERνA detector. In the future, this helium target will be used for studies of nuclear dependence.

3.5 The scintillating strips

The active part of the MINERνA detector is built with triangular prisms of solid scintillator (polystyrene, Dow 663) doped with POP (1% per weight) and POPOP (0.03% per weight) coated by a reflective layer of TiO_2 and traversed by a 1.2 mm WLS optical fiber (Kuraray Y11 doped at 175 ppm) as shown in figure 3.11. The WLS fibers go to optical connectors in both ends of the modules from where clear fibers guide the light to multianode photomultipliers.

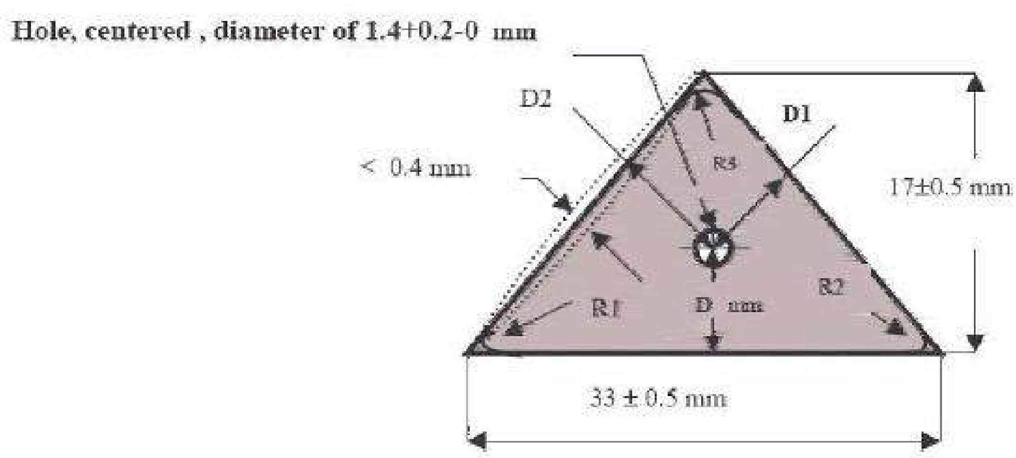

Figure 3.11: Transversal cut of the triangular scintillating prism used in the Inner Detector.

To improve coordinate resolution these triangular elements are assembled in planes (figure 3.12). Interpolation of the charge split between neighbor scintillating strips allows the determination of the coordinate. If stacked horizontally, so that the length runs parallel to the Y axis, each strip corresponds to a different X coordinate. This orientation, is the called $Xview$. The U and V views result from rotations in the XY plane by $+60°$ and $-60°$ respectively. These three views provide a stereoscopic 3D image of interactions in the MINERνA detector and gives redundant measurements of the two orthogonal candidates X and Y that can be used to resolve ambiguity in the formation of 3D tracks. A 0.2 cm thick hexagonal lead collar covers the outermost 15 cm of each plane of the detector upstream face. This $SideECAL$ estimulates electromagnetic showers and thus reduces the amount of energy leaving the Inner Detector(ID) .

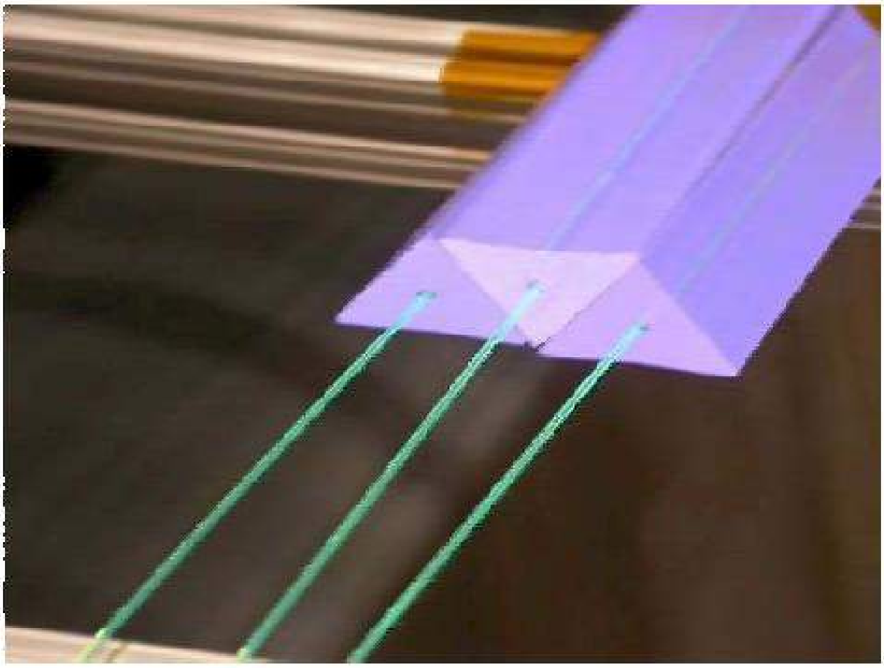

Figure 3.12: Scintillating prisms arranged to form a plane. Each prism holds an optical fiber along its full length.

3.6 Photodevices

The light collected in the scintillators must be converted into electric pulses whose characteristics represent the deposited energy. The light signal is strong enough for photodevices with 15% quantum efficiency. MINERνA uses 507 Hamamatsu Photonics H8804MOD-2 multianode PMTs to amplify the scintillation light[4]. Each multi-anode PMT is a collection of 64 individual PMTs distributed in an 8x8 grid[5] measuring 4 cm^2. The pixels consist of a bialkali photocathode with a borosilicate glass window and a twelve stage dynode amplification chain. The photocathode quantum efficiency is required to be at least 12 %, at 520 nm and the maximum to minimum pixel gain ratio can be no more than three. The gain of the dynode chain, defined as the number of electrons collected at the anode divided by the number of photoelectrons arriving at the first dynode, is $\sim 5{\times}10^5$. The scintillation light from a minimum ionizing particle typically produces a few photoelectrons at the photocathode resulting in a few-hundred fC electrical signal at the anode. The PMT and base circuit board are installed inside a 2.36 mm thick steel cylindrical box that provides protection from ambient light, dust, and residual magnetic fields. The PMT boxes are mounted onto racks directly above the detector. A total of 64 clear optical fiber are connected to the faceplate of each PMT box. In the interior of the box, the light is delivered from the faceplate connector to each pixel by clear optical fibers. An 8x8 cookie, mounted onto the face of the PMT, ensures the alignment of each fiber with its corresponding pixel. The fibers are mapped such that the light from adjacent scintillator strips is not fed to adjacent pixels in the PMT, what minimizes the effect of PMT cross talk, the process by which signal in one pixel can induce a signal in neighboring pixels, on event reconstruction. Figure 3.13 diagrams the fiber mapping.

The MINOS detector magnetic coil creates magnetic fields in the vicinity of MINERνA that can be around 30 gauss. The performance of the PMTs is adversely affected by magnetic fields higher than 5 gauss, so shielding is necessary. The PMT box itself provides some magnetic shielding. Additionally, the PMTs are oriented perpendicular to the residual field and the 40 PMT boxes closest to the MINOS detector are fitted with a high permeability metal shielding.

3.7 Calorimeters

MINERνA measures the energy of charged particles $(p, \pi^{\pm}, K^{\pm}, \mu^{\pm})$ and neutral particles (π^0, K^0, γ) with energies in the order of few GeV by means of two systems of calorimeters: a set of alternated lead and scintillator planes downstream of the active target for electromagnetic calorimetry and a set of alternated steel and scintillator planes downstream of the active target for hadronic calorimetry; a set of lead, steel, carbon and scintillator blocs assembled around the active target for both electromagnetic and hadronic calorimetry.

[4] essentially the same PMTs used by MINOS [84] and [85]

[5] Henceforth, the multi-anode PMT will be referred to as PMT and the component channels will be called pixels.

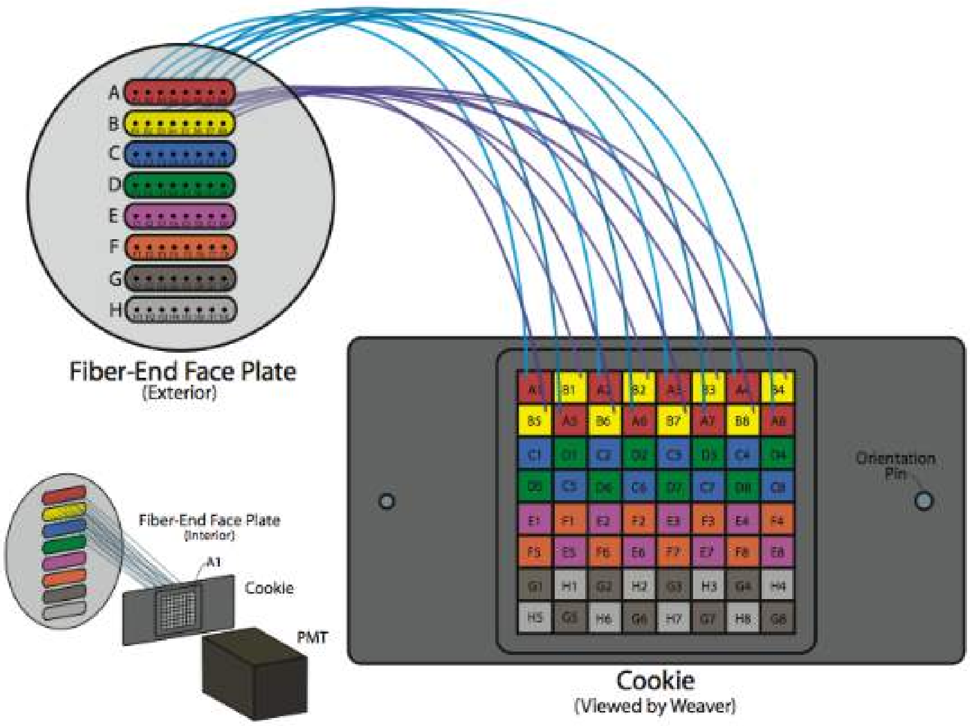

Figure 3.13: Fiber mapping of MINERνA PMT.

3.7.1 Electromagnetic calorimeter

High energy photons are detected by means of the production of pairs of charged particles (*bremsstrahlung*) that give rise to a shower of e^+, e^- and γ. Since pair production cross section is proportional to Z^2, lead sheets are commonly used to produce showers of reasonable size. The typical length of the shower varies with the energy; however, for photons of a few GeV, as the ones we expect in our experiment, 99% of the energy will stay in 4 cm of Pb (7 radiation lengths).

The electromagnetic calorimeter downstream of the active target is made of 20 layers of Pb (2 mm thick each) alternated with scintillating planes formed by the triangular scintillating prism of scintillator described in 3.5. The expected energy resolution is $6\%/\sqrt{E}$ where E is given in GeV. The side electromagnetic calorimeter is also made of 2 mm thick layers of Pb alternated with layers of scintillator. Photons penetrating the side electromagnetic calorimeter in an angle up to 25^o relative to the beamline are absorbed. Photons penetrating at higher angles will not be totally absorbed by the electromagnetic side calorimeter and will penetrate the side hadronic calorimeter where the remaining shower will be totally contained.

Since the main objective of the downstream layers of Pb, Fe and C (that are thicker) is to work as a target, the calorimetry is not as efficient in this region as it is in the upstreem modules. The way the targets are positioned presents an interaction length between 5 and 10 to the shower. Since the photons in this direction are of lower energy the showers that initiate in the central region will be totally contained in the detector.

The granularity of scintillator in the ECAL is just as fine as in the dedicated tracking region, which is easily sufficient to track charged particles.

3.7.2 Hadronic calorimeter

The downstream hadronic calorimeter is placed just after the electromagnetic calorimeter and is made of 20 layers of Fe (2.54 mm thick each) alternated with scintillating planes. The combined action of 4 cm of Pb and 50 cm of Fe stops muons with energy up to 600 MeV and protons with energy up to 800 MeV or even higher[6]. The side hadronic calorimeter has layers of Fe and scintillator (totaling 43.4 cm of Fe and 12.5 cm of scintillator) that is enough to stop 750 MeV protons penetrating at 90^o and 1 GeV protons penetrating at 30^o. The expected energy resolution of the hadronic calorimeter is around $50\%\sqrt{E}$ for hadrons with energy above 1 GeV. For less energetic particles the resolution is expected to be 50% or less, depending of the energy.

3.8 Nuclear targets

MINERνA has nuclear targets of Fe, C, Pb, He (table 3.3). Iron is a cheap and common absorber used in neutrino experiments. Ideally the nuclear targets should consist of many thin targets interleaved with tracking layers so as to allow the determination of the multiplicity of final states and the energy of each low energy particle. However, several factors limit the size and number of targets and tracking layers. The intrinsic detector spatial resolution is of the order of 1 cm in the z direction (the beam direction) making thiner targets ineffective. Sheets thicker than 2.5 cm (like MINO's) would not significantly improve our knowledge of low energy particles spectrum that is one of MINERνAs objective and, to improve statistics, we would have to use about 1 ton of each target.

The nuclear target region contains 22 tracking modules and 5 solid passive targets. There are four tracking modules between targets, which is adequate for reconstructing tracks and showers. A schematic of the nuclear targets region is shown in figure 3.14. Passive targets are numbered

[6] Since the interaction length for Fe is 16 cm protons and pions of higher energy are likely to be stopped

Target material	Mass (ton)	Charged current sample (K)
Helium	0.25	14
Carbon	0.12	9.0
Iron	0.99	54
Lead	1.02	57
water	0.39	20

Table 3.3: Charged current events expected at each nuclear target.

upstream to downstream 1-5. The targets are built out of transverse segments of carbon, iron and lead. The mass of each nucleus is spread around the detector in both the longitudinal and transverse direction to reduce systematic errors from both the event rate and the development of showers originating in upstream targets. Thicker targets are the most upstream, so that they interfere with fewer final state products from interactions in other targets. Targets 1,2 and 5 contain iron and lead, which are divided diagonally on a 20.5 cm offset from the center of the hexagon. Target 3 is made of carbon, iron and lead which occupy $\frac{1}{2}$,$\frac{1}{3}$ and $\frac{1}{6}$ of the are of the target respectively. Target 4 contains only lead. Some features from the targets are:

- Target 1: The most upstream target. Difficult to analyze due to the small number of tracking planes which can be used to identify particles produced outside of MINERνA.
- Target 2: Orientation of iron and lead is flipped horizontally from that of Target 1.
- Target 3: The carbon slice is three times as thick as the iron and lead, which are the same thickness as the iron and lead in Targets 1 and 2. All materials are flushed at the upstream end, so that there is an air gap downstream of the iron and lead.
- Target 4: Much thinner than the other targets. It is intended to induce electromagnetic interactions of particles from the upstream targets before they enter the low Z tracking region.
- Target 5: Has the same shape as Target 1 but is half the thickness. As the large, fully active tracking region is inmediately downstream of this target, the tracking is a bit more precise than in the other targets.

3.9 The Outer Detector OD

The Outer detector (OD) is a steel hexagonal shell with inner apothem 1.168 m and outer apothem 1.727 m. All steel frames are 3.49 cm thick except for frames surrounding the thicker

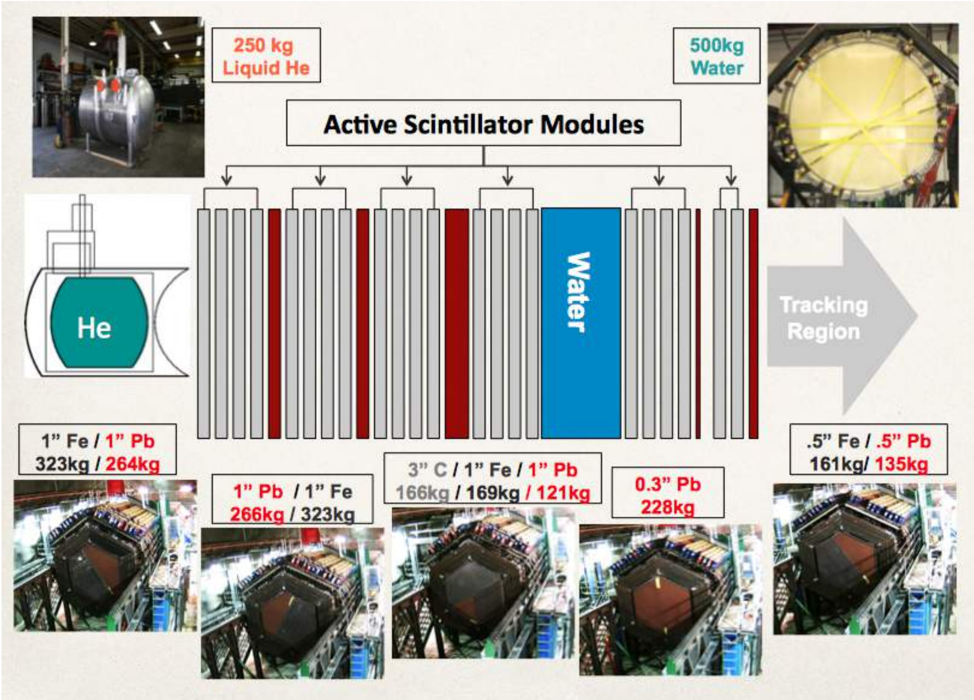

Figure 3.14: MINERνA Nuclear targets.

downstream HCAL where they are 3.81 cm thick. Each frame has four slots which hold a pair of 2.54 $\times$ 2.54 cm^2 rectangular scintillator strips for calorimetry and tracking.

3.10 Electronic and data acquisition (DAQ)

Table 3.4 summarizes the requirements of the electronics of the MINERνA detector. That are motivated by the following objectives:

- Fine spacial resolution taking advantage of the light sharing between adjacent scintillating bars;
- $\pi^{\pm}$ and p identification by dE/dx;
- Efficient patern recognition using timming to identify the direction of the trajectory and to identify interactions that occur during the same spill;
- Ability to identify strange particles and muon decays through coincidence techniques;
- Neglegible dead time in each spill.

MINERνA DAQ requirements are modest due to the relatively low event rate (about 100 kBytes/s).

Parameter	value
spill	12 μs
Repetition time	>1.9 s
Number of channels	30,972
Occupation per spill	2%
gain variation of the photodevice	4.5 dB
Time resolution	3 ns

Table 3.4: Some parameters and requirements for the electronics at MINERνA .

3.10.1 DAQ hardware

MINERνA active elements have their signals sent to multianode photomultipliers (MAPMT). Information about amplitude and time is digitalized by the electronics and stored for readout by the data acquisition system (DAQ). Each readout electronic front-end board (FEB) is connected to one single fotomultiplier.

Groups of up to 10 FEB are read and the result sent to a crate read-out controller (CROC) housed in a VME crate. Each CROC can accommodate 4 chains of FEB readout. A total of 12 CROCs is needed for the whole MINERνA detector. The VME crates also house a CROC interface module (CRIM), a MINERνA timing module (MTM) and a 48 V power supply. There are no CPUs in the VME crates. The DAQ works during the whole spill. After a period of 12 μs the DAQ reads all channels that have a signal above a predefined threshold. Even with a high occupancy rate the total number of bytes that are read in each spill is below 200 kB with zero suppression (1 MB without zero suppression). Dead time is negligible.

The photomultipliers are powered by 48 V power supplies. MINERνA uses the same hardware for data acquisition and for the detector control system (DCS). A single connection is used for the FEB readout and as communication channel for the control of the detector (as, for instance, the control of the MAPMT voltages). The main computers for the DAQ and for the slow control system (the system that controls and monitors the slow varying variables) are close to the VME electronics and are connected to FERMILAB network by two high speed TCP/IP lines. A two CPU server controls the whole system: one CPU dedicated to data acquisition and the other dedicated to control and monitoring. All DAQ machines run on Scientific Limux.

3.10.2 DAQ software

MINERνA software runs in the GAUDI framework originally developed for the LHCb collaboration. The expected average of data without data suppression is only 100 kB/s and a two second window is available for each 10 μ spill. The highly predicable beam time makes a complex trigger system unnecessary and we simply have a gate signal that opens immediately before the arrival of the beam and all charge an time information from the whole detector is registered just after the end of the spill. The slow control system is also simple with each MAPMT having its own local power supply and with the FEB being in charge of reading the high voltages, temperatures and other parameters used for monitoring and control. A schematic diagram of the DAQ is shown in figure 3.15.

3.10.3 MINOS Near Detector

The Main Injector Neutrino Oscillation Search (MINOS) is a two detector neutrino oscillation experiment situated on-axis in Fermilab's Main Injector [86]. The near detector is at Fermilab, and the far detector is 735 km away in Soudan, Minnesota. Both MINOS detectors are made of interleaved steel and plastic scintillator modules, similar to the MINERνA HCAL. The MINOS detectors are magnetized, which makes them capable of reconstructing the charge and momentum of the (anti)muons produced by charged current (anti)neutrino interactions. The near detector, shown in figure 3.16, is 2 m downstream of MINERνA and composed of 282 planes. MINERνA's optical system was based on MINOS, so there are many similarities: the scintillator composition is identical to that used by MINERνA; the strips are oriented ± 45 degrees with respect to the positive y-axis, with the orientation alternating in successive planes[7]. The MINOS detector is magnetized by a magnetic coil that runs the entire length of the detector (along the beam direction) inside a hole through the detector interior. The magnetic field inside the detector is toroidal with an average strength of 1.3 T. Muon momentum and charge can be measured from the curvature of the muon track through MINOS. Additionally, the momentum can be measured from the track range if the track is contained in the detector. The major difference is that MINOS scintillator strips are rectangular with a cross sectional area of $1.0 \times 4.1\ cm^2$. The steel modules are 2.65 cm thick. The near detector is divided longitudinally into two regions: the upstream calorimeter and downstream spectrometer. In the calorimeter, there is one scintillator plane between each pair of steel planes, whose granularity is adequated for reconstructing the energy of a hadronic system. The spectrometer is meant to reconstruct muons and has one scintillator plane after every fourth steel plane.

[7] The two orientations, referred to as the MINOS U and V views, differ from the U and V views used by MINERνA

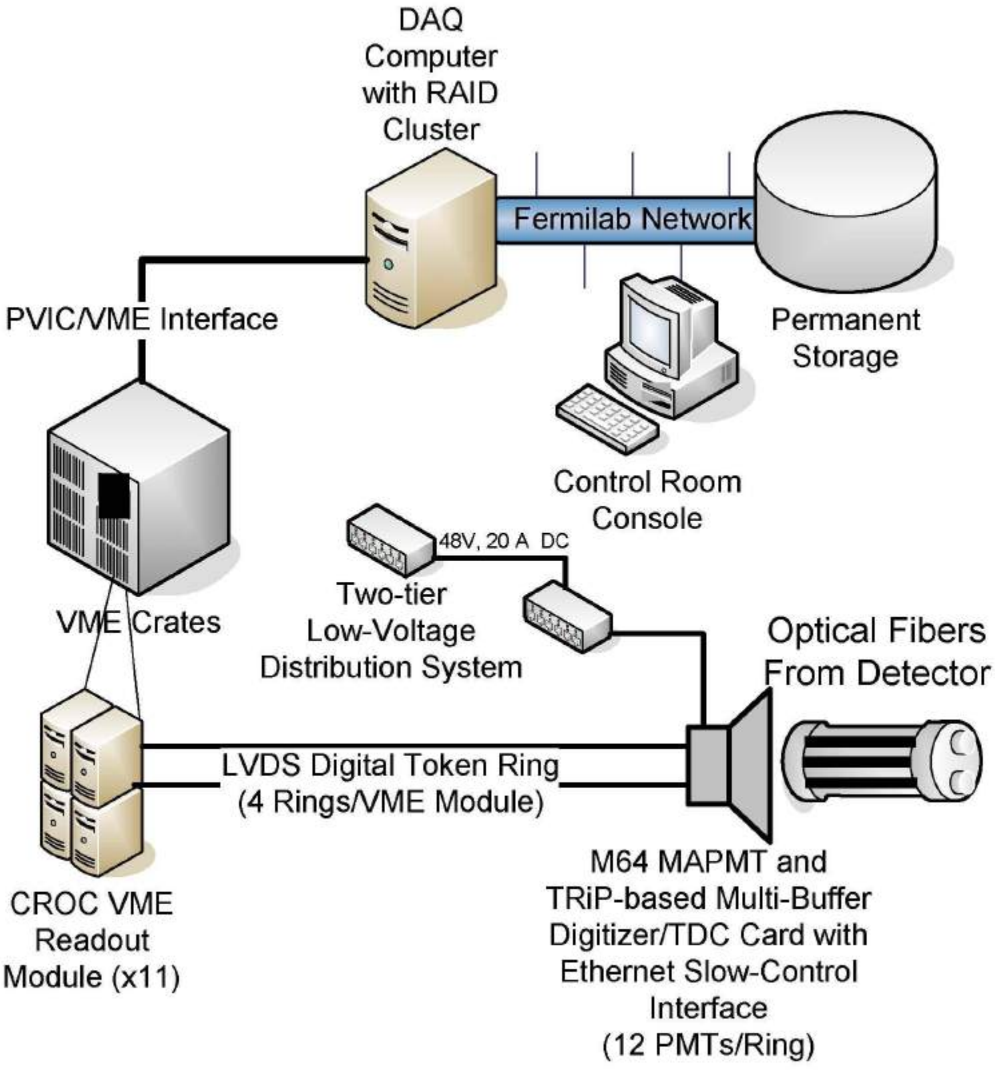

Figure 3.15: Schematic diagram of MINERνA data acquisition system.

3.10.4 Data Run Periods

MINERνA has been collecting data since October of 2009. The Low Energy Run refers to data taken between October of 2009 and April 2012, shown in figure 3.17. This run ended when the accelerator complex was shut down for upgrades. The primary goal of the upgrades was to increase the energy, intensity, and repetition rate of the NuMI beam for NOvA oscillation experiment [79]. This is also quite beneficial for many analyses that can be performed in MINERνA. The upgrade was completed in September 2013, when the Medium Energy Run

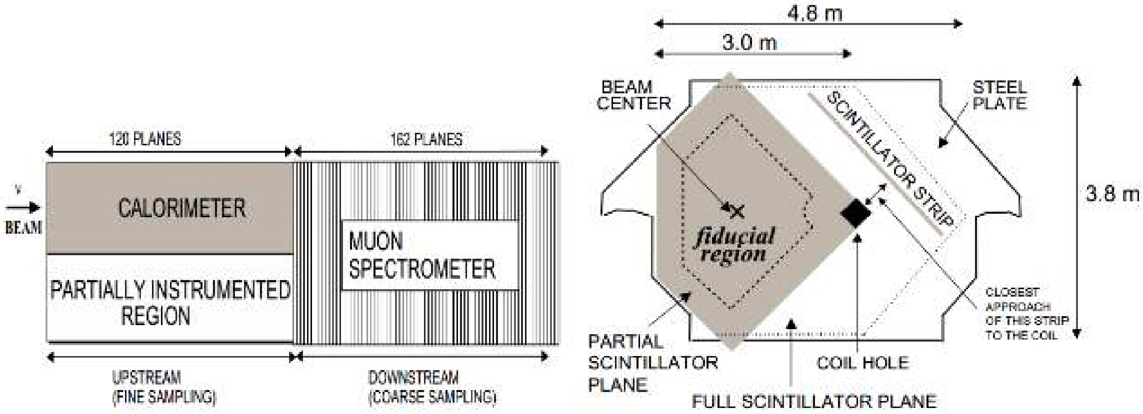

Figure 3.16: The MINOS near detector (left) as viewed from above and (right) as seen by the beam.[87].

begun and should last at least another five years. For its first four months of data taking, a partially-constructed (∼50 percent) MINERνA recorded ν_μ mode data from NuMI. Neither this data nor the detector configuration are relevant to the analysis presented here. MINERνA

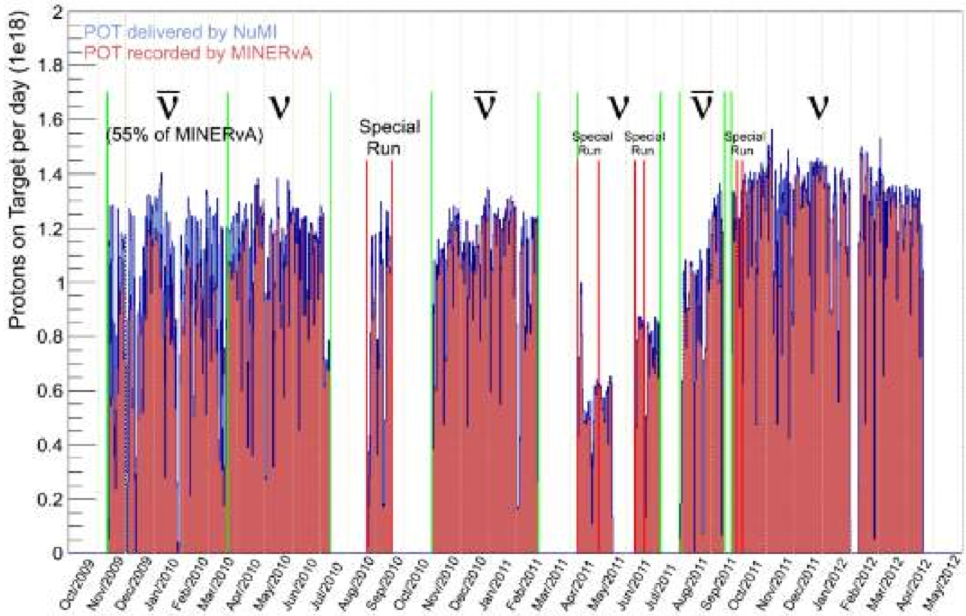

Figure 3.17: NuMI beam data recorded by MINERνA. The first months were taken with half of the detector installed. Vertical bars indicate changes in the beam. Special runs are related to different NuMI horn currents and target configurations.

completed detector instalation by the end of March 2010, with the exception of the water target, helium target, and veto wall. The detector recorded NuMI beam data in different beam configurations until the end of the Low Energy Run. Only the ν_μ mode data is relevant to the analysis to be presente in this thesis. In addition, about one week of data was collected in each May and June of 2011. Table 3.5 shows a summary of exposure to the NuMI beam in ν_μ mode.

Start	End	$POT(x10^{20})$	Information
March 22 2010	July 12 2010	0.941	2 most upstream modules not instrumented
May 7 2011	May 13 2011	0.025	
June 22 2011	July 1 2011	0.064	
October 18 2011	April 30 2012	1.914	Veto installed. He and water targets present.

Table 3.5: Data run periods from the ν_μ focusing NuMI beam mode.

Chapter 4

Reconstruction and Simulation

4.1 Introduction

This section describes the reconstruction of charged current inclusive (CCINC) interactions on plastic scintillator in the MINERνA detector. A particle detector measures the position, time, and energy of ionization caused by the passage of charged particles through its mass. These three quantities are not directly measured, but must be inferred from analog-to-digital conversion (ADC) and time-to-digital conversion (TDC) signals, and from knowledge of the detectors optical and electronic components. Our detector must therefore be calibrated to account for any deviations or processes which are not well modeled. The algortihms of reconstruction interpret calibrated measurements of energy deposits in the detector as particles. In neutrino scattering experiments, all of the detector activity is due to the products of the interactions with the different components of the detector; neutrinos do not participate in electromagnetic processes like ionization. The process by which a neutrino interacted in the detector and the kinematics of that interaction are inferred based on the reconstruction of its final state products. We will describe the calibration and reconstruction of raw hit information following references [88] and [89].

4.2 Hit Calibration

Figure 4.1 shows the steps in the collection of light and conversion to ADC that requires calibration. Some calibrations were measured ex situ on components prior to installation on the detector or with a separate bench test. Others are measured in situ using the full detector. The following is a summary of the effects that cause a priori measurements of detector activity to differ from the actual activity and thus must be calibrated.

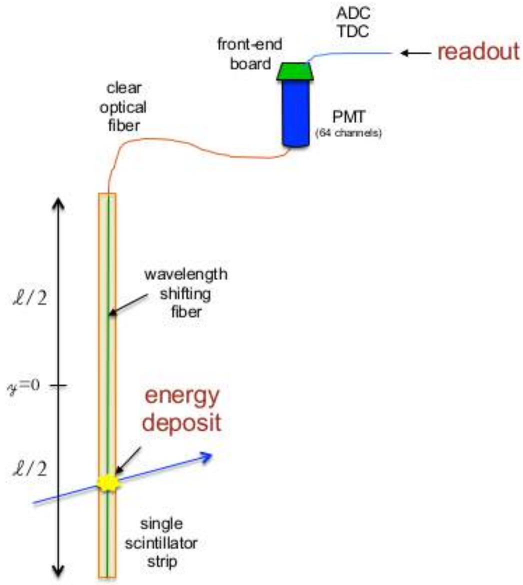

Figure 4.1: Effects to be taking into account in hit calibration [88].

4.2.1 Position

A big difference appears between the true and observed position when a channel is not connected to the strip predicted by the plex, which is the mapping of electronics to detector channels. There are deviations from the nominal position of modules due to imperfections in construction, and the stress and shear from adjacent modules.

4.2.2 Time

Calibrations must account for the time it takes the light to travel though the optical fibers to reach the photomultipliers (PMT). This calibration is different for each of the ∼32000 channels because of variations in fiber lengths and imperfections of fibers. The time it takes to the Front End Board(FEBs) to respond varies due to their different distances from the VME crate and also inherent variations in their manufacturing.

4.2.3 Energy

Many corrections must be made to interpret ADC counts as energy depositions in the Minerνa detector. The conversion of measured ADC_i to energy deposition E_i in channel i can be parameterized as:

$$E_i = ADC_i \times [G_i(t)Q_i(ADC)e^{l_i/\lambda_{clear}}\eta_i^{att}(d)C(t)S_i(t)] \tag{4.1}$$

where:

- $G_i(t)$ is the amplification of signal in the PMT dynode chain.
- $Q_i(ADC)$ is the conversion of charge to ADC, or gain of the TriP-t chip.
- $e^{l_i/\lambda_{clear}}$ is the attenuation of light in the clear optical fiber with attenuation lenght $\lambda_{clear} = 7.83$ m.
- η_i^{att} is the attenuation of light in the WLS fiber which is a function of the position of the fiber.
- $C_i(t)$ is the time dependent absolute energy scale.
- $S_i(t)$ is the time dependent relative energy scale of the channel with respect to the others. This accounts for variation in extrusion of scintillator, bubles in optical fibers, connection of the fibers to the PMT, enviromental conditions across the detector (temperature, humidity, dripping water), and any other variation.

4.3 Ex situ calibrations

Part of the calibrations was made on different components before the installation on the detector using a separate test bench.

4.3.1 Front End Boards

The conversion of charge to ADC count was measured on each FEB for all three gain settings (low, medium, high) before their installation. A known charge from a capacitor was injected into the FEB, and the resulting ADC count response was fit to a tri-linear function to calibrate each channel.

4.3.2 Photomultiplier Tubes

PMTs were tested on a test stand at Rutgers University before being enclosed in steel boxes. The test stand illuminated one pixel at a time using light from a blue LED that was directed through a green WLS fiber. 64 groups of six clear optical fiber were used so that six PMTs could be tested at once. Figure 4.2 shows the setup that was used.

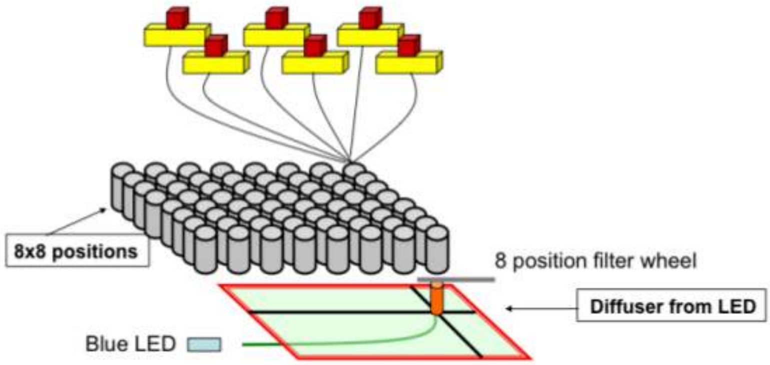

Figure 4.2: Rutgers PMT test stand.

4.3.3 Mapper Modules

The optical attenuation in the WLS fibers in each scintillator plane was mapped using γ radiation from a ^{137}Cs source. The source was directed up and down each strip in the plane longitudinally while strip response was measured. The resulting calibration is an attenuation scale factor for each channel that is a function of the energy depositions in the longitudinal position in the strip.

4.4 In situ calibrations

In situ calibrations are necessary to characterize time-dependent effects and account for variations or changes due to detector construction. Measurements for these calibrations use either rock muons or special triggers, which are explained below. Rock muons are the final state products of neutrino interactions in the rock of the detector hall that enter MINERνA. They are plentiful; often, several are recorded in a beam spill. Muons are minimum ionizing particles, thus their energy deposition pattern in the detector is consistent and well understood. The MINERνA DAQ can send triggers to readout the detector between NuMI spills, provided there is enough time to be ready to trigger for the next spill. There are two special types of trigger important for calibration: pedestal and light injection.

4.4.1 Pedestals

A pedestal signal in a digital channel corresponds to the zero of the input signal. Reading a FEB will result in a nonzero ADC count even when no charge has been recorded. This ADC count is called the pedestal.

The pedestal is measured simply by reading out the detector when there is expected to

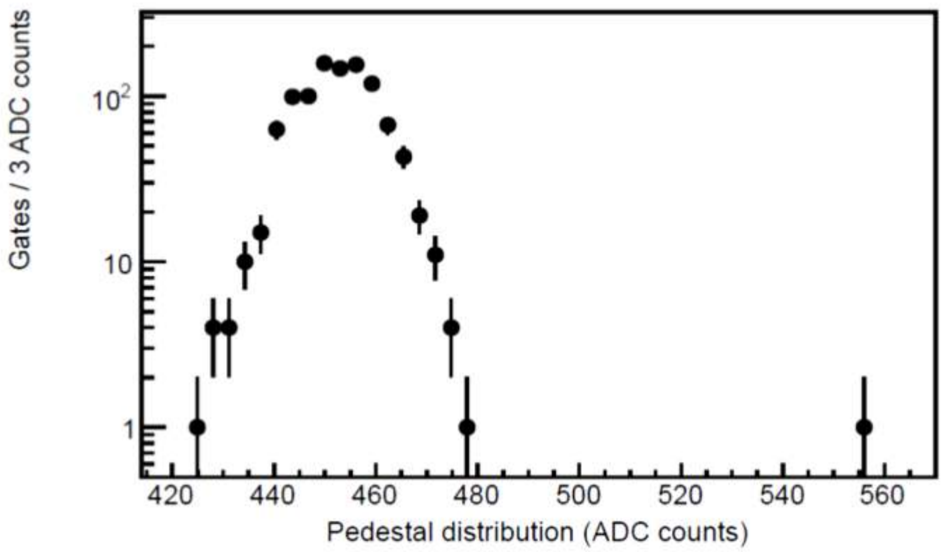

Figure 4.3: Example of a high gain pedestal distribution for a single channel. The outlier can be originated from a cosmic ray event.

be no light. This is accomplished by taking pedestal triggers between NuMI triggers, when there is no beam. The mean of the ADC distribution is taken as the value of the pedestal and subtracted during calibration. Pedestal data is taken by switching to a mixed NuMI-pedestal trigger mode roughly twice a day for one half hour each. The pedestal data is taken once every 32 subruns, where a subrun consists of approximately 750 NuMI gates. Figure 4.3 shows an example of a high gain pedestal distribution for a single channel.

4.4.2 PMT Gains

The gain of each PMT channel changes with time. Each PMT box has two ports into which optical fibers from a light injection system are connected[1] Assuming a probabilistic model for amplification in the dynode chain, the gain can be calculated from the difference between the RMS of the pedestal ADC and the one-photoelectron ADC. Light injection data is taken between NuMI spills, in a mixed trigger mode.

4.4.3 Channel to Channel Calibrations

A channel-to-channel calibration is performed to normalize channels relative to each other.

The calibration is performed on a sample of tracked rock muons that enter the front and exit the back of MINERνA; such muons are called through-going muons. The energy per length

[1] a diffuser in each port spread the light across the whole face of the PMT.

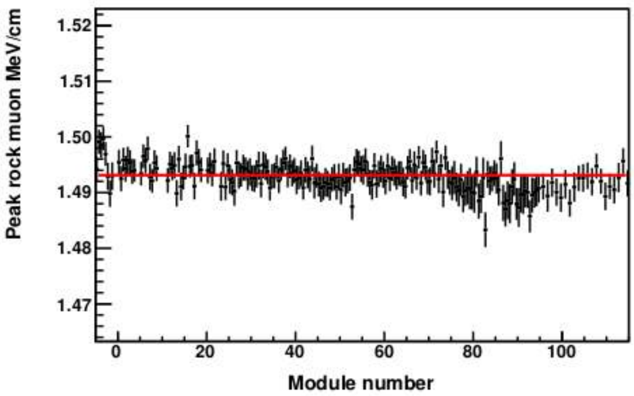

Figure 4.4: Peak muon energy per length for all planes. Consistency in energy response is related to the channel-to-channel calibration.

E/L of scintillator traversed is measured and variations in the peak of the E/L distribution are calibrated out. Consistency in the energy response of modules after channel-to-channel calibration is shown in figure 4.4 .

4.4.4 Absolute Energy Scale

The absolute energy scale of the detector is set by comparing the peak energy deposited by a muon in a scintillator strip, called the muon energy unit (MEU), in data to simulation. The use of simulation is safe because the mechanism of muon energy loss through ionization is very well understood. Through-going rock muons with a reconstructed momentum are used for the calibration. The MEU is extracted from a fit to the distribution of energy deposited by the

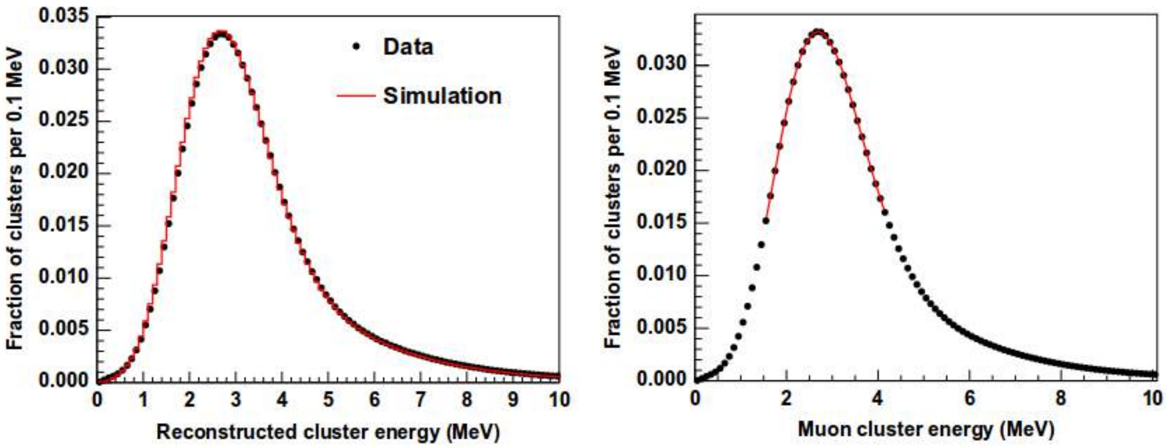

Figure 4.5: (Left) The energy distribution of clusters along a muon track in data and the simulation. (Right) Fit to the peak of the energy distribution gives the value for MEU.

muons and the calibration is the ratio of data to simulation. Only one scale factor is necessary for the detector since the previous channel-to-channel calibration removes all variations. Figure 4.5 shows a comparison of data and simulated muon energy deposited per length and a fit to the distribution to tune the MEU.

4.4.5 Timing

Timing calibrations are accomplished using fitted through-going rock muon tracks. The calibration procedure is iterative; the best known timing calibrations are applied to find even better timing calibrations until convergence is achieved. The time of each hit is compared to the truncated mean time of hits on the track to form a residual, taking into account the travel time of the muon and previous timing calibrations. Time slewing is calibrated for each channel. The calibration moves the center of the peak of the hit time residual to 0. The slewing calibration been energy dependent is done in bins of deposited energy. A separate time calibration accounts for the time offset between FEBs. This calibration is done for each group of 32 channels connected by a TriP-t chip.

4.4.6 CrossTalk

Crosstalk is measured in situ using rock muon tracks. The ideal measurement of crosstalk is made by iluminating just one pixel at a time, as in section 4.3. Muons are an adequate light source because they usually deposit energy into only two strips per plane. Cross-talk is identified as signal measured in channels that were not traversed by the muon but sit on the same PMT as channels that were traversed by the muon. The frequency and energy distribution of crosstalk hits is compared to the simulation to calibrate the probabilistic algorithm that simulates crosstalk.

4.5 Reconstruction

Reconstruction of events in MINERνA begins by grouping hits in a gate into time slices, which usually are collections of all the activity produced by physical events in the detector. Subsequent reconstruction algorithms act on single time slices, and hits in different time slices do not interfere. Hits are then spatially grouped within planes into clusters. Groups of clusters that resemble the path of a charged particle are associated as a track. Tracks are fit to the expected path of a charged particle to better understand its trajectory. Tracks are identified as muons by looking for corresponding activity in MINOS. Clusters that are not associated with the muon are assumed to come from the recoil system, and their energies are summed to get the total recoil energy.

4.5.1 Clustering Hits by time

Multiple events can be observed during a single NuMI beam spill. Given that the MINERνA detector has a timing resolution of about 3.0 ns, events within a gate can be efficiently untangled based on their timing profile. The time slices are formed by probing the NuMI gate time distribution, which consists of hits originating from both the ID and OD detectors. Probing forward in time, the photoelectrons within a time window of 30 ns are integrated. A time

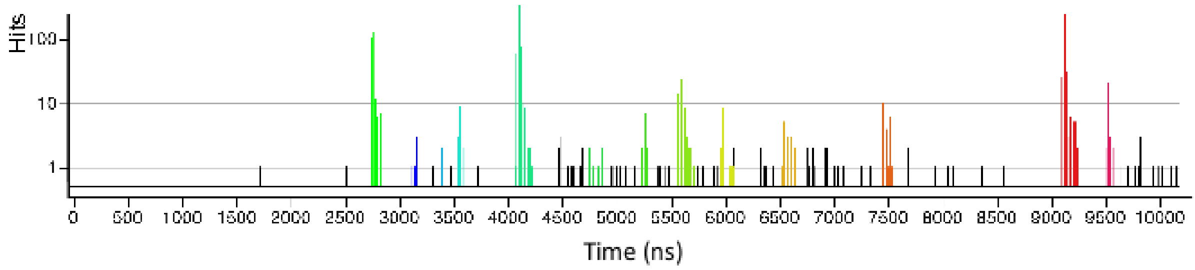

Figure 4.6: Time distribution of hits in a NuMI beam spill.

slice is created if the integrated charge exceeds the default minimum value and hits that occur close in time to the time slice are associated with that candidate. The adding of hits continues while the total integrated charge does not surpass the default minimum value. The width of the integration time for the time slices is given by the integration time of the FEBs, which is 150 ns. Figure 4.6 shows an example of hit time histogram for a gate. Colored peaks in the distribution are time slices. A typical beam spill from NuMI in ν_μ focusing mode contains 512 time slices.

4.5.2 Clustering Hits by position

The first step of spatial pattern recognition is merging hits within a plane into clusters. Hits that are contiguous are merged into a cluster (see figure 4.7), that is made out of the maximum number of contiguous hits. All hits are used to create clusters, which implies the existence of one-hit clusters. Clusters are 2-dimensional objects with either a X-Z, U-Z, or V-Z coordinate. For clusters in the ID, the Z position is given by the Z-center position of the plane in the detector and the transverse position (X, U, or V) is determined by the charge-weighted mean position of the hits. The energy of a cluster is the sum of energies of its constituent hits. Its time is taken from the time of the most energetic hit. Because of the alternating triangular design in

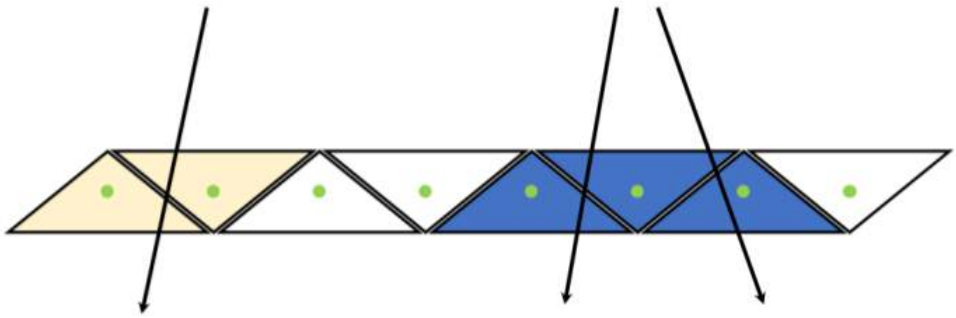

Figure 4.7: Example of cluster formation in the inner detector when particles pass trough the scintillator planes. Colors are associated with the energy deposition.

scintillator planes, it is extremely likely that a particle passing through a plane will intersect more than one strip. Since the energy loss profile of the particle depends on its mass and initial momentum, the energy density of the clusters can vary as the particle propagates through the detector. Thus, different particles with various momentum can generate various topologies of clusters. For example, muons tend to produce very narrow clusters, and showering hadrons produce very high energy broad clusters. Clusters are classified as low activity, trackable, heavy ionizing, cross-talk, or supercluster according to their energy, number of hits, and energy of hits. Hits are classified by their energy. The classification criteria for clusters is provided below.

- **Low Activity**: Clusters with energy less than 1 MeV.
- **Trackable**: clusters with energies between 112 MeV and containing fewer than 5 hits. The cluster must have at least one hit with energy in the range of 0.512 MeV, but no more than two. If there are two hits with 0.512 MeV, they must be adjacent.
- **Heavy Ionizing**: clusters have energies greater than 12 MeV and containing fewer than five hits. The cluster must have at least one hit with energy greater than 0.5 MeV, but no more than three. If there are two or three hits with energies greater than 0.5 MeV, they must be contiguous.
- **Crosstalk**: A cluster is identified with hits which are correlated with the PMT pixels associated with a particular cluster. If hits are located directly adjacent to pixels which corresponds to the energy deposition of a particle, then those hits are tagged as cross talk.
- **Superclusters**: do not fit the criteria of any of the above categories. Practically, this means clusters that are very wide or have hit patterns consistent with multiple particles are superclusters.

4.5.3 Event information based on a track

A track is a reconstructed object which traces the trajectory of a particle. For particles that are not subjected to a dramatic change in direction due to an interaction in the detector, a single track is capable of estimating their trajectories. But for the case when the particle undergoes a hard collision, multiple linked tracks are needed to approximate its trajectory. Compared to muons, hadrons that propagate through the MINERνA detector are far more likely to require multiple tracks. The main analysis that is described here looks for charged current inclusive events with a muon in the final state. MINERνA has developed an algorithm to build events which is focused primarily on finding the muon track. In order to efficiently track the hadrons, multiple track algorithms must be used: the LongTracker and the ShortTracker. Since the LongTracker is designed and optimized to efficiently reconstruct good muon tracks, it is the only tracker activated during the running of the common reconstruction algorithms. Note that good means that the muon trajectory has been successfully reconstructed.

Creating the events using the trajectory reconstruction

There are several steps which are needed to create high quality tracks. Figure 4.8 shows an illustration of the 3 steps that are described below.

- **The Anchor Track** :
  The anchor track is created at the reconstruction stage using the LongTracker pattern recognition scheme. The LongTracker creates tracks out of the trackable and heavy ionizing clusters within a time slice. The longest track, which is typically the muon, is selected and identified as the anchor track. The anchor track must spann at least 25 planes, otherwise the track is discarded. Since the anchor track is assumed to be traveling in the forward direction the event vertex is initialized at the most upstream cluster on the track.

- **Creating Anchored Tracks**:
  Both the long and short trackers are used to create anchored tracks from clusters that are unused by the anchor track. The type of clusters that are selected depends on the track pattern recognition routine. In addition, each pattern recognition scheme has a different set of consistency requirements for the anchored tracks. The basic idea behind the consistency checks is to ensure that the vertices from the anchor and anchored tracks are compatible. If the anchored track is incompatible with the anchor track, then the anchored track is deleted. The search for anchored tracks continues until no further tracks satisfying the consistency criteria can be created. For each iteration, the anchor and anchored tracks are fitted simultaneously to form a common vertex (see subsection

4.5.4), where the updated event vertex replaces the previous one. Figure 4.8 demonstrates how anchored tracks are created.

- **Creating Secondary Tracks** :
  If the particle undergoes a hard collision, the trajectory can change direction or a multiple of particles can be produced. Therefore, the search for anchored tracks continues by leveraging the end position of each anchored track that was defined above. If a secondary anchored track is created, then the anchored and secondary anchored track are fitted simultaneously to form a common vertex, known as the secondary vertex, as shown in figure 4.8.

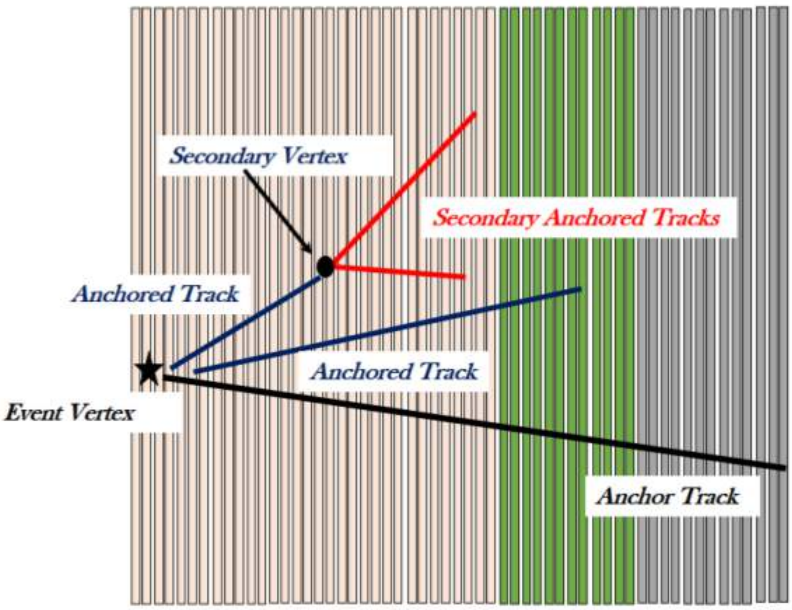

Figure 4.8: Ilustration of procedure for creating a track-based event for a high multiplicity neutrino interaction in the MINERA detector.

Long Tracker Scheme

The pattern recognition scheme for the LongTracker employs multiple stages: Adding clusters to a track, track formation and the track cleaning. Figure 4.9 shows a plot of the track position resolution for through-going rock muons, where the plot includes all of the clusters along the muon track.

- **Track Formation**:
  The first step in track formation is to form track seeds out of trackable and/or heavy

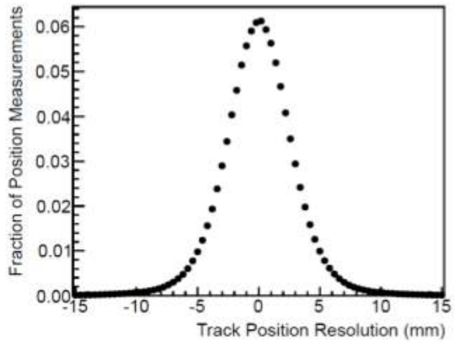

Figure 4.9: Difference between the fitted positions relative to the measured cluster positions for rock muon events.

ionizing clusters. Track seeds are grouped by views (X, U, or V module) and consist of three consecutive clusters in the same view. Each seed is fitted to a 2-dimensional line, where the χ^2 from the least squares fit determines the quality of the seed. Track seeds are combined to form track candidates, where the seeds in the same view are merged if the following conditions are satisfied:

a) Share at least one cluster

b) Can not share different clusters in the same plane

c) The slopes are consistent

The merging procedure starts from the downstream end of the detector and moves toward the upstream region. This serves as a way to avoid the influence of heavy vertex activity that may have developed from a high energy neutrino interaction. After all of the possible track candidates are created the compatible candidates may be joined even in the presence of a missing cluster in a scintillator plane between two candidates.

The final merging step is executed sequentially by two different techniques (2- dimensional and 3-dimensional algorithms) with the common goal of creating 3-dimensional objects called tracks. The 3-dimensional routine searches for all possible combinations of X, U, and V orientations and creates a track if the candidates overlap along the longitudinal axis and are compatible with the same line. After the 3-dimensional algorithm has tested all the permitted track combinations and exhausted its merging capabilities, the 2-dimensional routine is executed and examines track candidates in pairs in order to create tracks. This method is quite sufficient for forming tracks when the track in a particular view is obscured by detector activity or inefficiencies such as missing clusters. Due to the prerequisite of the track candidate combinations mentioned above, the minimum number of planes a track can span is eleven. As a result, the ShortTrackers are essential for reconstructing particles which span less than nine planes and scatter at high angles with respect to the longitudinal axis. Finally, all created tracks are fitted by a Kalman filter that accounts for multiple Coulomb scattering [90]. See reference [89] for detailed information on the application the Kalman filter in the MINERνA track and vertex reconstruction framework.

- **Adding clusters to the Tracks**:
  The fitted track is projected into both the upstream and downstream directions. If the track projection intersects an unused cluster, then the cluster is added to the track. For the case of a supercluster with an energy deposition greater than that of a minimum ionizing particle (MIP), the cluster (also referred to as the parent cluster) is broken apart, where a MIP fraction of energy is given to each one of its daughters. The daughter cluster with the MIP (2.25 MeV/cm) amount of energy is then placed onto the track, whereas the others are discarded and made available to other reconstruction algorithms. In addition, the track adding technique uses clusters associated to a plane to fill in gaps in the track.

- **Track Cleaning**:
  Both the hadron and muon track candidates go through a procedure commonly known as track cleaning that breaks clusters apart and removes additional energy from the track that does not originate from the particle that is being tracked. The removed energy is freed to be used by other tracking and/or reconstruction algorithms. If the dE/dx per plane is inconsistent with a muon energy loss profile, any extra energy is removed from the anchor track. Only the superclusters are cleaned for the anchored tracks that are assumed to correspond to hadrons. If a supercluster is close to the end of the anchored track, the cleaning procedure becomes extremely relaxed, meaning that more than a MIP worth of energy remains is the parent cluster.

The ShortTrackers

The ShortTrackers are essential for the reconstruction of tracks with large scattering angles with respect to the longitudinal axis of the detector and particles with trajectories that span less than nine planes.

4.5.4 Vertex Fitting

For track fitting MINERνA uses an implementation of the well-known Kalman filter method [90]: minimizes the sum of standardized distance between the position of the energy deposited in a layer of scintillator and the estimate of the track parameters. For each cluster the algorithm

produces a position, slope, and covariance matrix that includes noise from multiple scattering [91]. The vertex reconstruction links two or more tracks to a common interaction point, taking as the initial vertex position the point of closest approach (POCA) of the tracks.
For $n_{tracks} > 2$, the POCA computes the vertex position for pairwise combinations and assigns a weight to each POCA. The initial vertex for $n_{tracks} > 2$ is the weighted average of the POCA for all pairs. The initial vertex is refitted using an adaptive Kalman filter minimization technique [92]. The routine assigns weights to the tracks using an adaptive fitter scheme, where the tracks that are incompatible with the vertex are weighted down in a way that tracks with poor compatibilty do not influence the reconstruction of the vertex. For more details on the implementation of the fitting procedure in MINERνA see reference [89].

4.5.5 Muon Reconstruction

The proper identification and reconstruction of muons is crucial to the analysis presented in this dissertation. A track in MINERνA is identified as a muon if it matches a track in MINOS.

MINOS Match tracking

MINERνA tracks that have at least one cluster in any of the five most downstream modules (in the HCAL) are considered candidates for matching. MINOS track-match candidates must have hits in at least one of the four most upstream MINOS planes. The MINOS and MINERνA tracks must occur within 200 ns of each other. All pairs of candidates are tested for compatibility in two ways. The first, and preferable, compatibility test projects the tracks to each other end points. The position and slope of the MINERνA track at its most downstream point is projected downstream into MINOS and compared with the MINOS track-match candidates most upstream position. The MINOS track is propagated upstream to MINERνA for a cross-check. If the residual of both projections is less than 40 cm, the two tracks are matched. If more than one MINOS track passes the matching criteria, the one with the lowest projection residual is used. The second test uses the distance of closest approach, and is used only if no track-match is found using the endpoint projection criteria. The MINERνA and MINOS tracks are simultaneously projected towards each other. The projection compatibility test is then evaluated at the point of closest approach. This matching method exists for the cases in which the muon scatters off material between MINERνA and MINOS.

Momentum and charge reconstruction

Muons are deflected by the MINOS magnetic field and the sign of curvature of this deflection determines the charge. The polarity of the magnetic field can be reversed so that either helicity can be focused and run two configurations: usually μ^- for ν_μ studies and μ^+ for $\bar{\nu_\mu}$. MINOS uses two methods for momentum reconstruction: range and curvature. The energy of muons is reconstructed by range method using the Bethe-Bloch equation [44] to calculate the total energy loss during the passage of the muon through the MINERνA and MINOS detectors, but is only possible for lower energy, lower angle muons that stop in the detector. Muons are reconstructed by curvature using:

$$K = \frac{1}{R} = \frac{0.3B}{p_\mu} \tag{4.2}$$

The energy which the muon loses in its passage through MINERνA is then added.

4.5.6 Reconstruction of Recoil System

Clusters in the recoil system (not associated with a muon track) must pass the requirements:

- Not be identified as crosstalk
- Be within a time window in the range of $[-25, 30]$ ns of the event time.
- Not be associated with a muon track.

Three corrections need to be taking into account to calculate correctly the clusters energy:

- Correct visible energy by accounting for passive material traversed.
- Multiply the above result by a scale factor $s_i(Recoil)$ that is tuned by Montecarlo.
- Use a polyline correction to the above result that applies an energy-dependent scale factor, also tuned by Monte Carlo.

The reconstruction can be represented by:

$$E_{had} = \alpha \times poly(E_{had}) \times \sum_{i}^{hits} E_{vis} \times F_i^{pass} \tag{4.3}$$

where α is a constant scale factor that depends on the vertex position, $poly(E_{had})$ is the polyline correction, E_{vis} is the visible energy of the hit, f_i^{pass} corrects for expected loss of energy in passive material near the hit.

Passive Material Correction

The passive material traversed by the particle is estimated using the hit location. To calculate how much energy is lost in the passive material, we assume that the number of MEUs per

g/cm^2 deposited in scintillator is also deposited in the passive material. The number of MEUs deposited in scintillator is given by:

$$n_{meu} = \frac{E_{vis}}{dE/dx_{sc} M_{sc} f_{active}} \tag{4.4}$$

where E_{vis} is the visible energy of the hit, dE/dx_{sc} is the energy lost in scintillator by a minimum ionizing particle in $MeV/g/cm^2$ and M_{sc} is the mass of the scintillator that recorded the hit in g/cm^2. The total energy deposited is then:

$$E = n_{meu} \times \sum_{i}^{materials} (M_i \times dE/dx_i) \tag{4.5}$$

the sum being done with the materials near the hit. The dE/dx for the scintillator tracker region in MINERνA has the value of 1.936 $MeV/g/cm^2$. [93]

Multiplicative Scale Factor

The multiplicative scale factor α is applied to the reconstructed recoil energy to account for additional losses of visible energy like neutral particles and first state interactions. The scale factor is tuned using the Monte Carlo by minimizing the error between the true hadronic energy and reconstructed recoil energy, where the true hadronic energy is defined as

$$E_{had} = E_\nu - E_\mu \tag{4.6}$$

The previous definition of true recoil energy is chosen to optimize the neutrino energy reconstruction, which is reconstructed for inclusive events as :

$$E_\nu = E_{had} + E_\mu \tag{4.7}$$

Only events that pass all analysis cuts and have true E_{had} between 1 and 10 GeV are used for the tuning. A different α is found for the tracking region and for each passive target, because showers emanating from different locations in the detector encounter different material and thus develop differently. The calorimetric scale factor α for different vertex locations are:

- Tracker : 1.60
- Target 5 : 1.57
- Target 4 : 1.59
- Target 3 : 1.67
- Target 2 : 1.78

Polyline Correction

An additional multiplicative correction is derived from the residuals in bins of E_{true}. A polyline is formed with points $(X, Y) = (\bar{E}_{true}(1+\mu), \bar{E}_{true})$ where E_{true} is the average true E_{had} in that bin and μ is the mean of the gaussian fit for the residual

$$Residual = \frac{E_{reco} - E_{true}}{E_{true}} \tag{4.8}$$

in that bin. The polyline starts at (0,0) GeV and ends at (50, 50) GeV.
Bins with $E_{true} < 300$ MeV are not used. The multiplicative correction for an event with E_{had} is determined from the two polyline points p^1 and p^2 such that $p^1_x <= E_{had} < p^2_x$. The energy after the polyline correction is:

$$E'_{had} = p^1_Y + (E_{had} - p^1_X)\frac{p^2_Y - p^1_Y}{p^2_X - p^1_X} \tag{4.9}$$

4.6 The Simulation

MINERνA simulation follows 4 different steps: the NuMI beamline; the MINERνA detector; the MINOS Near detector and the neutrino interactions. First G4numi is used to predict the neutrino flux. The neutrino flux is then used by GENIE (Neutrino event generator version 2.6.2) to determine if and how these neutrino interact in the MINERνA detector. GEANT4 and additional MINERνA simulation codes simulate the detector response to the final states products of the neutrino interaction. In the last step any simulated particle exiting the back of MINERνA is propagated to MINOS where GEANT3 version 21.14a is used for the MINOS simulation.

4.6.1 NuMI Flux

G4numi package is used to simulate the NuMI beamline and the hadrons that are produced after the interacion of the protons of the beam with the graphite target. G4numi is a NuMI specific implementation of GEANT4 version 9.2.p03 that uses by default, the QGSP (Quark Gluon Strin precompond) for modeling the hadron production, reinteraction with the hadron production target, magnetic horns and propagation [94]. In March of 2013 MINERνA switched from using the QGSP to FTFP BERT (Fritiof with precompound Bertini Cascade) as the input hadronic physics model in G4numi. For energies greater than 5 GeV, FTFP BERT uses the FRITIOF string model to generate the primary hadronic collision, the Lund model for fragmentation into hadrons, and precompound splines to de-excite the remanent nucleus. The Bertini model for intranuclear cascade is used for lower energy hadrons. G4numi has a description of the NuMI beamline geometry and generates 120 GeV/c $p + C$ collisions one proton at a time with a beam spot size of 1.1 mm. The hadronic models used in the simulation were found to disagree significantly; so, external hadron production data is used to reweight these predictions. This reweighting is significant and is discussed in section 4.6.1. The products of primary $p + C$ collisions are allowed to propagate through the material of the NuMI beamline, where they may reinteract. The products of these interactions are focused according to a description of the magnetic horns and made to decayed by G4numi. Figure 4.10 shows that the neutrino energy

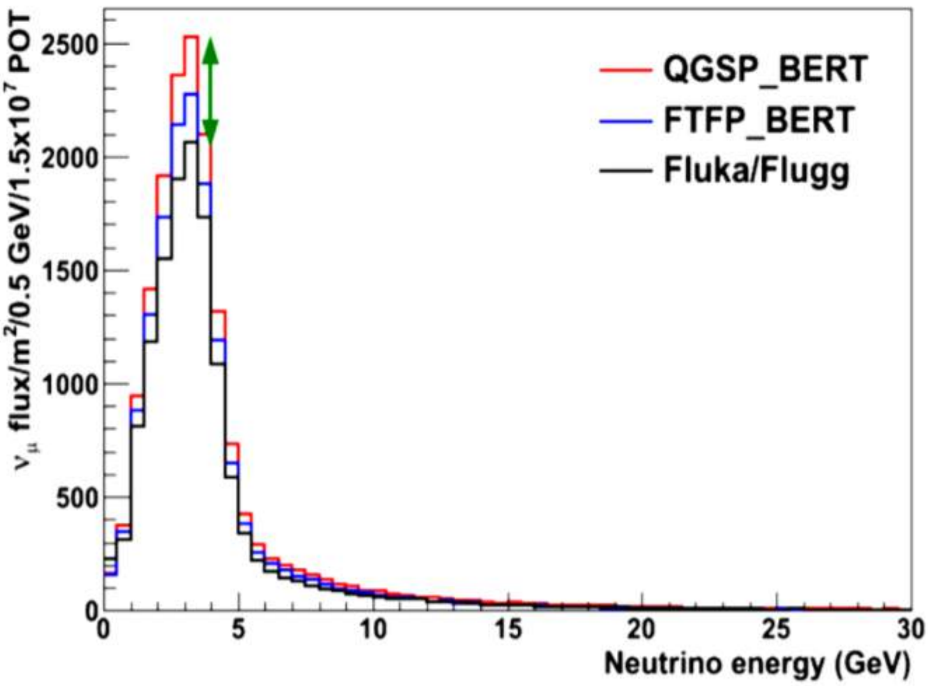

Figure 4.10: Neutrino energy distributions using the same montecarlo geometry with different input hadronic physics models. The green arrow shows the discrepancy between the peaks of the distributions [95].

spectrum depends significantly on the input hadronic model. The discrepancies demonstrate that there is uncertain on the modeling of the mesons propagation in the production target and magnetic horns [96]. MINERνA applies different ideas with the objective of explore different datasets and techniques to tune the neutrino flux. Among these ideas we mention the following:

- Use special runs data that were collected with the NuMI target horn system positioned in different configurations. In the figure 4.11 the different neutrino energy distributions correspond to different currents in kA for the magnets horns and positions between the graphite target and the magnets.

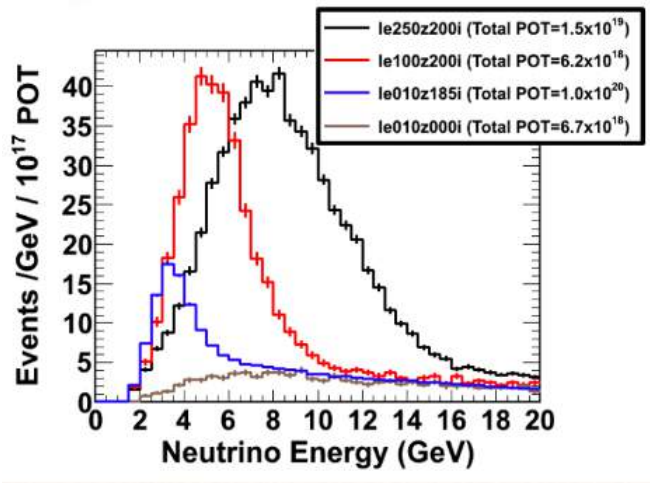

Figure 4.11: Neutrino energy distributions for a set of special runs taken with different target positions and horn currents for charged current inclusive events in the tracker region.

- Use data collected from muon monitors to measure the muon flux that is relate to the neutrino flux [97].

- Apply the neutrino-electron scattering analysis as a constraint by sampling various regions of the predicted neutrino flux [98].

- Reweight the model predictions of hadrons produced by the $p+C$ collisions using external hadron production data. In april 2014 the fixed-target MIPP experiment, Fermilab E907, that was designed to measure the production of hadrons from the collisions of hadrons with momentum ranging from 5 to 120 GeV/c on a variety of nuclei, published [99] data that will generally improve the simulation of particle detectors and predictions of particle beams used at accelerators. MIPP has collected 1.42×10^6 events of 120 GeV Main Injector protons striking a target used in the NuMI facility. The data that has been published and analyzed is related to charged pion yields per proton-on-target determined in bins of longitudinal and transverse momentum between 0.5 and 80 GeV/c with combined statistical and systematic relative uncertainties between 5 and 10 percent. In the near future MINERνA will include all this recent results in its flux framework reweighting scheme. (see figure 4.12).

- Analyze the events with low recoil energy for a neutrino interaction process [100].

For now the external hadron production data has been used for constraining the flux used in the analysis presented in this dissertation. The raw external hadron data has better agreement with the FTFP BERT hadron physics model for the prediction of both the ν_μ and $\overline{\nu}_\mu$ energy

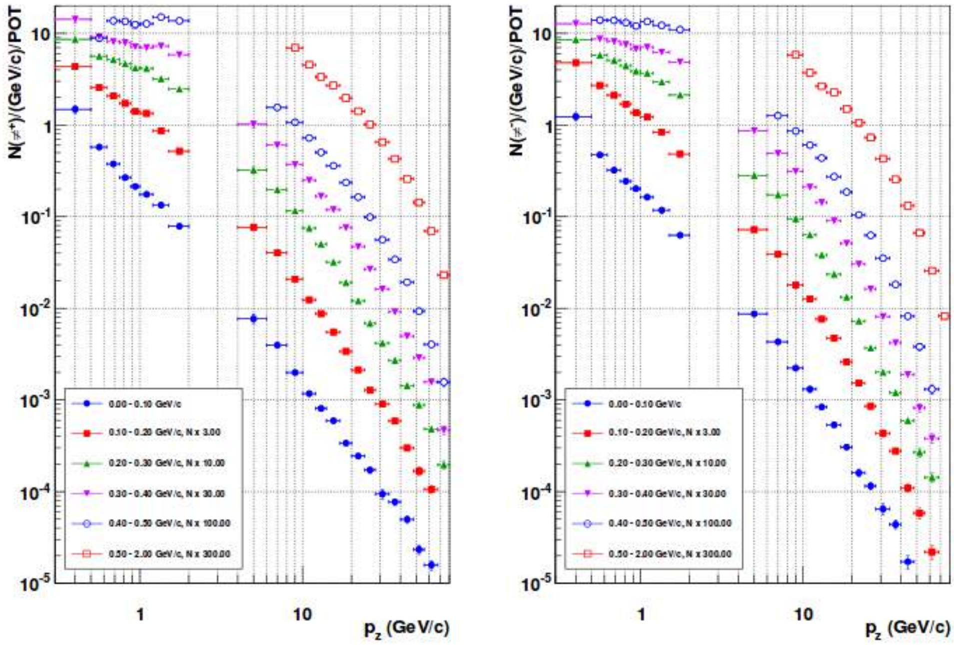

(a)π^+ yields. (b)π^- yields.

Figure 4.12: Pion yields as a function of p_z in bins of p_T. Different colors and markers represent bins of p_T , and the yields are scaled such that the points in different p_T bins do not overlap. All efficiency corrections have been applied. Statistical and systematic error bars are plotted.

spectra, which validated the change from QGSP to FTFP BERT for G4numi hadronic physis model in MINERνA [95].

4.6.2 Reweighting of $p + C$ interactions

To correct the G4numi neutrino flux prediction one needs to reweight the events based on previous measurements from external $p + C$ hadron production data. The main idea is use the data collected to reweight the production cross sections for different process like:

$$p + C \to \pi + X \tag{4.10}$$

$$p + C \to K + X \tag{4.11}$$

$$p + C \to p + X \tag{4.12}$$

MINERνA reweigths events according to measurements from two $p + C$ hadron production experiments:

- NA49 [101] that collected data in a 158 GeV/C proton beam.

- Barton, et. al. that produced measurements for the $p + C$ collisions with a 100 GeV/c beam using the Fermilab Single Arm Spectrometer in the M6E beamline [102].

Taking into account that the NuMI production target is exposed to a 120 GeV/c proton beam that differs from both of the external hadron production experiment, an energy scaling correction is applied to the NA49 dataset using the Monte Carlo package FLUKA [95]. Barton and NA49 have reported the measured cross sections as functions of the outgoing particle transverse momentum, p_T , and Feynman x, x_F, defined as:

$$x_F = \frac{2p_L}{\sqrt{s}} \tag{4.13}$$

where p_L is the outgoing particle longitudinal momentum and $\sqrt{s}$ the total center of mass energy. Figure 4.13 shows a comparison of the $p + C \rightarrow \pi \pm X$ cross sections predicted by

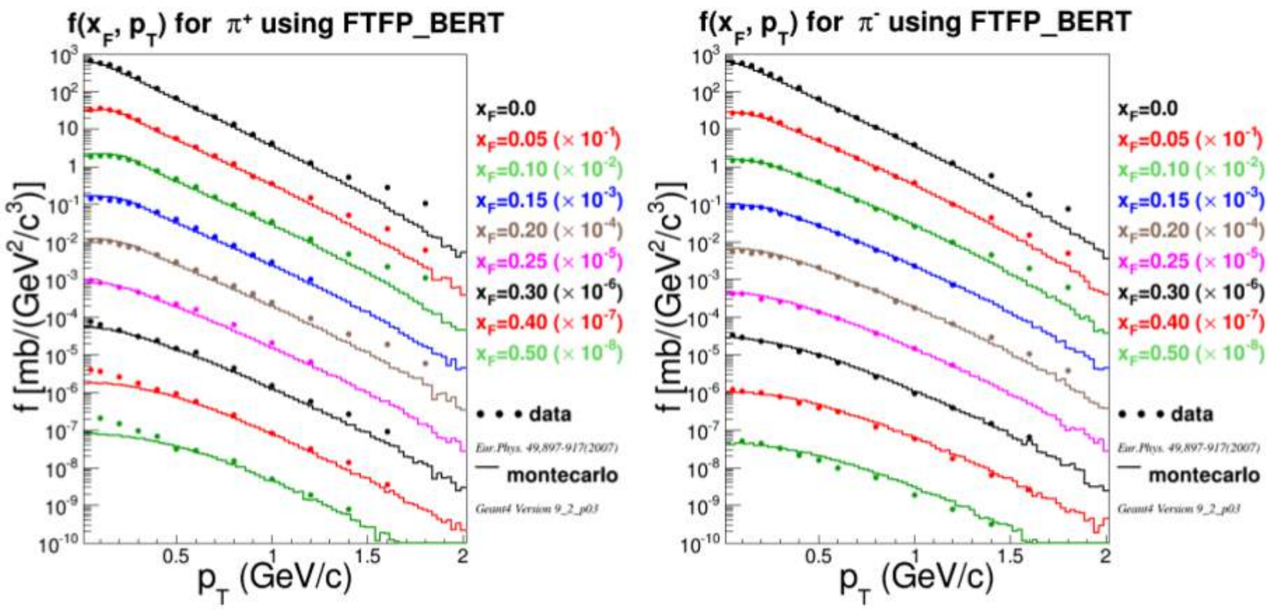

Figure 4.13: The plots show a comparison of the FTFP BERT predicted cross section to the NA49 data for the $p + C \rightarrow \pi^+ + X$ (left) and $p + C \rightarrow \pi^- + X$ (right).

the FTFP BERT model from the data collected by NA49 [101]. The kinematic region relevant to ν_μ production for MINERνA is approximately in the ranges $p_T = [0.1, 0.6]$ GeV/c and $x_F = [0.05, 0.15]$. The reweight factor is the ratio of the data to the physics model FTFP BERT values of the invariant cross sections:

$$f(E, x_F, p_T) = E\frac{d^3\sigma}{dp^3} \tag{4.14}$$

The reweighting factor for a simulated event to data collected at 158 GeV/c can be written as:

$$Wg_{NA49} = \frac{f_{NA49}(E = 158GeV, x_F, p_T)}{f_{g4numi}(E, x_F, p_T)} \times \frac{f_{FLUKA}(E, x_F, p_T)}{f_{FLUKA}(E = 158GeV, x_F, p_T} \tag{4.15}$$

The reweighting factor for the Barton data is calculated by:

$$Wg_{Barton} = \frac{f_{Barton}(x_F, p_T, E = 100GeV)}{f_{g4numi}(x_F, p_T, E)} \tag{4.16}$$

The extracted weights from NA49 and Barton datasets are applied to the kinematic regimes of interest as summarized in the table 4.1. The events that fall outside of the kinematic ranges of interest or produce a final state that was not measured are assigned a re-weighting factor equal to 1. Furthermore, weights are applied to correct for the attenuation of the primary proton beam that interacts within the NuMI target (the NuMI production target is approximately 2 nuclear interaction lengths).

Datasets	Cross Section	Kinematics
NA49 [101]	$p + C \rightarrow \pi^{\pm} + X$	$x_F < 0.5$
Barton et al [102]	$p + C \rightarrow \pi^{\pm} + X$	$x_F > 0.5$
NA49 [101]	$p + C \rightarrow K^{\pm} + X$	$x_F < 0.2$
Barton et al [102]	$p + C \rightarrow p + X$	$x_F < 0.95$

Table 4.1: Summary for the kinematic regimes of hadron production interaction constrained by the NA49 and Barton measurements.

4.6.3 Flux Results

Figure 4.14 shows the ν_μ and $\overline{\nu}_\mu$ and the hadron production reweight factors, where the NuMI ν_μ beam flux is used for the analysis presented in this dissertation. The methodology that is used to obtain the uncertainty on the flux is discussed later in the thesis.

4.6.4 GENIE: The neutrino event generator

MINERνA uses the ROOT-based Monte Carlo generator GENIE 2.6.42 [103] to generate neutrino interactions in nuclear matter, as well as modeling the transportation of the hadrons through the nucleus. GENIE is able to simulate neutrino interactions with an energy spectrum in the range of $[1 \quad MeV, 100 \quad TeV]$ for all neutrino flavors interacting with different types of nuclear targets. Introducing the theoretical predictions and phenomenological models of neutrino interactions in the few-GeV regime (neutrino energy range 1-5 GeV) is one of the main challenges for GENIE. This is essential for current and future neutrino oscillation experiments,

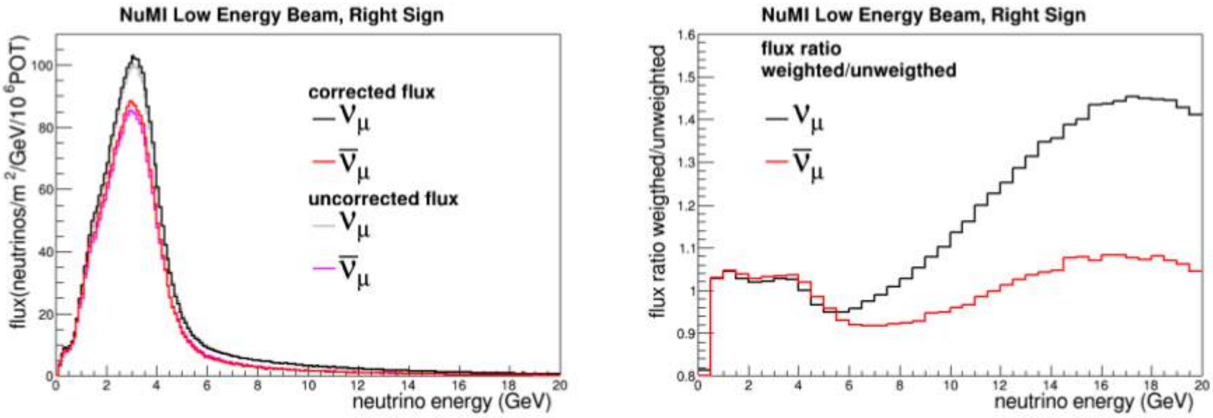

Figure 4.14: Right: Ratio of the hadron reweighting distributions where the dip region corresponds to the fallind edge of the focusing peak. Left: ν_μ and $\overline{\nu}_\mu$ simulated fluxes with and without the hadron production weights.

as well as for a better interpretation of the nuclear physics observed from the neutrino scattering data. There are 3 steps to GENIE simulation, each with its own family of models: Nuclear Physics, neutrino cross sections and final state interactions (FSI). Each stage has been tuned to and/or validated against data where available. This section summarizes the current GENIE models implementations that are used for simulate the different neutrino interaction channels that are important for the analysis presented in this dissertation.

Nuclear Physics Model

GENIE uses the relativistic Fermi gas (RFG) [62] for modeling the nuclei. The impulse approximation (section 2.8.5) is used for modeling the neutrino nucleon scattering, where the recoil nucleons are assigned an average binding energy based on electron scattering data. GENIE has an implementation of the Bodek and Ritchie model that describes the high momentum tail of the nucleons after the nucleon-nucleon interaction. However, all neutrino processes are modeled assuming scattering from a quasi-free nucleon. Pauli blocking is implemented by disallowing quasi-elastic events which produce a nucleon in the final state that does not have a momentum greater than the Fermi momentum. The Fermi momentum p_F and binding energy E_b for relevant nuclei are summarized in table 4.2. The other nuclear models are relevant only for certain neutrino interaction processes and are discussed below, in the context of those interaction processes.

Nucleus	$p_F forproton(neutron) MeV/c$	$E_b(MeV)$
Iron	251(263)	36
Carbon 221(221)	25	
Lead	245(283)	44
Oxygen	225(225)	27

Table 4.2: Relativistic Fermi Gas parameters in GENIE.

Cross Section Models

GENIE gives the differential cross section on an event by event basis for an interaction channel for a given flavor of neutrino which can scatter of a different kind of nuclei. The first stage is to determine if and where a neutrino with a given energy E_ν (obtained by the NuMI beam simulation) interacts in our detector. This is obtained calculating the interaction probabilities based on the total neutrino cross section at a determined E_ν, which is the sum of calculated cross section over all the interaction proccess i such as scattering from the nucleons, individual nucleons, quarks and atomic electrons:

$$\sigma(E_\nu) = \sum_i \sigma_i(E_\nu) \tag{4.17}$$

The $\sigma(E_\nu)$ calculated by GENIE has been tuned to available data as shown in fig 4.15. If a neutrino undergoes a scattering process, the physical process C is sampled via the probability function:

$$P_C(E_\nu) = \frac{\sigma_C(E_\nu)}{\sigma_{total}(E_\nu)} \tag{4.18}$$

With the interaction channel known, the modeling of the differential cross section for that particular process determines the event kinematics.

Quasi Elastic Scattering

The Llewellyn-Smith formalism described in section 2.8.5 [58] for modeling the quasi-elastic scattering is used. The vector form factors come from the BBBA05 parameterization [59] and the axial form factor is modeled as a dipole with $M_A = 1.01\ GeV/c^2$.

$$F_A(Q^2) = \frac{F_A(0)}{(1 + \frac{Q^2}{M_A^2})^2} \tag{4.19}$$

where $F_A(0) = -1.267$ is measured from neutron decay and the axial mass $M_A = 0.99\ GeV/c^2$. Using the partially conserved vector hypothesis (PCAC) [104] the pseudo-scalar form factor is related to the axial form factor by:

$$F_p = \frac{2M_n^2 F_A}{M_\pi^2 + Q^2} \tag{4.20}$$

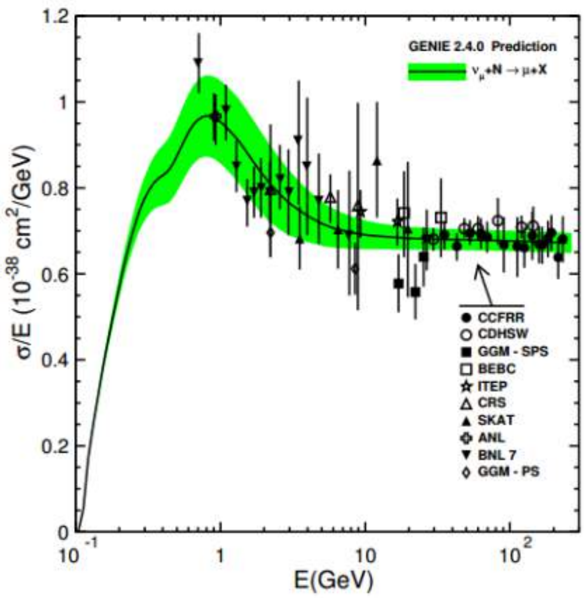

Figure 4.15: A comparison of GENIEs charged current inclusive NuMI cross section for an isoscalar target to world data. The shaded band is the uncertainty on free nucleon cross sections.

Pauli blocking in the Relativistic Fermi Gas is implemented for quasi-elastic scattering, so the outgoing nucleon must have $p > p_F$. GENIE assumes that the axial form factor follows the dipole form and assigns the value of 0.99 GeV/c^2 to the free mass parameter M_A.

Resonance Production

GENIE uses the Rein-Seghal model for neutrino-induced baryon resonance production [105]. The cross sections of the 16 resonances are summed incoherently to obtain the total resonance production cross section. The following resonances are included:

$$P_{33}(1232),\ S_{11}(1535),\ D_{13}(1520),\ S_{11}(1650)$$
$$D_{13}(1700),\ D_{15}(1675),\ S_{31}(1620),\ D_{33}(1700)$$
$$P_{11}(1440),\ P_{13}(1720),\ F_{15}(1680),\ P_{31}(1910)$$
$$P_{33}(1920),\ F_{35}(1905),\ F_{37}(1905),\ P_{11}(1671)$$

where the resonances are labeled with the incoming partial wave $L_{2I,2J}$ where I is the isospin and J is the total angular momentum. The resonance channel is the biggest source of background observed in the charged current quasi-elastic analysis that is partially treated in this dissertation. The axial and vector masses are 1.12 GeV/c^2 and 0.84 GeV/c^2 respectively.

Deep Inelastic Scattering

The Deep Inelastic Scattering (DIS) cross section is modeled using the Quark Parton Model, where the low Q^2 regime is described by modifications from Bodek and Yang. GENIE defines a DIS event as an event that does not produce an excited resonance from the neutrino inelastic scattering. GENIEs definition of DIS differs from the commonly used kinematic definition of $Q^2 > 1\ (GeV/c)^2$ and W > 2 GeV.

Transition from resonance to DIS

As mentioned in section 2.8 the experimental distinction between resonance production and DIS is somewhat arbitrary. GENIE handles this disputed region by restricting resonance production to W < W_{cut} , where $W_{cut} = 1.7\ GeV$. The DIS cross section is restricted to W greater than the mass of the Δ^{++} ($W_{min} = M_{\Delta^{++}} = 1.232 GeV$). The transition region is between W_{min} and W_{cut} where both DIS and resonance production occur. DIS interactions with resonance-like final states, meaning 1π and 2π, are suppressed in this region to avoid double counting.

Hadronization

GENIE uses the AGKY hadronization model [104]. The model joins two descriptions of hadronization: KNO scaling and PYTHIA/JETSET [106]. The AGKY use of KNO scaling is a phenomenological hadronization model developed for use in few-GeV neutrino scattering that is relevant for lower values of W. First, the model selects the type and number of hadrons that will be generated using KNO scaling. Then, it assigns momentum to these hadrons by distributing the available W among them and performing a phase space decay. PYTHIA/JETSET is a comprehensive set of codes that is the standard for simulating high energy hadron collisions. It has a wide range of validity but is not tuned to neutrino-induced hadronization. Hadronization is calculated with the phenomenological Lund string fragmentation model [107]. AGKY uses KNO scaling for events with W < W_{min} = 2.3 GeV and PHYTHIA/JETSET for W > W_{max} = 3.0 GeV. Either model for hadronization can be used between these bounds. The probability of using KNO scaling goes from 100 % at W_{min} to 0 % at W_{max}.

Final State Interaction Models

Hadrons produced from the neutrino scattering in nuclear targets with A > 1 may rescatter before escaping the nucleus. GENIE models the final state interactions using an intranuclear cascade simulation, which is handled by the INTRANUKE subpackage. The INC model assumes that the nucleus is an ensemble of quasi-free nucleons that contain Fermi motion and binding energy. The ejected hadron may interact with a single spectator nucleon through a series of encounters which is defined as a cascade. For the DIS process, before the quark interacts with the residual nucleus, the quarks are first modeled by the concept of hadron formation, the length and time it takes the quarks to materialize into hadrons. During the hadron formation, the strong interaction is turned off, thus the hadrons are more likely to exit the nucleus without experiencing any effects from FSIs. The INC models the pions and nucleons propagation through the nucleus with the primary goal of correct the simulating the missing energy lost in the nuclear medium. The INC tracks particles in steps of 0.05 fm through the nuclear environment. The probability that the hadron will interact at that step is based on the calculated mean free path which is a convolution of the hadron cross section, $\sigma_{hN}(E_h)$, and the density of the nuclear medium, $\rho(r)$. If the hadron interacts, then the interaction type is determined from the measured cross section for a particular process based on hadron nucleus scattering data [108]. The data used by GENIE, comes from hadron interactions on Fe (see figure 4.16), where the total reaction cross section for all other nuclei are obtained by scaling by $A^{\frac{2}{3}}$. At the last stage the kinematics are determined from the parameterization of data

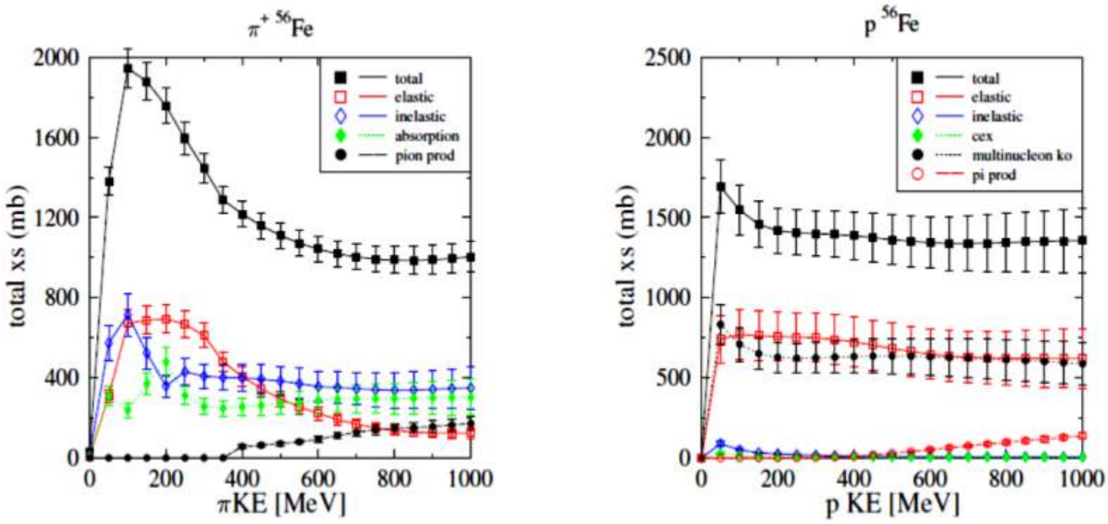

Figure 4.16: Cross sections used in the hA model [109]. Right: $p + Fe$ Left: $\pi^+ + Fe$.

distributions or sophisticated nuclear models such as CEM03 [109]. GENIE has two alternative hadron transportation models, denoted h_A and h_N, where h_A is the default mode used in the analysis presented in this thesis but MINERνA will use the h_N model in the future because it has been shown to give a more accurate description of FSI in neutrino interactions. The h_A model implementation has been extensively tested and verified with data [109], [103]. The h_N model differs by walking each hadron through the nuclear environment and by simulating the complete particle cascade using angular distributions as function of energy obtained by the

GWU group [109]. As a full INC model, the h_N calculates all of the reactions on all nuclei. Figure 4.17 illustrates the differences between the h_A and h_N models, where, for the h_N , the cascade is fully modeled.

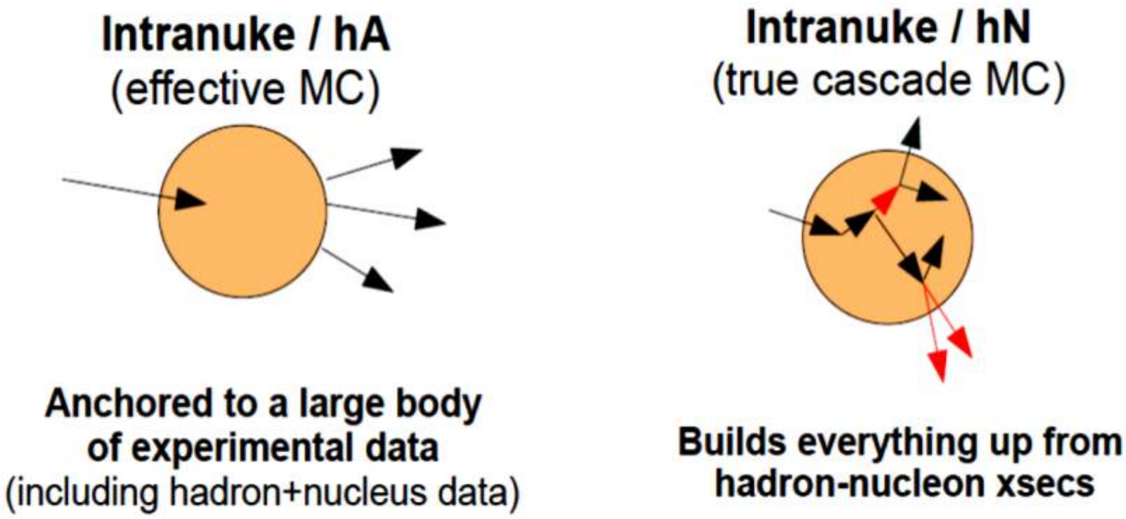

Figure 4.17: Differences between the h_A and h_N intranuke cascade models.

4.6.5 Event simulation on the MINERνA detector

MINERνA events are simulated in two steps: the propagation and energy loss of the final state products; collection and interpretation of energy deposited into the active materials. To make the simulation match data as well as possible, the generated neutrino events are overlaid onto beam data gates.

Particle propagation in MINERνA

GEANT4 9.4.p02 is used to simulate the propagation of particle trough the mass of the MINERνA detector [104]. The basic functionality of simulation is related to propagate particles in time steps and then determine if and how they interact with the material. The hadron physics is simulated using the QGSP BERT module, which uses a Bertini model for the intranuclear cascade for hadrons with energies less than 10 GeV. Almost all final state hadrons in the analysis presented in this dissertation are less energetic than 10 GeV, and QGSP BERT here outperforms other modules because quark gluon string calculations are not expected to be as effective at these range of energies.

Overlaying simulate events with NuMI spill gates

The simulation is not able to reproduce all the effects seeing in data like, for instance, dead channels, dead time, rock muon events, and miss-calibrations. Instead of trying to incorporate this complicated extensions into the simulation we import them from data. The data overlay procedure is preferable as it is clearly more representative of the data than any simulation of these effects could be. With this purpose, each generated neutrino event is paired with one gate that comes from the run period being modeled. Gates that contain more than 5×10^{12} POT are used, because empty spills will not be analyzed. Beam spill and hits information from the gate are used throughout the rest of the simulation. When analyzing a Monte Carlo with overlaid data it is important not to consider overlaid data as signal candidates.

Readout

Figure 4.18 show the NuMI beam batch structure. It is necessary to place neutrino interactions in time with the spill structure. The MINERνA simulation framework also includes the simu-

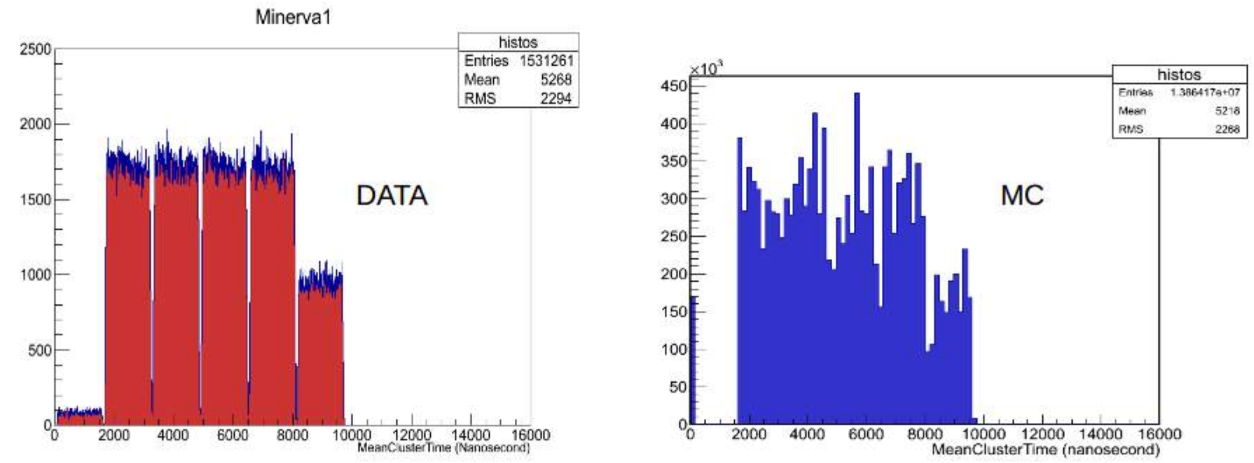

Figure 4.18: Spill batch structure. Left: Data Right: Montecarlo.[110]

lation of the optical readout and electronics systems. This requires that GEANT4 prediction of the particles energy loss to be converted into photoelectrons. The propagation of the simulated photoelectrons through a MINERνA simulated optical readout channel ensures that the simulated light output accurately describes the data. After this process, the tuned simulation (Monte Carlo) is now prepared to enter the reconstruction stage, where both the simulation and data have the same format and undergo the same reconstruction process.

MINOS Near detector Simulation

The positions and momenta of simulated particles that exit through the back of MINERνA are fed into a MINOS-owned GEANT3 simulation of the MINOS near detector [106]. The simulation includes the passage of charged particles through the MINOS magnetic field and the readout of energy deposited in the active elements. Reconstruction is then performed using the hits generated by these simulated particles. Hit and track information is retained from the MINOS gate that corresponds to the MINERνA gate used in the data overlay procedure.

Chapter 5

Measuring the total cross section for charged current inclusive $\sigma_{ccinc}(E_\nu)$ and charged current quasi-elastic $\sigma_{ccqe}(E_\nu)$ interactions in MINERvA

5.1 Introduction

This chapter describes the event selection, the background subtraction, the efficiency correction and the flux and target normalization for the CCQE and CCINC channels with the purpose of obtaining the total cross section in function of neutrino energy for both interaction channels. The data used in this analysis was collected between March and July 2010 (see figure 3.17) representing 9.60×10^{19} protons on target (POT). This POT corresponds to about $\frac{1}{4}$ of the total data collected in the NuMI beam low energy configuration. For the distributions where both data and MC are presented, MC is either:

1. **POT Normalized**: the MC absolute normalization

$$\frac{POT_{DATA}}{POT_{MC}} \tag{5.1}$$

2. **Area Normalized**: the MC shape normalization

$$\frac{N_{data}}{N_{MC}} \tag{5.2}$$

where N_{data} is the number of events in data.

5.2 Event Selection

Charged Current Inclusive Analysis (CCINC):

The CCINC neutrino scattering process is described by:

$$\nu_\mu + A \rightarrow \mu^- + X \tag{5.3}$$

The signature for CCINC (see figure 5.1) consists of a muon track with a MINOS match plus all the energy that is not associated with the track refered as recoil energy. The interaction

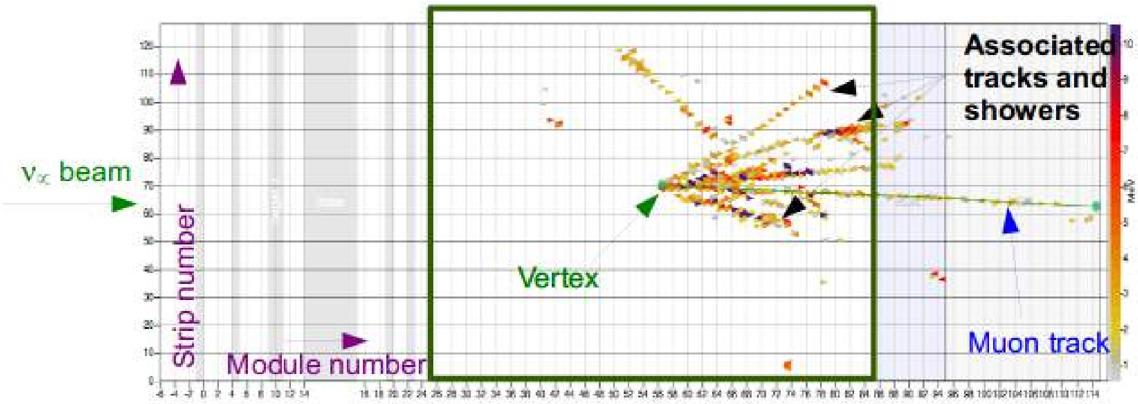

Figure 5.1: Event display for a charged current inclusive interaction in the fiducial tracker region.

nucleus is identified by the position of the reconstructed vertex. In the following sections we describe the requirements of event candidates for the CCINC scattering channel.

Charged Current Quasi-Elastic Analysis (CCQE):

For the CCQE analysis is used the machinery and event selection described in [111], and for this thesis is described the recent implementations with purpose to obtain the cross section ratio analysis. The CCQE interaction signature consists of a proton and a muon as final state particles. Figure 5.2 shows one simulated CCQE interaction in the MINERνA detector where the proton and the muon are visible. For a considerable fraction of interactions , the proton track is below the detection threshold (around 200 MeV of kinetic energy) and cannot be reconstructed. In the CCQE analysis the selection of events rely on the detection of the muon and zero to low reconstructed recoil energy outside the vertex region. A charged current quasi-elastic rich sample is selected, both data and montecarlo, by applying the requirements described in the following section.

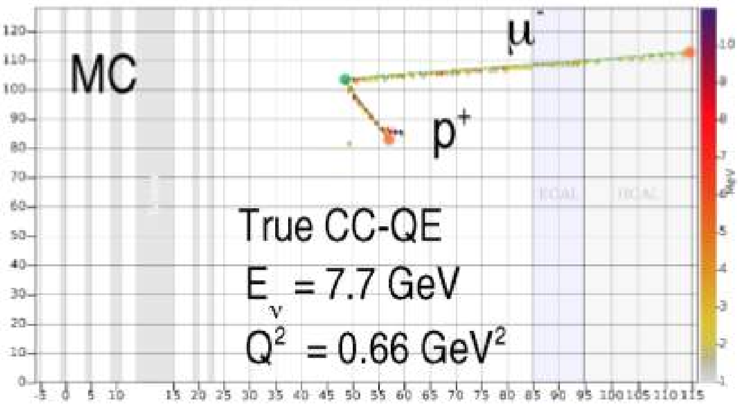

Figure 5.2: Event display for a simulated charged current quasi-elastic interaction in the fiducial tracker region.

5.2.1 Muon Identification: CCINC and CCQE

For both analysis (CCQE and CCINC) we select events with one and only one reconstructed muon. This requirement ensures that the muon started at MINERνA and has been completely reconstructed by range or curvature in the MINOS near detector. Muons that do not reach

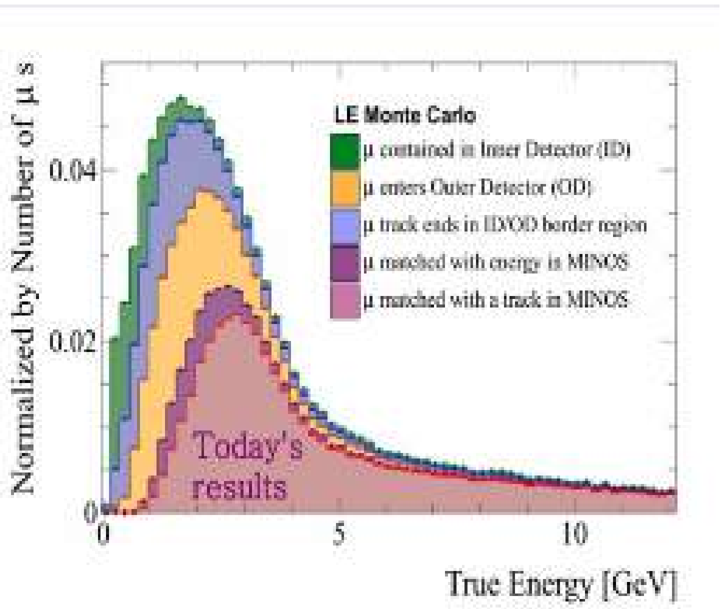

Figure 5.3: Classification of different types of muons present in MINERνA.

MINOS, either because they exit at a high angle or because they stop in the MINERνA detector, can not have the charge reconstructed and are not used in the analysis (see figure 5.3). Due to the relative position of the MINOS and MINERνA detectors this requirement has an impact on the acceptance of events since only muons with energy above 2 GeV and θ_μ below 25° can be identified (see figure 5.4).

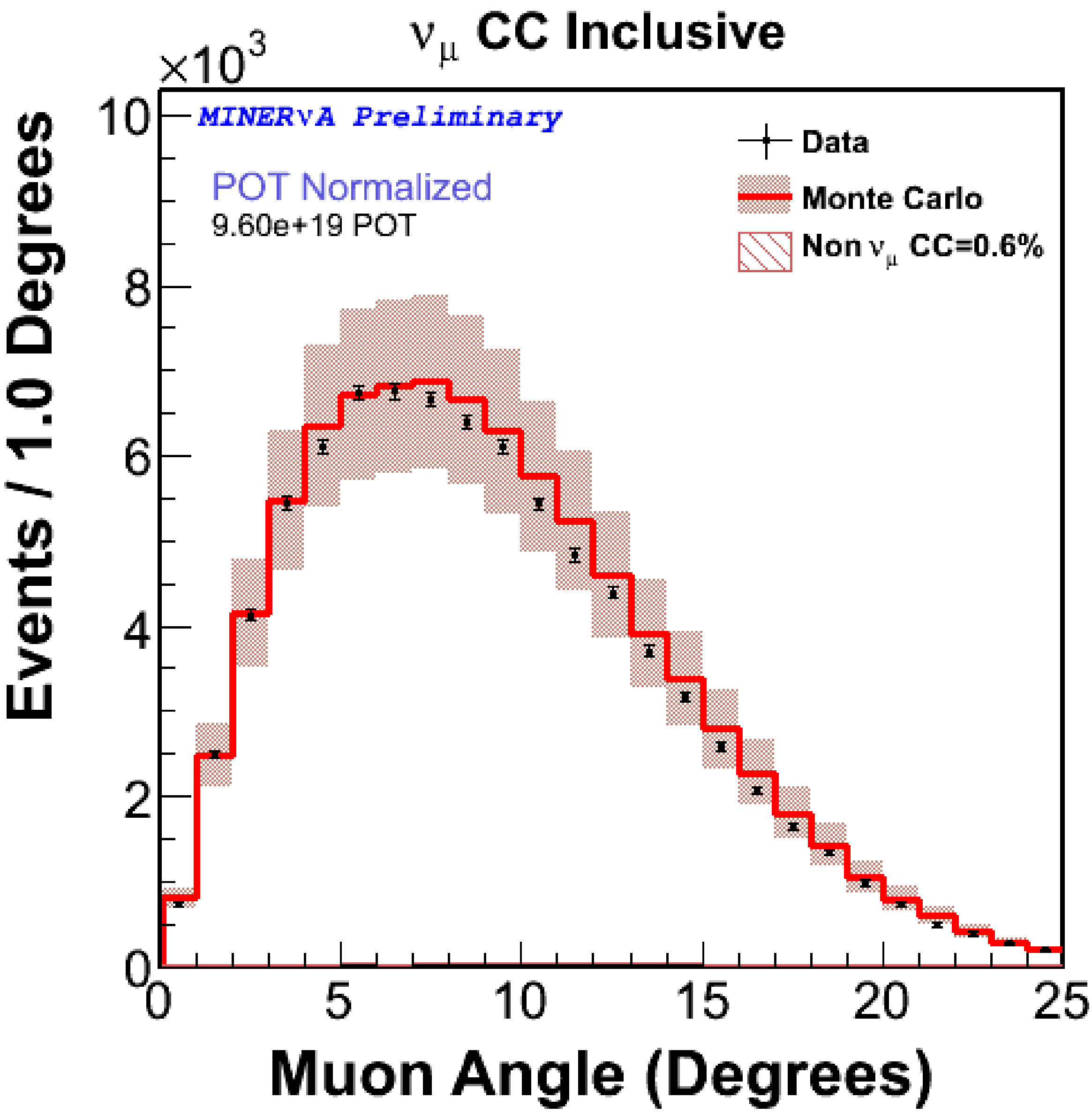

Figure 5.4: Muon Angle distribution for charged current inclusive interactions in the tracker region.

5.2.2 Fiducial Volume: CCINC and CCQE

The event interaction vertex is determined by the beginning of the muon track and must be within a regular hexagonal area with apothem 850 mm. The hexagonal area guarantees that the interaction does not occur in the lead of the electromagnetic calorimeter that surrounds the perimeter of the detector. Furthermore, the interaction vertex is required to be inside a fiducial volume inside MINERνA active tracker region (plastic scintillator) whose limits are defined by hexagons of 850 mm apothem drawn in each module in the interval between module 27 (z = 5,980 mm) and 80 (z = 8,422 mm) . The mass of the fiducial volume is 6.6 tons and it was estimated that it contains 1.534×10^{30} neutrons.

5.2.3 Reconstructing the neutrino Energy

CCINC:

The neutrino energy distribution for the charged current inclusive analysis is reconstructed as:

$$E_\nu = E_\mu + E_{recoil} \tag{5.4}$$

Where E_{recoil} is calculated for the clusters that are not classified as crosstalk (see section 4.5.2). The procedure to obtain the muon energy by range or curvature was explained in the section 4.5.5. The neutrino energy was selected in the range of 2 - 10 GeV.

CCQE:

In the results presented in [70] and [111] the neutrino energy and Q^2 were reconstructed under the CCQE hypothesis using the muon kinematics (see equation 5.5).

$$E_\nu^{\mathrm{QE}} = \frac{2(M_n - \mathrm{E_B})E_\mu - \left[(M_n - \mathrm{E_B})^2 + m_\mu^2 - M_p^2\right]}{2\left[(M_n - \mathrm{E_B}) - E_\mu + \sqrt{E_\mu^2 - m_\mu^2} cos\theta_\mu\right]} \tag{5.5}$$

Where is assumed that the target nucleon is at rest and quasi-free inside the nucleus (RFG aproximation described in section 2.8.5). By using the conservation of 4-momentum in a two body elastic collision and neglecting the neutrino mass we obtain the neutrino energy expression 5.5. M_n, M_p and m_μ are the neutron, proton and muon masses. The muon energy is defined as:

$$E_\mu = T_\mu + m_\mu \tag{5.6}$$

θ_μ is the angle of the muon track with respect to the neutrino direction, and E_B is the nuclear binding energy in carbon (see table 4.2).
The extension of the CCQE analysis that was developed for this dissertation has an implementaion of the neutrino energy reconstruction for the CCQE scattering using:

$$E_\nu^{QEINC} = E_\mu + E_{recoil} \tag{5.7}$$

where, instead of using the CCQE hypothesis we use the recoil energy and the muon energy from the MINOS match track. A new definition of recoil that includes the energy around the vertex has been implemented as shown in equation 5.8:

$$E_{recoil} = E_{vertex} + E_{isolated} + E_{dispersed} \tag{5.8}$$

The validity of the implementation of the new neutrino energy reconstructed definition can be observed by the E_ν resolution(subtracting the predicted from the reconstructed neutrino energy) as shown in figures 5.5 and 5.6 and defined as:

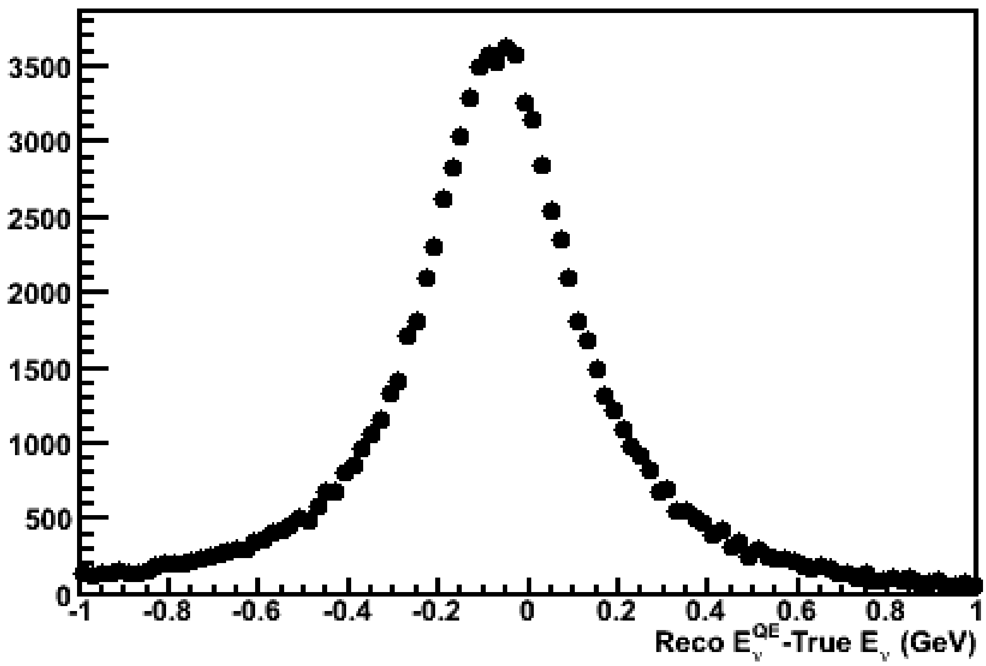

Figure 5.5: Neutrino Energy resolution using the CCQE Hypothesis definition.

$$Resolution_{QE} \quad Hypothesis = E_\nu^{QE} - E_\nu^{Truth} \tag{5.9}$$

$$Resolution \quad Implemented = E_\nu^{QEINC} - E_\nu^{Truth} \tag{5.10}$$

For the resolution using the CCQE hypothesis we find a mean value of ≈ -0.07 GeV and for the resolution using the new implementation (see equation 5.7) we find a mean value of ≈ 0.04 GeV.

Another expression used in the event selection (and that was not modyfied for the CCQE extension presented in this thesis) is the 4-momentum transfer to the target nucleon represented by the relativistic invariant $Q^2 = -q^2$ where q is the 4-momentum of the $W^\pm$, and can be

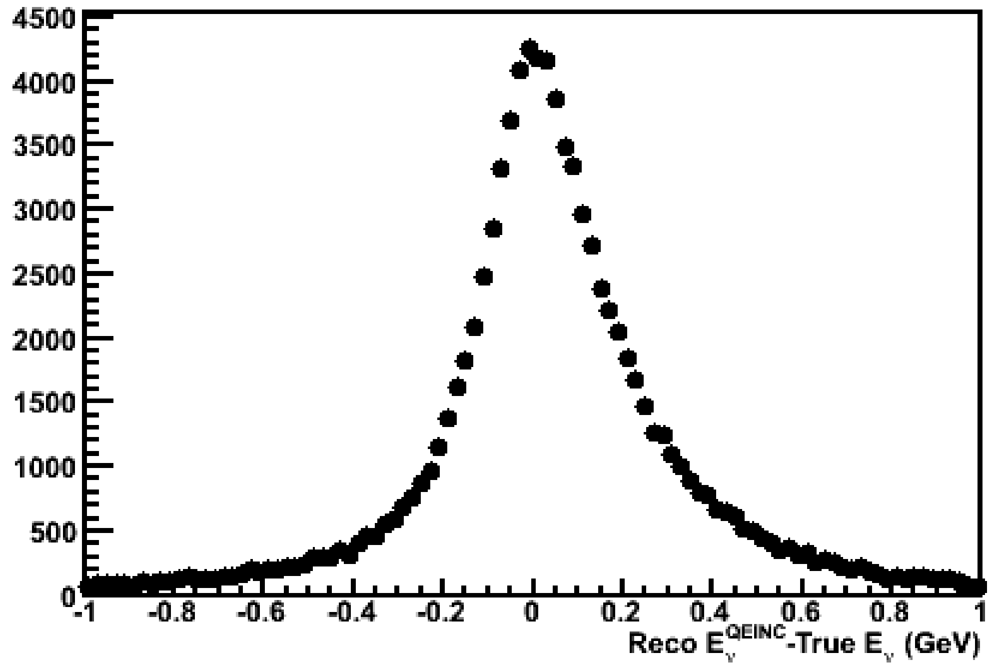

Figure 5.6: Neutrino Energy resolution using the implemented definition.

reconstructed as :

$$Q^2_{\rm QE} = -m_\mu^2 + 2E_\nu^{\rm QE}\left(E_\mu - \sqrt{E_\mu^2 - m_\mu^2}cos\theta_\mu\right) \tag{5.11}$$

The superscript QE in E_ν^{QE} and Q^2_{QE} are there to remind us that these formulas have been deduced using CCQE hypothesis. The neutrino energy for the seleted events is in the 2-10 GeV range. Events with energy greater than 10 GeV, far away from the neutrino flux peak at $\approx$ 3 GeV, are rejected since they are mostly background (DIS) and are not used in the measurement. Due to the requirement that the muon track must have a match in the MINOS near detector the sample does not contain events with neutrino energy less than $\approx$1.5 GeV.

5.2.4 Recoil Energy

CCINC:

Recoil energy is initially reconstructed from the sum of all tracks that were not identified as the primary track and from all reconstructed inner detector blobs[1]. Once these structures are assembled there is an aditional clean up of all the inner and outer detector in time clusters that are not identified as LowActivity and or XTalkCandidates (see section 4.5.2) during the cluster formation. The energy value of the recoil is computed calorimetrically. For more details see

[1]blob: groups of spatially contiguous clusters

section 4.5.6.

CCQE:

For the CCQE scattering the recoil energy calculation uses the clusters that do not belong to the muon track and are reconstructed and classified in different ways:

Vertex Energy : the energy in clusters within 300 mm of the reconstructed vertex is summed and called *vertex energy*. Given the geometry of the detector, the shape of the space over which energy is summed is not a sphere but rather the intersection of three cylinders of half-length $R = 300$ mm at 60° angles to each other. The 300 mm radius corresponds to about 6 modules in each direction along the z-axis and about 18 strips in each direction within a plane. It is also the maximum distance a ~ 225 MeV proton and a ~ 225 MeV pion will travel in scintillator before losing all its energy.

Isolated Blobs Energy : the remaining clusters, whose energy is not below 1 MeV and where $|t_{cluster} - t_{muontrack}| < 25$ ns, are considered to build independent shower-like groups of clusters called *isolated blobs*. These objects are required to contain clusters in several views so they can be reconstructed in 3-dimensions. This means they have to be big energy deposits. The energy of isolated blobs is summed and called *isolated blobs energy*.

Dispersed Energy : all the remaining energy in the tracker and ECAL regions of the inner detector is summed and called *dispersed energy*. Only clusters within 25 ns of the muon track time are considered.

Recoil Energy : this is just the sum of *isolated blobs energy* and *dispersed energy*.

$$E_{recoil} = E_{isolated} + E_{dispersed} \tag{5.12}$$

It represents the total energy outside the vertex region.

CCQE interactions are expected to have low recoil energy away from the vertex. The recoil energy reconstructed in the way described here is useful to isolated a CCQE sample of neutrino interactions in MINERνA tracker region. An example of how the recoil energy is reconstructed in data is given in figure 5.7 where a non-CCQE interaction candidate with a considerable amount of recoil is reconstructed.

Number of Isolated Blobs:

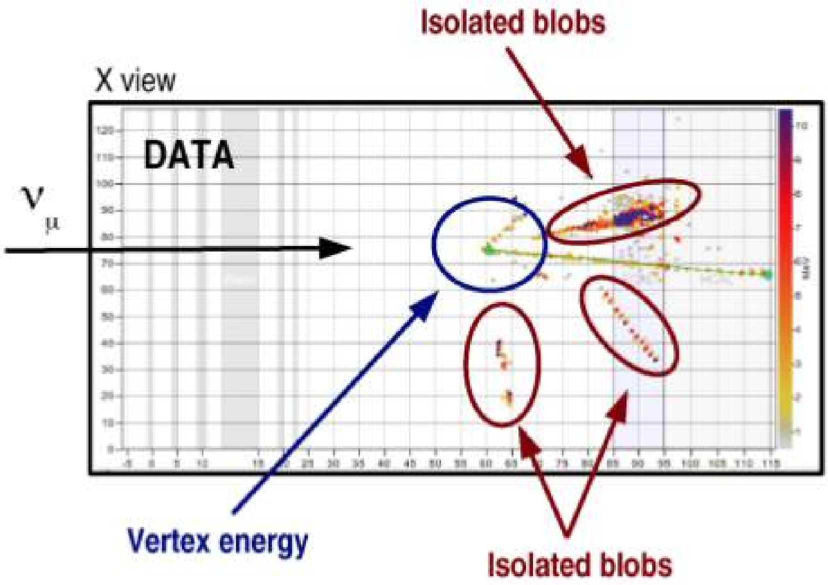

Figure 5.7: Non CCQE interaction and different recoil energy classifications.

We require less than three isolated blobs unattached to the vertex in the fiducial volume (see figure 5.7). This requirement removes events with energetic showers. According to the MC, most of the events removed are deep inelastic scattering (DIS) and resonace (RES) that are likely to develop big showers. On the other hand, quasi-elastic events (QE) tend to have zero, one or two isolated blobs as is presented in [70].

Non-vertex recoil energy:

To avoid biasing the analysis by relying in the MC simulation of vertex energy, we select QE events by looking at the non-vertex recoil energy. Vertex energy has been studied very carefully and is published in [112]. The purpose is to remove both DIS and RES events which tend to deposit larger amounts of energy outside the vertex region compared to QE events. To prevent the loss of QE events with high Q^2, that also tend to deposit large amounts of energy, the value of the non-vertex recoil energy below which we select events depends on Q^2_{QE}. The procedure to obtain a Q^2_{QE} dependent non-vertex recoil energy cut is decribed elsewhere [111]. In order to have a continuous cut, we will use the parametrizations and fits obtained in the published CCQE analysis [70] as below:

$$SignalCut(Q^2_{QE}) = \begin{cases} 0.05 & \text{if } Q^2_{QE} < 0.166 \\ -0.05 + 0.64Q^2_{QE} - 0.22(Q^2_{QE})^2 & \text{if } 0.166 \leq Q^2_{QE} < 1.61 \\ 0.41 & \text{if } Q^2_{QE} \geq 1.61 \end{cases}$$

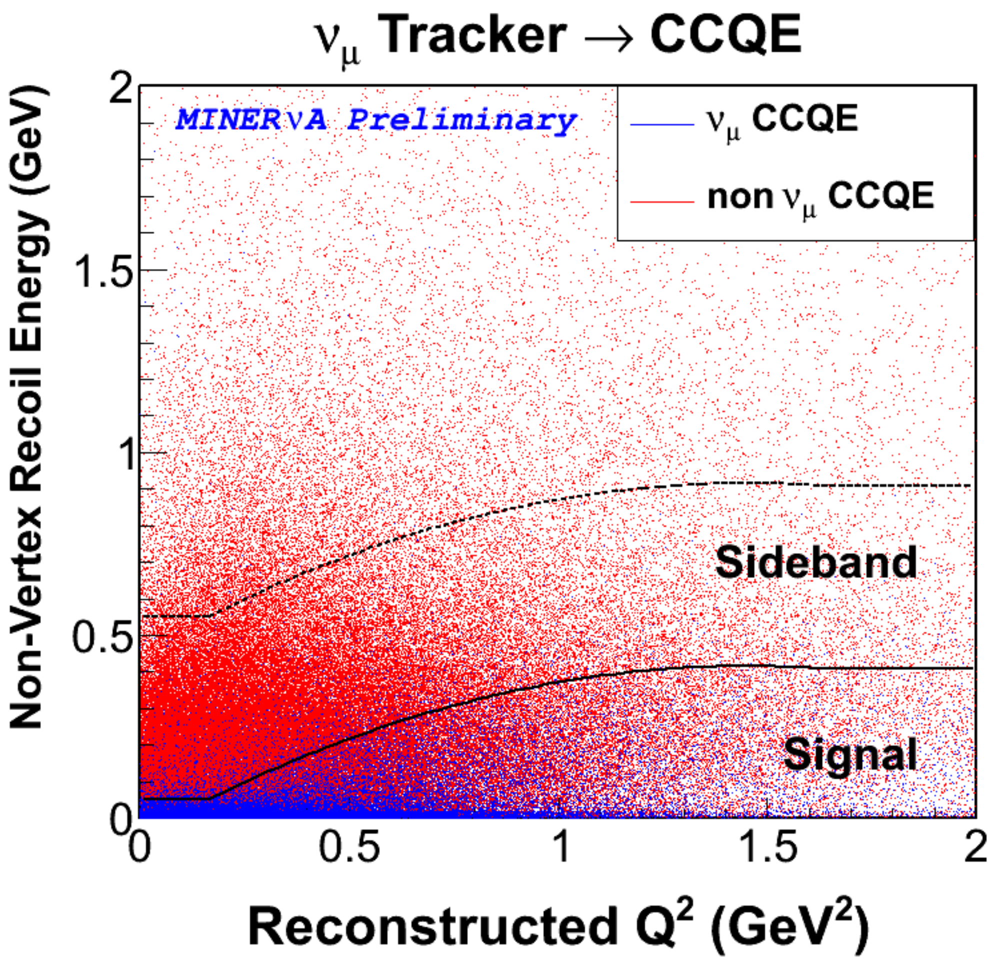

Figure 5.8: Non-vertex recoil energy in function of Q^2. CCQE events in red and non-CCQE events are in blue.

$$SidebandCut(Q^2_{QE}) = \begin{cases} 0.55 & \text{if } Q^2_{QE} < 0.166 \\ 0.45 + 0.64Q^2_{QE} - 0.22(Q^2_{QE})^2 & \text{if } 0.166 \leq Q^2_{QE} < 1.61 \\ 0.91 & \text{if } Q^2_{QE} \geq 1.61 \end{cases}$$

Figure (5.8) shows the distribution of simulated events as a function of non-vertex recoil energy and Q^2_{QE} together with the SignalCut(Q^2_{QE}) and SidebandCut(Q^2_{QE}) curves. Events falling below the signal cut curve make our signal sample. Events between signal cut and sideband cut define the sideband sample. The events in the sideband sample are events with characteristic pretty similar to the ones on the signal sample but, due to the high recoil, they contain a big fraction of non-CCQE background events.

5.3 Selected Samples

After applying the event selection to data, 105,245 events are selected as CCINC interactions candidates. In the case of the CCQE channel there are 30,000 events selected. Figures 5.9 and 5.10 show the distribution of selected events. For the CCQE case, the neutrino energy distribution is obtained from the events present in the signal region (see figure 5.8).

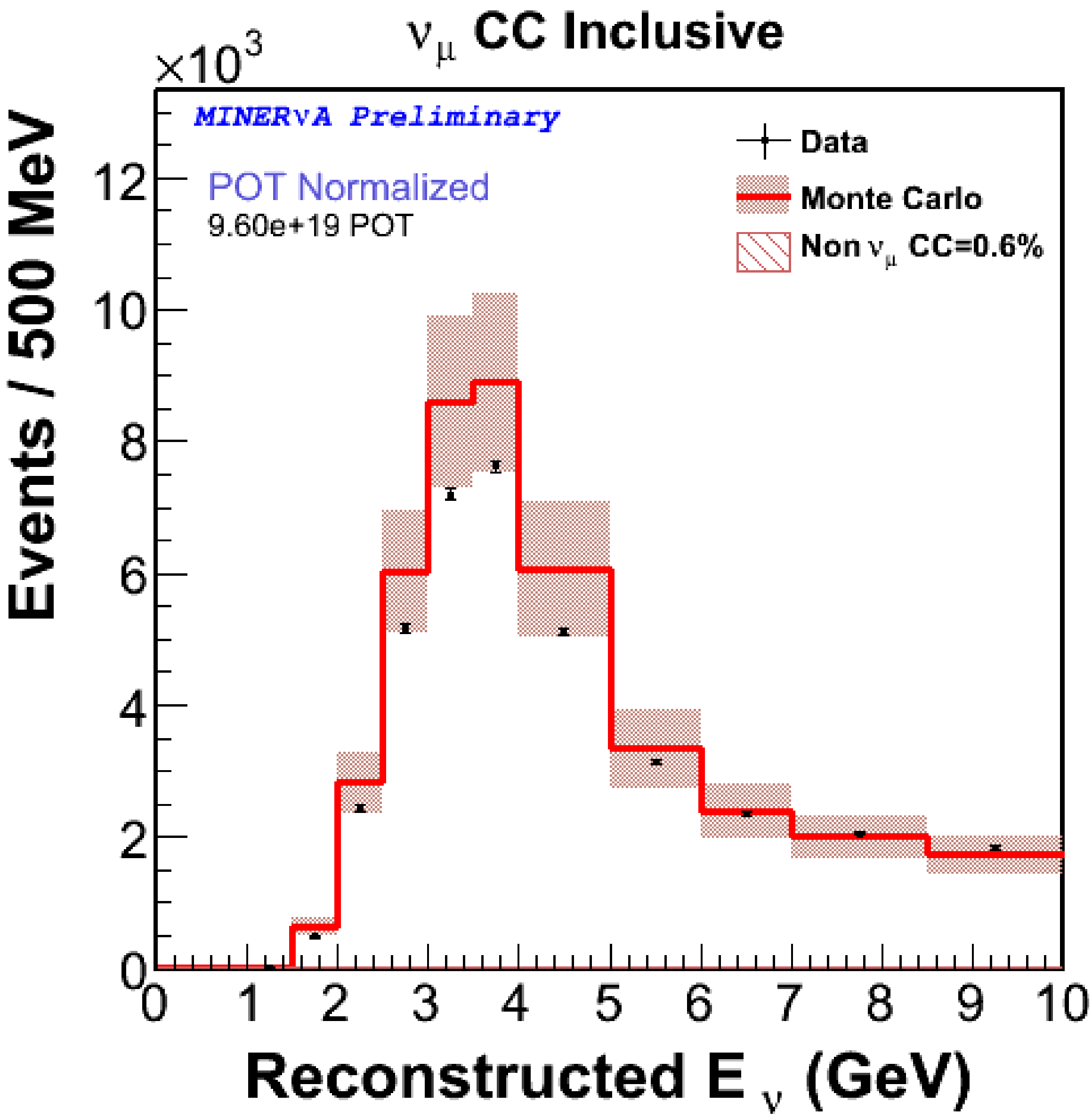

Figure 5.9: Neutrino Energy distribution for charged current inclusive (CCINC) candidates.

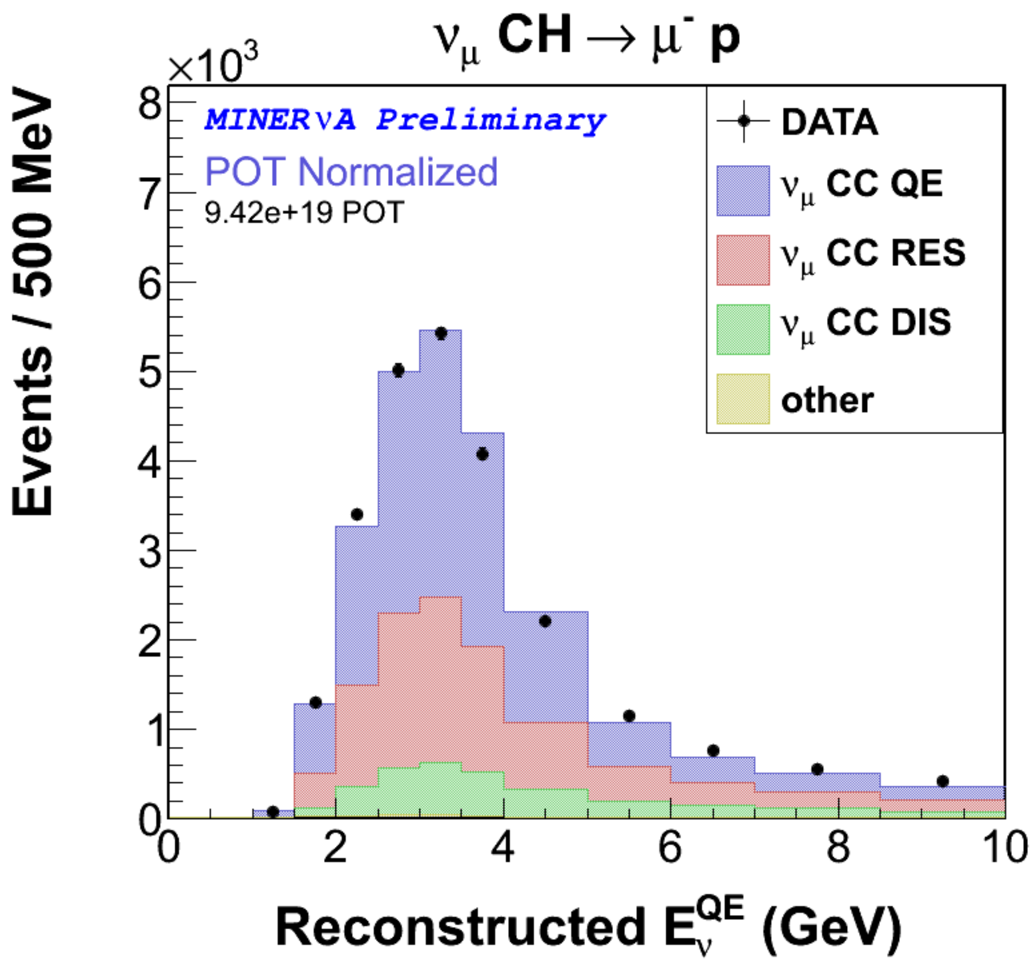

Figure 5.10: Neutrino Energy distribution for charged current quasi-elastic (CCQE) candidates.

5.4 Measurement of CCINC and CCQE cross sections

The final result of our analysis is the ratio between CCQE and CCINC cross sections. In this section we describe how both cross sections are calculated in function of neutrino energy in the tracker region of the MINERνA detector. In order to calculate the total cross sections for CCINC and CCQE in function of neutrino energy from the number of reconstructed events identified as CCINC and CCQE candidates showed in the previous section, we correct both distributions for expected background event rates, known kinematic smearing effects in the reconstruction using the unfolding procedure and selection efficiency. Furthermore, the corrected distribution is normalized by the integral of the flux in each energy bin and the number of targets in the fiducial volume. All the previous description is summarized by equation 5.13 that shows the total cross section in the i^{th} bin of E_ν:

$$\sigma_i = \frac{\sum_j U_{ij}(N_j^{data} - N_j^{bg})}{\phi_i T \epsilon_i} \tag{5.13}$$

where:

- ϕ_i is the flux in the i^{th} bin.
- T is the number of targets in the fiducial volume. In the case of the CCINC channel T is the number of nucleons and for the CCQE channel T is the number of neutrons.
- U_{ij} is a matrix that describes the migration from the true E_ν bin i to the reconstructed E_ν bin j, due to finite resolutions and realistic biases in the reconstruction of the CCINC and CCQE events.
- N_j^{data} is the measured distribution of selected events in bins of reconstructed E_ν.
- N_j^{bg} is an estimate for the number of background events in bins of reconstructed E_ν.
- ϵ_i is the efficiency for reconstructing and selecting signal events as a function of the true variable.

5.4.1 Background Subtraction

This section describes the sources of background for CCINC and CCQE scattering channels. Furthermore, for the special case of CCQE, it presents the constraint of the background MC prediction using the MINERνA data.

CCINC

For the charged current inclusive channel in the tracker region we find three sources of background:

- **Neutral current events**: the neutral current events do not produce a charged lepton in the final state. There is a small number of pions that exit MINERνA and form a track in MINOS. There is also a small quantity of pion decays producing muons that satisfy the signal requirements. This background is negligible.
- **Wrong sign (WS) events**: antineutrinos producing antimuons that fake a muon in the MINOS near detector. The vast majority of the wrong sign events is occasionated by a reconstruction failure in MINOS. The WS contamination is minimum near the flux focusing peak, where the charge selection of the mesons in the beamline is the most effective.

- **Rock Muon events**: muons produced via charged current interactions in the upstream rock. This background is controled with the fiducial vertex selection. To have an idea of the rock muon contamination in the tracker region of MINERνA a visual scan effort was done. The results show that there is no significant contamination for the tracker region.

As shown in figure 5.9 we have an estimated background wiht NC and wrong sign events in the tracker region of ≈ 0.6 % for the neutrino energy distribution over all the energy range. To subtract the background we follow the procedure given by:

$$BS_i = N_i^{data} - N_i^{bg(MC)} \tag{5.14}$$

where:
N_i^{data} is the number of events in the i^{th} bin for the neutrino energy distribution and $N_i^{bg(MC)}$ is the number of background events predicted by the MC in the i^{th} bin. The background subtracted distribution of the selected sample can be seen in figure 5.11.

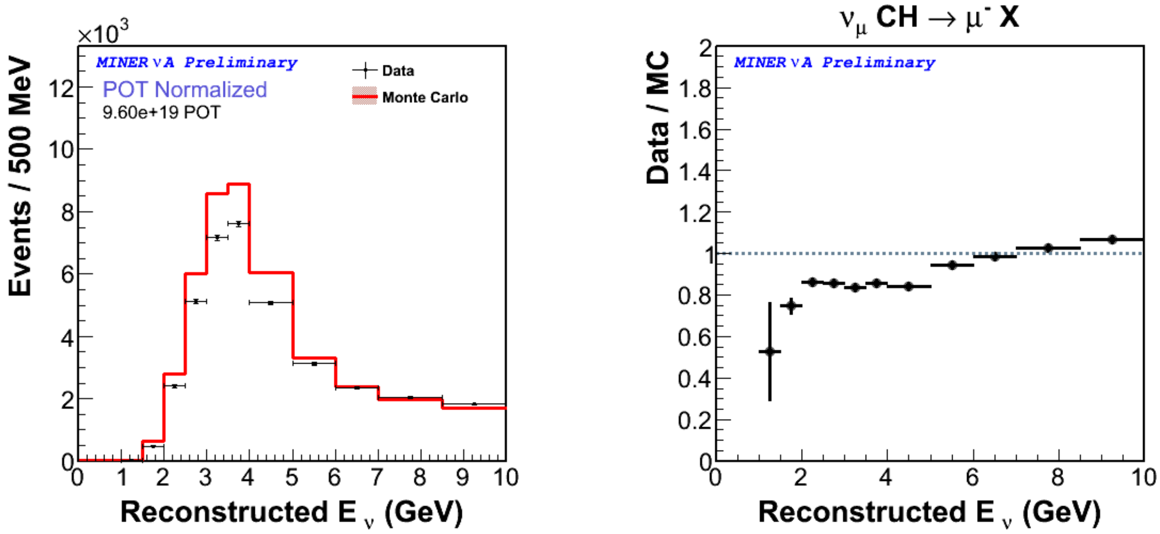

Figure 5.11: Left: Neutrino Energy background subtracted distribution for charged current inclusive interactions. Right: Ratio $\frac{DATA}{MC}$.

CCQE

MC simulation allows us to predict the level of non-CCQE background that can not be suppresed by the CCQE event selection described in section 5.2. From figure 5.10 we see that the background consists mainly of resonant pion production (RES) and deep inelastic scattering (DIS) interactions. They enter in the signal sample due to the fact that the recoil final state particles (mostly pions) are contained in a 300 mm radius sphere around the interaction vertex or are absorbed before exiting the atomic nucleus. To avoid model dependence MINERνA data is used to constraint the non-CCQE background prediction in the selected sample of CCQE candidates using the sideband sample showed in figure 5.8. Figure 5.12 shows the reconstructed

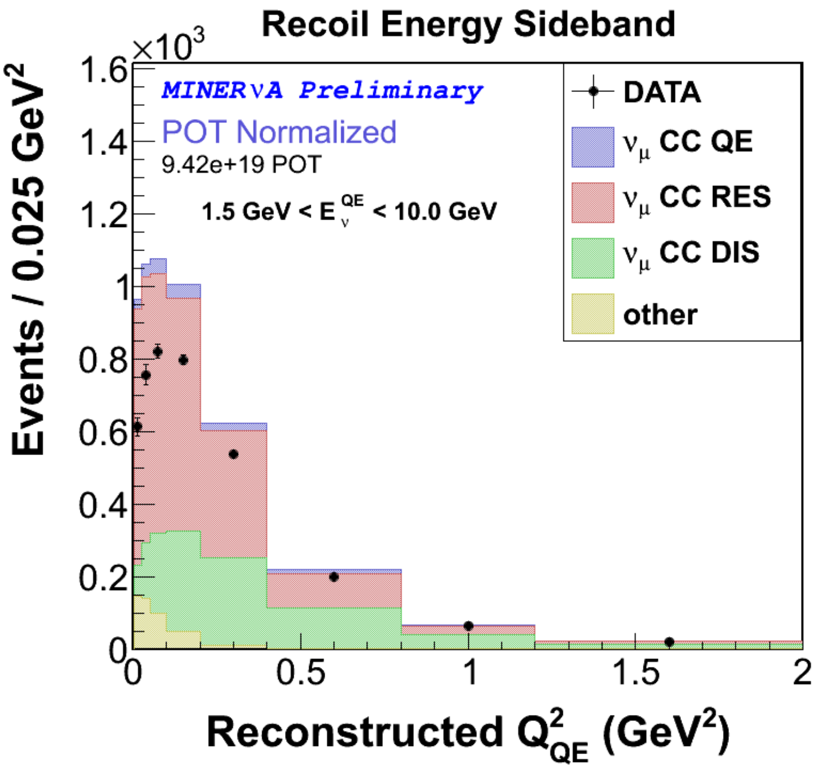

Figure 5.12: Q^2 distribution for events in the sideband.

Q^2_{QE} distribution of events in the sideband sample. From the Q^2_{QE} distribution we use equation 5.15 to calculate a background scale (see figure 5.13) as a function of reconstructed Q^2_{QE}. The background scale is applied to background events in the sideband for a perfect agreement between data and MC as shown in figure 5.14.

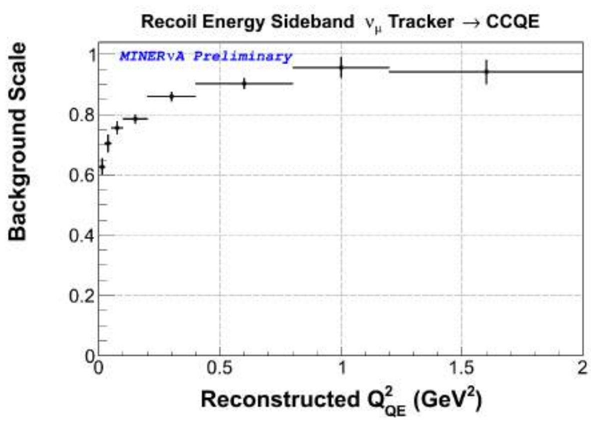

Figure 5.13: Background scale in bins of Q^2.

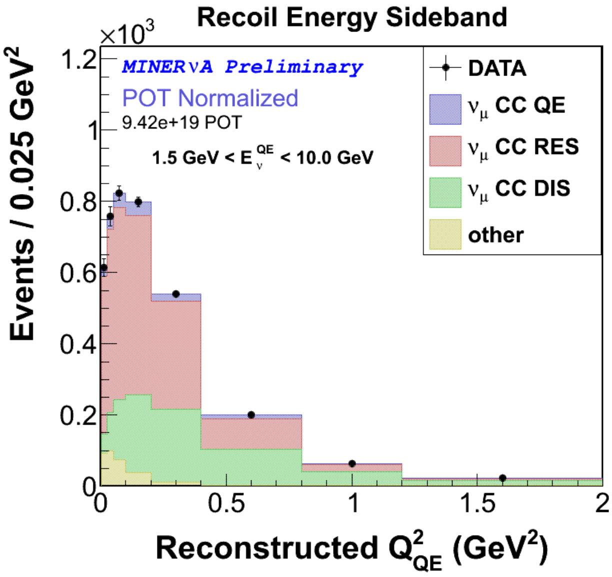

Figure 5.14: Q^2 distribution after applying the background scale to the background events in the sideband.

$$BS_i = \frac{N_i^{data} - N_i^{CCQE}}{N_i^{non-CCQE}} \tag{5.15}$$

where: i is the i^{th} Q^2_{QE} bin , BS_i is the background scale for the i bin , N_i^{data} is the number of data events in the bin i, N_i^{CCQE} is the number of simulated CCQE events falling in bin i, $N_i^{non-CCQE}$ is the number of simulated non-CCQE (background) events falling in bin i. Figure 5.13 shows the background scale distribution that was obtained for this thesis using the recent updates in the machinery of CCQE. Once constrained, the background is subtracted from the neutrino energy event candidate distribution and the result is shown in figure 5.15

5.4.2 Unfolding

It is not possible to reconstruct quantities with perfect precision and some events are always reconstructed in the wrong bin. We must know if an event observed in bin j, really happened there. That means to know the probability that an event observed in bin j occurs in bin k. We can use our MC to form a migration matrix indicating what fraction of events generated in each true bin k was observed in each reconstructed bin j. If the reconstruction makes a good work, we expect to see a diagonal matrix. To get the unsmearing matrix U_{jk} we must invert the migration matrix. This inversion generally gives poor results and we often need to apply a more sophisticated method and we use the Bayesian unfolding technique. We want to know the proability $P(k|j)$ that an event observed in reconstructed bin j ocurred in true bin k that

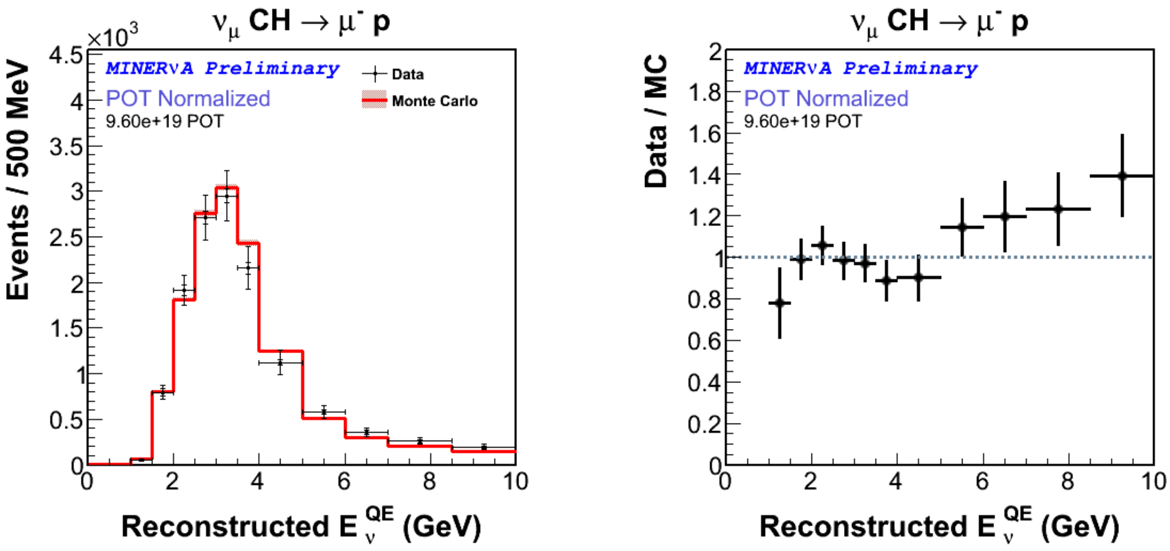

Figure 5.15: Left: Neutrino Energy background subtracted distribution for charged current quasi-elastic interactions. Right: Ratio $\frac{DATA}{MC}$.

according to the Bayes theorem of probability is given by:

$$P(k|j) = \frac{P(j|k)P(k)}{P(j)} \tag{5.16}$$

Using our Monte Carlo we can estimate $P(k)$:

$$P(k) = \frac{N_k}{N_{total}} \tag{5.17}$$

and:

$$P(j|k) = \frac{N_{jk}}{N_k} \tag{5.18}$$

where: N_k is the number of events in true bin k. N_{jk} events observed in j and generated in k. Finally we use 5.17 and 5.18 in 5.16:

$$P(k|j) = \frac{N_{jk}}{N_j} \tag{5.19}$$

where N_{jk} are the elements of our unsmearing matrix. Data with small statistics may unfold to bins with higher statistics, increasing uncertainty in those bins. Furthermore, the unfolding has some dependence on the model that is used to generate our true distribution. Without unfolding the measurements cannot be directly compared to the results of other experiments. In the analysis presented in this thesis E_ν is the quantity measured and, due to its finite resolution, there is a migration from a generated (true) value of E_ν to a different reconstructed value. MC simulation is used to construct the migration matrices for CCINC and CCQE that contains the probability of an event migrate between E_ν bins when we change from its generated to reconstructed E_ν. The migration matrix is unique for each experiment and depends on the properties of the detector. Figures 5.16 and 5.17 show the migration matrices for the MINERνA E_ν bins, for both neutrino scattering channels CCINC and CCQE. The Bayesian method [113]

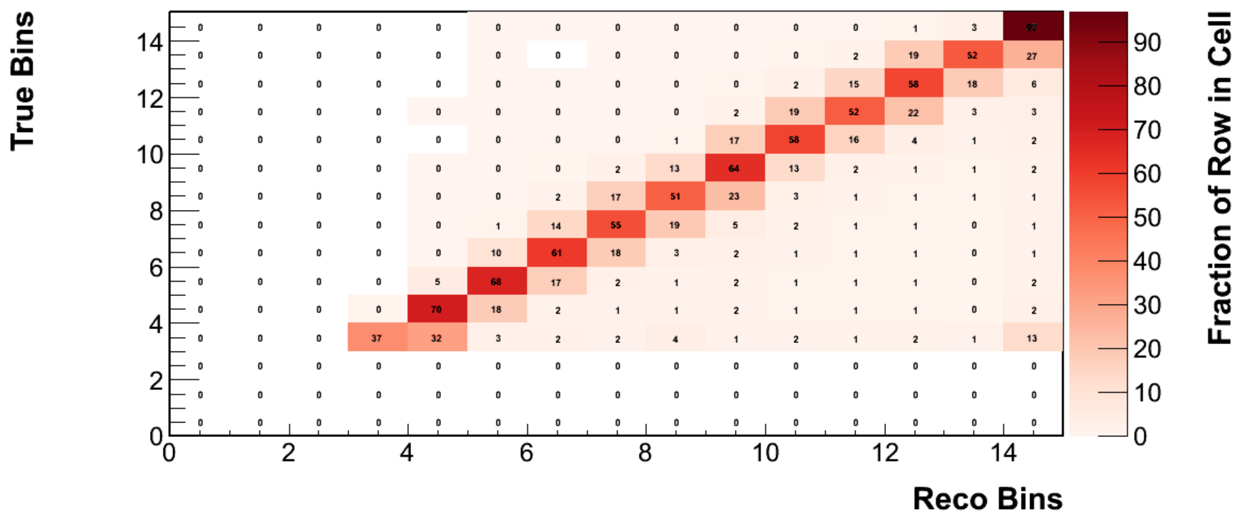

Figure 5.16: Migration Matrix for CCINC analysis. The different values in the matrix represent the probability of an event to migrate from a generated to a reconstructed E_ν bin.

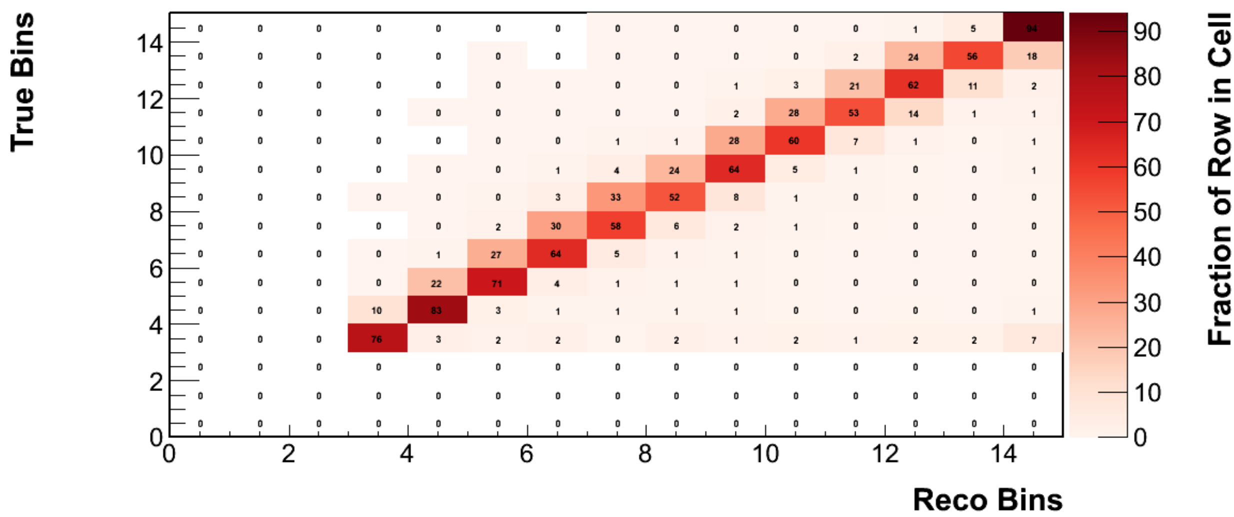

Figure 5.17: Migration Matrix for CCQE analysis.

briefly described in the beginning of this section[2] was perfromed with four iterations. After the background subtraction we applied the unfolding technique to estimate the true E_ν distribution

[2]More information about Bayesian method in [113]

from the reconstructed E_ν and the migration matrix. The results for CCINC and CCQE after the unfolding are shown in figures 5.18 and 5.19.

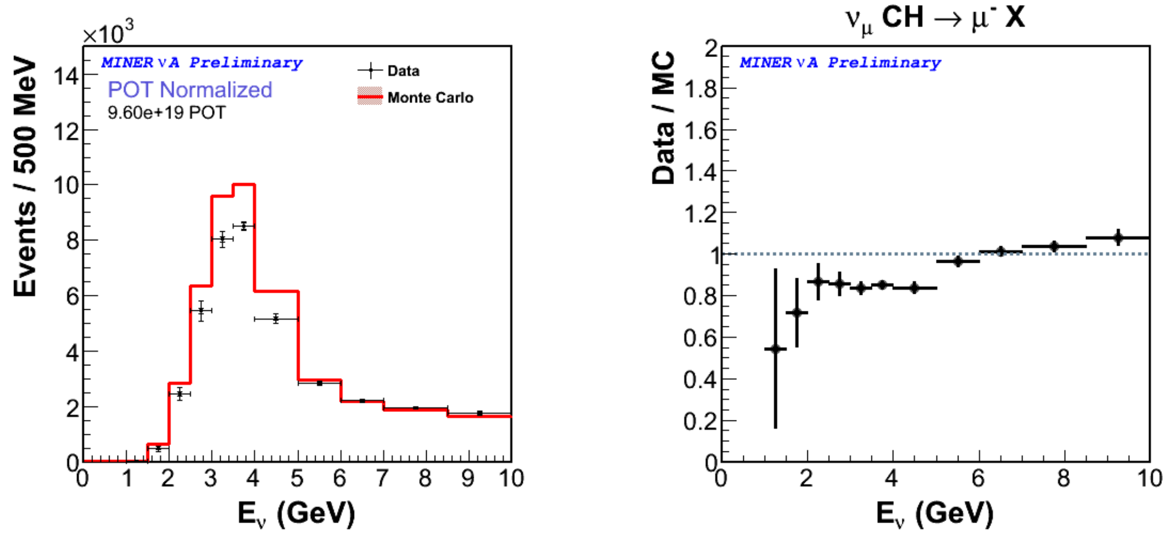

Figure 5.18: Left: Neutrino Energy background subtracted and unfolded distribution for charged current inclusive interactions. Right: Ratio $\frac{DATA}{MC}$.

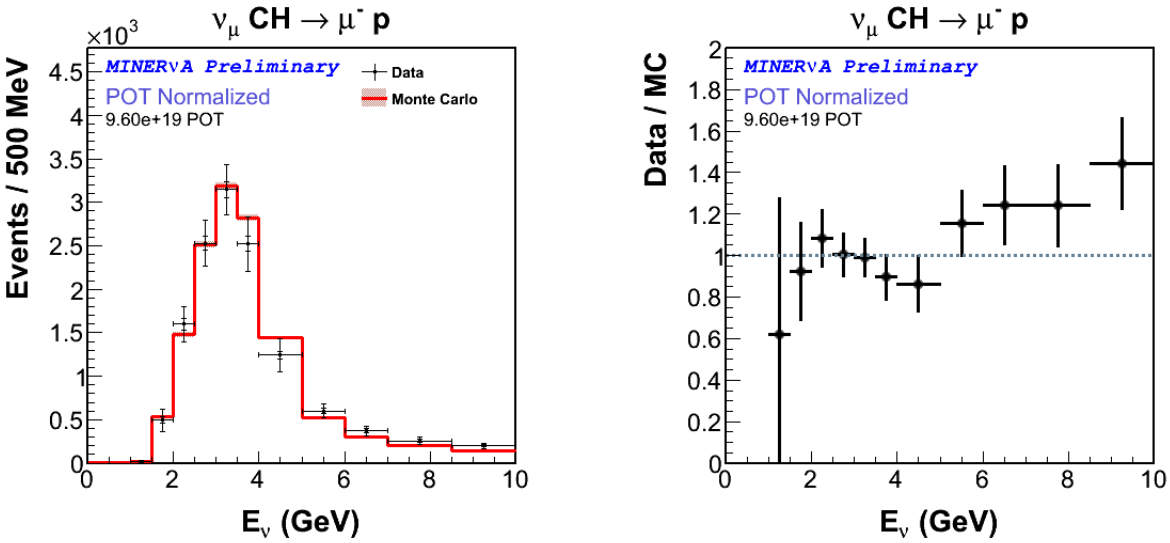

Figure 5.19: Left: Neutrino Energy background subtracted and unfolded distribution for charged current quasi-elastic interactions. Right: Ratio $\frac{DATA}{MC}$.

5.4.3 Efficiency Correction

Our signal cuts described in the section 5.2 are unable to reconstruct some fraction of our signal events. Some reason for loss of events are:

- **Reconstruction efficiency**: neutrino event signature is challenging and dificult to identify. Our selection cuts removes background events that usually contains some fraction of the signal.

- **Detector acceptance**: events that we are unable to detect or reconstruct because the limitations of our detector technology and geometry.

Having in mind the previous constraints, efficiency correction is the next step after the unfolding. The efficiency for true kinematics is measured in simulation as :

$$Efficiency(\epsilon_i) = \frac{N^{selected}_{channel,i}}{N^{Total}_{channel,i}} \tag{5.20}$$

where:

- $N^{total}_{channel,i}$ is the total number of MC signal events generated (where channel refer to CCINC or CCQE) in the i^{th} neutrino energy bin.

- $N^{selected}_{channel,i}$ is the number of MC signal events (CCINC or CCQE interactions) in the selected sample in the i^{th} neutrino energy bin.

Relation 5.20 uses the MC to calculate the geometrical acceptance. The efficiencies for CCINC and CCQE in function of the true E_ν has been calculated using equation 5.20 and are shown in the figures 5.20 and 5.21. One of the main reasons for the loss of events is the requirement that the muon must match a track in the MINOS near detector. Other reasons are the muon tracking efficiency in both detectors, the muon tracking matching efficiency between MINERνA and MINOS, and the efficiency on selecting signal events.
Table 5.1 summarizes the efficiency corrections applied in the analysis. The way that the tracking efficiency has been measured in MINERνA and MINOS is described in [114]. Finally, according to equation 5.13, we correct the unfolded distribution dividing it by the efficiency distributions obtained for each channel (see figures 5.20 and 5.21). The result, after efficiency correction for, both channels is shown in figures 5.22 and 5.23.

Dataset	Source of efficiency correction	Correction
3/22/10 to 6/12/10	MINERνA tracking	0.973 ± 0.002
	MINOS tracking ($p_\mu^{MINOS} > \frac{3GeV}{c}$)	0.982 ± 0.001
	MINOS tracking ($p_\mu^{MINOS} < \frac{3GeV}{c}$)	0.934 ± 0.002

Table 5.1: Muon tracking reconstruction efficiency corrections.

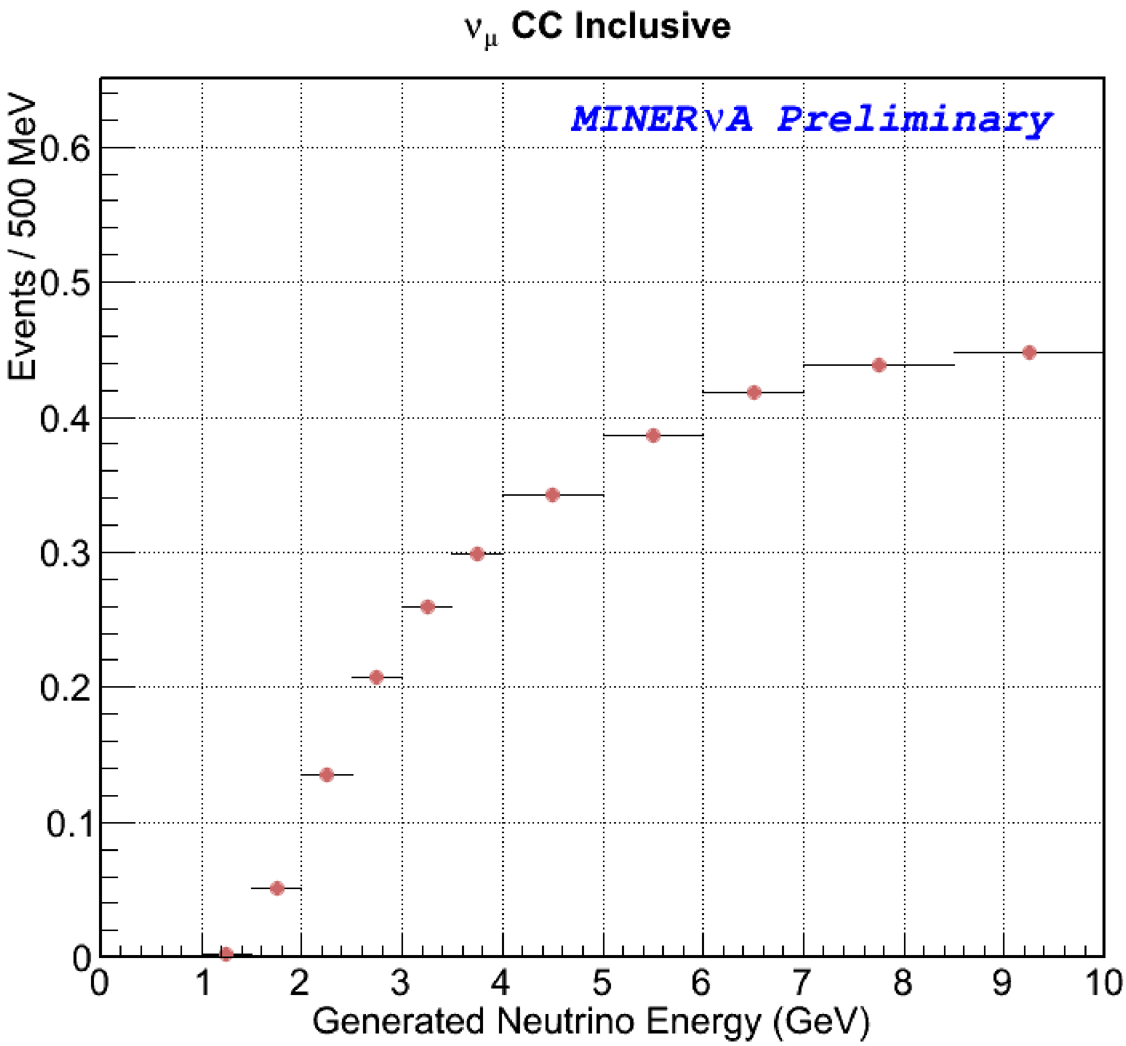

Figure 5.20: Efficiency in function of generated E_ν for CCINC analysis.

5.4.4 Flux and target normalization

The last step in calculating the cross section is divide the efficiency corrected distribution by the flux in each neutrino energy bin, the number of targets in CCINC and CCQE channel and the width of the E_ν (see equation 5.13). For CCINC the number of targets (nucleons) in the fiducial volume is:

$$T_{CCINC} = 3.294 \times 10^{30} \tag{5.21}$$

For CCQE the number of targets (neutrons) in the fiducial volume is:

$$T_{CCQE} = 1.534 \times 10^{30} \tag{5.22}$$

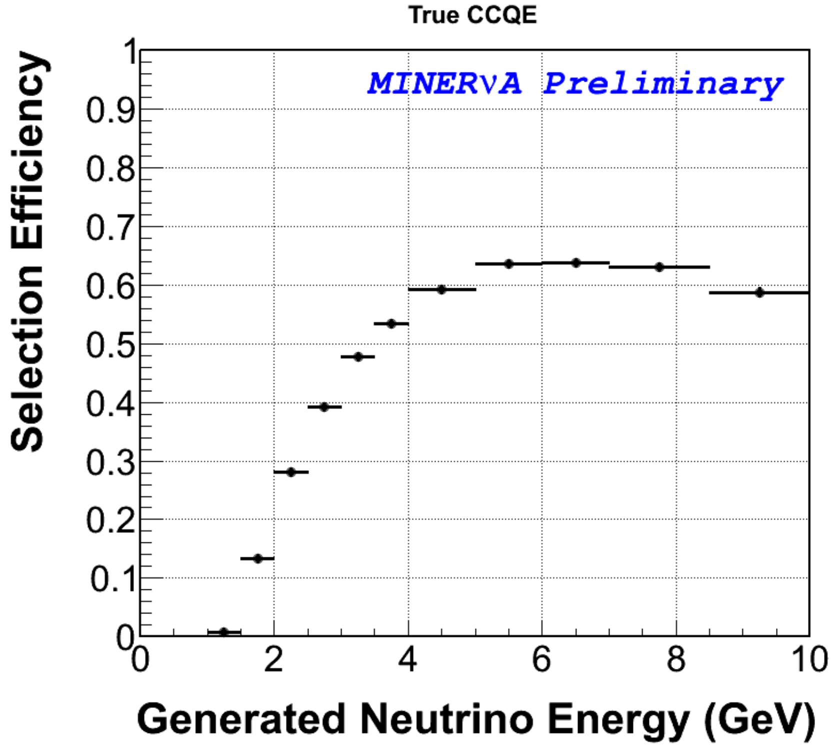

Figure 5.21: Efficiency in function of generated E_ν for CCQE analysis.

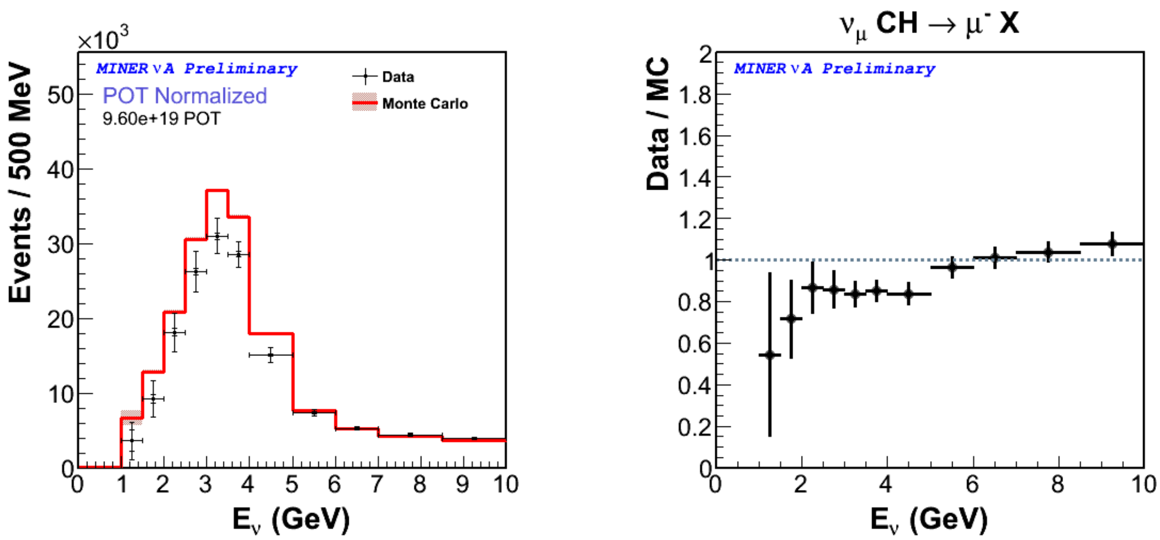

Figure 5.22: Left: Neutrino Energy background subtracted, unfolded and efficiency corrected distribution for charged current inclusive interactions. Right: Ratio $\frac{DATA}{MC}$.

The neutrino flux distribution per proton on target (POT) used for both channels (CCINC and CCQE) was calculated and described in section 4.6.1 and is presented in figure 5.24. Figures 5.25 and 5.26 show the total cross section result in function of neutrino energy for the CCINC

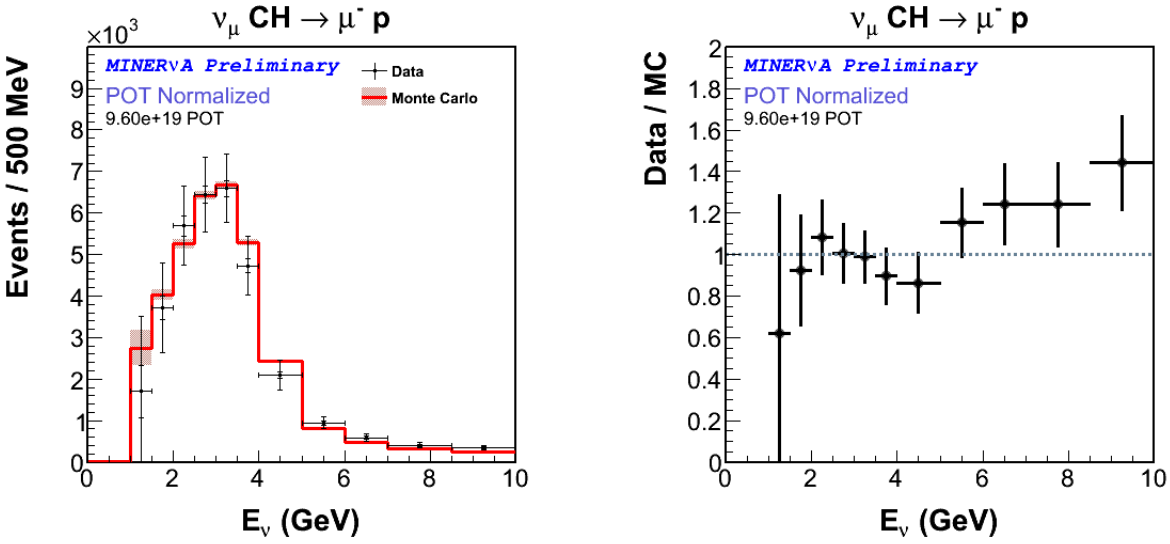

Figure 5.23: Left: Neutrino Energy background subtracted, unfolded and efficiency corrected distribution for charged current quasi-elastic interactions. Right: Ratio $\frac{DATA}{MC}$.

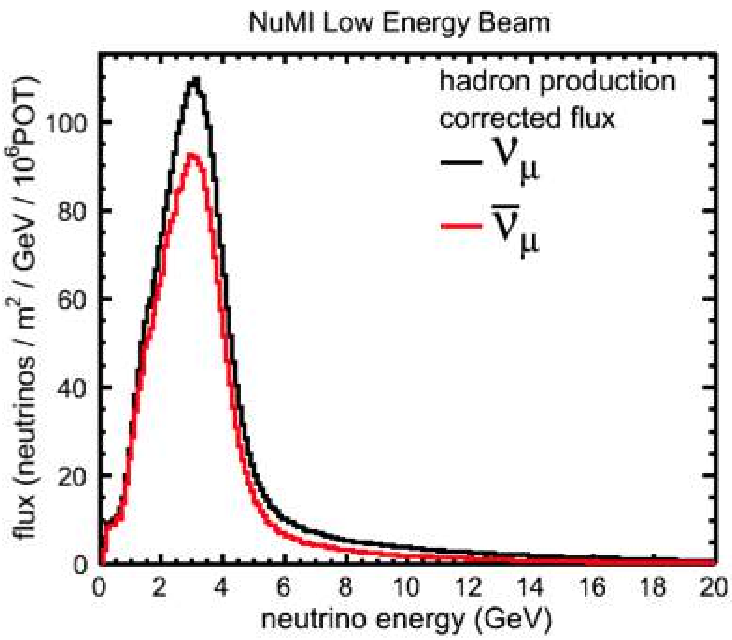

Figure 5.24: Neutrino Flux used in CCQE and CCINC analysis and obtained as was described in section 4.6.1.

(per nucleon) and the CCQE (per neutron).

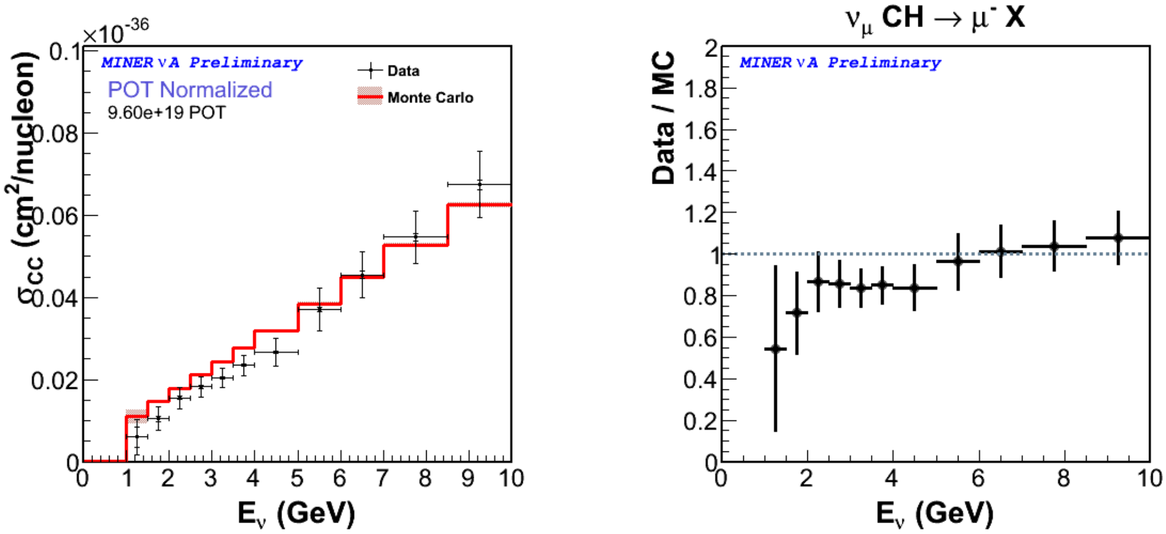

Figure 5.25: Left: Total cross section in function of E_ν for charged current inclusive interactions as defined in equation 5.13. The inner (outer) error bars correspond to the statistical (total) uncertainties. Right: Ratio $\frac{DATA}{MC}$.

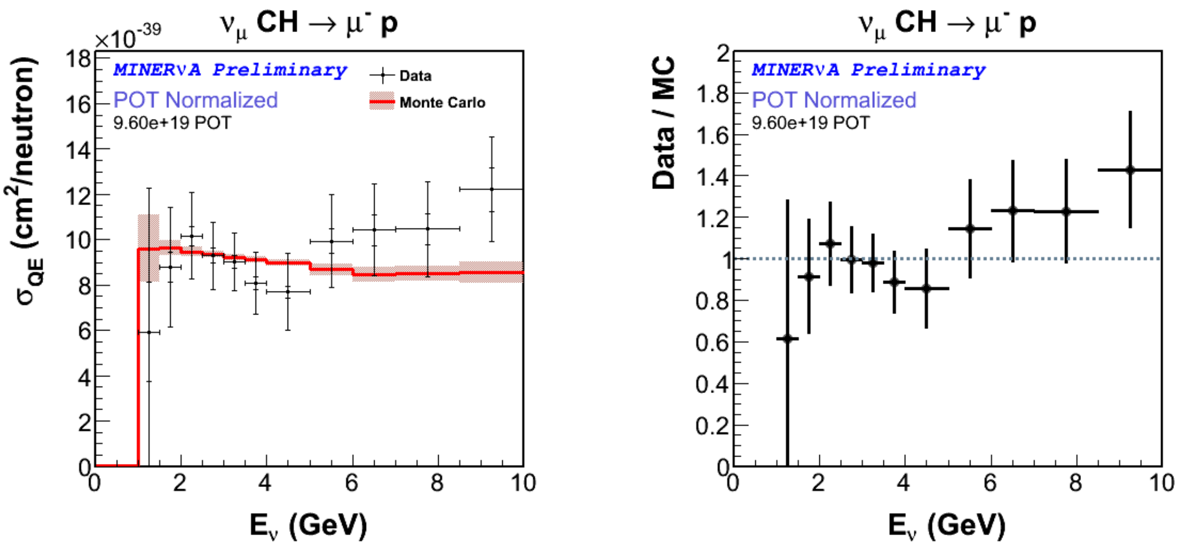

Figure 5.26: Left: Total cross section in function of E_ν for charged current quasi-elastic interactions as defined in equation 5.13 The inner (outer) error bars correspond to the statistical (total) uncertainties. Right: Ratio $\frac{DATA}{MC}$.

5.5 Systematic Uncertainties

In the previous sections we say that the results of the CCINC and CCQE analysis depend on our detector simulation, flux, reconstruction parameters and cross section models. These simulations depend on parameters that are known and have uncertainties associated with them.

These uncertainties are translated into systematic uncertainties for both cross section analysis. We use the **Many Universes** method [115] to calculate these systematic uncertainties. For a given source of systematics the correspondent parameters are shifted within their measured $\pm 1\ \sigma$ uncertainties and the cross sections are re-extracted by the complete analysis procedure. Each variation is commonly referred to as an **universe**, which represents the deviation from the measured nominal value (see equation 5.23).

$$\sigma(E_\nu) = \frac{\sum_j U_{ij}^{uni}(N_j^{data} - N_{j,uni}^{bg})}{\epsilon_{uni,i} T \phi_{\nu,uni}} \tag{5.23}$$

We use 100 **universes** to reduce the statistical uncertainties on the systematic uncertainties. From the equation 5.23 we see that the efficiency in the event selection, the flux and the migration matrix are recalculated for each universe. This was implemented inside all the CCINC analysis package in a user friendly way, letting to the future user of the CCINC package just to declare the number of **universes** that should be used. The covariance matrix and the errors are calculated as:

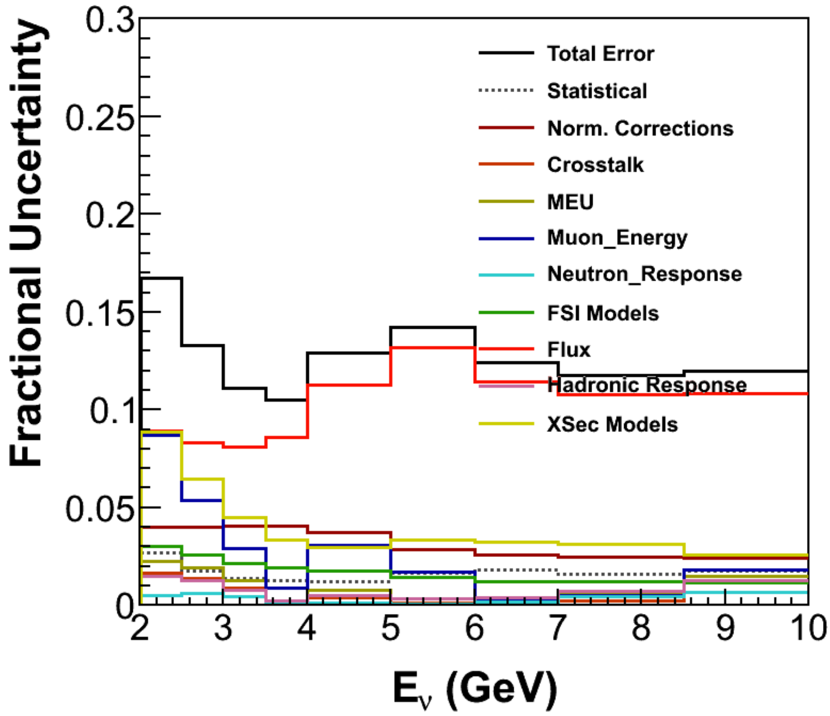

Figure 5.27: Fractional uncertainties for the total charged current inclusive cross section in function of reconstructed E_ν.

1. **Covariance Matrix**:

$$cov(j,k) = \frac{1}{N}\sum_i (N_{i,j} - N_j^{CV})(N_{i,k} - N_k^{CV}) \tag{5.24}$$

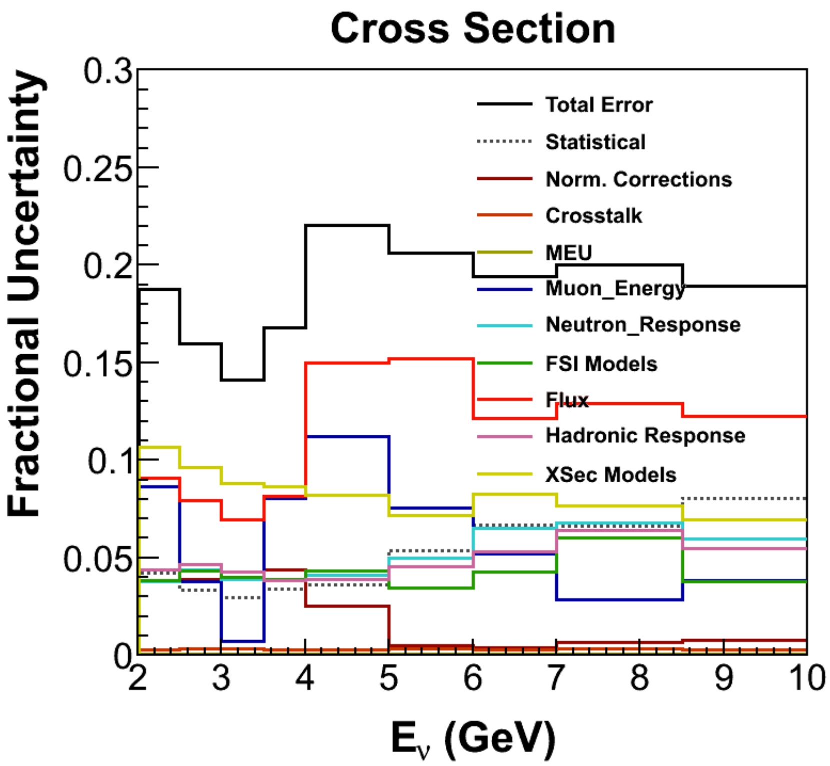

Figure 5.28: Fractional uncertainties for the total charged current quasi-elastic cross section in function of reconstructed E_ν.

2. **Error**:

$$\sigma_j = \sqrt{\frac{1}{N}\sum_i (N_{i,j} - N_j^{CV})^2} \tag{5.25}$$

Where:

- $N_{i,j}$ is the number of events in the bin j in the i^{th} universe.
- CV stands for the central value (nominal value).
- N is the number of universes, with N = 100 for the CCINC and CCQE analysis.

Figures 5.27 and 5.28 present the error summary for all the systematics uncertainties that were taking into account in the total cross section measurements. The systematic uncertainties are described below.

5.5.1 Flux

The biggest contribution on systematic uncertainties for neutrino experiments comes from the Flux. One of the main motivations to make the ratio analysis between the CCINC and CCQE is to reduce the uncertainties coming from the flux simulation. For the analysis presented in this dissertation the uncertainites due to the neutrino flux are divided in three types:

Beam Focusing

These uncertainties come from the proton beam and focusing system of the NuMI beamline. They were evaluated for the MINOS experiment by considering performance of the beamline monitoring equipment and the precision in the construction of different components belonging to the beamline. They are estimated to be small but the biggest impact is at the focusing peak where is ≈ 8 % as can be seen in figure 5.29.

NA49 and MIPP constrained

If the simulation of a proton carbon ($p + C$) interaction is constrained by external data, the uncertainty in the interaction is the uncertainty on the constraining cross section measurement. For $p + C$ interaction in the NuMI target at 120 GeV/c there is new data coming from the MIPP collaboration and that was briefly described (see section 4.6.1 and figure 4.12). This data has recently come to the public, and will have to be implemented inside the MINERνA framework. The dataset that constrains hadron production in the NuMI beam is coming from NA49, that has measured $p + C$ interactions at 158 GeV/c [116].

Other hadron production

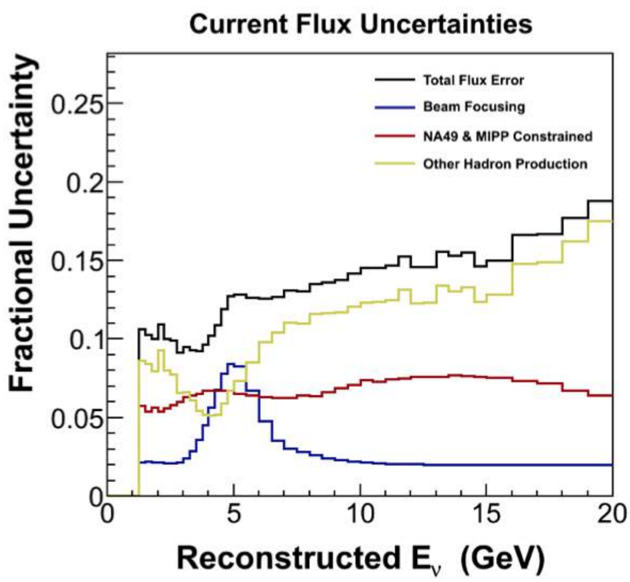

Figure 5.29: Flux uncertainties for charged current inclusive events in the tracker region in function of reconstructed E_ν.

The uncertainties on the cross section of $p+C$ interactions that are not constrained by data are evaluated using comparisons among simulation models (see figure 4.10). The maximum spread among the models shown in figure 4.10 is the error on the flux contributed by $p + C$

interactions that were not constrained by data.
From the charged current inclusive analysis events discussed in sections 5.2 and 5.3, we have obtained the uncertainties in the flux in function of reconstructed neutrino energy shown in figure 5.29 .

5.5.2 Muon Energy Reconstruction

The muon energy reconstruction is the main component in the signature of the CCINC and CCQE interactions presented in this thesis; therefore, it is important to have the total uncertainty on the muon energy scale. The total uncertainty in the muon energy reconstruction arises from three effects [117]:

1. **MINOS Curvature Measurement**: when the muon is reconstructed in MINOS near detector by curvature the uncertainty for muons with momentum lower than 1 GeV/c is 2.5% and for muons with momentum higher than 1 GeV/C is 0.6%.

2. **MINOS Range Measurement**: When the muon is reconstructed in MINOS by range the uncertainty has a value of 2%. This value on uncertaintie is due to simplifications in the reconstruction's implementations of the geometry and errors in the dE/dx model.

3. **Energy loss in MINERνA**: there are two independent components to calculate the uncertainties due to energy loss in MINERνA. First, the material assay add 11 MeV to the error on muon events in scintillator. The second one is the dE/dx model, adding 30 MeV to the error on muon events in scintillator. These errors depend on how much material the muon traverses in MINERνA detector, so there will be larger error assigned to events in the upstream nuclear target region.

To obtain the total uncertainty **Muon Energy** the effects listed above are added in quadrature. Each of the 100 universes used to create the systematic error band associated to the muon energy reconstruction is filled with simulated interactions where the muon energy is shifted by **Muon Energy** $\times$ **J** (J is a random number sampled from a normalized gaussian distribution).

5.5.3 Unfolding

The error on iterative Bayesian unfolding after iteration i is equal to the difference in the cross section distribution between iteration i and $i+1$. The evaluation of this error is calculated using equation 5.26 and is presented in the table 5.2.

$$\delta\sigma_{channel}(E_\nu) = (\sigma_{channel}(5it) - \sigma_{channel}(4it)) \tag{5.26}$$

where:

$\sigma_{channel}(nit)$ is the total cross section for CCINC or CCQE channel using the bayesian unfolding with n iterations. For the ratio analysis presented in this dissertation, the evaluation shows

Bin (GeV)	$\delta\sigma(E_\nu)$ CCINC	$\delta\sigma(E_\nu)$ CCQE
2 - 2.5	0.004	0.006
2.5 - 3	0.002	-0.042
3 - 3.5	-0.003	0.043
3.5 - 4	0.007	-0.015
4 - 5	-0.013	-0.047
5 - 6	0.021	0.012
6 - 7	0.006	0.001
7 - 8.5	-0.006	-0.009
8.5 - 10	-0.005	0.012
Average	0.008	0.020

Table 5.2: Unfolding uncertainties for the CCINC and CCQE channels for each neutrino energy bin.

that the error in the unfolding in the neutrino energy is negligible.

5.5.4 Recoil Reconstruction

Reconstruction of the recoil energy has two sources of systematic uncertainties:

Detector response

The detector energy response to hadronic particles is estimated using a MC prediction of the composition of the hits identified as recoil system. The uncertainties in the detector response to each source of visible energy are summarized in table 5.3. For a extended description on how each of them is calculated see reference [89]. Figure 5.27 shows the the total cross section systematic summary for the CCINC analysis. The detector response systematics has been grouped in three different systematic error bars:

1. **Neutron Response**: Composed by the 3 components of the neutron energy response (LE,ME,and HE represented by cyan error bar).

2. **Hadron Response**: All the other detector energy responses that are not associated with the neutron and crosstalk (pink error bar).

Energy Source	Uncertainty %
Proton	3.5
LE Neutron(KE $<$ 50 MeV)	25
ME Neutron (50$<$KE$<$150MeV)	10
HE Neutron (KE $>$ 150 MeV)	20
Muon	2.4
γ,π_0,$e^{\pm}$	3
$\pi^{\pm}$, Kaon	5
CrossTalk	20
Other	20

Table 5.3: Uncertainties on detector response.

3. **Crosstalk**: The uncertainty on the detector response to crosstalk is dominated by optical rather than electrical crosstalk, because more than 90% of visible energy coming from crosstalk is due the optical variety. Optical crosstalk was measured in two different ways: first, using a test stand with light injection; second, in-situ by looking at visible energy near rock muon tracks. Both methods disagree at the level of 20% which is the error reported on table 5.3 (orange error bar).

5.5.5 Final State Interaction Models (FSI Models)

FSI models describe what occurs to a particle generated by the neutrino interaction before it exits the nuclear enviroment. Most of these uncertainties are calculated reweighting the montecarlo events. Reweightable FSI model parameters are shifted following their uncertainty, then the probability of the FSI scattering process is recalculated. The cross sections for CCINC and CCQE analysis are repeated for each $\pm 1\sigma$ excursions of model parameters. The FSI reweightable model parameters used in CCINC and CCQE are summarized in table 5.4. However, there are FSI model parameters that cannot be handled through event reweighting, then it is necessary to evaluate this non-reweightble model parameters using statistically independent MC samples. The non-reweightable parameters used in CCINC and CCQE analysis are:

1. **Effective Nuclear Radius**: This parameter is related to the size of the nucleus for low energy hadrons. The uncertainty for scintillator events with hadronic energy (E_{HAD}) less than 2 GeV is 2%, and for E_{HAD} greater than 2 GeV is 0.25%.

2. **Formation Time**: Time necessary for a quark to undergo hadronization. For scintillator events with E_{HAD} less than 2 GeV the uncertainty is 1.5%, for E_{HAD} greater than 2 GeV

Model Parameter	$\pm 1\sigma$ (%)
Pion mean free path	20
Pion charge exchange probability	50
Pion elastic reaction probability	10
Pion inelastic reaction probability	40
Pion absorption probability	20
π production probability	20
Nucleon mean free path	20
Nucleon charge exchange probability	50
Nucleon elastic reaction probability	30
Nucleon inelastic reaction probability	40
Nucleon absorption probability	20
Nucleon π production probability	20
AGKY model x_f distribution	20
Pion angular distribution	isotropic $\rightarrow$ Rein-Sehgal
Resonance branching ratios decay to photon	50

Table 5.4: Uncertainties in FSI models in GENIE.

the uncertainty is negligible.

3. **Hadronization Model**: The AKGY model uses a phase space reweighting scheme to simulate hadronization of final state particles. This reweighting suppresses the transverse momentum of decayed meson with increasing p_t^2. The uncertainties on this model for scintillator events is 1% for events with E_{HAD} lower than 10 GeV. For bigger energies the error is 1.5%.

4. **Birk's Parameter**: Birk's empirical law for the expected light yield for energy deposited in scintillator is scaled by:

$$(1 + k_B \frac{dE}{dx}) \tag{5.27}$$

where k_B is Birk's parameter due to saturation effects on scintillator. We have studied the saturation phenomena and k_B using the MINERνA test beam detector. From the study, we found an uncertainty of 30 % on the nominal value of k_B = 0.133mm/MeV used in the simualtion [117]. For the CCINC event sample the error is 5% for events with E_{HAD} lower than 1 GeV, for bigger energies the error is 1%.

Finally, each parameter (reweightable and non-reweightable) is treated independently and are added in quadrature to obtain the total **FSI Models** uncertainty systematic error bar (green) presented in the figure 5.27.

5.5.6 Cross section Models (XSec Models)

The use of GENIE neutrino event generator introduces a cross section model dependence. The uncertainties that come from cross section models are evaluated using GENIE event reweighting infrastructure. The cross section model parameters are varied by $\pm 1\ \sigma$ and the cross section for a generated event is recalculated. The parameters used in CCINC and CCQE analysis are summarized in table 5.5. All parameters are treated independently and are added in quadrature

Model Parameter	Process	1σ (%)
Axial Mass for NC elastic	QE	$\pm$ 25
Strange axial form factor η for NC elastic	QE	$\pm$ 30
Axial mass for CCQE	QE	-15, +25
Normalization of CCQE	QE	-15, +20
Pauli suppresion in CCQE at low Q^2	QE	$\pm$ 35
CCQE vector form factor model	QE	BBA05$\rightarrow$Dipole
Normalization of CC resonance production	RES	$\pm$20
Normalization of NC resonance production	RES	$\pm$ 20
Axial mass for CC resonance production	RES	$\pm$ 20
Vector mass for CC resonance production	RES	$\pm$ 10
Non-resonance CC1π production for νp	DIS	$\pm$ 50
Non-resonance CC2π production for νp	DIS	$\pm$ 50
Non-resonance CC1π production for νn	DIS	$\pm$ 50
Non-resonance CC2π production for νn	DIS	$\pm$ 50
A_{HT} parameter in Bodek-Yang model	DIS	$\pm$ 25
B_{HT} parameter in Bodek-Yang model	DIS	$\pm$ 25
C_{v1u} parameter in Bodek-Yang model	DIS	$\pm$ 30
C_{v2u} parameter in Bodek-Yang model	DIS	$\pm$ 40

Table 5.5: Uncertainties on cross section models [109].

to obtain the total **XSec Models** uncertainty systematic error bar (yellow) presented in the figure 5.27.

5.5.7 Reconstruction efficiency corrections (Norm. Corrections)

There are two sources of corrections that we must take into account for observed data and MC differences in reconstruction efficiencies:

1. MINERνA tracking efficiency: the muon tracking efficiency in MINERνA is estimated by

pointing muon tracks reconstructed in MINOS back to MINERνA and checking for the expected matched track.

2. MINOS tracking efficiency: this is estimated measuring momentum dependence of the efficiency for matching muons in MINERνA to a track in MINOS. The approach is made to separate low and high momentum muons based on the amount of transversal displacement of the reconstructed muon track in the downstream MINERνA calorimeter [114].

The values used for the MINOS and MINERνA tracking efficiency are included in both CCINC and CCQE cross section analysis machinery and presented in table 5.1.

5.5.8 Detector Mass Scale

The uncertainty on the mass of the detector components translates into an error in the number of target nucleons. The uceratinty on the mass and the chemical composition of scintillator is 1.4 % [117]. This uncertainty is added in quadrature with the reconstruction efficiency corrections (see section 5.5.6) previously discussed and is presented in the error summary distribution 5.27 like the systematic error bar (coffee) called $Norm.Corrections$.

5.5.9 Absolute Eneryg Scale (MEU)

The absolute energy scale calibration affects the dE/dX measurement. An uncertainty of 2.4 % is applied to account for this.

Chapter 6

Measurement of ratio $\frac{\sigma_{ccqe}(E_\nu)}{\sigma_{ccinc}(E_\nu)}$ in neutrino energy range 2 - 10 GeV

6.1 Introduction

This chapter presents the first measurement of the muon neutrino charged current quasi-elastic to charged current inclusive cross section ratio on a hydrocarbon target at neutrino energies in the 2-10 GeV range. Chapter 5 describes the calculation of the charged current inclusive and charged current quasi-elastic total cross section in function of neutrino energy.

6.2 Ratio Calculation

To obtain the ratio we use as input the total cross section calculated in the chapter 5 for CCINC and CCQE scattering channels (see figures 5.25 and 5.26):

$$Ratio_{\frac{ccqe}{ccinc},i} = \frac{\sigma_{ccqe,i}(E_\nu)}{\sigma_{ccinc,i}(E_\nu)} \tag{6.1}$$

where 6.1 $\sigma_{ccinc,i}(E_\nu)$ is the value of the cross section for CCINC in the i^{th} neutrino energy bin. The result for the ratio is presented in figure 6.1. Having in mind that each cross section has implemented the many universes method described in section 5.5 we need to be careful and make the ratio universe by universe for all the systematic uncertainties that compose the measurement of each cross section. This can be expresed as:

$$Ratio_{\frac{ccqe}{ccinc},uni} = \frac{\sigma_{ccqe,uni}(E_\nu)}{\sigma_{ccinc,uni}(E_\nu)} \tag{6.2}$$

where $\sigma_{channel,uni}(E_\nu)$ represent, the measurement of the cross section for the CCINC or CCQE channels in the i^{th} universe.

6.2.1 Results

Figure 6.1 presents the ratio obtained using the equation 6.1 and figure 6.2 presents the systematics summary using 6.2. Figure 6.1 shows that the CCQE fraction of the CCINC muon

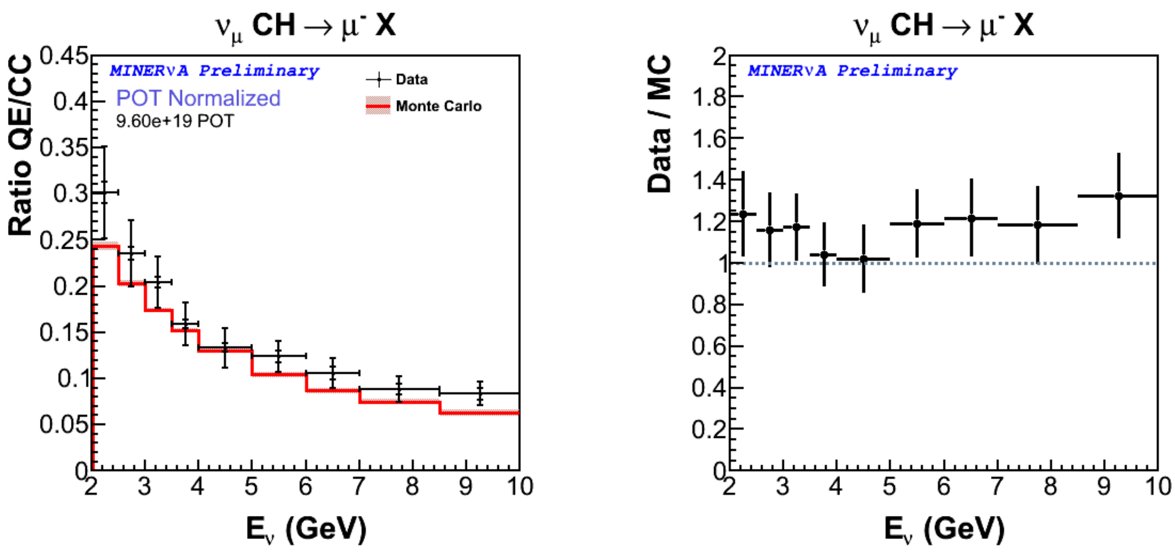

Figure 6.1: Left: Total cross section ratio $\frac{\sigma_{ccqe}}{\sigma_{ccinc}}$ in function of neutrino energy Right: $\frac{Data}{MC}$ comparison.

neutrino interactions is bigger in the energy range of 2-5 GeV. Increasing the energy implies the reduction of CCQE and leaves the assumption that DIS and RES channels are the main components of the CCINC neutrino interactions, as was described in chapter 2 (see section DIS and RES). Besides, the agreement betweend MC and data at low neutrino energies suggests the success of the current models implemented inside GENIE but, for energies higher than 5 GeV, GENIE does not make the best description of our measurement. We neede to compare the result presented in this thesis with other modern neutrino event generators as NuWro [118]. From the figure 6.2 can also be seen the reduction in the main source of systematic uncertainty related to the flux components going in average over all the neutrino energy bins from ≈12% in the CCINC or CCQE cross section measurements (see figures 5.25 and 5.26 red error bar) previously presented to ≈4% using the ratio calculation presented in this dissertation. Furthermore, the biggest component of systematic uncertainty is the one related to the neutrino interaction models **XSec Models** with an average ≈12% in the low neutrino energy region (2-5 GeV).

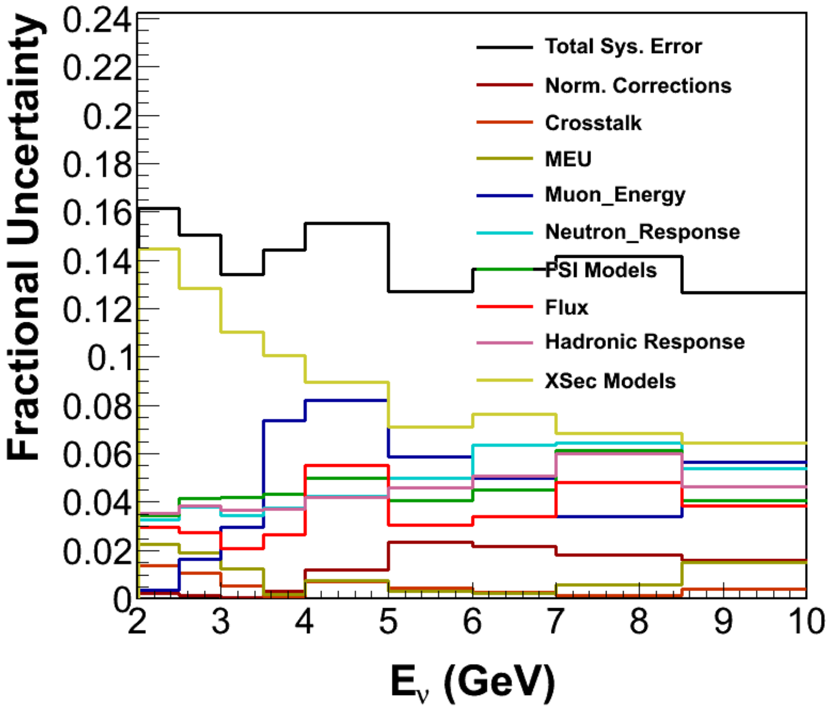

Figure 6.2: Fractional Uncertainties in the total cross section ratio $\frac{\sigma_{ccqe}}{\sigma_{ccinc}}$ in function of neutrino energy.

6.3 Angular acceptance cut

In order to reduce the systematics uncertainties associated to events that were not reconstructed due to MINERνA acceptance limitations (see figure 5.4 and 5.3), an angular acceptance cut has been made when calculating the efficiency correction for both CCINC and CCQE neutrino scattering channels. Figure 6.3 represents the phase space in function of muon energy and muon angle for the MC generated charged current inclusive interactions in tracker region. It can be seen that a selection of a muon angular cut of 20^0 is enough to cover the big majority of the events that we want to be analyzed. The efficiency has been evaluated as:

$$\epsilon_{\theta_\mu<20^0,i} = \frac{N_{selected,i}}{N_{total<20^0,i}} \tag{6.3}$$

where the only change is in the denominator:

$$N_{total<20^0} \tag{6.4}$$

compared with the previous definition discussed in section 5.4.3 , with the purpose of including our previously selected angular cut. Equation 6.4 represents the total number of MC signal events generated with a muon angle cut $< 20^0$. Figures 6.4 and 6.5 present the efficiency

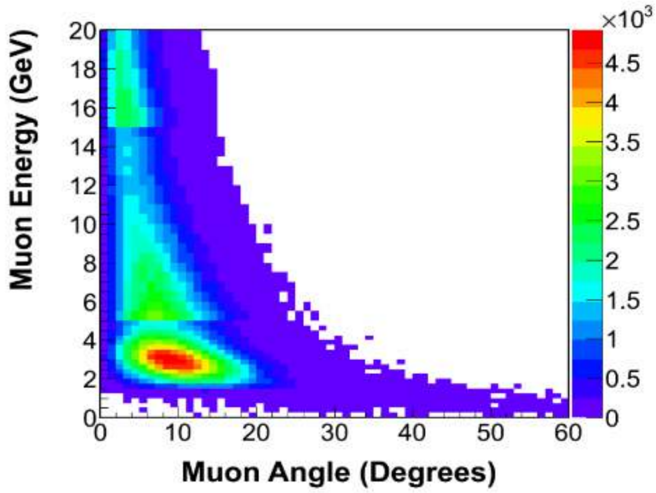

Figure 6.3: Muon Angle vs Muon Energy for MC CCINC generated events in the tracker region.

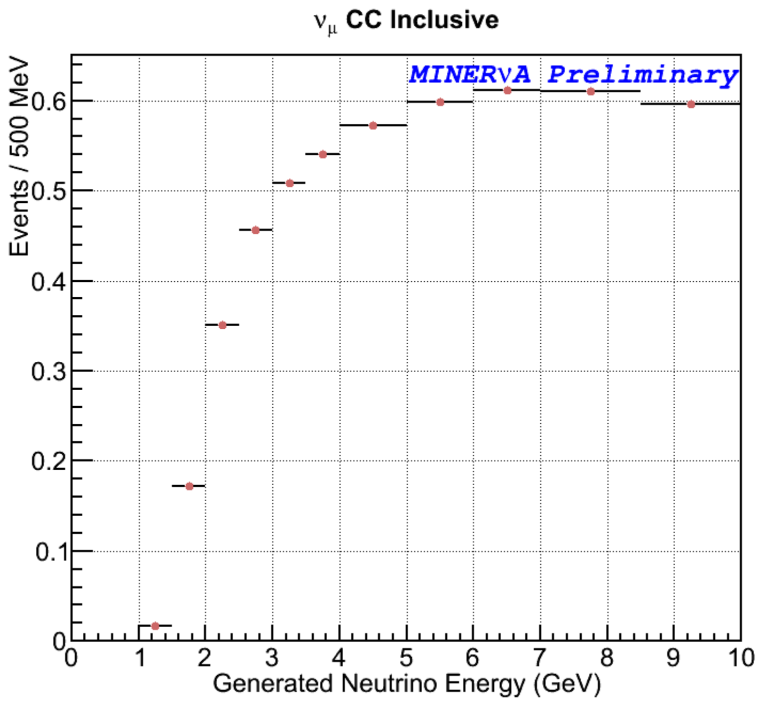

Figure 6.4: Selection efficiency for CCINC interactions in function of true E_ν for $\theta_\mu < 20^0$.

distributions in function of true neutrino energy for the CCINC and CCQE channels for $\theta_\mu < 20^0$.

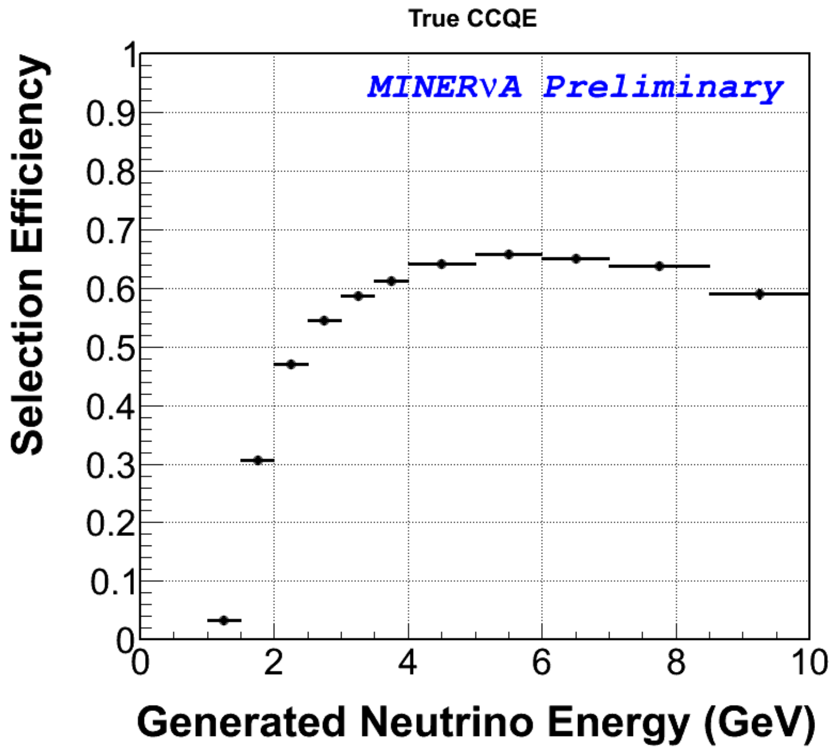

Figure 6.5: Selection efficiency for CCQE interactions in function of true E_ν for $\theta_\mu < 20^0$.

6.3.1 Results obtained with $\theta_\mu < 20^0$

We re-calculate the cross section for both CCINC (see figures 6.6 and 6.8) and CCQE (6.7 and 6.9) following the procedure described in chapter 5, with our efficiency corrections including the 20 degrees angular cut,

$$\sigma_{channel<20^0,i} = \frac{\sum_j U_{ij}(N_j^{data} - N_j^{bg})}{\phi_i T \epsilon_{i,\theta_\mu<20^0}} \tag{6.5}$$

where $\epsilon_{i,\theta_\mu<20^0}$ is calculated using the equation 6.3. Finally, we obtain the ratio between both cross sections as:

$$Ratio_{\frac{ccqe<20^0}{ccinc<20^0},i} = \frac{\sigma_{ccqe<20^0,i}(E_\nu)}{\sigma_{ccinc<20^0,i}(E_\nu)} \tag{6.6}$$

Figure 6.10 presentes the ratio distribution for data and MC using the $\theta_\mu < 20^0$ cut. Figure 6.11 clearly shows the reduction in the systematic uncertainty related to the neutrino interaction models **XSec Models** as expected. Using the 20^0 cut in the muon angle and comparing with the result presented in the previous section 6.2 without the angular cut, a decrease of the **XSec Models** uncertainty is present in the low energy region (2-5 GeV) from ≈12% to ≈5%. This is mainly due to the fact that we want avoid correcting for events that can not be reconstructed due to our detector acceptance.

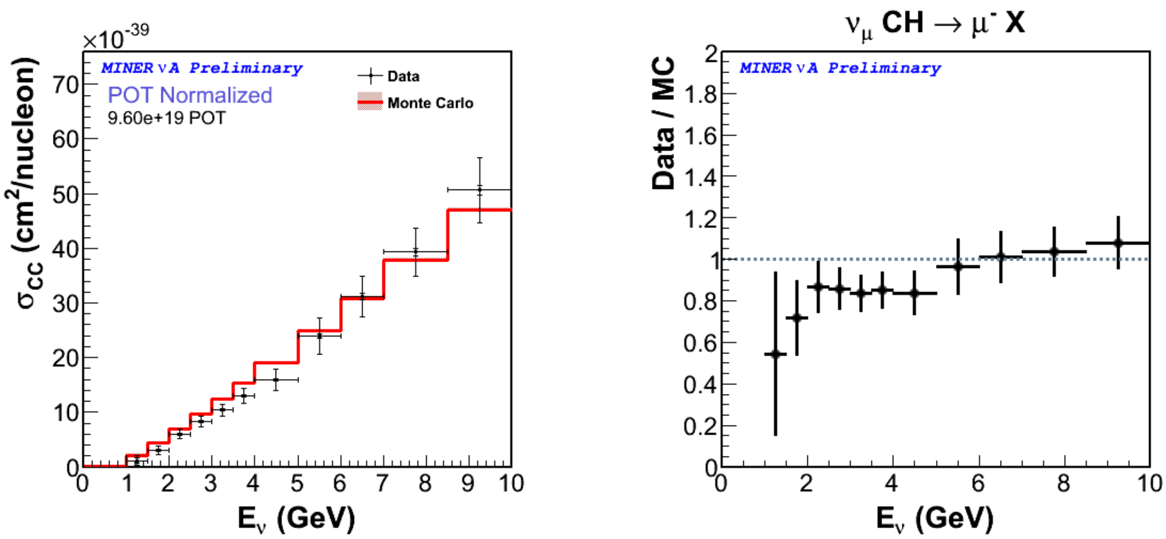

Figure 6.6: Left: Total cross section in function of E_ν for charged current inclusive interactions as defined in equation 6.5 with $\theta_\mu < 20^0$. Right: Ratio $\frac{DATA}{MC}$.

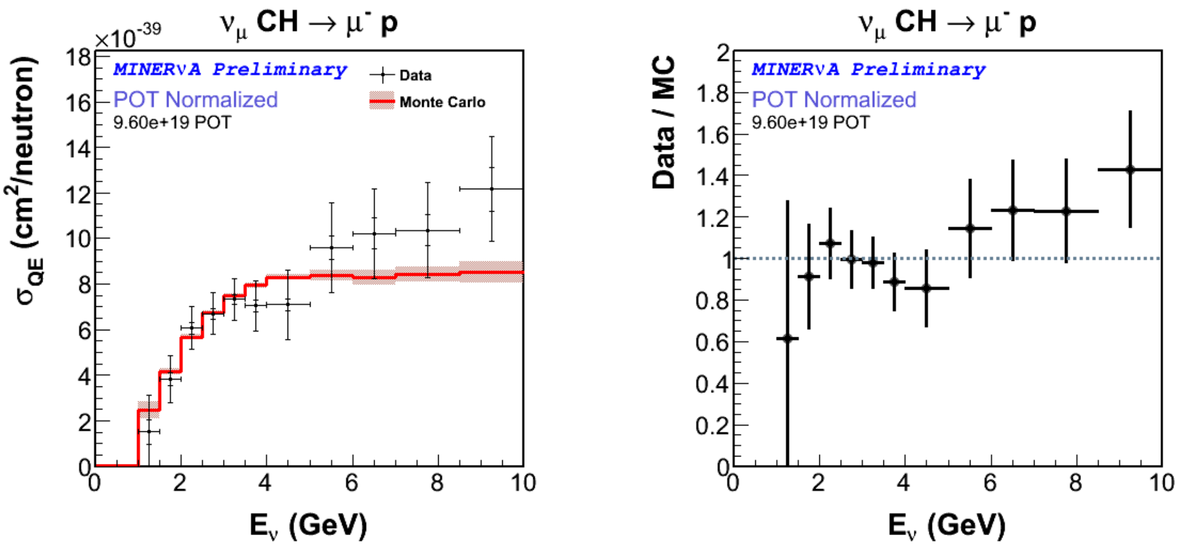

Figure 6.7: Left: Total cross section in function of E_ν for charged current quasi-elastic interactions as defined in equation 6.5 with $\theta_\mu < 20^0$. Right: Ratio $\frac{DATA}{MC}$.

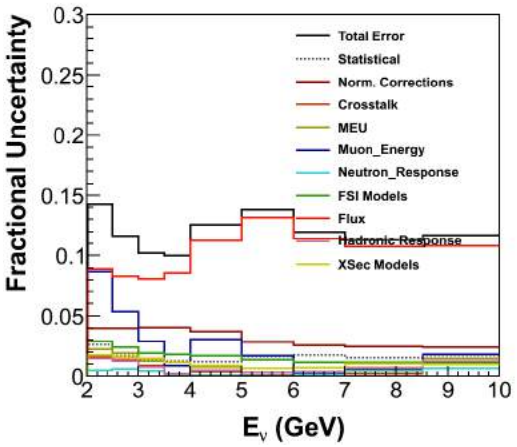

Figure 6.8: Fractional uncertainties for total CCINC cross section in function of reconstructed E_ν with $\theta_\mu < 20^0$.

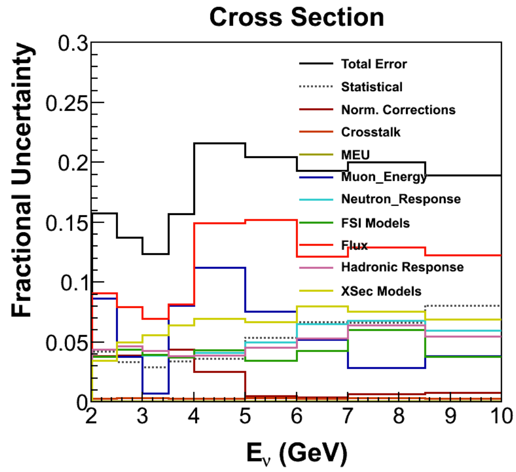

Figure 6.9: Fractional uncertainties for the total CCQE cross section in function of reconstructed E_ν with $\theta_\mu < 20^0$.

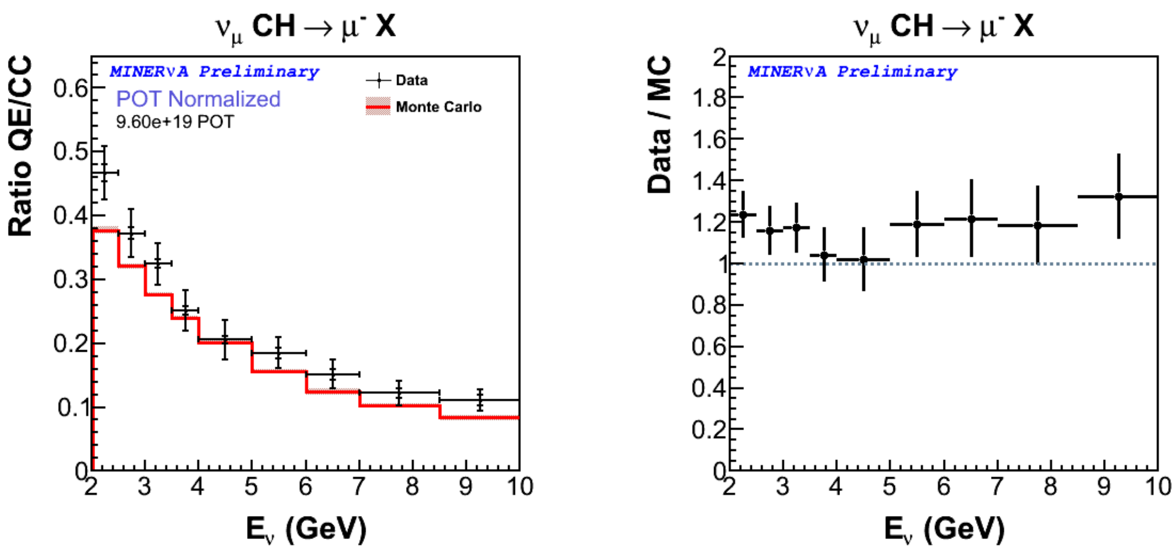

Figure 6.10: Left: Total cross section ratio $\frac{\sigma_{ccqe}}{\sigma_{ccinc}}$ in function of neutrino energy for $\theta_\mu < 20^0$ .Right: $\frac{Data}{MC}$ comparison.

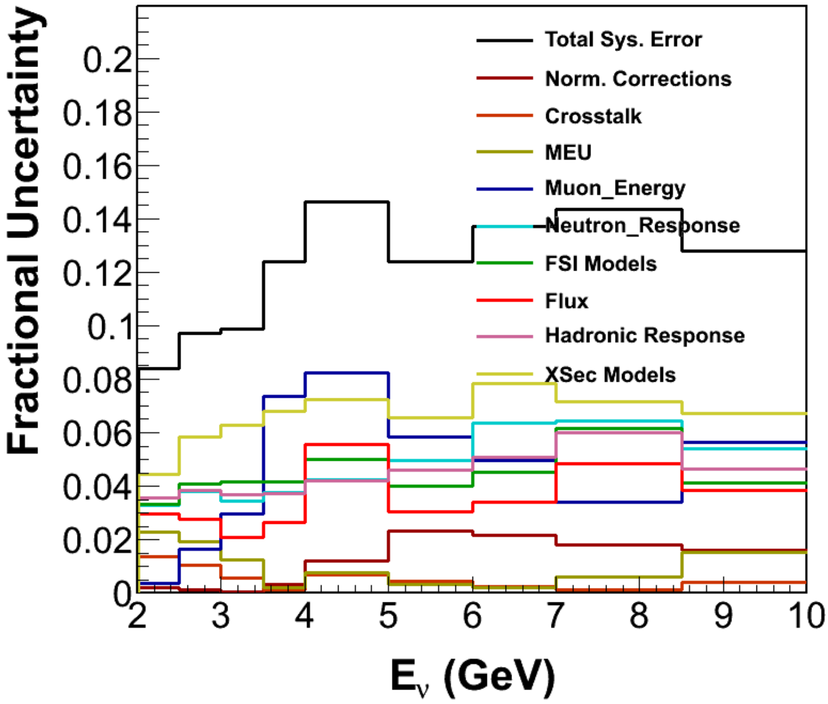

Figure 6.11: Fractional Uncertainties in the total cross section ratio $\frac{\sigma_{ccqe}}{\sigma_{ccinc}}$ in function of neutrino energy for $\theta_\mu < 20^0$.

Chapter 7

Conclusions

In this thesis we present the first measurement of muon neutrino charged current quasi-elastic to charged current inclusive cross section ratio on a hydrocarbon target at neutrino energies 2-10 GeV. The data used in this analysis represents $\frac{1}{4}$ of the total data collected by MINERνA in the NuMI beam low energy configuration. The ratio measurement presented here shows that the CCQE fraction of the CCINC muon neutrino interactions is bigger in the low energy range (2-5 GeV) . The reduction in the fraction of CCQE at higher energies (5-10) suggests the presence of DIS and RES neutrino interactions that can be the main components of the CCINC interactions at these energies. Furthermore, for low energies our ratio shows a good agreement between data and MC. In the near future we must include several models comparisons with other modern neutrino event generators as [118]. Although the systematic uncertainties related to the flux do not cancel completely, the ratio analysis presented in this thesis shows a significant reduction to a level of an average of $\approx$ 4% in all neutrino energy bins. We also present a preliminar study with a muon angular cut necessary to avoid correcting for events that have not been reconstructed due to our detector acceptance. This angular cut produces a significant reduction in the systematic uncertainty related to the modeling of neutrino interactions inside the used neutrino event generator (GENIE 2.6.2).

This dissertation presents the ratio for CCINC and CCQE cross section in function of neutrino energy. The current machinery developed for this thesis makes it possible to calculate the ratio in function of other kinematic variables as Q^2, Bjorken x, and also in extended neutrino energy ranges taking advantage of the current data that MINERνA has been taking since september 2013 with the NuMI beam medium energy configuration. Using the current machinery and the preliminary results presented in chapter 5 (see figure 5.26) MINERνA will be able to elucidate the discrepancies (see figure 7.1) in the cross section measurements reported by NOMAD and MiniBooNE [63].

All the infrastructure developed for the calculation of charged current inclusive and the recent

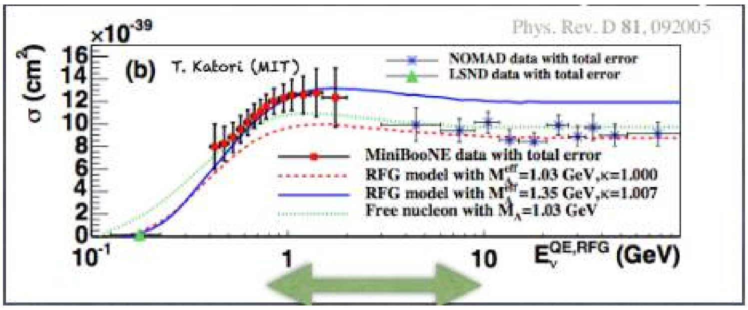

Figure 7.1: Flux-unfolded MiniBooNE muon neutrino CCQE cross section in function of neutrino energy compared with results from LSND and NOMAD experiments.

improvements in the charged current quasi-elastic cross section measurements presented in this thesis will be used by MINERνA for upcoming papers, for both neutrinos and antineutrino data. Papers that could be produced using the current charged current inclusive machinery presented in this thesis are:

1. Measurement of the structure functions on an hydrocarbon target.
2. Measurement of the total neutrino and antineutrino charged current inclusive cross sections on an hydrocarbon target.
3. Measurement of the absolute neutrino cross section on Helium in function of neutrino energy.
4. Measurement of the cross section ratio between neutrino and antineutrino charged current inclusive cros sections in function of diferent kinematical variables.

Appendix A

Work inside MINERνA collaboration

During my master and doctorate studies I worked in many tasks in the MINERνA collaboration. A brief description of them is presented in the coming sections.

A.1 Commisioning of the Test Beam Project

Incoming 16 GeV π collide with a graphite target to produce a tertiray beam composed by several particles in the 0.4 - 2 GeV energy range. Time of flight TOF scintillator counters measure transit time of particles. Hits on Wire Chamber (WC) WC1 through WC4 help reconstruct the trajectory of the charged particles (see figure A.1). During my Master studies I worked on the

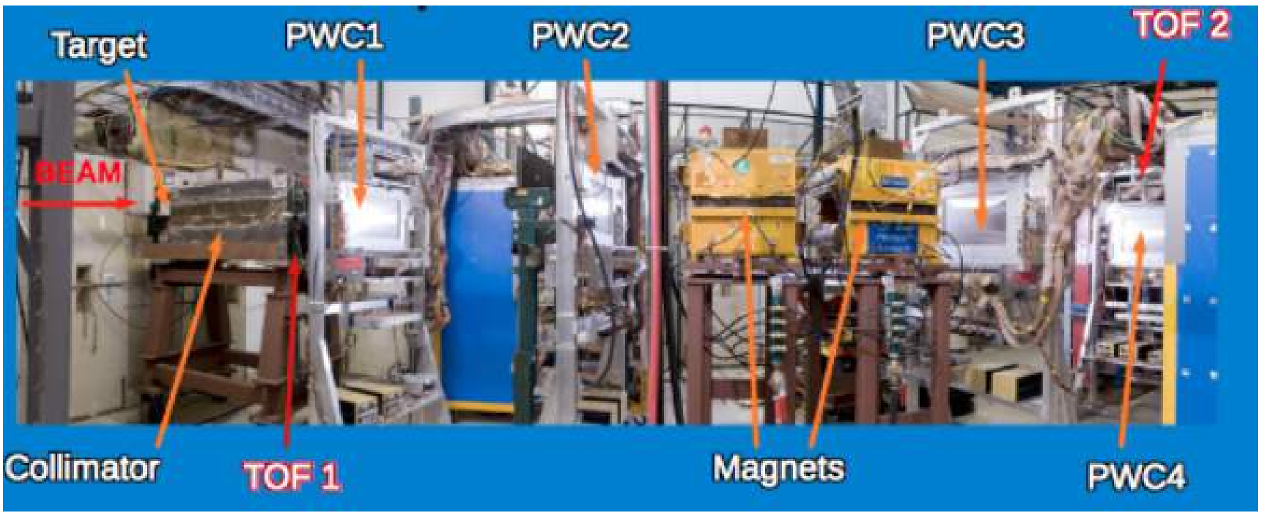

Figure A.1: Picture of the beamline installed in MT6 at Fermilab.

MINERνA neutrino scattering experiment, acquiring hardware and software skills participating on the commissioning, assembling, data acquisition, software development and data analysis for test beam experiment (see figure A.1), a new tertiary beamline to produce, identify and momentum-analyze low energy hadrons. The beamline was developed in conjunction with the Fermilab test beam facility and now is available to be used by other experiments. My work with the test beam group achieved the following goals and has been presented as my Master degree thesis [119]:

- Assembling and testing of beamline wire chambers making them operational (see figure A.2).
- Operation and preliminary mapping of magnetic field in the beamline (see figure A.3).
- Assembling, testing and operation of time of flight system, improving the particle identification (see figure A.4).
- Software used for the data adquisition system, identification and trajectories reconstruction for the particles present on the flux (see figure A.5).

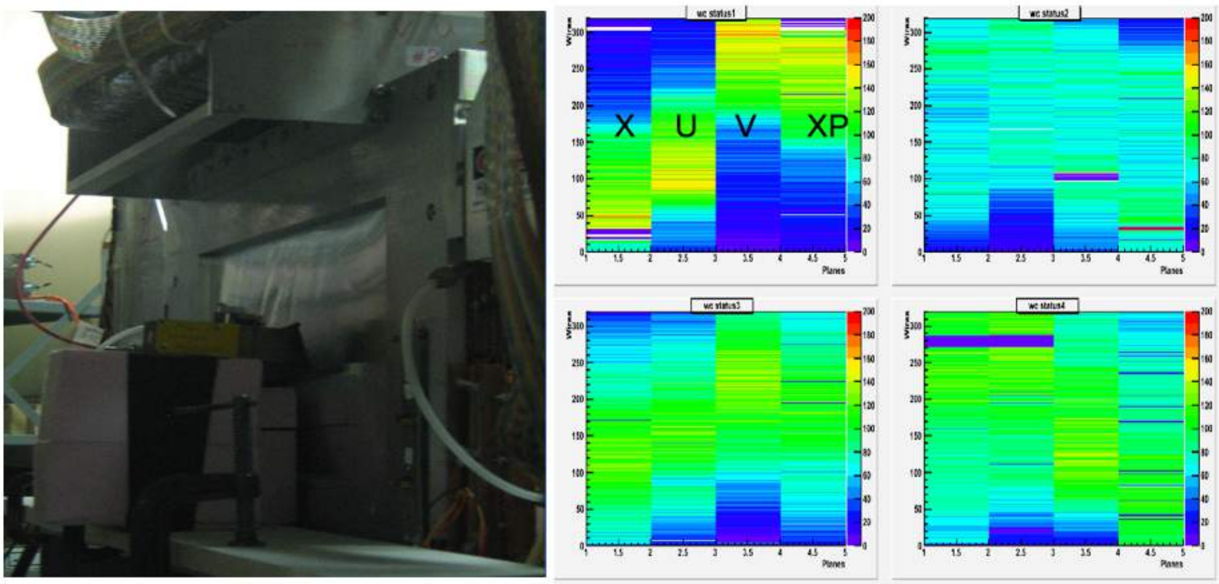

Figure A.2: Left: Wire Chamber source testing configuration Right: WC occupancy plots on a test beam run.

A.2 PMT Testing

I have participated in the testing of crosstalk of the multianode PMTS that are used for the readout of MINERνA detector and whose function is described in chapters 3 and 4. Figure A.6 shows that in average we find a crosstalk of 4.8 % for the 4 nearest pixels.

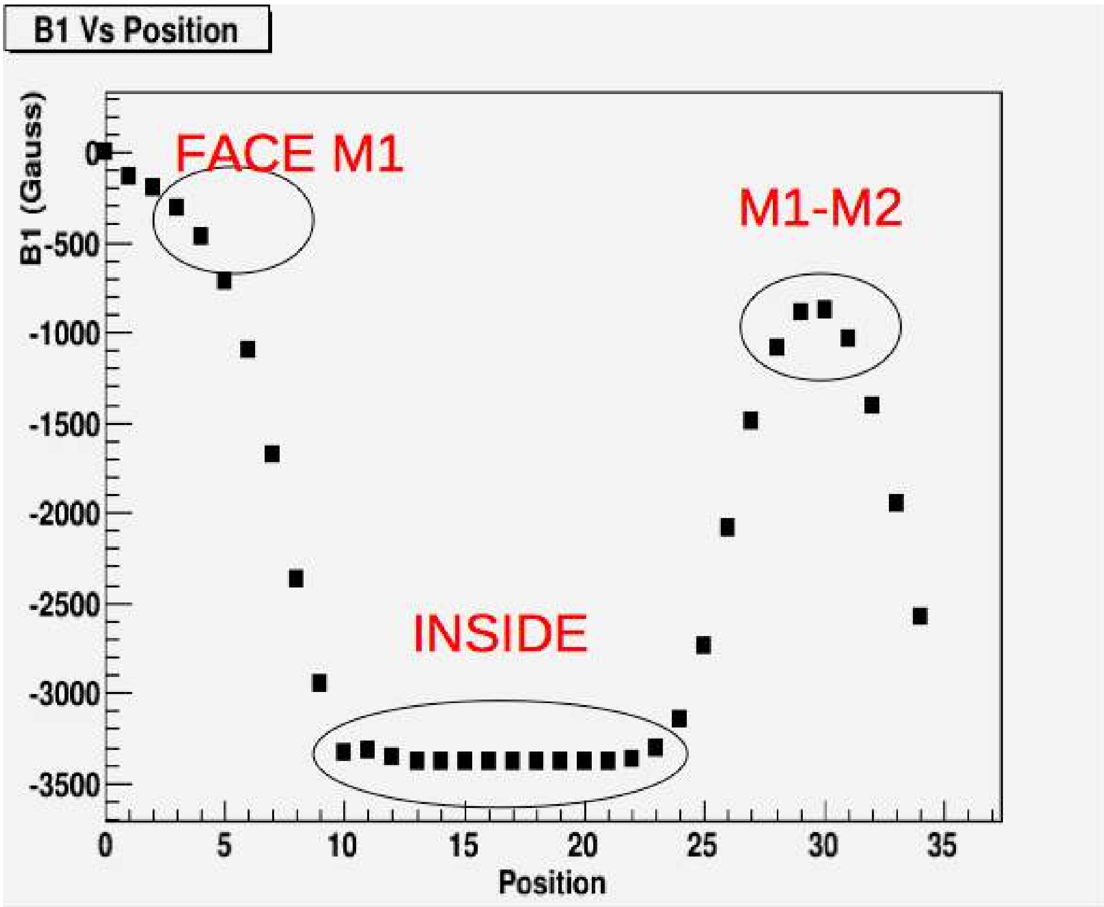

Figure A.3: Magnetic field measurement for one of the magnets in the beamline.

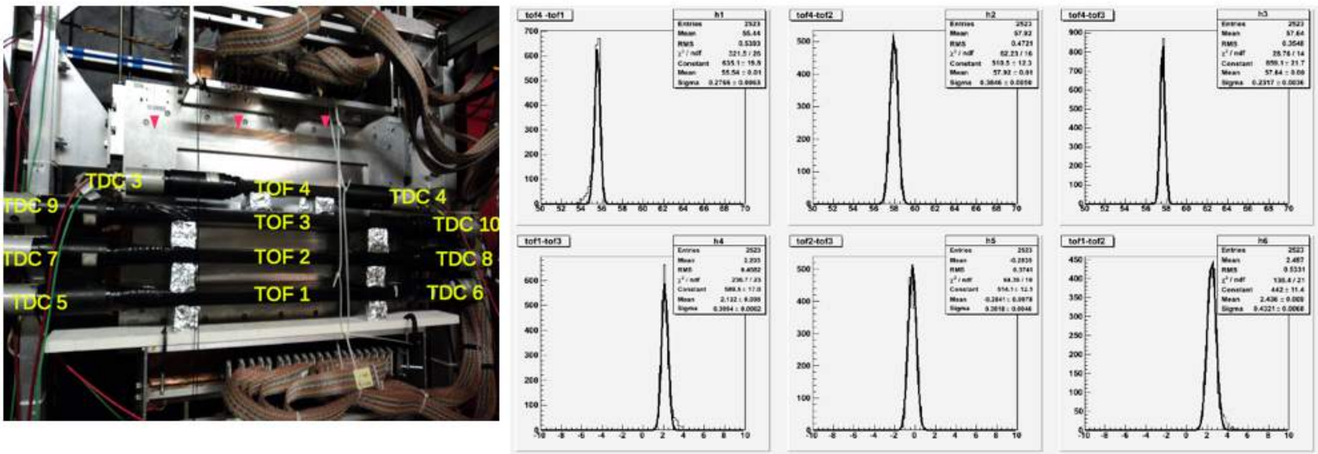

Figure A.4: Left: Time of flight system (TOF) testing Right: Resolution for different TOF configurations.

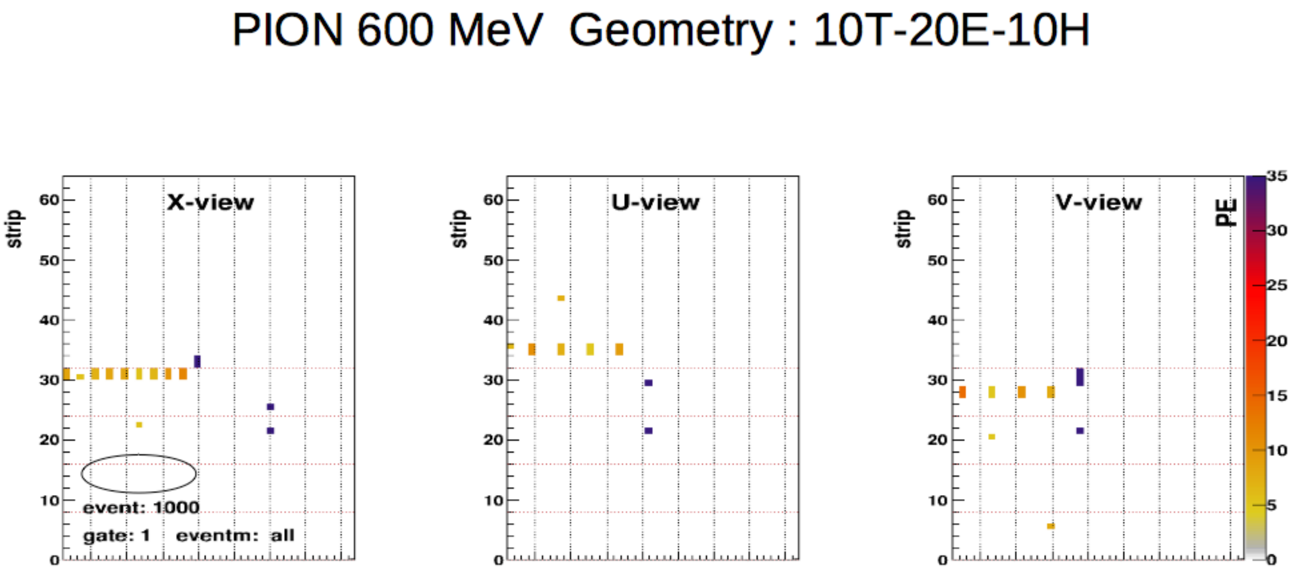

Figure A.5: Event display for a 600 MeV pion interacting on the MINERνA testbeam detector.

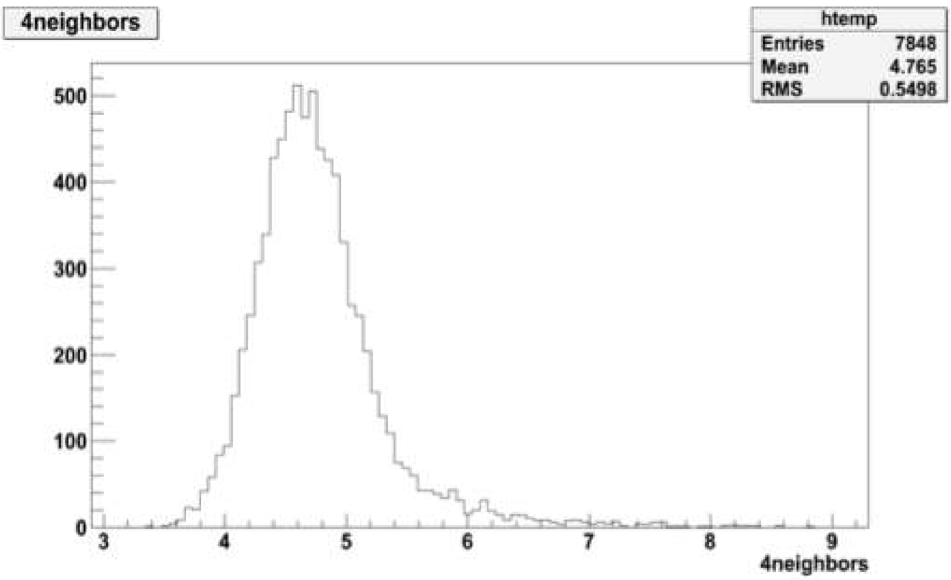

Figure A.6: Crosstalk distribution for the 4 neirest neighborhoods.

A.3 Charged current inclusive cross section machinery over different datasets

Comparison for different kinematic variables between different datasets over the entire data recorded by MINERνA (see figure A.7) to understand NuMI beam intensity effects.

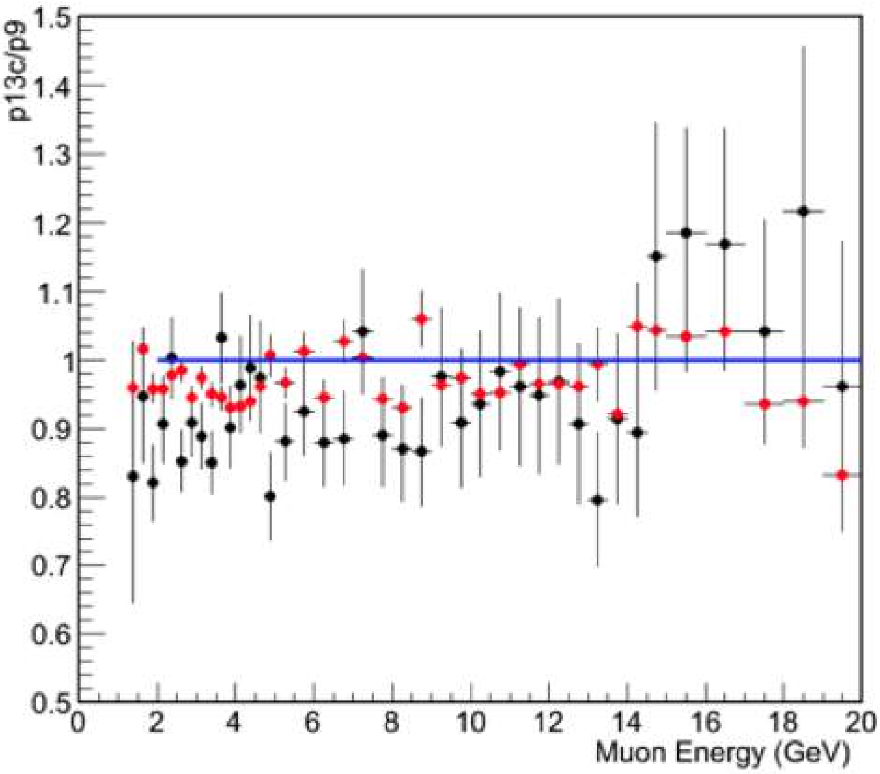

Figure A.7: Muon energy ratio for charged current interactions on tracker between two datasets with different NuMI beam intensities.

A.4 Special Runs

Analysis of data with different horn current and target position configurations.(Work done with Kenyi Hurtado see figure A.8)

A.5 Rock Muon Algorithm

Achievements:

- Locate the cross-talk digits over the rock muons.
- Include new classifications to the prongs *ExitBackID* and *ExitSideID* where ID refers the MINERνA inner detector.
- Extract Rock Muons from timeSlice.

An example of a rock muon on a timeslice can be seen on figure A.9.

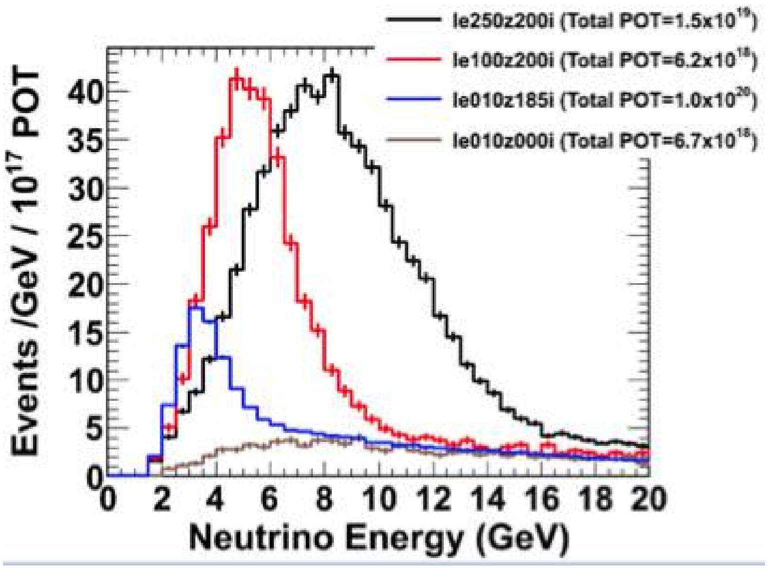

Figure A.8: Neutrino energy spectrum for different NuMI beam configurations.

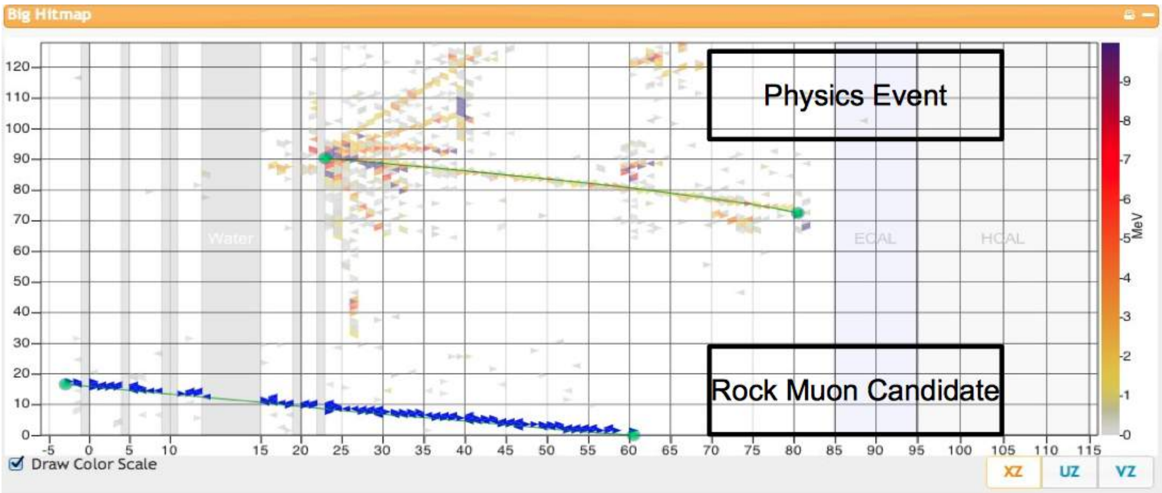

Figure A.9: Event display where is presented the rock muon superposed with a physics event.

A.6 Cross talk studies

Using the cross talk rejection algorithms on small samples of data and see the effect over different reconstructed kinematic variables (work done with Jeremy Wolcott see figure A.10).

A.7 RawDigit Checker

Main goal is identify **Problems** over raw data using the RawDigitCheckerTool.

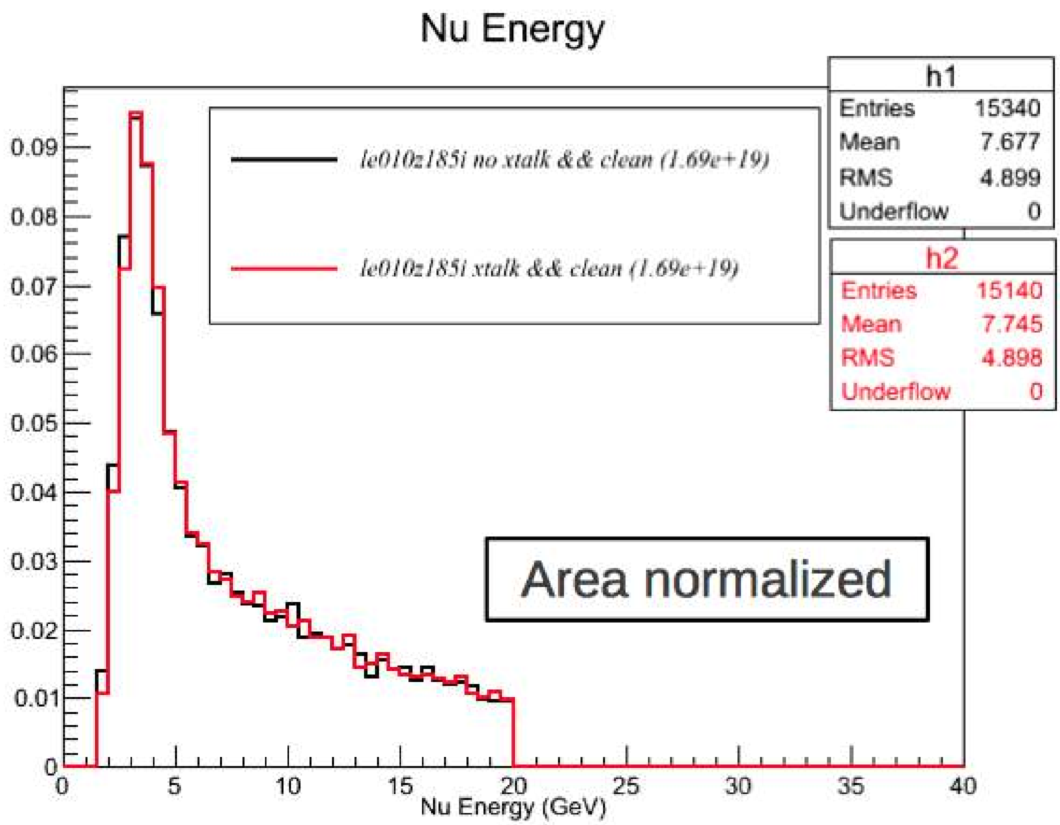

Figure A.10: Neutrino enery distribution for a subsample with (RED) and without (BLACK) cross talk rejection.

A.8 Multiple Vertex Studies Algorithm

Achivements:

- Keep multiple reconstructed vertices that are part of the same neutrino interaction in a single PhysicsEvent object.
- Split multiple vertices in the same timeSlice but from different neutrino interactions into separate PhysicsEvent objects (see figure A.11).

A.9 Data taking Shifts

This is a fundamental labor, due to is needed to have data to be analyzed by the experiment. I have participated taking shifts during all the data taking for the NuMI low energy configuration. (see figure A.12).

Finally is important to mention that all of the previous studies and algorithms were necessary for the current and future publication goals in MINERνA.

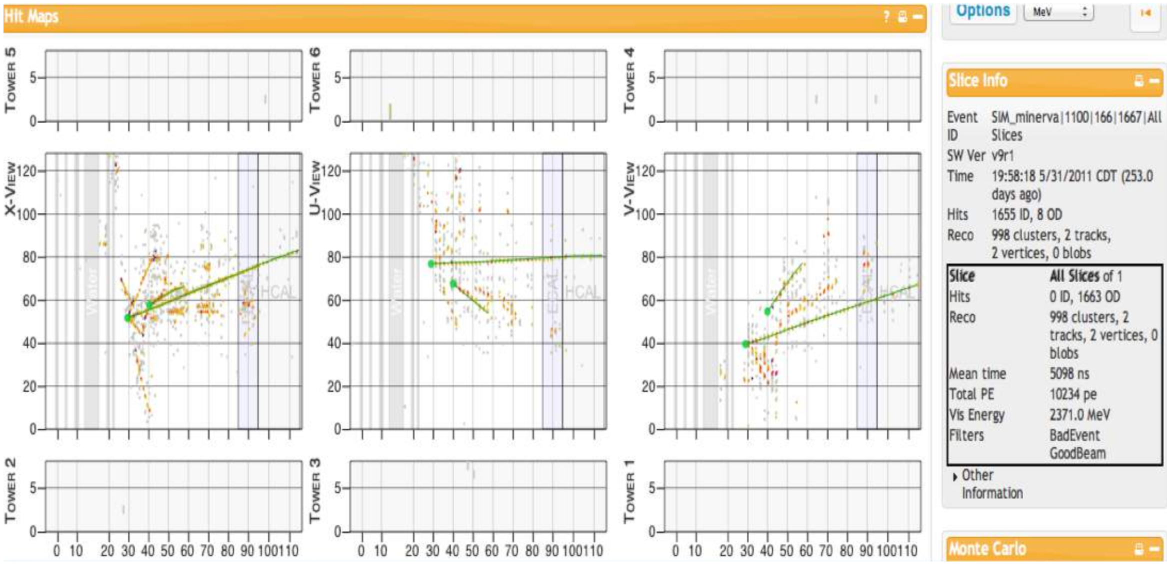

Figure A.11: Event display for multiple vertices that should be only one physics event.

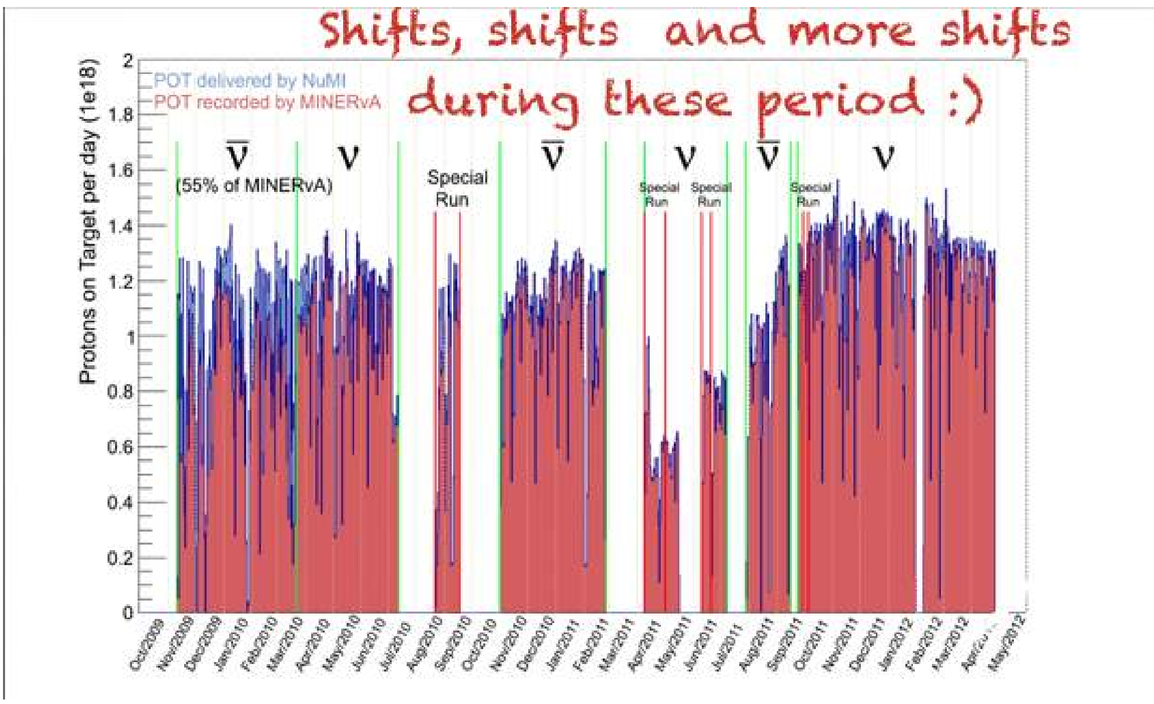

Figure A.12: Data run periods for MINERνA.

Bibliography

[1] Review of Particle Physics. Particle Data Group Collaboration (K.A. Olive (Minnesota U.) et al.) Chin. Phys. C38 (2014) 090001

[2] Z. Maki, M. Nakagawa, and S. Sakata, Prog. Theor. Phys. 28, 870 (1962).

[3] von Bayer, O. Hahn, L. Meitner, Phys. Zeitschrift, 12, January, 1911, p. 378

[4] C.D. Ellis, B.A. Wooster, The average energy of desintegration of Radium E,Proc. Roy. Soc. A117(1927) 109-123

[5] W. Pauli, carta enviada à Conferência de Tubingen, Dec. 1930.

[6] J. Chadwick, Possible existence of a neutron, Nature 129 (1932)12.

[7] E. Fermi, Ricercha Scient.**2** 12(1933).

[8] F.Perrin, Comptes rendues **197**, 1624(1933).

[9] E. Fermi, Z. Physik, **88** 161(1934).

[10] F. Reines and C.L. Cowan, The neutrino, Nature 178 (1956)446.

[11] M. Goldhaber, L. Grodzins, and A.W. Sunyar, Helicity of neutrinos, Phys. Rev. 109 (1958)1015.

[12] R. Davis and D.S. Harmer, Attempt to Observe the $Cl^37(\overline{\nu},e^-)Ar^37$ Reaction Induced by Reactor Antineutrinos, Bull. Am. Phys. Soc. 4, (1959)217.

[13] G. Danby et al., Observation of high-energy neutrino reactions and the existence of two kinds of neutrinos, Phys. Rev. Lett. 9 (1962)36.

[14] Gargamelle Neutrino Collaboration: F.J. Hasert et al., Observation of neutrino-like interactions without muon or electron in the Gargamelle neutrino experiment, Phys. Lett. B **46** (1973)138.

[15] R. Davis,D.S. Harner, and K.C. Hoffman, Search for neutrinos from the sun, Phys. Rev. Lett. 20 (1968)1205.

[16] DONUT COllaboration: T. Patzak, First direct observation of the tau neutrino, Europhys. News 32, 56 (2001).

[17] V.N. Gribov and B. Pontecorvo, Phys. Lett B **28**(1969)493.

[18] ALEPH Collaboration:D. Decamp et al., Determination of the Number of Light Neutrino Species, Phys. Lett. B **231**(1989)519.

[19] Delphi Collaboration:P.A. Aarnio et al.,Measurement of the Mass and Width of the Z0 Paricle from Multi-Hadronic Final States Produced in the e+ e- Annihilation, Phys. Lett. B **231** (1989)539.

[20] L3 Collaboration:B. Adeva et al.,A Determination of the Properties of the Neutral Intermediate Vector Boson Z0, phys. Lett. B **231** (1989)509.

[21] OPAL Collaboration:M.Z. Akrawy et al.,Measurement of the Z0 Mass and Width with the OPAL Detector at LEP, Phys. Lett. B bf 231 (1989)530.

[22] C. Athanassopoulos et ala., Candidate Events in a Search for Anti-Muon-Neutrino -¿ Anti-Electron-Neutrino Oscillations, Phys. Rev. Lett. 75, 2650, 1995.

[23] C.S. Wu et al., Phys. Rev. **105** (1957)1413.

[24] C. W. Kim, Neutrino Physics: Fundamentals of Neutrino Oscillations, Proceedings J. Korean Phys. Soc., Suppl. 1996. hep-ph/9607391

[25] P. Minkowski, Phys. Lett. B 67 (1977) 421.

[26] S. L. Glashow, Quarks and Leptons ed M Le vy et al (New York: Plenum) p 707, 1980.

[27] R. N. Mohapatra and G. Senjanovich, Phys. Rev. Lett. 44 (1980) 912.

[28] Steen Hannestad. Primordial neutrinos. In: Ann.Rev.Nucl.Part.Sci. 56 (2006), pp. 137161

[29] Gary Steigman. Primordial Nucleosynthesis in the Precision Cosmology Era. In: Ann.Rev.Nucl.Part 57 (2007), pp. 463491.

[30] Kenneth Greisen. End to the cosmic ray spectrum In: Phys.Rev.Lett. 16 (1966),pp. 748750.

[31] G.T. Zatsepin and V.A. Kuzmin. Upper limit of the spectrum of cosmic rays. In: JETPLett. 4 (1966), pp. 7880.

[32] A.M. Taylor. The Cosmogenic Neutrino Flux and Its Dependence on the Cosmic Ray Primary Composition. In: Cosmology, Galaxy Formation and Astrophysical Physics on the pathway to the SKA (2006)

[33] Yoshida S. url: $http://www-ppl.s.chiba-u.jp/\ syoshida/intro_astro/index.htm$ l.

[34] Leslie Camilleri, Eligio Lisi, and John F. Wilkerson. Neutrino Masses and Mixings:Status and Prospects. In: Ann.Rev.Nucl.Part.Sci. 58 (2008), pp. 343369.

[35] Anthony Mezzacappa. ASCERTAINING THE CORE COLLAPSE SUPERNOVA MECHANISM: The State of the Art and the Road Ahead. In: Ann. Rev. Nucl. Part. Sci. 55(2005), pp. 467515

[36] John F. Beacom. Supernova neutrinos and the neutrino masses. In: (1999). arXiv:hep-ph/9901300.

[37] T.K. Gaisser and M. Honda. Flux of atmospheric neutrinos. In: Ann.Rev.Nucl.Part.Sci.52 (2002), pp. 153199.

[38] Carlo Bemporad, Giorgio Gratta, and Petr Vogel. Reactor-based neutrino oscillation experiments. In: Rev. Mod. Phys. 74.2 (2002), pp. 297328.

[39] J. Goldstone. Field Theories with Superconductor Solutions. In: Nuovo Cim. 19 (1961),pp. 154164.

[40] Yoichiro Nambu. Quasiparticles and Gauge Invariance in the Theory of Superconductivity. In: Phys.Rev. 117 (1960), pp. 648663.

[41] M. Ravonel. Measurement of the Inclusive ν_μ charged current cross section in the near detector of T2K experiment. Phd Thesis, University of Geneva, September 2012.

[42] A. Salam, 1969, Proc. of the 8th Nobel Symposium on Elementary Particle Theory, Relativistic Groups and Analyticity, Stockholm, Sweden, 1968, edited by N. Svartholm, p. 367-377.

[43] S. Weinberg, Phys. Rev. Lett., 19, 1264-1266, 1967.

[44] J. Beringer et al. (Particle Data Group), Phys. Rev. D86, 010001 (2012).

[45] G. Aad et al. ATLAS Collaboration, "Observation of a new particle in the search for the Standard Model Higgs boson with the ATLAS detector at the LHC" Phys. Lett. B 716, 1 (2012) arXiv:1207.7214 (hep-ex)

[46] S. Chatrchyan et al. CMS Collaboration, "Observation of a new boson at a mass of 125 GeV with the CMS experiment at the LHC" Phys. Lett. B 716, 30 (2012) arXiv:1207.7235 (hep-ex).

[47] Remarks on the unified model of elementary particles. Ziro Maki, Masami Nakagawa, Shoichi Sakata, Prog.Theor.Phys. 28 (1962) 870-880

[48] B. Pontecorvo, J. Exptl. Theoret. Phys. 33, 549 (1957); ibid. 34, 247 (1958).

[49] J.Jo. Aubert et al. (EMC). The ratio of the nucleon structure functions f_2^N for iron and deuterium. Physics Letters B, 123(3):275278, (1983).

[50] J. A. Formaggio, G. P. Zeller, From eV to EeV: Neutrino cross sections across energy scales, Rev. Mod. Phys.: Volume 84.1307 (2012).

[51] J. Nieves, Jose Enrique Amaro, and M. Valverde. Inclusive quasi-elastic neutrino reactions. In: Phys.Rev. C70 (2004), p. 055503.

[52] Dieter Rein and Lalit M. Sehgal. Neutrino Excitation of Baryon Resonances and Single Pion Production. In: Annals Phys. 133 (1981), pp. 79153.

[53] V Lyubushkin et al. A Study of quasi-elastic muon neutrino and antineutrino scattering in the NOMAD experiment. In: Eur.Phys.J. C63 (2009), pp. 355381.

[54] S. Adler. In: Phys.Rev. B135 (1964), p. 963

[55] Veljko Dmitrasinovic and T. Sato. PCAC constraints on pion production / absorption within nonrelativistic nuclear dynamics. In: Phys.Rev. C58 (1998), pp. 19371947.

[56] R. Fiore and V.R. Zoller. Color dipoles, PCAC and Adlers theorem. In: JETP Lett. 85 (2007). 14 pages, 2 figures, pp. 309314.

[57] D. Rein and L.M. Sehgal. PCAC and the Deficit of Forward Muons in pi+ Production by Neutrinos. In: Phys.Lett. B657 (2007), pp. 207209.

[58] C. H. Llewellyn Smith, Neutrino reactions at accelerator energies, Phys. Rept. 3 (1972) 261.

[59] A. Bradford, A. Bodek, H. Budd and J. Arrington, A New Parametrization of the Nucleon Elastic Form Factors, Nucl. Phys. Proc. Suppl. 159, 127 (2006).

[60] M. Day, K. S. McFarland, Differences in Quasi-Elastic Cross-Sections of Muon and Electron Neutrinos, Phys. Rev. D 86, 053003 (2012).

[61] Bernard, V., et al., 2002, J. Phys. G 28, R1.

[62] Smith, R. A., and E. J. Moniz, 1972, Nucl. Phys. B43, 605.

[63] A. A. Aguilar-Arevalo, et. al. First measurement of the muon neutrino charged current quasielastic double differential cross section. Phys. Rev. D 81, 092005. May 2010

[64] A. Bodek, H.S. Budd and M. E. Christy, Neutrino Quasielastic Scattering on Nuclear Targets: Parametrizing Transverse Enhancement (Meson Exchange Currents), Eur. Phys. J. C 71 (2011) 1726.

[65] Baker, N., et al., 1982, Phys. Rev. D 25, 617.

[66] Baranov, D., et al., 1979, Phys. Lett. B 81, 255.

[67] Ciampolillo, S., et al. (Gargamelle Neutrino Propane Collaboration, Aachen-Brussels-CERN-Ecole Poly-Orsay-Padua Collaboration), 1979, Phys. Lett. B 84, 281.

[68] Nakajima, Y., et al. (SciBooNE Collaboration), 2011, Phys. Rev. D 83, 012005.

[69] B.G. Tice et al. Measurement of Ratios of ν_μ Charged-Current Cross Sections on C, Fe, and Pb to CH at Neutrino Energies 220 GeV. Phys. Rev. Lett. 112, 231801 .

[70] G. A. Fiorentini et al. Measurement of Muon Neutrino Quasielastic Scattering on a Hydrocarbon Target at E_ν 3.5GeV. Phys. Rev. Lett. 111, 022502 .

[71] L. Fields et al. Measurement of Muon Antineutrino Quasielastic Scattering on a Hydrocarbon Target at E_ν 3.5GeV. Phys. Rev. Lett. 111, 022501

[72] T. Walton. A MEASUREMENT OF THE MUON NEUTRINO CHARGED CURRENT QUASIELASTIC-LIKE CROSS SECTION ON A HYDROCARBON TARGET AND FINAL STATE INTERACTION EFFECTS. Phd Thesis, Hampton University, May 2014.

[73] B. Eberly. CHARACTERIZATION OF FINAL STATE INTERACTION STRENGTH IN PLASTIC SCINTILLATOR BY MUON-NEUTRINO CHARGED CURRENT CHARGED PION PRODUCTION. Phd Thesis, University of Pittsburgh, March 2014.

[74] P. Adamson et al. Improved search for muon-neutrino to electron-neutrino oscillations in MINOS. In: Phys.Rev.Lett. 107 (2011), p. 181802.

[75] Y. Abe et al. Indication for the disappearance of reactor electron antineutrinos in the Double Chooz experiment. In: Phys.Rev.Lett. 108 (2012), p. 131801.

[76] F.P. An et al. Observation of electron-antineutrino disappearance at Daya Bay. In:Phys.Rev.Lett. 108 (2012), p. 171803.

[77] J.K. Ahn et al. Observation of Reactor Electron Antineutrino Disappearance in the RENO Experiment. In: Phys.Rev.Lett. 108 (2012), p. 191802.

[78] M. Tortola, J.W.F. Valle, and D. Vanegas. Global status of neutrino oscillation parameters after recent reactor measurements. In: (2012). arXiv:1205.4018

[79] D.S. Ayres et al. NOvA: Proposal to build a 30 kiloton off-axis detector to study $\nu_\mu \to \nu_e$ oscillations in the NuMI beamline. In: (2004). arXiv:hep-ex/0503053

[80] Sanjib Kumar Agarwalla, Sandhya Choubey, and Amitava Raychaudhuri. Unraveling neutrino parameters with a magical beta-beam experiment at INO. In: Nucl.Phys. B798 (2008), pp. 124145.

[81] J. Hylen et al., NuMI Technical Design Handbook, Internal NuMI report (2003).

[82] R. M. Zwaska, Accelerator Systems and Instrumentation for the NuMI Neutrino Beam, PhD thesis University of Texas at Austin, 2005.

[83] Fermi National Accelerator Laboratory. The Fermilab Main Injector Technical Design Handbook. FERMILAB-DESIGN-1994-01, (1994).

[84] http://minerva-docdb.fnal.gov:8080/cgi-bin/ShowDocument?docid=2169

[85] N. Tagget al. Performance of Hamamatsu 64-Anode Photomultipliers for use with Wavelength-Shifting Optical Fibres. Nucl. Inst. and Meth., Phys. Res. Sect. A, 539:668678,(2005)

[86] D.G. Michael et al. (MINOS collaboration). The Magnetized steel and scintillator calorimeters of the MINOS experiment. Nucl. Inst. and Meth., Phys. Res. Sect. A, 596:190228, (2008).

[87] P. Adamson et al. (MINOS collaboration). Neutrino and antineutrino inclusive charged-current cross section measurements with the minos near detector. Phys. Rev. D, 81(7):072002, (2010)

[88] L. Aliaga et.al. Design, Calibration and Performance of the MINERvA Detector. Nucl. Inst. and Meth. A743 (2014) 130.

[89] B. Tice. MEASUREMENT OF NUCLEAR DEPENDENCE IN INCLUSIVE CHARGED CURRENT NEUTRINO SCATTERING. Phd Thesis, Rutgers University, January 2014.

[90] R. Fruhwirth. Application of Kalman filtering to track and vertex fitting. Nucl.Instrum.Meth. A262:444-450 (1987)

[91] E.J. Wolin and L.L. Ho. Covariance matrices for track fitting with the Kalman filter. Nucl. Inst. and Meth., Phys. Res. Sect. A, 329:493500, (1993)

[92] W. Waltenberger. Adaptive vertex reconstruction. Technical Report CMS-NOTE-2008-033, CERN, Geneva, (2008).

[93] D.E. Groom, N.V. Mokhov, and S.I. Striganov. Muon stopping power and range tables 10 MeV100 TeV. Atomic Data and Nuclear Data Tables, 78(2):183356, (2001).

[94] Z. Pavlovic. G4numi beam Monte Carlo, (2010). LBNE Beam Simulations Meeting.

[95] M. Kordosky , et. al. A brief documentation of the flux used in the may 2013 analyses, (2013). MINERvA Internal Note.

[96] L. Aliaga. MINERvA Flux: Current Uncertainties And Future Plans, (2012). Flux Measurement and Determination in the Intensity Frontier Era Neutrino Beams Workshop.

[97] L.J. Loiacono. Measurement of the muon neutrino inclusive charged current cross section on iron using the MINOS detector. PhD thesis, University of Texas at Austin, (2010).

[98] J. Park. Neutrino-Electron Scattering in MINERvA for Constraining the NuMI Neutrino Flux, (2013). MINERvA Internal Note No. 041

[99] J. M. Paley et al. Measurement of Charged Pion Production Yields off the NuMI Target. http://arxiv.org/pdf/1404.5882.pdf. April 2014.

[100] A. Bodek et al. Methods to Determine Neutrino Flux at Low Energies: Investigations of the low Method. Eur.Phys.J C72:1973 (2012).

[101] NA49 collaboration. NA49 Homepage. (1997). URL http://na49info.web.cern.ch/na49info/.

[102] Barton et. al. Experimental study of the a-dependence of inclusive hadron fragmentation. Phys.Rev. D27:2580 (1983).

[103] C. Andreopoulos , et. al. The genie neutrino monte carlo generator. Nucl.Instrum.Meth. A614:87-104 (2010).

[104] T. Yang, C. Andreopoulos, H. Gallagher, K. Hoffmann, and P. Kehayias. A hadronization model for few-GeV neutrino interactions. Eur. Phys. J. C, 63(1):110, (2009).

[105] D. Rein and L. M. Sehgal, Neutrino Excitation Of Baryon Resonances And Single Pion Production, Annals Phys. 133, 79 (1981)

[106] T. Sjostrand et al. . High-energy-physics event generation with pythia 6.1. Computer Physics Communications, 135(2):238259, (2001)

[107] T. Sjostrand and M. Bengtsson. The Lund Monte Carlo for jet fragmentation and e^+ e physics-jetset version 6.3an update. Computer Physics Communications, 43(3):367379, (1987).

[108] W.P. Abfalterer et al. Measurement of neutron total cross sections up to 560 MeV. Phys. Rev. C, 63(4):044608, (2001).

[109] L. Alvarez-Ruso ,et. al. The GENIE Neutrino Monte Carlo Generator: Physics and User Manual, (2013).

[110] L. Rakotondravohitra. Time spill structure. MINERvA document 9414-v2.

[111] A. Fiorentini. Measurement of muon neutrino quasi-elastic scattering on a Hydrocarbon target at $E_\nu \approx 3.5$ GeV. Phd thesis, Centro Brasileiro de Pesquisas Fisicas (CBPF). May 2013.

[112] G. A. Fiorentini et. al.; Measurement of Muon Neutrino Quasi-Elastic Scattering on a Hydrocarbon Target at $E_\nu \sim 3.5 GeV$; Phys. Rev. Lett. 111, 022502 (2013).

[113] G. D' Agostini A multidimensional unfolding method based on $Baye's$ theorem, Nucl. Instrum. Methods in Phys. Res. Sect. A 362 (1995) 487-49

[114] David W. Schmitz, MINERvA Technical Note No. 016:Reconstruction efficiency corrections. available at http://minerva-docdb.fnal.gov:8080/cgi-bin/ShowDocument?docid=8646.

[115] B.G. Tice. Post-framework analysis histograms for MINERvA. MINERvA Internal Note TN22, (2013)

[116] C. Alt et al., Inclusive production of charged pions in p + C collisions at 158 GeV/c beam momentum. Eur. Phys. J. C 49, 897917 (2007).

[117] L. Aliaga et. al.; Design, Calibration, and Performance of the MINERvA Detector; Nucl.Inst.Meth. A473 (2014) 130; arxiv:1305.5199.

[118] T. Golan, C. Juszczak, J. T. Sobczyk, Effects of final-state interactions in neutrino-nucleus interactions, Phys. Rev. C 86 (2012) 015505.

[119] D. Martinez Caicedo. Comissionamento e Analise do Feixe de Teste do Experimento MINERνA. Master Thesis, Centro Brasileiro de Pesquisas Fisicas (CBPF), July 2010.